Evaluation of a laser Land-based Mobile Mapping System for measuring sandy coast morphology

Maja Bitenc

TU Delft Delft University of Technology

Challenge the future

Cover illustration: Background image of a sandy forms and the top image of a beach near Egmond an Zee are adapted from Google Earth tagged photos. The lower image shows the laser L-MMS system so-called StreetMapper. The photo was taken during the acquisition mission of the pilot-project Egmond aan Zee.

MSc Geomatics Graduation Thesis

Evaluation of a laser Land-based Mobile Mapping System for measuring sandy coast morphology

Maja Bitenc

March 8, 2010

Department of Optical and Laser Remote Sensing
Faculty of Aerospace Engineering
Delft University of Technology
The Netherlands

Graduation Professor: Prof. dr. M. Menenti
Supervisors: Dr. R.C. Lindenbergh and Dr. K. Khoshelham
Co-reader: Ir. E. Verbree
Contact email address: bitenc.m@gmail.com

Preface

Being at the end and looking at the beginning of my MSc Geomatics study at Delft University of Technology (TU Delft), I realize how fast time has passed. I had the opportunity to work individually on practical assignments, be challenged to solve a real problem within a small group of Geomatics students and finally to study for more than nine months on a specific topic of my interest, laser remote sensing. My research of laser technique started with an Airborne Laser Scanning (ALS) technique in 2007, when I successfully concluded the one year diploma thesis at the University of Ljubljana. In 2008 I was part of the Terrestrial Laser Scanning (TLS) team of the bimonthly Geomatics Synthesis project. The recommendation following the synthesis project results directed my attention to the relatively new and fast developing technique laser Land-based Mobile Mapping System (L-MMS). By chance an opportunity arose to obtain the real laser L-MMS data that were acquired on the Dutch coast for a Dutch Ministry of Transport, Public Works and Water Management (RWS, Rijkswaterstaat) pilot-project. But how useful L-MMS actually is and what advantages, in comparison with known techniques, it brings when measuring the beach morphology and its changes, was the question that started my master thesis.

This report presents the results of my intensive master thesis research. Because the laser L-MMS is a new research topic at the Department of Optical and Laser Remote Sensing (TU Delft), this report includes information of a wider scope. To avoid the confusion of commonly (mis)used expressions a few sections were added to explain how those expressions are used in this report. Moreover, the chapters of this report are extended with background theoretical explanations, examples and case studies of the developed methodology in order to ease their implementation in further research. However, I did my best to keep the content as simple and short as possible. At the beginning of each chapter an overview of the sections' content is given and at the end of the chapter the main information is summarized.
Those who are unfamiliar with the coastal area characteristics and would like to know what objectives and requirements drove this research, are referred to Chapter 2. If for someone the concept of the Mobile Mapping System (MMS) technology is unknown, the background information of MMS and detailed description of laser L-MMS is given in Chapter 3. The next five chapters cover more practical issues aiming at evaluation of the laser L-MMS for measuring the sandy coast morphology. Of special interest might be Chapter 8 presenting the analysis of the most important laser L-MMS results. That is, the evaluation of the laser L-MMS Digital Terrain Model (DTM).

The research and especially this report would not be so wide and complete if it would not have been supervised by Roderik Lindenbergh. Many thanks to Roderik for all ideas and questions that directed and deepened my research, thanks for patiently and carefully checking all sections and persistently sharpening my sentences. Half way through the research the "drop by office" meetings with Kourosh Khosh Elham became longer and more frequent, and finally turned into official supervision. I would like to thank Kourosh for enthusiastically sharing his time and great expertise. It was my great pleasure to debate and find solutions much easier with his help. I would like to express my thanks as well to Massimo Menenti who could find the time in his busy schedule to frequently check my work and comment on it always in a very stimulating manner. At this point many thanks to all Geomatics department, lecturers, administrative staff and also my fellow M.Sc. students. I could say this was a little happy family, I could rely on whether it was about a technical question, legal documents to be sent in time or any help when studying in Delft. Furthermore, I would like to thank Pieter van Waarden from Data-ICT-Dienst department of RWS, to mediate the data of their pilot-project and to give his practical view on the topic. Thanks also to Civil Engineering and Geosciences colleagues. It was interesting to hear the coastal engineer aspects of what is important when measuring the coast. I am especially grateful to the TerraSolid team that provided licenses of their modules, I could use to process the laser data. Last but not least many thanks for the persistent support and animation during the dark days of the research to all my friends here in the Netherlands and at home in Slovenia. You were my source of energy and motivation when calling, mailing, giving little surprise presents, hosting me for months or nights, reading and commenting the report. In particular, I would like to thank my mum and dad I could always feel a stream of good wishes and warm presence, brother and sister in law to whom I could express my personal worries and happiness and boyfriend Rabih who gave me the freedom to work hard on this thesis and did his best to take care of me.

Being at the end and looking in the future, I feel that now I could start real laser L-MMS research. Many interesting topics showed up during the research and many different applications follow from the system. Therefore, I hope that this report contributes to the spread the laser L-MMS usage and inspires the reader for further research.

I wish everyone a pleasant drive through the laser L-MMS research.

Maja Bitenc
Delft, February 2010

Contents

Summary

The coastal area is an important territory for many reasons, e.g. as a recreational area, natural parks and reservoirs, protection against sea flood and storms. The last usage is especially crucial in the Netherlands, because the most densely populated areas are located just behind the coastal defense and are partly below the mean sea level. Therefore, it is essential to continuously monitor and maintain the coast in order to protect the Dutch hinterland from the sea. Since 1965 the Dutch Ministry of Transport, Public Works and Water Management (RWS, Rijkswaterstaat) annually acquire the JAarlijkse KUStmetingen (JARKUS) data. The cross-shore topography and bathymetry is measured along profiles $250m$ apart. The disadvantage is, that the JARKUS data are too sparse in time and space, to ensure sufficient observations of the dynamic coast environment. The time is especially important, when a high energy event occurs that can cause most dramatic changes. Therefore, a flexible system is needed that can access a damaged area immediately after the storm and enables (near) real-time processing of the captured data. To make right and timely decisions it is important that results, e.g. DTM, are available shortly after the acquisition itself. Besides, to estimate in detail the beach erosion caused by heavy storm events, high spatial resolution measurements are needed.

According to the above described application and requirements the most appropriate acquisition technique and processing has to be chosen. Advances in the hardware and software technologies enable to directly acquire 3D models from real world environments [Grinstead et al., 2005]. Compared to the laser airborne system, i.e. ALS, which is commonly used by now to map the beach topography, the vehicle platform is considered to be more flexible. One of the potential techniques is the laser L-MMS. It is a complex real-time, multi-tasking and multi-sensor system. It integrates line scanners and optionally digital cameras for mapping, Global Navigation Satellite Systems (GNSS) for positioning and usually Inertial Navigation System (INS) to measure platform orientation. The measurements from those sensors are integrated and result in a 3D laser point cloud. In principle it is possible to quickly obtain 3D data of a large extended area with a high spatial resolution. On the basis of the mentioned properties, RWS decided to initiate a pilot-project using a laser L-MMS. The requirements for the acquired data are that the vertical accuracy of DTM is at least $10cm$ at a grid spacing of $1\times1m$ and that this result is available close to the real-time.

In this master thesis the level of obtainable quality of the laser L-MMS data and de-

rived laser L-MMS DTM is investigated in detail. This evaluation is performed in three steps. First, an a-priory analysis is performed on the basis of the L-MMS geo-referencing model. This model includes L-MMS measurements of the three sensors and calibration parameters connecting those sensors. The result is 3D laser point cloud. By nature, the observations entering the geo-referencing model include errors and therefore effect the 3D laser point positioning quality. To estimate this quality a theoretical random error budget is constructed. It shows the relative components of random errors within the system and the expected quality of the laser point positioning. The specifications and estimated observations' random errors of the L-MMS system called StreetMapper are considered in a practical random error budget computations. Results show that the GPS/INS positioning error impacts the 3D laser point position the most. The second biggest contributors are errors of the laser scanner measurements, i.e. errors in range and scanning angle. The range error effects more the horizontal and scan angle error the vertical positioning error. Because the StreetMapper GPS/INS positioning solution on the open beach area is relatively good, the further laser point quality improvements should consider laser scanners of higher precision.

In the second analysis the theoretical model of the described pre-analysis is applied on the real L-MMS data. That is, the height precision due to the L-MMS measurement and calibration errors (measuring precision) is computed for each laser point. Besides, the intersection geometry of the laser beam with the relatively horizontal and flat beach is investigated. The scanning geometry is changing a lot over the beach and gets poorer further away from the trajectory. This means that the distance from the laser scanner to the target as well as the incidence angle increases. Those geometric attributes are teken into account to compute the so-called geometrical precision. Together with the measuring precision they define the theoretical precision of the laser point height. Besides, an empirical quality measure is obtained by a relative Quality Control (QC). The relative QC is here developed considering the land-based laser data advantage, like a high laser point density that results in overlapping footprints. Height differences between the two overlapping laser points, called identical points, are considered as the empirical quality measure. The comparison of the theoretical and empirical quality measures shows big differences. Most likely the theoretical precision is estimated too pessimistic, because the random errors of the measurements and calibration parameters are mostly overestimated. It is therefore recommended to first verify the theoretical error model by comparing the values obtained in this research with reference data of a higher quality. This way also the systematic errors could be verified, that are here assumed to equal zero. On the other hand, the assumptions on the identical points should be further tested.

In the third analysis a laser L-MMS DTM is evaluated. DTM is the most important or in other words, the most widely used L-MMS product that should be provided to the end user together with a detailed quality description. This way, a DTM user can better trust and rely on the DTM height information. Here, the goal is to answer the RWS question, weather the DTM of $1\times1m$ size can have a quality better than $10cm$. The L-MMS and ALS dataset are used in this analysis. First, the L-MMS terrain laser points are divided

into a $1 \times 1m$ grid cells. A weighted Moving Least Squares (MLS) is performed for each grid cell to fit a tilted plane to its terrain points. The weight matrix is constructed from the individual theoretical laser point variances. This method is applied on the StreetMapper terrain points that lie on the sandy beach and part of the dunes. Resulting interpolated grid point heights do not differ much from the averaged height of those terrain points. Therefore it is concluded, that the simple averaging interpolation can be used to construct a laser L-MMS DTM on the Dutch beach. The resulting L-MMS DTM quality is highly dependent on the number of terrain points within a grid cell. Because the L-MMS point density is in general very high, those redundant data reduce the random errors of laser point positioning. Thus, the DTM has on average higher quality than the input laser data. It is concluded that the RWS requirement on the laser L-MMS DTM accuracy can be easily met for the beach and the dune area. Most of the grid cell on the beach have the height precision better than $1cm$. To achieve similar accuracy also in the dune area, a measurement set-up needs to be changed in order to acquire more points. Thus, it is recommended that the vehicle drives closer to the dune foot and that the laser scanners are lifted higher above the ground. The comparison of L-MMS and ALS data shows the advantage of the L-MMS technique due the high laser point density. On the other hand ALS technique offers better data coverage on the coast. However, higher laser scanner platform might minimize the L-MMS data voids that occur behind elevated features in the pre-dune area. This way the completeness, reliability and the quality of the laser L-MMS DTM DTM could be improved.

List of abbreviations

ALS	Airborne Laser Scanning
TLS	Terrestrial Laser Scanning
MMS	Mobile Mapping System
L-MMS	Land-based Mobile Mapping System
A-MMS	Airborne Mobile Mapping System
GNSS	Global Navigation Satellite Systems
GPS	Global Positioning System
DGPS	Differential Global Positioning System
INS	Inertial Navigation System
IMU	Inertial Measurement Unit
POS	Position and Orientation System
RTK	Real-Time Kinematic
WGS84	World Geodetic System 1984
TOF	Time-Of-Flight
PD	Phase Difference
LASER	Light Amplification by Stimulated Emission of Radiation
LIDAR	LIght Detection And Ranging
RWS	Rijkswaterstaat; en. Ministry of Transport, Public Works and Water Management
DID	Data-ICT-Dienst
WD	Water Dienst

JARKUS JAarlijkse KUStmetingen

DTM Digital Terrain Model

DEM Digital Elevation Model

DSM Digital Surface Model

TIN Triangular Irregular Network

AHN Actueel Hoogtebestand Nederland; en. The current elevation map of the Netherlands

GCP Ground Control Point

QA Quality Assurance

QC Quality Control

RMSE Root Mean Square Error

GIS Geographical Information System

CAD Computer-Aided Design

MLS Moving Least Squares

LSA Least Squares Adjustment

MAD Median Absolute Deviation

List of Figures

List of Tables

Chapter 1

Introduction

1.1 Motivation

The Dutch coast typically consists of a relatively flat sandy beach lined on one side by the dunes, which are partly covered by marram grass. This coastal area is important for the Netherlands for many reasons, e.g. as recreational and nature area, and as protection against a sea flood and storms. The last usage is especially crucial, because the most densely populated areas in the Netherlands are located just behind the coastal defense and are partly below the mean sea level. Therefore, it is essential to continuously monitor and maintain the coast in order to protect the Dutch hinterland from the sea. In 1990 a national coastal policy was adopted, with the aim of maintaining the seaward position of the coastline. This coastline is taken as a Basal Coast Line (BKL) according to its situation on January 1, 1990. To successfully maintain BKL, first the processes that occur within the coastal area must be well understood. Secondly, the most suitable acquisition technique to measure beach morphology and its changes needs to be employed.

Since 1965 the Dutch Ministry of Transport, Public Works and Water Management (RWS, Rijkswaterstaat) annually acquires the JARKUS data. First leveling and the Global Positioning System (GPS) technology was employed. Nowadays JARKUS data are derived from echo sounding and ALS. For the JARKUS data collection the cross-shore topography and bathymetry is measured along profiles 250 m apart. Afterwards, long-term beach erosion and sedimentation are mapped [NCK, 2010]. The disadvantage is, that the JARKUS data are too sparse in time and space, to ensure sufficient observations of the dynamic coast environment. The temporal sampling is especially important, because high energy events like storms may occur causing large changes. Therefore, a flexible system is needed that can access a damaged area immediately after the storm and provide the results of morphologic changes as quickly as possible (in one day). Besides, to estimate in detail the beach erosion caused by heavy storm events, high spatial resolution measurements are needed.

With these requirements in mind, new techniques that appeared in the last decades due

to fast technological development, are considered and tested. One of the potential techniques is the L-MMS. An L-MMS is a complex real-time, multi-tasking and multi-sensor system, which integrates (i) a number of line scanners and digital cameras for surface mapping, (ii) GNSS for positioning and (iii) additional sensors like for example INS to monitor the vehicle motion. Those sensors are usually mounted on a rigid platform, placed on the roof of a vehicle. The L-MMS linear laser scanners can be of different type and orientation, which makes every L-MMS system unique in terms of performance and thus quality. Using L-MMS it is in principle possible to quickly obtain 3D geo-referenced data of a large extended area, such as a beach. Besides, the high frequency laser pulse measurements enable high spatial resolution. Compared to the laser airborne system (i.e. ALS), which is commonly used to map the beach topography, the vehicle platform is considered to be more flexible. Additionally, higher point density is expected in case of the land-based system, because the measured ranges are smaller. On the other hand, more data voids might occur behind elevated features when measuring from the ground. Besides, attention must be paid to the intersection geometry of the laser beam with the relatively horizontal beach. This scanning geometry is expected to be changing a lot over the acquisition area. If scanning a horizontal surface, the geometry gets poorer further away from the trajectory. This decreases the laser point positioning quality.

In order to test the L-MMS performance on the Dutch coast RWS initiated a pilot-project. The main interest is to monitor coastal changes on the temporal and spatial scale of storm impacts. This means, that the L-MMS is capable to measure few tens of kilometers with a high spatial resolution. A continuous monitoring during the storm season is preferable, to observe the resulting small scale changes on the beach. Within the pilot-project the particular interest of the RWS is the level of obtainable accuracy and processing time of a final topographic product. The most important result derived from the laser L-MMS data is a DTM. Preferably also the DTM quality description is provided together with the DTM. In this way, a DTM user can better trust and rely on the height information. The RWS requirement for the vertical accuracy of a DTM is to be at least $10cm$ at a grid spacing of $1\times1m$. Moreover, RWS require that the results are available close to real-time.

1.2 Research objective and questions

This master thesis project joined the RWS pilot-project, shortly introduced in the previous section. The laser Land-based Mobile Mapping System (L-MMS) is employed to acquire the topography of the Dutch coast and the system performance is evaluated considering the requirements of RWS.

The main research objective of this master thesis is:

Evaluate the laser Land-based Mobile Mapping System (L-MMS) for measuring the morphology of sandy coasts.

To reach the main research objective, five research questions are set up:

1. ***What error components contribute to the performance of the laser L-MMS system?*** The L-MMS is multi-sensor system, where measurements of three main sensors are combined to obtain 3D laser point coordinates. Each measurement has errors which influence the final results. Therefore, to predict the quality of 3D laser points, each component of L-MMS system will be studied and the impact of their errors on the point positioning will be analyzed. Such an error pre-analysis of the L-MMS system aims to construct and quantify the error budget of the system and so to validate the expected L-MMS performance.

2. ***What is the quality of the individual L-MMS laser points?*** The answer to this question is needed, because the laser points are expected to exhibit different positioning quality. The reason is, that the points might be acquired with different laser scanners of different quality and orientation. Moreover, the individual quality of laser points is changing with the scanning geometry. The question to be answered here is how they are related.

3. ***What is the quality of the derived laser L-MMS DTM?*** A DTM is derived from the terrain laser points. Their quality, which is estimated already within the previous research question, and besides some other factors influence the final DTM quality. Hence, the main aim is to estimate error components that contribute to the DTM quality and finally to estimate this quality as a whole. It will be investigated if the requirements of RWS on the DTM accuracy, as written in Section 1.1, can be met.

4. ***What are the advantages of the laser L-MMS technique compared to ALS?*** In Section 1.1 the pros and cons of both techniques were already introduced. Here the real laser L-MMS data will be compared to the already tested ALS data. Besides the accuracy of both DTMs, also the coverage of both L-MMS and ALS data is of special interest.

5. ***What L-MMS measurement set-up leads to optimal results for coastal monitoring?*** Measuring the morphology of a sandy beach with the L-MMS technique is rather an experimental project. Therefore, an optimal L-MMS measurement set-up for coastal monitoring is analyzed. System set-up parameters as the height of the laser scanner(s) above the ground, the driving speed and the position of trajectories with regard to the foot of the dunes will be considered.

1.3 Research methodology

The main research objective, which is decomposed in to five research questions, is investigated by combining different methodologies. At first, an extensive literature study is needed to get an insight into the topic. Because the laser L-MMS technique is relatively new, not much literature is found. However, the knowledge from other MMS systems is

used and combined in this research. Another issue to be solved beforehand is, to find an appropriate software. The laser data include millions of 3D points, which requires efficient processing algorithms and visualization methods. In this research the TerraSolid modules are used to resize the data, which are further on analyzed in Matlab.

The first research question is investigated on a theoretical basis, using the mathematical model of geo-referencing. The observations included in this mathematical model, i.e. the L-MMS measurements and calibration parameters, by nature include errors. The errors influence the quality of the derived unknowns, i.e. laser point coordinates. To quantify the overall expected quality of the 3D laser points, a first order error pre-analysis is performed linearizing the geo-referencing equation. In other words, an a-priory system validation is performed by the random error propagation through the geo-referencing model. A theoretical error budget of the L-MMS will be determined. At this point, no real measurements enter the calculation. Thus, the result is a theoretical (a-priory) quality of the derived 3D laser point cloud.

To answer the second research question, the real laser L-MMS data acquired on the coast near Egmond aan Zee is examined. First, simple geometrical rules are applied to reconstruct the scanning geometry at the time of each laser point acquisition. Then the theoretical height precision of each laser point is calculated. To do so, the first order model of error propagation as obtained in the first question analysis is used. Secondly, a proper Quality Control (QC) procedure will be looked for to estimate an empirical quality of laser points. Considering the available L-MMS data, an empirical relative QC of so-called identical points is developed. The height differences between identical points are taken as an empirical quality measure. Those differences are analyzed in order to check the L-MMS laser point heights for systematic errors. Finally, the statistical measures such as Root Mean Square Error (RMSE) are employed to compare the theoretical and empirical measures of laser point height precision. Attributes of laser points such as range and incidence angle will be taken into consideration for this analysis.

The third research question is investigated using the terrain laser points of the Egmond aan Zee data set. Those points are used to construct a laser L-MMS DTM by an interpolation method and estimate its quality. First a grid of $1\times1m$ size is laid over the terrain. For grid cells, which include 4 or more terrain laser points, a tilted plane is modeled by weighted least square. That is, the 3D coordinates of the terrain laser points and their variances enter a Moving Least Squares (MLS) adjustment. The main results are an interpolated grid point height, a propagated error of original terrain points and a terrain roughness measure. Those results are influenced by factors such as the density and distribution of terrain laser points, the height precision of individual terrain laser points, the interpolation method and the terrain roughness. Therefore, those influencing factors are individually evaluated and their impact on the obtained precision of the grid point heights is investigated.

The fourth research question is investigated by using the laser points acquired by the

L-MMS system StreetMapper in November 2008 and the terrain laser points acquired by the ALS system Harrier56 in April 2008. Both datasets are gridded using the same grid position and spacing of $1 \times 1m$. Grid cell attributes as point density, height standard deviation and average height are compared. The average height of the laser points within a grid cell is taken as the grid point height. The DTMs obtained with this simplified interpolation method are subtracted and the height differences are analyzed.

The fifth research question is answered by synthesizing the results obtained within the research on the previous research questions.

1.4 Thesis outline

This report is the final product of a master thesis project, where the theory and all important results are presented in a logical sequence of processing. The chapters are written so as to be understandable to a wider public as well as to geo-science professionals. In this section the thesis outline is presented. It can be used as a reading guide to better understand how the different parts of analysis contribute to the overall objective of the research. At the end of each chapter a short summary section is added, where the main points and information of the chapter are collected.

The structure of this thesis is as follows:

- In Chapter 2 the application in hand, i.e. measuring the morphology of sandy coasts, is introduced. First, the characteristics of the acquisition area, i.e. Dutch coast, are described. Further on, the requirements for the measurements to map beach morphologic changes during and after a storm are given. With those requirements in mind the potential acquisition techniques are described and compared. Among them, the laser L-MMS technique was chosen by RWS to be tested. Therefore, in the following the organization, objectives and initial results of this pilot-project Egmond aan Zee are described. At the end, the relevance of the pilot-project to this master thesis is given.

- In Chapter 3 the concept of the MMS technology is given as a whole. First some background information and development of MMS technology is described. Then the focus is directed to the laser L-MMS system. Its variable applications and subsystems are presented. Finally, the actual laser L-MMS system employed in the pilot-project Egmond aan Zee is described and its geo-referenced data are presented.

- In Chapter 4 the error pre-analysis is made to validate the expected laser L-MMS performance. At the beginning theory on quality measures, i.e. accuracy and precision, and the law of error propagation is given. This theory is applied on the L-MMS georeferencing model that includes all L-MMS measurements and calibration parameters needed to derive the laser point coordinates. The derived first order error model

is then used to construct and quantify the error budget of the StreetMapper system.

- In Chapter 5 the real laser L-MMS data are used to asses the quality of individual laser point. First, this quality is estimated theoretically employing mathematical models based on geo-referencing formula. Secondly an empirical approach is used. A relative QC that employs the height differences between so-called identical points is developed. In both cases the influence of the scanning geometry is investigated.

- In Chapter 6 the individual laser point height precisions are presented. Sections with results follow the methodology description given in Chapter 5. Therefore, first the additional attributes of scanning geometry and theoretical height precisions are visualized and analyzed. Then the empirical quality measures, i.e. the height differences between the identical points are presented for three different cases. Finally, the results of comparison between theoretically and empirically obtained quality measures are given and discussed.

- In Chapter 7 the methodology to estimate the laser L-MMS DTM quality is developed. The chapter begins with the explanation of the factors influencing the DTM computation and its quality. Then the theoretical models to validate the DTM are described. The main part is the explanation of the interpolation method Moving Least Squares (MLS), which is used here to derive grid point heights and their precision. On its basis the methodology of laser L-MMS DTM quality assessment is developed.

- In Chapter 8 the results of the laser L-MMS DTM validation are shown. The chapter is conceptually divided in two parts. In the first part the influencing factors and the DTM quality estimation results are presented. Those results are obtained following the methodology given in Chapter 7. Considering the outcome of the laser L-MMS DTM quality, an optimum measurement set-up is suggested. In the second part the results of L-MMS and ALS data comparison are presented.

- Finally, in Chapter 9 the thesis is completed by an overview of the conclusions of this research and recommendations for future research on this topic.

Chapter 2

Coastal monitoring

Monitoring of landforms and areas that are potentially hazardous to human life and assets has become an increasingly important issue. In case of the Netherlands, maintaining the coastal area plays an important role, preventing firstly sea to flood the inner land and secondly storms to erode the land. Failing to predict and react on geomorphologic changes that affect the stability of both natural and built environment has big legal and financial implications. Therefore, accurate and effective monitoring is essential. Recent advances in technology allow for different methodologies to be investigated and used.

In Section 2.1 the typical characteristics of the sandy Dutch coast and the requirements for the measurements are described. According to those characteristics and requirements, most suitable acquisition techniques are discussed in Section 2.2. The Dutch Ministry of Transport, Public Works and Water Management (RWS, Rijkswaterstaat) initiated the pilot-project on the Dutch coast near Egmond aan Zee to test the land-based Mobile Mapping technique. In Section 2.3 background information on the pilot-project Egmond aan Zee is given. In Section 2.4 the chapter is finished by a summary.

2.1 Coastal area characteristics and requirements for the measurements

The coastal area is a specific very dynamic environment, where many different human and natural forces influence its existence and condition. Therefore it is important to know what phenomena are present, what processes are forming the coast and influence most the coastal morphology and vegetation, in order to efficiently monitor them. Digital mapping is a task that has inherent constraints or requirements, depending on the application. These requirements have to do with the target environment, the structures to be digitized, the size and expense of the equipment to be used, the time available for data acquisition, the purpose for which the models are to be used, etc. Some of these requirements are constant, and some depend on the application, for example what resolution is necessary for the model. Perhaps one of the main requirements is the time on site necessary to acquire the data [Grinstead et al., 2005].

In this research the target environment is the sandy Dutch coast and the application in hand is measuring the coastal morphology and its changes. Therefore, in Section 2.1.1 the characteristics of the Dutch coastal area are described and the terminology used later in the report is explained. To observe the processes and morphological changes in the coastal area, certain requirements for the acquisition technique must be fulfilled. In Section 2.1.2 those requirements are explained.

2.1.1 Characteristics of the sandy Dutch coast

The Dutch coast is dominated by broad sandy beaches and extensive dune ridges. Fig. 2.1 shows a schematic overview of the typical Dutch coastal zone and defines the important subareas where different processes are going on. The research described in this report considers mostly the beach and dune area (indicated with ellipse in Fig. 2.1).

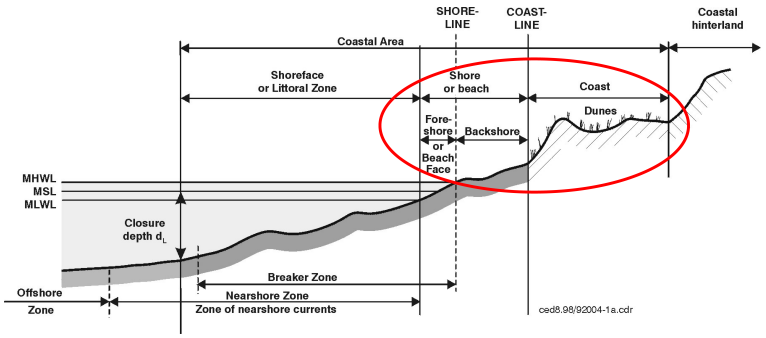

Figure 2.1: Definition of terms describing the coastal area and its division in subareas [CERC, 1984].

In the following some technical terms concerning coastal morphology, which are used later on in this report, are shortly described. The main source is [Coastalwiki, 2010].

Beach or shore is the zone of unconsolidated material (sand) that extends from the mean low water line to the place where there is a marked change in material or physiographic form, or to the line of permanent vegetation (the effective limit of storm waves and storm surge), i.e. to the coastline. The Dutch beach is relatively horizontal with a typical width of up to $300m$ (for an example see Fig. 2.2(a)). The beach or shore is divided in foreshore and backshore, as denoted in Fig. 2.1.

Backshore is the part of the beach lying between the foreshore and coastline. The backshore is dry under normal conditions, is often characterised by berms and is without vegetation. The backshore is only exposed to waves under extreme events with high tide and storm surge.

Coastline is technically the line that forms the boundary between the coast and the shore (see Fig. 2.1), i.e. at the foot of the dunes. But more commonly it is the line that forms the boundary between land and water.

Shoreline is the intersection between the mean high water line and the shore. The line delineating the shoreline on Nautical Charts (Sea Maps) approximates this Mean

High Water Line. The shoreline is not easy to identify in nature in contrast to the coastline, which is based on a clear morphologic shift between shore and coast.

Coast is the strip of land that extends from the coastline inland to the first major change in terrain features, which are not influenced by the coastal processes. The main types of coastal features are dunes, cliffs and low-lying areas, possibly protected by dikes or seawalls.

Ripples are sedimentary structures that were deposited in a flow that indicate agitation by water (current or waves) or wind.

(a) A typical Dutch coastal area with flat sandy beach and vegetated dunes.

(b) Small scale features on the beach, so-called ripples.

(c) Typical dune slope vegetated by Marram Grass.

Figure 2.2: Morphological shapes typical for the Dutch coast [GoogleEarth].

Dunes are ridges or moulds of loose, wind blown sand (fine to medium). Dunes are mostly formed on the backshore and mainly by wind. In general the development of the dunes is determined by two factors: wind variability and sand supply. Dunes are active coastal elements acting as a flexible sand reservoir and as a kind of flexible natural protection against erosion and flooding. At eroding coasts they are moving backwards in parallel with the erosion process.

Dune vegetation. Dunes are more or less vegetated. When vegetation exists in sufficient quantity, grasses will continuously trap sand as they grow and the dunes increase in size. On the other hand, if the vegetation is damaged by for example too much traffic or grazing the integrity of the dunes may be endangered.

Dune erosion involves that, during a severe storm surge, sediments from the mainland and upper parts of the beach are eroded and settled at deeper water within a short time period; this is a typical cross-shore sediment transport process as shown in Fig. 2.3. The red line represent a normal situation, when the see is at the Mean See Level (MLS). And the blue line shows a situation after a storm, when the storm surge level (SSL) erodes the dune sand and deposits it lower on the beach. The degree of the dune erosion can vary significantly along the coast.

Tidal inlets. In flat tidal lands water does not vanish totally during low tide, but areas of water coverage remain and the boundary between tidal land and water can not be extracted accurately. Those areas cause also problems to laser systems, since the laser light reflects away from the sensor (like on a mirror surface).

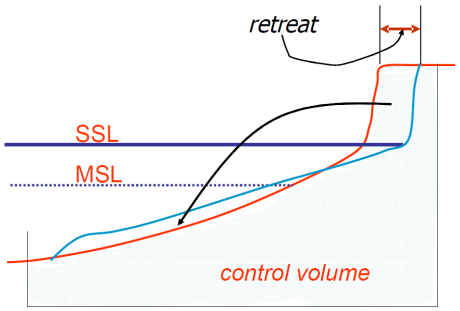

Figure 2.3: A schematic representation of the dune erosion [Coastalwiki, 2010].

Groyne is a rigid hydraulic structure built perpendicular to the shore, extending from the upper foreshore or beach into the water. All of a groyne may be under water, in which case it is a submerged groyne. The areas between groups of groynes are groyne fields. Groynes are generally made of wood, concrete, or rock piles, and placed in groups. They interrupt water flow and limit the movement of sediment.

Storm event is of great importance for sand transport. These events result in large transport rates of larger particles due to high energetic winds. Storms are defined as periods of wind speeds over 20 m/s [Bitenc et al., 2008]. For morphodynamic purposes it is interesting to look at storm duration and frequency.

The sandy sediment of the beach and the dune area is vulnerable to transport by water or wind. The transportation rate and direction determines the shape of the coast. Besides those natural processes, also human interventions have an impact on the coastal system. A challenge for coastal engineers is to manage the coastline in such a way that it stays within certain limits. The main method applied to counteract structural erosion is sand nourishment in the coastal zone. Beach nourishments as well as shoreface nourishments have been performed for 35 years, more extensively since 1990. A total amount of approximately 15 km^3 of sand per year is supplied on the beach and shoreface. However, the effect of beach nourishments is limited and has a rather short lifetime of about 1 to 2 years. According to Rijn and Walstra [2002] the nourishment of sand in deeper water is a promising method to counteract structural erosion. The question remains how and where the nourished sand moves in time.

2.1.2 Requirements for coastal monitoring

The combination of coastal areas with long coastlines (large, linearly extended areas) and dynamic processes make the application of surveying difficult. The main difficulty is that individual stretches of coastline cannot usually be separated for individual study. The prevalent processes can affect the flow of sediment around wide areas; the construction of defenses in one area for example may compound problems further along the coast [Mills et al., 2005]. Because of occurring changes, national large-scale mapping may become

rapidly obsolete. Frequent updates are needed to accurately portray the changing coastline.

In 1990 a new national coastal policy, so-called Dynamic Preservation policy, was adopted aiming both at safety against flooding and at sustainable preservation of the dunes and beaches. The policy intends to maintain the seaward position of the coastline according to its situation on January 1, 1990. This coastline is taken as a Basal Coast Line (BKL). The BKL indicates the desired coastal state that must be preserved as much as possible together with the natural dynamics of the coastal zone [Deltares, 2010]. In recent storm seasons a number of times a dune erosion has appeared along the North Sea coast of the Netherlands, particularly on the coast of the islands Texel, Vlieland and Ameland [Rijkswaterstaat, 2009]. Sometimes, large parts of the dunes vanish during one storm event (see Fig. 2.4).

Figure 2.4: Two real examples of a dune erosion on the Dutch coast and the possible consequence of a dune retreat [GoogleEarth].

To investigate the dune erosion, RWS uses a model, which accounts for dune erosion in one dimension with a sand budget orthogonal to the coastline. Due to the fact that this model is an over-simplification of reality, it is not suitable for accurate real-world case studies. To improve the dune erosion model, measurements in laboratory are carried out by Deltares. These measurements and the erosion model need to be verified with field measurements. The currently available JARKUS measurements provide a map of a sand erosion and dune movements only once a year and with a mutual distance of $250m$. These intervals however are longer in time and larger in space than many morphologic processes. Thus, more measurements are needed to monitor the rapidly changing morphology. This extra measurements would enable to get a good picture of the storm scope and a reliable estimation of the erosion that happened during the storm on a small area as well as on the coast as a whole [RWS, 2010].

Requirements to measure and model coastal changes per storm event concern: the spatial and temporal resolution, accuracy and precision (quality) of results, parameters as flexibility, portability and ease of use of technique, speed of data acquisition and processing, costs, safety and additional information. Some of those parameters are explained in the following.

Spatial resolution should be high i.e. at least $1m$ for a DTM. Thus a detailed surface

model can be obtained and an accurate interpretation of results is enabled. Techniques that provide continuous coverage of the coastal zone are required.

Temporal resolution. Applications such as change detection require data with high temporal resolution [Barber and Mills, 2007b]. During the storm season this means for example to perform the acquisition at least once a month. The more often acquisitions can be carried out, the more detailed will be the model of coastal changes and also the better the understanding of beach processes e.g. sand transportation, dune erosion.

Flexibility of technique. To measure changes on storm scale a flexible system is needed. This means firstly that it can be used at predefined time e.g. when the tide is low or possibly also at night. Secondly flexibility means that the technique can adapt to a storm situation i.e. is available and ready for measurements immediately after the storm. In other words it is important that the technology provides the data capture on demand.

Portability means the ease for a surveyor to move sensors in different environments and to access certain (remote) locations.

Ease of use of technique means how easy it is for a surveyor to perform measurements with the technique.

Real-time processing methodology is preferred. The processing of acquired data should be easily performed by engineer in a short time. The reason is that the storm can cause big and maybe fatal changes that have to be identified as soon as possible in order to make right decisions.

Costs. When estimating the costs of a technique, one must distinguish between different tasks that are performed to finally derive a beach morphologic model. Here three tasks are considered: initial costs to buy the equipment, money spend to acquire the data and at last the costs for the data processing and deriving the final products.

Control monumentation. In order to assess reliable morphologic changes of the coast, the need for control and datum registration between temporal datasets is paramount. The success of a monitoring scheme depends on being able to establish correspondence between the epochs of data collection. However, in coastal monitoring the establishment of permanent monumentation is often a difficult task. Direct consequence is, that monitoring schemes have often been restricted to small areas or of an accuracy lower than $1dm$, or were carried out only in built-up areas where control monumentation is facilitated [Mills et al., 2005].

2.2 Data acquisition techniques

In this section the most promising technologies are presented that satisfy in Section 2.1.2 described requirements to monitor the coastal area. In Section 2.2.1 traditional techniques,

which need a direct contact with a measured surface, are described. The next two sections deal with remote-sensing techniques, which are divided according to a platform. First, in Section 2.2.2 the pros and cons of airborne techniques are given. Secondly, in Section 2.2.3 the alternative land-based techniques are described. Both remote-sensing techniques are further divided according to the applied sensor (video, laser scanner, positioning and orientation sensors). In Section 2.2.4 the properties of all techniques are summarized and compared.

2.2.1 Traditional contact techniques

Traditional contact methods of data collection and map generation to study the beach profile changes include low technology approaches as differential leveling, traversing, static and kinematic GPS. These techniques are not only costly, time-consuming, and labor-intensive but also do not have the spatial or temporal resolution required to precisely quantify and study the processes of the beach erosion. Sampling with traditional in-situ sensors is viewed as impractical, if not dangerous when making an effort to access the area.

Kinematic GPS, for example, results in the best accuracy when mapping individual points. But the data are too sparse to provide more than a wire frame surface representation on an area of a few hundred meters. Usually the GPS measurements are used to georeference the measurements of other survey platforms and to measure smaller areas e.g. the profile of some parts of the beach and dunes. Those data serve as an additional dataset and allows to fill the gaps of the other measurement techniques. For instance, when measuring in the coastal area, some parts of the beach remain covered with the water also during low tide. Therefore those areas can not be measured with remote sensing techniques like photogrammetry or laser scanning. However, these areas are accessible by GPS.

2.2.2 Airborne remote-sensing techniques

2.2.2.1 Photogrammetry

Conventional photogrametry is expensive and not flexible. The processing of images is complicated and requires several days or even weeks. Ground Control Point (GCP)s are needed, which raise expenses of a field work and extends the data processing time. In case of capturing the coastline strip the number of images in general increases, which additionally requires more GCPs. Digital photogrammetry provides a useful solution to speed up digital image processing and compute Digital Elevation Model (DEM)s. Besides, nowadays the images can be directly positioned and oriented using a Position and Orientation System (POS), which reduces the need for GCP and shortens the processing time and thereby costs. But the use of photogrammetry is still limited on areas with a poor image texture, as is the case of sandy beaches. The less distinct texture may cause problems for the image matching routines. Another disadvantage using digital photogrammetry for beach monitoring is, that the collection of imagery heavily depends on tides, weather and atmospheric conditions, and season. Problems can be partly evaded using digital Small Format Aerial Photography (SFAP) [Warner et al., 1996]. Advantages of SFAP are the use of a lighter camera platform

allowing rapid deployment, a lower flying height that decreases weather dependency, and overall system simplicity [Mills et al., 2005]. However, those unconventional techniques still need to be verified for mapping the beach morphology in terms of final costs, flexibility, resolution and quality.

2.2.2.2 Airborne Laser Scanning (ALS)

Airborne Laser Scanning (ALS), also called LiDAR, is most often used in combination with a POS, which negate problem of ground control points. It is a rapid, highly accurate and efficient method that directly capture 3D data of large areas. Because an active laser sensor is used, it is less dependent on the season, i.e. vegetation cover. Therefore it is widely used for an airborne terrain mapping and proves to be an ideal tool for applications such as flood plain mapping, mapping agricultural or forestry sites, urban areas, industrial plants etc. In the Netherlands ALS measurements started in 1995 and since 1996 only ALS data are used to acquire beach profiles to study large scale beach erosion. More current ALS systems can measure from lower attitudes and so improve the spatial resolution and quality. They are capable of high pulse rates up to 100kHz and scanning frequency above 100 scans per second. Thus, more than 10 laser returns per square meter can be acquired. This sampling capability enables the detection of submeter-scale changes in the shoreline position and dune heights [Fernandez, 2007].
The ALS technique has limitations in case of projects that include cost effective capturing of 3D data or when dense point coverage of the vertical features is required (e.g. steep dune slopes). Besides, the ALS systems can not provide data on demand. First, because flying permissions are needed and secondly after-storm weather conditions may hinder or prevent the acquisition. Therefore ALS does not provide a satisfactory solution when it is necessary to quantify changes that might occur between short time periods, for example between successive tides, or immediately after significant events such as a major storm. The ALS method, which is used most often nowadays for mapping the morphology, offers good results in terms of quality and reliability. However, ALS is not flexible.

2.2.3 Land-based remote-sensing techniques

2.2.3.1 ARGUS video technique

Due to the natural difficulties associated with dynamic processes of the coastal zones, monitoring techniques based on videogrammetry have been successfully developed. Land images are recorded continuously and then the sophisticated, video analysis methods enable the metric quantification of for example shoreline, erosional and accretional sediment volumes, subtidal beach bathymetry etc. [Coastalwiki, 2010]. A video camera from an aerial platform can be used or an advanced and automated terrestrial video station.

An example of videogrammetry applied on monitoring coastal changes is the Argus video monitoring system which has been developed since 1992. Nowadays it features a fully digital video technology, which provides high image quality (high pixel resolution). The system typically consists of four to five video cameras, spanning a 180° view, and allowing full coverage of about four to six kilometers of beach (see Fig. 2.5). Cameras

Figure 2.5: ARGUS video monitoring station at Noordwijk, The Netherlands [Coastalwiki, 2010].

are mounted on a high location along the coast and connected to an ordinary PC on site. Data sampling is usually hourly and continues also during rough weather conditions. As the process of data collection is fully automated, the marginal operating costs are virtually zero [Aarninkhof, 2003]. The geo-referencing of oblique video data enable the quantification of image features like sand bars, shorelines and foam patterns. Currently, 30 Argus stations and 120 cameras are operating daily in eight countries. One of the ARGUS stations is also in Egmond aan Zee. The disadvantage is that the system is not portable, thus the ARGUS measurements cover only particular parts of the beach.

2.2.3.2 Static Terrestrial Laser Scanning (TLS)

Stationary scanning is applicable for one-off mapping and has beneficiary use in applications such as structural monitoring and heritage documentation, potentially for ground surveing [Barber et al., 2008a]. To register scans together into a common coordinate frame, targets identifiable in laser point cloud need to be placed in the acquisition area and GCP must be measured to geo-reference the point cloud into a mapping frame. Therefore it is considered too slow and too costly for measuring wide areas, especially for long corridor projects with a lot of detail [Hohner, 2008]. Inefficiency and extensive labor work using TLS for coastal monitoring was also experienced during the Geomatics Synthesis Project 2008 [Bitenc et al., 2008].

2.2.3.3 Land-based Mobile Mapping System (L-MMS)

The use of static TLS for the 3D data capturing of smaller scenes as well as ALS for data collection of large areas are well established and general excepted tools. However, both methods have their limitations for projects that include capturing of 3D data in corridor environments (along a narrow strip) such as coastlines, rail or road networks. Especially, if these sections include tunnels or if dense point coverage of the vertical features e.g. facades, bridges, road/street furniture, vegetation, pole is required. To extend the applicability of laser scanning to these kinds of projects, laser scanners have been mounted on vehicles and the Land-based Mobile Mapping System (L-MMS) was born. L-MMS is designed for collecting engineering or survey grade laser data (centimeter scale point spacing) over large areas that are impractical with static TLS but require an accuracy and resolution that exceeds airborne technologies. L-MMS captures location information for every object

in its range, including objects not traditionally mapped, e.g. the position of lamp posts or street signs. When comparing the L-MMS to other techniques listed in the previous paragraphs the following advantages can be pointed out:

- High accuracy that provides data of high quality.
- High resolution (point density) on smaller areas: laser point density depends on the laser scanner measuring and scanning rate, speed of the vehicle and the measurement geometry. It ranges from several hundreds to several thousands of points per square meter. Increased resolution offers unprecedented 3D details, meaning that smaller features can be mapped.
- Higher productivity: the L-MMS increases the mobility of the laser sensor and is therefore faster than traditional terrestrial-based surveys. It provides cost effective data, considering the amount of data and the speed at which they are captured.
- Cost effective deployment: the costs to deploy the system are much lower than for an aircraft.
- Flexibility: rapid deployment of the acquisition system, technique can be used under most weather conditions and also at night.

Within this master thesis the aim is to research the opportunities offered by L-MMS for monitoring the coastal area. The method is therefore described in more detail in Chapter 3.

2.2.4 Summary of the acquisition techniques

In Table 2.1 the summary of advantages and disadvantages of different surveying techniques as discussed in the previous sections is given. The comparison is made for those techniques that are most commonly used for beach surveying or have promising characteristics. The parameters of comparison are explained in Section 2.1.2.

2.3 Pilot-project Egmond beach

In this section the pilot-project of the L-MMS acquisition on the beach near Egmond aan Zee is presented. The aim is to give a background information of the project and summarize what was done on the pilot-project data before this research started. The information is taken from the technical reports written by project leader, the Dutch Ministry of Transport, Public Works and Water Management (RWS, Rijkswaterstaat).

First in Section 2.3.1 the RWS motivation to initiate pilot-project Egmond aan Zee is explained and the organization of tasks among the involved parties is described. In Section 2.3.2 the pilot-project acquisition area is shown and the reasoning for the choice of this area is given. In Section 2.3.3 the details of acquisition mission, which included the L-MMS and RTK-GPS measurements, are described. According to the objectives that RWS set up for this pilot-project, their conclusions are given in Section 2.3.4. Finally in Section 2.3.5, the relevance of the pilot-project Egmond aan Zee to this master thesis project is explained.

Table 2.1: Overview of the most promising techniques for the coastal monitoring and their comparison according to some parameters.

Parameter		GPS	Photogrammetry	ALS	TLS	L-MMS
Data quality		++	-	o	+	+
Spatial resolution per unit time[a]		–	o	+	++	++
Spatial coverage per unit time		–	++	+	-	o
Flexibility		++	–	–	+	+
Portability		o	++	++	o	+
Ease of use		+++	-	-	+	++
Real-time processing		+++	-	++	o	++
Costs	Equipment	$	$$$	$$$$	$$	$$$
	Acquisition	$	$$$$	$$	$$$	$
	Processing	$	$$$	$$	$$$	$$

[a] The spatial resolution is estimated considering the time when the metric 3D data are available. This means that besides the acquisition time, also the duration of processing the data is taken into account.

2.3.1 Motivation and organization of the pilot-project

As explained alredy in Section 2.1, RWS has the need to fill the gap between the subsequent JARKUS measurements by additional measurements. New monitoring techniques which can fulfill the information need are available or are emerging, but the question is whether they can be deployed by RWS and if they can deliver the information according to the requirements set by RWS. As a potentially suitable techniques to measure quickly and accurately the changes in the coast profile straight after the storm a mobile 3D laser scanning system was chosen. To test the feasibility of the laser system, it has been decided to do a pilot-project at the end of 2008.

Main parties involved in this pilot-project are Data-ICT-Dienst (DID) and Water Dienst (WD), both departments of RWS, joint company DELTARES and surveying/processing company GEOMAAT. The company Geomaat from the province of Groningen cooperates with 3Dlasermapping and has a laser system available since January 2009[1]. The laser system is known as the Streetmapper system. RWS has given Geomaat the instructions to execute the pilot at Egmond aan Zee.

2.3.2 Pilot-project area

In accordance with Deltares, two L-MMS acquisition areas have been selected on the beach of Egmond aan Zee as shown in Fig. 2.6. The choice for the areas was based on the following

[1] The British company 3Dlasermapping has carried out such measurements in the South of England already in December 2007 [Barber and Mills, 2007b].

reasons:

- they can be reached easily;
- the permit to assess the area is available;
- other measurements are available for verification (JARKUS and, in case of test area 2 if needed, ARGUS monitoring system);
- the presence of a sea-dike, so-called Hondsbossche Zeewering and the construction that is connecting the dike with the dunes (area 1, see Fig. 2.7(a))

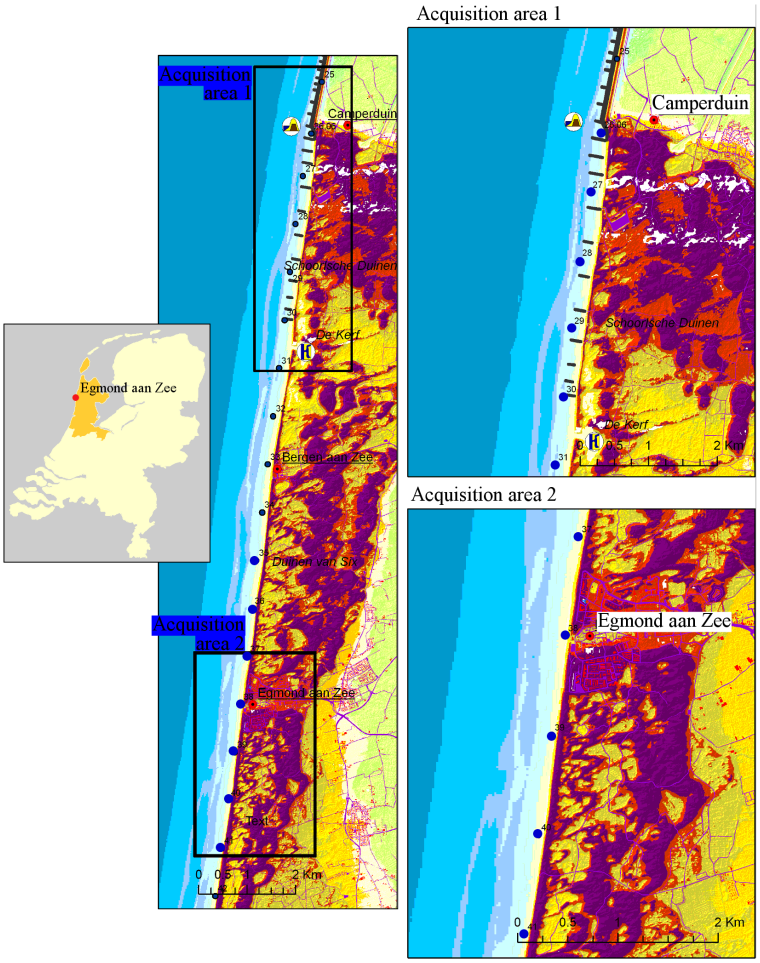

Figure 2.6: The pilot-project area on the west coast of the Netherlands, near Egmond aan Zee and a detailed map of the two acquisition areas [Rijkswaterstaat, 2009].

On November 5, 2008 (before the measuring campaign), an in situ investigation has been carried out by RWS, where the following interesting features were observed [Rijkswaterstaat, 2009]:

- the presence of the foundation for beach tents;
- the presence of Marram Grass on the side of the dunes;

- higher pre-dunes on the beach side that can cause shadow effects;
- variations in beach height and the presence of small islands (part of a beach is covered with water - resulting in beach-water-beach areas as can be seen in Fig. 2.7(d))
- groyne constructed by wooden poles (area 1, see Fig. 2.7(b))
- a break through in the sea bar (area 1 at De Kerf)
- a hole in the dunes (area 2, see Fig. 2.7(c))
- a high crane or tower (see Fig. 2.7(d))

(a) Sea-dyke Hondsbossche Zeewering (area 1).

(b) Wooden groyne (area 1).

(c) Hole in the dunes (area 2).

(d) The crane (area 2).

Figure 2.7: An example of the interesting features found on the acquisition area 1 and 2.

2.3.3 Acquisition mission and data delivery

The measurement campaign took place on November 27, 2008. At the time, low tide was reached around 12:00 hours (local time). The coverage of the StreetMapper system was 25 m to both sides of the vehicle. Therefore, more tracks had to be driven to cover the entire test area. However, it proved to be sufficient to measure for one day only. The first test area was measured during the morning and the second in the afternoon. Measurements acquired during the morning were processed in the afternoon and the preliminary result of the point cloud could be visualized. The time between data acquisition and the availability of the data is a vital issue for RWS. The data need to be available as soon as possible, preferably in real-time. Later the data were processed by 3Dlasermapping and distributed by Geomaat. Due to the fact that everything was delivered in one package (data, photographs, and videos), the final delivery was two weeks after the measurement acquisition.

To check the absolute altitude position a small reference field and a longitudinal (direction) profile was measured with GPS-RTK by the Meet- en Informatiedienst of RWS Dienst

Noord-Holland. The expected standard deviation of the RTK-GPS height measurements is approximately 4-5 cm. This is sufficient for the pilot-project, which requires a decimeter-level precision. But GPS-RTK showed a height difference of -3.9 cm on a reference point known in NAP (Nieuw Amsterdams Peil). If this bias is considered as representative for the reference field, the difference with GPS-RTK is only 2.8 cm. However, RWS wrote in the report that hardly no conclusions can be drawn from the reference data that were measured on one small field and a profile. Besides, RWS compared the L-MMS data with the available ALS measurements acquired in April 2008. Due to the high L-MMS point density, they predict that the L-MMS height reliability could be similar to the ALS. Therefore, the L-MMS is considered suitable for the beach monitoring.

2.3.4 RWS questions and conclusions

The main objective of the pilot-project is to gain insight in the suitability of the laser L-MMS system to measure the coastline and dunes, in particular for monitoring this area after a storm. RWS set some questions for the pilot-project, which are listed in the following paragraphs together with RWS conclusions [Rijkswaterstaat, 2009]:

- **How soon are the measurements available?**
  The measurements were available after approximately 14 days. However, it should be noted that this test was also a pilot for both 3Dlasermapping and Geomaat. The data from NETPOS have been supplied within a few days. Geomaat claims that delivery of data is feasible within a few days; with the new system Streetmapper 360 even within a few hours [Geomaat, 2010].

- **Are shadow effects present?**
  Based on a comparison of the data with aerial laser measurements it is concluded, that shadow effects are present in the data. This means, that this method is not suitable for yearly acquisition of JARKUS measurements.

- **To what width can be measured in one go?**
  Since the laser measurement setup had a range of 25 m to both sides, this has not been tested any further. The new system Streetmapper 360 has a larger range (up to 300 m).

- **Is there a relation between point density and accuracy of the measurements?**
  The used point density is 360 to 1440 points/m^2 depending on the velocity of the vehicle. This point density is more than sufficient for beach measurements. Special attention has to be paid to the amount of data, which may have to be reduced for certain applications.

- **Influence of vegetation?**
  Based on the test results and the experience of DID on this topic, it is assumed that the vegetation can be removed by filtering by the data supplier.

- **Is it possible to detect litter?**
  Taking into account the maximum point density and the fact that geodetic equipment was visible on the reference field, it can be stated that this method can be used for measuring objects that are washed ashore. The suitability depends on factors such as the driving speed of the vehicle, the size of the objects, and processing of the data (filtering techniques in particular). It is still unknown how well the system operates at a distance of about 300 m and during sand storms.

In general, the RWS conclusion based on the test results is that the Streetmapper data are not suitable as a replacement of the JARKUS measurements. The L-MMS data cover only the JARKUS line on the beach, but not also behind the dunes. However, the data are suitable for fast inventory of the dune erosion caused by water, because those differences are more likely to happen at the well sampled foot of the dunes. The quality of obtained data is satisfactory.

2.3.5 Relevance for the master thesis

An investigation of different measurement techniques that can efficiently acquire the sandy beach morphology was performed already in November 2008, during the Geomatics Synthesis Project 2008 (see report [Bitenc et al., 2008]). One of the recommendations of this research is, to use the laser L-MMS system. To research the laser L-MMS possibilities to map the Dutch beach, the master thesis was set up, at the same time as the possibility occurred to gain the real L-MMS data. The RWS mediated the data of the pilot-project Egmond aan Zee to the Optical & Laser Remote Sensing chair of the Faculty of Aerospace Engineering, Delft University of Technology. According to the open questions in the RWS work and their main requirements on the DTM accuracy the objective of this master thesis project is set up, as described already in Chapter 1.

Table 2.2: Properties of the 3D point data-sets available for the master thesis research.

Data set	ALS	L-MMS	GPS
System/method	Harrier56 by Toposys GmbH	StreetMapper by Geomat	RTK GPS
Date	April, 2008	November 27, 2008	
No. of points	10.5 million	56.6 million	227
Region covered [m] (length×width)	4340×220	5480×180	/
Density [points/m^2]	15-33	up to 126	/

For the purpose of the master thesis project three data sets are available, namely the Airborne Laser Scanning (ALS), Land-based Mobile Mapping System (L-MMS) and RTK-GPS data. The first data set was acquired on a regular basis for the needs of Actueel

Hoogtebestand Nederland; en. The current elevation map of the Netherlands (AHN) and the next two were acquired during the pilot-project Egmond aan Zee. The properties of the data are summarized in Table 2.2. Those 3D points are all given in a common coordinate system, i.e. in Dutch RD/NAP. The L-MMS data include only the laser points acquired in area 1 (see Fig. 2.6).

2.4 Summary

In this chapter the last part of the thesis title, i.e. measuring sandy coast morpgology, is discussed. That is, the particular application in hand is described by first characterizing the area of interest, i.e. Dutch sandy coast with the dunes aside, and second listing the requirements for the acquisition, i.e. measurements. The sandy coast is dynamically changing and is daily exposed to natural forces as sea waves and wind, as well as to human interventions. Further more, the occurrence of a strong storm, can have a great impact on the natural environment and can cause a big damage on human objects, lives. To prevent those losses, efficient monitoring of the coastal area is needed. The RWS would need a reliable measurements and information about the coastal situation immediately after the storm in order to take right decisions in-time. The traditional contact techniques are inappropriate because first, it might be unsafe for the surveyor to take measurements and secondly, the techniques mostly can not provide the required spatial resolution in a short time. The commonly used airborne techniques, as ALS and photogrammetry, offer a good spatial resolution and data coverage of a flat beach and the dunes. However, they are not flexible. Among the terrestrial remote-sensing techniques the most suitable would be the laser L-MMS. It enables fast acquisition of large, extended areas, resulting in a high spatial resolution. The 3D morphology of the beach is derived from the data shortly after the acquisition, due to the direct geo-referencing of the sensor platform and because of automatized processing of the digital data. To test the actual capabilities of laser L-MMS for monitoring the Dutch beach and to verify, if the technique can fulfill certain requirements, RWS initiated a pilot-project on the beach near Egmoond aan Zee. The RWS objectives and results are presented in this chapter. By coincidence at the same time the master thesis project on the topic of laser L-MMS started at Department of Optical and Laser Remote Sensing. Therefore, the pilot-project Egmond aan Zee data were requested. They are used in this master thesis project to further investigate the initial RWS work and so reach the research objective to “Evaluate the laser Land-based Mobile Mapping System (L-MMS) for measuring the morphology of sandy coasts.”. Before the evaluation starts, in the following Chapter 3 the middle part of the thesis title, i.e. a laser Land-based Mobile Mapping System, is described in detail.

Chapter 3

Laser Land-based Mobile Mapping System

In Chapter 2 the characteristics of the area to be measured and the requirements for the measurements and derived results are given. Out of different possible techniques, which are available and able to map the coastal morphology and its changes, the laser Land-based Mobile Mapping System (L-MMS) was chosen to be tested on the sandy Dutch beach. Because the laser L-MMS technology is relatively new, in this chapter more background information and extended description of the technology is given.

In Section 3.1 a general definition of Mobile Mapping System (MMS) is given and its advance to L-MMS is described. In Section 3.2 different applications of laser L-MMS are listed. In Section 3.3 the three components of the laser L-MMS system are described and the basic principles of their measurements are given. In Section 3.4 the L-MMS system called StreetMapper, which is analyzed in this master thesis, is described in detail. In Section 3.5 the StreetMapper dataset acquired on the beach near Egmond aan Zee is presented. Finally, in Section 3.6 the main information of this chapter is summarized.

3.1 Background information of the Mobile Mapping System

A definition of the Mobile Mapping System (MMS) after Ellum and El-Sheimy [2002] is: "MMS integrate navigation sensors and algorithms together with sensors that can be used to determine the positions of points remotely. All the sensors are rigidly mounted together on a platform; the former sensors determine the position and orientation of the platform, and the later sensors determine the position of the points external to the platform."

The main strength of MMS technology is the direct geo-referencing technology that uses the navigation sensors to directly determine position and orientation of the mapping sensor relative to a mapping coordinate frame. Neither ground control points are needed nor traditional requirement of photogrammetric block or image-sequence adjustments employing measured image coordinates. The most common technologies used for

direct geo-referencing purpose are GNSS, mostly employing GPS satellites, and inertial navigation using an Inertial Measurement Unit (IMU). Although each technology can in principle determine both position and orientation, they are usually integrated in such a way that the GPS receiver is the main position sensor, while the IMU is the main orientation sensor. The integration of GPS/IMU sensors with digital mapping sensor results in greater flexibility and efficiency, and lower costs of the system and data processing [El-Sheimy, 2005].

Most of the existing MMS systems are designed to be a modular package and can be broken down into 3 main sub-systems:

1. Remote sensing technologies like a laser scanner(s) (geometry acquisition sensor) and/or high resolution cameras (texture sensor).
2. Navigation technique that usually joins the differential GPS (DGPS) and Inertial Measurement Unit (IMU) observations for positioning and orientation. This integrated position estimation module is also called Position and Orientation System (POS).
3. The data fusion and processing system.

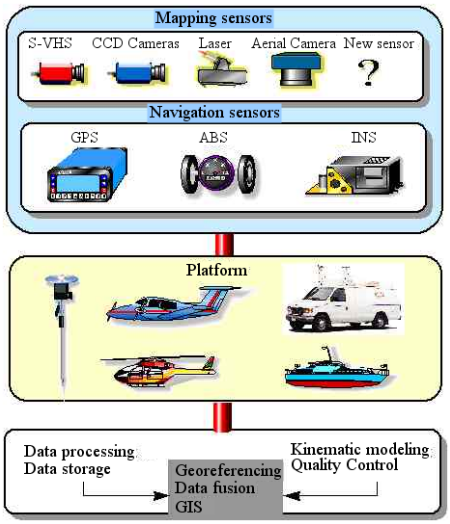

Figure 3.1: Multi-sensor integration on different platforms for Mobile Mapping applications [El-Sheimy, 2005].

The first two are hardware systems, mounted on a common moving platform and can be changed to meet the specific needs of the application at hand. The third subsystem is software-based, which is used to manipulate the data collected by the MMS. The software is as important as the MMS itself. It is actually part of the MMS, as nearly every MMS has dedicated software developed for it [El-Sheimy, 2005]. In Fig. 3.1 those subsystems are shown, together with different possibilities of platforms to mount the mapping and

navigation sensors on. MMS can be classified according to the physical carrier (platform) into airborne, terrestrial and marine based systems. In the first air-case the acquisition sensors can be deployed on a plane or helicopter, in the second land-case on various vehicles e.g. 4×4 vehicle, quad bike (larger models), robot or train [StreetMapper, 2010]. Besides, the development of robots and Backpack MMS is in progress [El-Sheimy, 2005]. A marine system can be realized on a boat or jet-ski. Mapping data (geo-referenced imagery or 3D laser points) captured by airborne, terrestrial and marine systems are different in the sense of direction, scale, coverage, hidden/visible features.

The idea of MMS has been around already since 1980s, as long as digital photogrammetry exists. Improving capabilities of digital mapping sensors, such as higher resolution digital cameras and wider availability of laser scanners, trigger fast development of different MMS systems and its applications. As a consequence of the advent of high accuracy GPS/INS systems, first airborne MMS systems, so-called ALS, evolved from the traditional airborne mapping. During the last decade of the twentieth century the concept of L-MMS has been established, thus representing the next generation in rapid collection of 3D data from the ground. It evolved from rather simple land-based systems to more sophisticated, real-time multi-tasking and multi-sensor systems. L-MMS can offer high accuracy, data complementarity and redundancy [Grejner-Brzezinska, 2000b]. ~~For an overview of the early L-MMS see [Ellum and El-Sheimy, 2002].~~ The first systems around acquired digital images (in 1991 GPSVan started operating) and later on the laser sensor was adopted. ~~In the following sections the main focus will be on the L-MMS, employing a laser scanner as a mapping sensor and integrated GPS/INS system as a main navigation sensor.~~

3.2 Applications of the laser L-MMS

Primarily the L-MMS systems were mainly used for mapping transportation infrastructure and included a video sensor. This first generation of L-MMS experienced difficulties to provide positioning accuracy better than one meter, especially in built-up urban areas. Therefore, the data captured by L-MMS and results obtained after processing, i.e. point cloud and/or images, were predominantly included "just" into various Geographical Information System (GIS) systems. Namely, GIS require positioning accuracy "just" of few decimeters. Due to the technological developments (as explained in previous section) the performance of current L-MMS can reach the cm-level, which opens up the field of engineering applications [Toth and Grejner-Brzezinska, 2001]. This means, the data can be used in most GIS and Computer-Aided Design (CAD) systems for a variety of applications, where precise measurements of the built or natural environment are required.

A wide range of different applications of L-MMS can be found on companies' web pages [Riegl, 2010; StreetMapper, 2010; 3D LASER MAPPING, 2010; RealityMapping, 2010; Faro, 2010]. Some of them are already tested and approved, others are still in development. Besides, also new applications are showing up. Key applications are:

- *Monitoring transportation infrastructure as roads or railways.* Surveys without disruption to traffic can improve maintenance and asset management of road surfaces [Li and Chapman, 2005] and street/railway furniture e.g. signs, markings, carriageways sidewalks, retaining walls, tunnels, bridges, guard-rails, road drainage structures etc [Redstall, 2006]. In case of transportation of oversize cargo, accurate and rapid mapping of route clearance (bridge height, road width) can be performed for the entire route [Hunter, 2006]. An example of a model derived from L-MMS data is shown in Fig. 3.2(a). This kind of applications were developed first and are well documented in literature e.g. [Tao, 1998; Blug et al., 2007; Madeira et al., 2005].

- *City modeling.* Rapid data acquisition enables the generation of medium resolution 3D city models (detailed building facades, street furniture inventory) that are used in town planning, tourism, 3D GIS, creating accurate virtual environments and the augmented reality models e.g. Google Street View [Redstall, 2007; Gandolfi et al., 2008]. An example of a raw 3D laser point cloud is shown in Fig. 3.2(b).

- *Overhead line surveys.* Wires as small as 3 mm in diameter can be accurately positioned. The data, as for example visualized in Fig. 3.2(c), are used for applications such as low wire identification, vegetation encroachment and sag measurement.

- *Landscape mapping.* The acquisition of a dense and accurate surface model over an extended area can be done with ease using a laser scanner. Measuring the environment and its topography is useful for flood defenses, and is also used when observing changes in natural environment e.g. river-sandbar or coastal erosion, coastal or sea-cliff land sliding [Barber and Mills, 2007a; Peel, 2008; Grinstead et al., 2005], glacier advance or retreat [Collins and Kayen, 2006]. The flexibility of MMS platforms allows laser scanning to be performed on most terrains.

- *Construction mapping and querying.* Some examples are accessibility studies, query and stock pile volumetrics and as-built surveys.

- *Vegetation mapping.* Vegetation and trees are accurately measured and used for utilities management and arborist contractors.

- *Mining sector.* Laser scanning is proving to be a tremendous asset in supporting mining operations through site monitoring and improving site safety [Peel, 2008]. Robotic Surveying Vehicle (RSV) is used for underground mining.

- *Accident reconstruction.* 3D digital "maps" can be created of known accident blackspots, which can be used by investigators after an accident as part of their scene recording. Using a database of pre-scanned laser data, as shown in Fig. 3.2(d), shortens the time required to record scenes and the time before the road can be cleared [Hunter, 2006].

(a) Mapping of route clearance [StreetMapper, 2010].

(b) City modeling [StreetMapper, 2010].

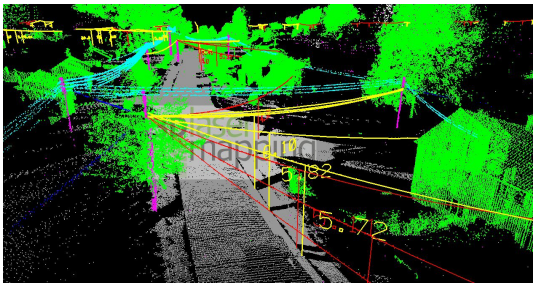

(c) Overhead line surveys [StreetMapper, 2010].

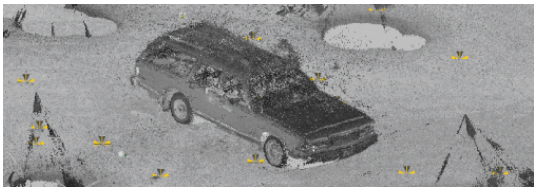

(d) Accident reconstruction [Faro, 2010].

Figure 3.2: Examples of laser L-MMS data used for different applications.

3.3 Principles of the laser L-MMS and system components

A typical laser L-MMS system consists of three main components: a GPS system to provide position information, an INS system to determine orientation, and a laser scanning unit to provide an oriented range (distance) between the laser-beam firing point and a ground point (laser footprint). A great variability of sensors exists on the market. When choosing the most appropriate one, it is important first to decide and agree on requirements for a final product and second to know constraints of an area to be measured. Usually the decision for the system is done based on the expected quality of the final results. Therefore this important topic, i.e. the accuracy and precision of the L-MMS measurements, is addressed in a separate chapter (see Chapter 4). But first in the following sections the three main subsystems and their measurements are described in more detail.

In Section 3.3.1 the technology of laser scanners is described. In Section 3.3.2 the fundamental information about the well known and widely used positioning technology Global Navigation Satellite Systems (GNSS) is given. The complementary technology of GNSS to determine a precise position and orientation of the moving vehicle is the Inertial Navigation System (INS). Its operating principles are presented in Section 3.3.3. The measurements from these three hardware systems are integrated together, which is shortly described in Section 3.3.4.

3.3.1 Laser Scanner

Currently there are many commercial-off-the-shelf laser scanners that can be included into L-MMS. The choice of laser scanner for a particular project depends on a careful analysis of the instruments specifications and the project requirements. A laser scanner consists of two main subsystems, namely the ranging unit, whose output is an accurate measurement of distance, and the scanning unit, measuring the scanning angle. These two units together create a certain scanning geometry pattern. Some laser scanners enable the recording of intensity. The laser scanner's key specifications are: range, range resolution, scan angle, azimuth and elevation resolution or point spacing, beamwidth, laser range measurement technique (pulsed or continuous wave) and laser wavelength, the scan rate and field of view (FOV).

Those specifications are explained in the following two sections, grouped according to main subsystems. That is, in Section 3.3.1.1 the ranging and in Section 3.3.1.2 the scanning unit are presented. In Section 3.3.1.3 the principles are joined in order to describe the scanning geometry.

3.3.1.1 Laser ranging principles

The laser scanner produces an optical pulse that is transmitted, reflected off an object, and returned to the scanners receiver. By measuring the phase difference (PD) or the Time

Of Flight (TOF) the distance from the sensor to an object can be computed. Each of these *range measurement principles* has its own set of strengths and weaknesses that are described in more detail in [Fernandez, 2007]. The most common type of ranging laser is TOF that precisely (in the order of a few nanoseconds) measures the time interval between emitting and receiving a pulse traveling at the speed of light, and convert it into a range measurement.

Range is the most important feature of a laser scanner, because it determines to a large extend the types of application. A distinction is made between short-range (up to $25m$), medium-range (up to $250m$) and long range (more than $250m$). The performance specifications should include both a maximum and minimum ranging distance. Since laser scanners operate in non-contact mode, the maximum range does not depend only on the type of laser scanner, but also on the object reflectivity ρ, light conditions, surface area of the illuminated target and the direction of the laser beam with respect to the surface.
Some manufacturers indicate the dependency of the range on the reflectivity by accompanying a range with the reflectivity coefficient ρ in percentage, also called albedo. The coefficient ρ describes either the amplitude or the intensity of a reflected wave relative to an incident wave. Reflectivity ρ varies with material characteristics as well as with the light used. In Table 3.1 the typical reflectivity coefficients ρ of a few different materials are presented; for more examples see [Wagner, 2005a]. The values are valid for laser light with a wavelength of $1\mu m$.
Due to light conditions in the acquisition area the range is considerably shorter in bright sunlight than under and overcast sky. At dawn or at night the range is even higher [TerraSolid, 2010]. The range could be limited in case the beam is falling on the surface almost parallel with it. The reason is that not enough energy can be scattered back to the laser scanner receiver.

Table 3.1: The reflectivity coefficient ρ of different surface materials at $1\mu m$ wavelength [Wagner, 2005a].

Surface material	Reflectivity coefficient [%]
Asphalt	20
Cement	40
Sandy soil dry	15
Sandy soil wet	30
Silty soil dry	60
Snow	25
Water, smooth surface	< 1
Water, wavy surface	< 30

Range resolution refers to the ability of the laser scanner to distinguish between features adjacent in the line of sight.

Intensity is defined as the ratio between the strength of the recorded light and that of the emitted light, and is therefore a relative number without units. Intensity is influenced mainly by the reflectance of the target surface (see Table 3.1) and the laser scanning geometry [Wagner, 2005b]. The measurement of the strength or the intensity of the returned echo could be a reasonable method for distinguishing between different surfaces or materials, as discussed in many papers for the ALS technique [Song et al., 2002; Lutz et al., 2003b; Hasegawa, 2006].

Laser wavelength is in the range of green or red or near infrared light. Visible lasers (red and green) are best when there is a need for water and glass penetration or when mapping wet surfaces. On the other hand most of the energy of infrared lasers is absorbed by moist surfaces and the return signal is very weak.

Beam divergence or laser beam width β is the dispersion of the highly directed laser beam. The most common definition of the laser beam diameter determines its size such that the diameter encircles 86% of the total beam power within the Gaussian irradiance distribution [Lichti et al., 2005]. Because an emitted laser beam expands linearly for large ranges, the divergence is often specified in terms of initial diameter plus a linear expansion factor or just the expansion factor itself, which may be expresses in *mrad*. The laser beam width strongly influences the point cloud resolution and the positional uncertainty.
The positional uncertainty due to the beam divergence is a consequence of inherent uncertainty in the angular location of the point to which the range is measured. The apparent location of the range observation is along the centerline of the emitted beam. However, the actual point location could lie anywhere within the projected beam footprint.

Laser safety Class is defined by the American National Standards Institute (ANSI) according to the degree of hazard presented to eye safety based on a maximum permissible exposure. The class depends on the laser power and wavelength. Laser scanners must be built to meet eye safety regulations, and the operator must be aware of what previsions and precautions must be taken [Fernandez, 2007].

3.3.1.2 Scanning principles

Traditionally, geodetic scanning instruments have used reflective optics coupled to a mechanical system. In principle the 2D movement of the laser beam is achieved through some type of scanning mechanism and the third dimension by rotating the complete instrument around vertical axis (3D panoramic scanner) or by moving the platform on which the scanner is mounted (2D line scanner). Both 2D and 3D laser scanners are suited for mobile mapping applications, but apply different processing methods.

Angular resolution defines to which degree (how precise) a scanning mechanism can read the value of current scan angle. It is included in the computation of the scan angle quality (see Section 4.3.2).

Field Of View (FOV). 3D laser scanners are called a panoramic view scanners and are typically capable of scanning 360° in azimuth (horizontal) by e.g. 80° in vertical (see [Lemmens, 2007] for more examples). 2D scanners are also called line scanners, as they scan along one line and can have any FOV from e.g. 30° (typically ALS scanners) up to 360° as for example Riegl VQ250 [Riegl, 2010]). Another type of scanners are the so-called camera view scanners that are usually implemented by two perpendicular deflection mirrors, one for the azimuth and the other for the elevation. This type of scanners have a fixed FOV typically of 45°×45°, which can be extended to a panoramic FOV with the aid of optional pan and tilt bases [Fernandez, 2007].

Scanning mechanism. The emitted laser beam is deflected in a certain direction by some type of scanning mechanism. The most common mechanism is the polygonal rotating mirror, which rotates continuously at an adjustable speed and provides a unidirectional scan within an FOV angle (see Fig. 3.9(b)). Other mechanisms are a rotating mirror and nutating mirror (so-called Palmer scanner). Another type is so-called fiber scanner, which is using a fibre-optic array to send and receive laser beams. Interested readers are referred to [Shan and Toth, 2008], Chapter 4 for a more detailed description of scanning mechanisms.

Scanning rate or scanning speed can be selected by the operator and defines the density of the scan lines on one hand and the spacing of consecutive laser points in the line of scanning on the other hand (an example is given in Section 3.4.1).

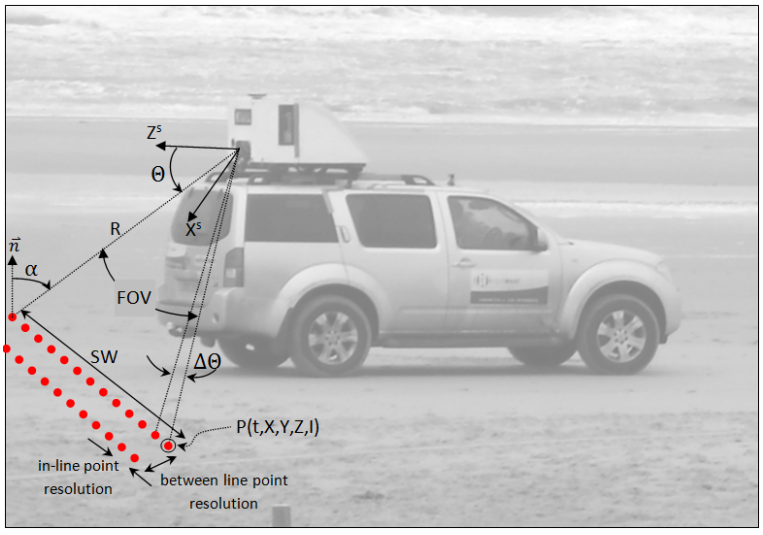

Figure 3.3: Principles of L-MMS: laser scanner measurements, scanning geometry and scan pattern. The underlying photo: StreetMapper system as used in pilot-project Egmond aan Zee [Rijkswaterstaat, 2009].

.

3.3.1.3 Scanning geometry and scan pattern

The scanning geometry is defined by the height of the sensor above the ground, the length (or range R) of the laser beam and the orientation of the laser beam with respect to the scanned surface. The scanning geometry together with the scanner specifications and driving speed of the vehicle (in case of a mobile 2D laser scanner) define firstly the quality of the measured 3D point positions and secondly the scan pattern (point density) as described in the following.

Incidence angle α ~~is the angle between the laser beam and the upward normal ($\vec{n}$) of the surface at the laser point position (see Fig. 3.3). When a beam hits a surface perpendicular to it, the incidence angle is 0° and when a beam is parallel to a surface the incidence angle is 90°.~~ In case of scanning a flat surface (like the beach) the incidence angle α is a function of the range R and height h of scanner above the ground and can be computed as $\alpha = \arccos(h/R)$. Fig. 3.4 shows how rapidly the incidence angle increases with the range. The scanning geometry improves (i.e. incidence angle is smaller), if the laser scanner is set higher above the ground; see the blue line with squares for a sensor height of $4m$. For ranges longer than $60m$ the incidence angle is bigger than 85°. The influence of incidence angle on the point quality is analyzed in Chapter 5.

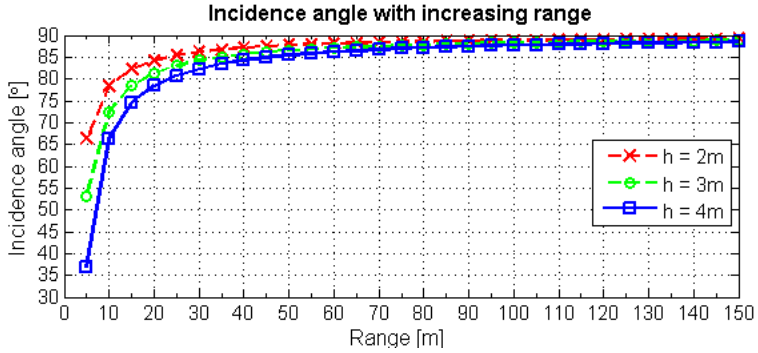

Figure 3.4: Rapid increase of the incidence angle with the range at different sensor heights above the ground.

Laser beam footprint is an area on the target surface illuminated by a laser beam. Size of a footprint depends on the laser beam width (given in specifications of laser scanner), which is changing with the rage and on the incidence angle. For accurate mapping a small footprint size is required, because the laser computes an average range of the entire illuminated area. The larger the area, the more chance is that a slope, reflectivity and smoothness variations affect the range measurements.

Scan pattern. The laser beam is moving in 3D space and makes a pattern on the scanned surface, which depends first on the surface orientation with respect to laser beam and the L-MMS specifications, namely on the 2D movement of the scanning mechanism and on the platform motion that adds the third dimension to the 2D line scans.

Considering just the L-MMS specifications, the following paragraph explains point spacing.
Point spacing within the line scan (in-line point resolution, see Fig. 3.3) is a measure for the smallest angular step between consecutive laser shots. In other words, it is the measure of the angular or linear separation between adjacent laser shots. It is defined by the scanning mechanism ability to steer the laser beam for small angular increments. Besides, it depends on the scanning rate and effective measurement rate. An example of in-line resolution is shown in Fig. 3.9(a). The resolution in direction of vehicle motion (between-line resolution, see Fig. 3.3) depends intuitively on driving speed of the vehicle and scanning rate.

Point density. Taking into account also the scanning geometry, besides the scanning resolution (point spacing), the point density is defined. The point density is a very important parameter, as it influences the accuracy of the final products (e.g. surface model) and defines the size of features that can be seen or modeled from the raw data. Empirical tests of a land-based laser scanning on the beach show, that the point density decreases very fast with the increasing range due to the low sensor height and flat acquisition area [Bitenc et al., 2008].

3.3.2 Global Navigation Satellite Systems

The Global Navigation Satellite System (GNSS) is a general term used to describe a generic satellite-based navigation/positioning system (e.g. American GPS, Russian GLONASS, new European system Galileo). The system can be used for determining one's precise location and provides a highly accurate time reference almost anywhere on Earth or in Earth orbit. Till now most often the GPS satellites are used, therefore the MMS positioning technology in literature mostly refers to GPS positioning. The main principle is that the GPS receiver on ground simultaneously measures ranges to at least three different satellites of which the positions are known. The intersection between the three distances i.e. triangulation determines the receiver position. However, the receiver clock may introduce error, which must be estimated. For this reason a range to a fourth satellite must be observed to provide a unique solution (see Fig. 3.5).

The fundamental GPS observable (to derive the range) is the signal travel time between satellite and receiver. The travel time can be computed from two types of measurements, provided by GPS. First from the code phase measurements, which give the time difference between signal reception time, as determined by the receiver clock, and the transmission time at the satellite, as marked (modulated) on the signal. The computed distance is called the pseudo-range. Secondly the time interval is computed indirectly from the carrier phase measurements. They give the phase difference between the phase of the receiver-generated carrier signal and the carrier received from the satellite at the instant of the measurement. The phase observable contains the ambiguity of the number of full phase cycles between the receiver and the satellite at the starting epoch, known as the integer ambiguity. If a

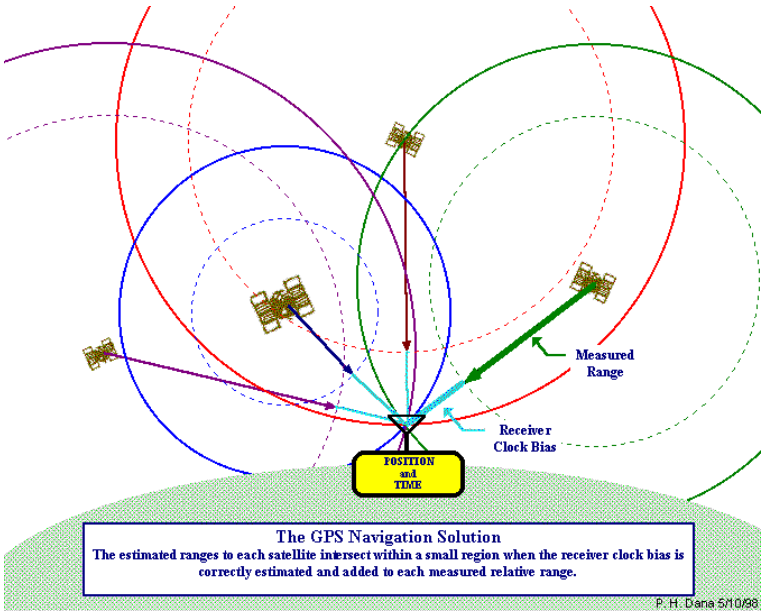

Figure 3.5: The principle of the GPS positioning, measuring the distances from the receiver to at least 4 satellites [Colorado, 2010].

GPS receiver loses a signal temporarily (loss-of-lock), due to obstructions for example, a discontinuity, so-called cycle slip, of an integer number of cycles occurs in the measured carrier phase. The jump in the integer part of the carrier-phase measurement results in the range error.

Bias error sources in GPS measurements are uncorrected satellite clock errors (one meter errors), ephemeris data errors (error in the positioning of the satellite; $1m$), tropospheric delays ($1m$), unmodeled ionosphere delays ($10m$) and multipath. The last error source, the multipath, is difficult to detect and sometimes hard to avoid. It is caused by reflected signals from surfaces near the receiver that can either interfere with or are mistaken for the signal that follows the straight path from the satellite. The impact on a pseudo-range measurement may be up to a few meters. In the case of carrier phase, the error is in the order of a few centimeters. Multipath may be mitigated to some extent through appropriate antenna design, antenna placement and special filtering algorithms within GPS receivers. Besides, the random errors are the combined effect of (PRN) code noise and noise within the receiver. GPS ranging errors are magnified by the range vector differences between the receiver and the satellites. In other words, the GPS positioning depends on both position and the number of visible satellites (i.e. satellites tracked by a GPS receiver).

Different techniques of GPS signal processing enable reducing or eliminating some of the errors. In L-MMS the most commonly used GPS positioning methods is the differential GPS (DGPS). The DGPS system, an enhancement to GPS, consists of a stationary base station at a known position and so-called rover on the mobile platform. At the reference/base station the difference between the position indicated by the satellite systems

and the known fixed position is computed and transmitted to a user's receiver (rover) (i) as a pseudo-range corrections (differential Code GPS, navigation level) or (ii) as a correction of carrier wavelengths number (differential carrier GPS, survey level). For both options the rover applies the corrections in the process of determining its position. It may be implemented in real-time through the provision of a communication link between the GPS receivers (satellites, radio link).

The differential Code GPS (code correction) removes errors common to both the reference and rover receivers, but not also multipath or receiver noise. This means that receivers must be close together, i.e. closet than 100 km. Differential position error reduces to 1-10 meters.

The differential carrier-phase tracking requires both a reference and remote receiver tracking carrier phases at the same time. Besides, they must be close enough to insure that the ionospheric delay difference is less than a carrier wavelength. This usually means that carrier-phase GPS measurements must be taken with a rover and reference station within about 30 kilometers of each other. Special software is required to process carrier-phase differential measurements. The Real-Time-Kinematic (RTK) technique allows for centimeter relative positioning [Colorado, 2010]. The surveying techniques so-called Real-Time-Kinematic (RTK) can provide centimeter relative positioning in real time when the rover is moving. This precision is possible if the baselines is smaller than 10 km, tracking five or more satellites and a real-time radio links between the reference and remote receivers is established.

3.3.3 Inertial Navigation System

Contrary to other means of navigation, inertial navigation does not rely on observation of landmarks or celestial bodies or measuring radio signals. Instead, it utilizes the inertial properties of sensors mounted aboard a vehicle, and provides selfcontained determination of instantaneous position and other parameters of motion of the vehicle, by measuring a specific force, angular velocity, and time. Inertial navigation provides real-time indication of position and velocity of a moving vehicle using Inertial Measurement Unit (IMU) sensors that react on the basis of Newtons laws of motion.

The IMU has a series of angular and linear accelerometers. The angular accelerometers or gyroscopes (rotation rate sensors) measure how the vehicle is rotating in space. The system orientation in space is measured with at least one sensor for each of the three axes and the results are angular rates, angular increments or total angular displacements from an initial known orientation relative to inertial space. Linear accelerometers (acceleration sensors) measure how the vehicle is moving in space. Since it can move in three axes (up and down, left and right, forward and back), IMU includes also three linear accelerometers, one for each axis. These measurements together provide the instantaneous velocity of the system, as well as the orientation. Besides, the IMU information can be used to estimate

the position of the system, through double integration of the measured accelerations.

To summarize, the knowledge of initial 3D position, velocity and orientation of the platform (achieved through initialization and alignment processes) along with the knowledge of inertial Earth rotation and parameters of the selected reference ellipsoid, allow the inertial navigator to derive final positioning information in an Earth centered Cartesian frame, and provide (NED: north, east, down) velocity, as well as heading, pitch and roll. The rotation angles are depicted in Fig. 3.6 and additionally explained in the following.

- roll ω - rotation clockwise or counterclockwise around x-axis that points in the moving direction,
- pitch φ - rotation up and down around y-axis that is directed across to the moving direction and
- yaw or heading κ - rotation left and right around z-axis that is perpendicular to the previous two and directed up or down, so the axes form a right-hand system.

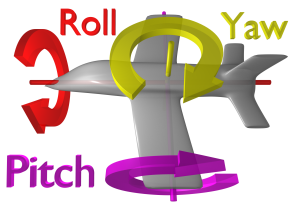

Figure 3.6: The angles roll ω, pitch φ and yaw κ that describe the orientation of the mapping sensor frame with respect to the reference mapping frame [Wikipedia].

The most commonly used modes of inertial navigation in MMS are strapdown inertial navigation systems, where gyros are mounted directly on the vehicle (strapped down to the vehicle). All inertial navigation systems must perform the following functions [Grejner-Brzezinska, 2000a]:

- Facilitate a reference frame for vehicle motion.
- Measure specific force.
- Have knowledge of Earths gravity field.
- Perform time integration of the specific force to obtain velocity and position information.

In principle, INS requires no external information except for initial calibration (initialization and alignment), including externally provided 3D initial position, velocity and attitude. In stand-alone mode the INS navigation results are primarily affected by the initial sensor misorientation, and sensor errors such as accelerometer biases and gyro drifts causing a time-dependent positioning error. Gyro drift rate that mainly determines the orientation accuracy of an IMU[1], defines how much the orientation measurements drift away from the true value in certain time. An illustration of the gyro drift is given in

[1] In Schwarz and El-Sheimy [2004] four classes of gyros are distinguished according to the constant drift rate.

the following section; see Fig. 3.7. Because the sensor errors grow with time, INS must be re-calibrated periodically to maintain reliable navigation quality [Grejner-Brzezinska, 2000a]. The accuracy can be improved, if a fixed reference is available - e.g., using the GPS points as keystones, and if the system is not allowed to drift without a reference for too long. As a consequence, the INS-determined vehicle trajectory will diverge from the actual path, depending primarily on the quality of the IMU sensors and the mission duration.

3.3.4 Integration of the sensors

Most of the modern L-MMS systems rely on high-accuracy differential GPS (DGPS) and quality strapdown INS[2]. GPS and INS, as navigation techniques, offer highly complementary operational characteristics by using entirely different positioning principles. As a radio navigation satellite system GPS provides essentially geometric information, while autonomous INS offers inertial information, i.e., the reaction to the applied force. GPS maintains its high accuracy and stability over time, enabling continuous monitoring of inertial sensor errors. This is possible on condition that the GPS receiver maintains a lock to a minimum of four satellites. The INS provides positioning and orientation with potentially high short-term accuracy. Compared to the conventional GPS output rate, which is usually 1-10Hz, INS provides much higher positioning update rates up to 256 Hz (see Fig. 3.7). Thus the INS provides precise position and attitude information between the GPS updates and during GPS losses of lock. Integration of these two systems, which is commonly named also Positioning and Orientation System (POS), provides a superior performance as opposed to either sensor in a stand-alone mode.

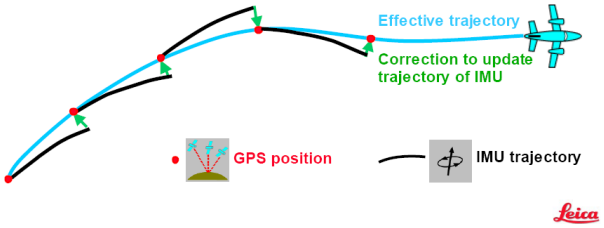

Figure 3.7: The integration of accurate, but low rate GPS measurements and high rate INS measurements which drift in time from the true position [Leica, 2009].

To combine the inertial and GPS measurements Kalman filtering is the most suitable technique [Grejner-Brzezinska, 2000a]. There are several alternative integration techniques, which can be selected based on the specific application, performance requirements, installation constraints and costs. The last factor is often decisive, as the cost of a quality INS is still much higher than GPS. However, over the past few years a substantial INS price drop allowed more widespread use of inertial navigation in mobile mapping, leading to a significant improvement in performance and automation. Three primary integration schemes

[2]Early systems used simpler, and lower quality dead-reckoning systems (wheel counter or odometer,directional and vertical gyros)

for GPS and INS are so-called uncoupled, loosely coupled, and tightly coupled modes. For more details on Kalman filter see [Grejner-Brzezinska, 2000a; Cramer, 1997].

3.4 StreetMapper system

StreetMapper is a commercial laser Land-based Mobile Mapping System (L-MMS). It incorporates 4 laser scanners, GPS/IMU sensors and 2 digital cameras, which are mounted on the roof-rack platform that can be placed on different vehicles. A general construction of StreetMapper hardware components on a rigid platform is shown in Fig. 3.8. The prime motivation for its development was to answer the demand for a system that surveys many kilometers of highways very rapidly, to be mobilized very quickly and to be less expensive than airborne scanning. Besides offering good relative and absolute accuracy, it incorporates eye-safe (Class I) scanners that give full field of view and scan at speeds of up to $80km/h$ [StreetMapper, 2010].

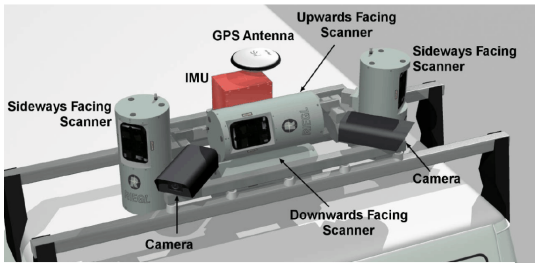

Figure 3.8: The StreetMapper multi-sensor platform with hardware components: laser scanners, IMU sensor, GPS antenna and video camera [Kremer and Hunter, 2007].

In Section 3.4.1 the multiple laser scanners mounted on the StreetMapper platform are presented with their specifications. Besides, the StreetMapper scanning geometry is discussed. In Section 3.4.2 the next two main components, GNSS and INS, as integrated within StreetMapper are presented. In Section 3.4.3 the video sensor is described that can be optionally mounted on the StreetMapper platform.

3.4.1 Laser scanners

The StreetMapper includes four Riegl high speed 2D line laser scanners directed left, right, down and up. As the main interest in this project is the beach topography and features on the beach, the data acquired by the upward directed scanner are not useful and therefore not included in the dataset. The main specifications of the other three laser scanners are summarized in Table 3.2. Some fields are empty, because the manufacturer's specifications do not provide the same data for all three scanners. Full description of the scanners specifications can be found on the manufacturer's website [Riegl, 2010].

Table 3.2: Summarized specifications of three different laser scanners mounted in StreetMapper system [Riegl, 2010].

	Q120	Q120i	Q140 - 80
Maximum range[a] :			
Natural targets $\rho \geq 80\%$	$\leq$ 150 m	-	$\leq$ 450 m, 50 mm resolution $\leq$ 350 m, 25 mm resolution
Natural targets $\rho \geq 20\%$	$\leq$ 75 m	-	-
Natural targets $\rho \geq 10\%$[b]	-	$\leq$ 150 m	$\leq$ 150 m
Wire targets d $\geq$ 6 mm	-	$\leq$ 45 m	-
Minimum range	2 m		
Ranging accuracy [c]	25 mm	20 mm	-
Precision[d]	15 mm		25 mm[e]
Measurement resolution	-		25 mm or 50 mm
Laser pulse repetition rate	30 kHz		
Data rate	10000 measurements/s		
Laser wavelength	Near infrared		0.9 μm (near infrared)
Laser beam divergence[f]	2.7 mrad		approx. 3 mrad
Scanning range	$\pm$ 40°		
Scanning mechanism	Rotating polygonal mirror		
Scanning rate, selectable	5 to 100 scans/s		1 to 40 scans/s
Angle step between consecutive laser shots	$\geq$ 0.04°		0.11°
Angular resolution	0.01°		0.036°
Scan type	Perfectly linear scan		

[a] Depending on the reflection coefficient ρ of the target. Typical values for average conditions. In bright sunlight, the operational range is considerably shorter than under overcast sky. At dawn or at night the range is even higher.

[b] Beam incidence perpendicular to target.

[c] Accuracy is the degree of conformity of a measured quantity to its actual (true) value.

[d] Precision also called reproducibility or repeatability, is the degree to which further measurements show the same result. One sigma @50m range under RIEGL test conditions.

[e] Standard deviation @25 mm resolution, plus distance depending error $\leq$ 20ppm.

[f] 1 mrad corresponds to 10cm beam width per 100m of range.

Multiple laser scanners enable high effective pulse rate and resolution. Each scanner obtains up to 10,000 measurements per second at a scanning rate of up to 100 scans per second. The scanning rate is chosen by the operator and influences the scan pattern on the surface i.e., the in-line point resolution (see Fig. 3.9(a)).

The scanners' rangefinder system is based upon the principle of time-of-flight measurements. In this project the range, scan angle, signal amplitude (intensity) and the time stamp are recorded for every measurement. As can be seen in Table 3.2 the values of

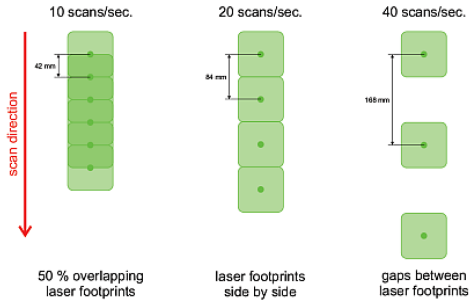

(a) A scan pattern of Riegl-Q120i within a scanning line and at a target distance of $30m$. The laser footprint measures $90 \times 90mm$.

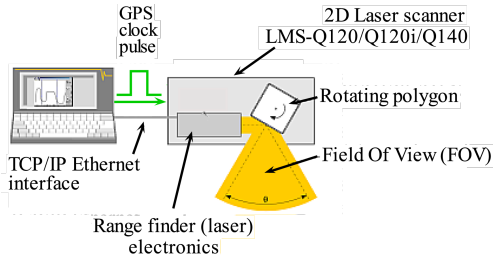

(b) Schematic presentation of Riegl laser scanner components.

Figure 3.9: Characteristics of the Riegel laser scanner components and the scan pattern [Riegl, 2010].

maximum ranges differ between scanners. This is because Riegl Q140 is a short range ALS scanner and can therefore measure longer ranges. On the other hand the Riegl Q120(i) is a terrestrial scanner primarily designed for the use in industrial environment. Therefore it measures shorter ranges. Maximum range for each scanner varies due to the different reflection coefficients ρ of targets (as explained in Section 3.3.1.1). According to the specifications of the Q120(i) scanner, this scanner can measure a sandy beach up to a distance of 120 m (Fig. 3.10). The maximum range depends also on the incidence angle to the target and is here assumed to be 0° i.e. laser beam is perpendicular to the target's surface. If the incidence angle increases, the maximum range decreases [Riegl, 2010].

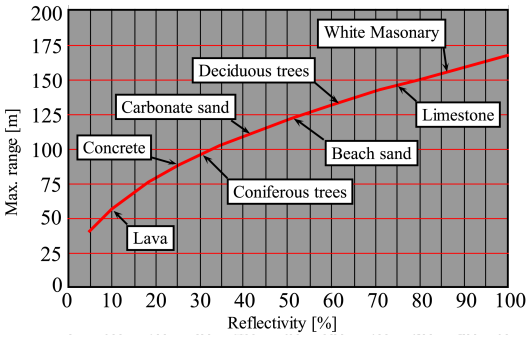

Figure 3.10: The correlation between a maximum range that can be measured with Riegl Q120 and a reflectivity ρ of surface material [Riegl, 2010].

The scanning geometry is rather complicated, as three different scanners are incorporated in the present L-MMS system. Scanners have different characteristics (as presented in Table 3.2) and orientations (see Fig. 3.11). The two side scanners Riegl Q120 and Riegl Q140 are mounted vertically looking back at an angle of 45° from the drive direction, on the left and on the right side, respectively (see Fig 3.11(a)). The third scanner, a Riegl Q120i, is laying horizontally and is directed 20° downward at the rear of the vehicle (see Fig 3.11(c)). All three scanners provided an 80° FOV and use a polygonal rotating mirror

as a scanning mechanism (see Fig. 3.9(b)). In case of the pilot-project the height of the laser scanner above the ground is approximately $2m$, therefore the strip (or swath) width (SW) can be computed for the down looking scanner Q120i and is approx. $9.5m$. It can measure ranges in the interval between approximately $5.8m$ (straight behind the vehicle, $\Theta = 90°$) and $8.7m$ at both sides left and right ($\Theta = 50°$ or $130°$, respecitvely). How far the side scanners measure, depends on the surface orientation. If the acquisition area is flat, the system developers estimates that laser scanners can measure approx. 25 meters on both sides of the vehicle [Rijkswaterstaat, 2009]. The point density is varying from 4 up to approximately 1400 points/m^2 (see results in Chapter 7). The actual scan pattern is shown later in Fig. 3.20.

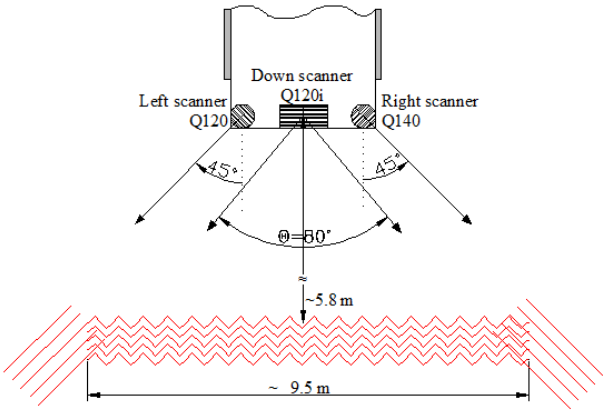

(a) Top view.

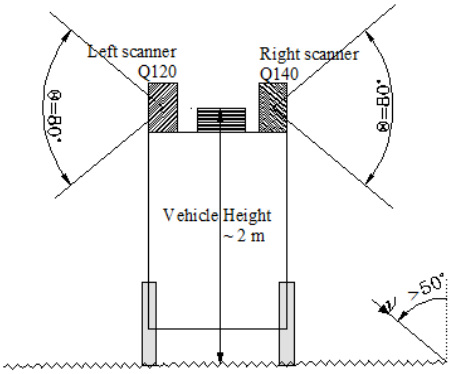

(b) Back view.

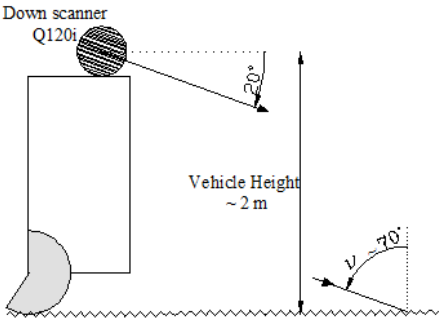

(c) Side view.

Figure 3.11: Schematic diagram of the StreetMapper system.

3.4.2 GNSS/IMU system within TERRAcontrol Computer

The TERRAControl GNNS/IMU system is used for position and attitude determination inside the StreetMapper and consists of several units. First it integrates the IGI IMU-IId fiber optic gyro based IMU with $256Hz$ data rate. It strongly supports the position accuracy in areas of weak or missing GNSS [Kremer and Hunter, 2007]. This high-grade IMU is quoted to provide 0.004° RMS in roll and pitch and 0.01° RMS in heading [IGI, 2010]. However, this high accuracy can not be fully exploited for the short scanning distances in this land-based application. Secondly the TERRAcontrol computer unit integrates high end dual frequency GNSS receiver and antenna. This receiver supports GPS, GLONASS and OmniSTAR HP real time corrections. However, the real time corrections from OmniSTAR HP are usually not used because the system is optimized for data processing in post processing mode [Kremer and Hunter, 2007]. Besides, TERRAcontrol comprises speed sensor to allow good accuracy under poor satellite conditions. The speed sensor slows down the error growth of the inertial navigation system (i.e. IMU) in periods of missing GPS signal. The later one cures when driving in a tunnel or under a tree cover. The TERRAcontrol computer is used during the acquisition to store the raw data from the IMU, the GPS receiver and speed sensor, to distribute an accurate GPS time stamp to all sensors for later synchronization of data streams and to control the performance of the acquisition mission. The last task is performed with the help of SMcontrol computer unit, a user interface with 8 inch TFT display. The operator can start and stop the operation of TERRAcontrol, access the actual GNSS status and synchronously start and stop the different laser scanners, as well as visualize the scanner data.

3.4.3 Digital video or still camera(s)

Optionally, StreetMapper offers two different imaging systems, depending on the survey applications. For most of the applications the main task of the imaging data is, to enable a better visual interpretation and to use videos or images for documentation purposes.
The first option is two 720×576 pixel geo-referenced high quality digital still cameras, mounted together with the other sensors on the StreetMapper rigid platform (Fig. 3.8). The second option is, to mount the digital video camera independently from the other sensors. In this case the rigid connection to the IMU is missing and videos can not be used as photogrammetric source material. But the information about the position and orientation of the camera is still good enough to use the resulting videos for visualization/interpretation purpose [Kremer and Hunter, 2007].

In case of the measuring campaign on Egmond aan Zee the second option was implemented, thus the camera was placed on the front part of the vehicle roof (see the underlying photo in Fig. 3.3). The unreferenced videos of the measured area are in this research used just as a side information to give an idea about the features that were scanned. An example of such digital video information of Egmond aan Zee beach is shown in Fig. 3.12.

Figure 3.12: A photo made during the acquisition mission, showing the detail of beach grass.

3.5 Data set Egmond aan Zee

The aim of the pilot-project employing the L-MMS StreetMapper system and the reasoning to scan the coast near Egmond aan Zee is given already in Section 2.3. In this Section the structure of the StreetMapper data and the attributes attached to the laser points are described in detail. This information is used later in Chapters 4, 5 and 7) for system evaluation.

In Section 3.5.1 the pre-processing steps are described, which were undertaken by the commercial contractor company Geomaat. In Section 3.5.2 the StreetMapper dataset, as it was delivered for this master thesis research, is described.

3.5.1 Data pre-processing

The L-MMS measurements Egmond aan Zee acquired with the StreetMapper system are available as a "commercial" product, namely as an already processed point cloud. This initial data processing, done by Geomaat can be divided into two main steps.

The first step includes all calculations that are needed to create the georeferenced point cloud. TERRAoffice software is used in the post processing step, which aims at merging the simultaneously acquired geometric profile information (laser scan data) with the position and orientation data of the scanning platform. Besides GNSS/IMU sensors on board StreetMapper, the locally operated base station was used to perform DGPS measurements. The base station was placed in the middle of the pilot-project area, therefore the baseline is not longer than $3km$. The calculation of the position and orientation of the sensor platform is done using TERRAoffice. Integrated observations determine the vehicle trajectory. Then the laser raw measurements are merged with the positions and (calibrated) orientations to calculate a geo-referenced point cloud using RiWorld from Riegel Laser Measurements Systems. At the end the 3D laser points were transformed into Dutch national coordinate

system, using TERRAoffice[3] [Kremer and Hunter, 2007]. The dataset covers an area of approximately $6km$ along shore and $180m$ cross shore, consisting of 56,6 millions laser points.

The second step is the creation of different kinds of products and databases out of the point cloud. This laser data post-processing step was done using TerraSolid modules as TerraScan, TerraModeler and TerraMatch which are based on MicroStation. In case of data set Egmond aan Zee the point cloud was first split into eight project tiles (blocks, marked as BL1-BL8) of $750 \times 750m$, each containing less than 8 million points (Fig. 3.13). Now the data can be easier handled by the software used for analysis. The laser points were classified using TerraSolid laser processing suite: TerraScan and TerraModeler. The exact procedure is not known, but can be studied from manuals on the Terrasolid website [TerraSolid, 2010] and by reading description of similar project on the coast at Filey Bay, North Yorkshire, UK [Barber and Mills, 2007b].

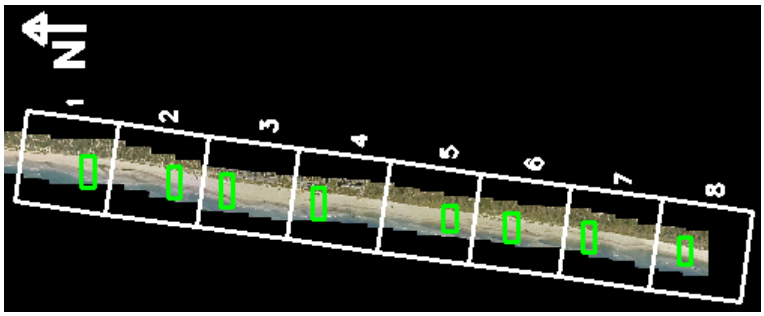

Figure 3.13: An ortophoto of the acquisition area on the beach near Egmond aan Zee. The position of the 8 blocks dividing the whole L-MMS dataset (white squares) and the cross-strips (green rectangles), which define the subareas of approximately 1 million laser points, are indicated.

3.5.2 Data description

At this point the StreetMapper laser point clouds were delivered to us, one per block in a binary *las* file format[4]. The attributes and characteristics of the dataset are on first instance examined in the TerraSolid modules, which enable fast and easy visualization of the huge amount of laser points and some simple analysis. But for a better control and validation of the laser point cloud, further analyses are done with the help of the programming software MATLAB. Here the plots of the attributes and their relations are made, to get an overview of the StreetMapper performance and its measurements. However, it is very time consuming, if not impossible (out of memory) to perform analysis with 8 million points in Matlab. For this reason, first a subset of laser points is chosen, but in a way that it still represents the whole acquisition area. Thus in each of the eight blocks (see Fig. 3.13) subareas the so-called cross-strips with a width of approximately 100 m

[3] TERRAoffice contains routines for laser data geocoding, transformation of the results into local mapping systems and various quality control tools.

[4] Industry standard format for laser data.

perpendicular to the coastline are chosen. They are drawn as green rectangles in Fig. 3.13. Approximately 1 million laser points that lie within each of the rectangles are extracted and exported from TerraScan as a text file (8 files, one for each block). They can be now easily read in Matlab for further processing. In the following paragraphs the attributes of the laser points are presented on an example of the cross-strip in block 8.

3.5.2.1 Attributes of laser points

ASCII files have 9 columns, where each column stands for an attribute of the laser point. For each attribute a short notation is written, which is used later on in this report. The attributes are visualized and their (typical) values are given, to get an idea of the L-MMS dataset. Figures of color-coded laser points made in TerraScan present the same area, the cross-strip in the last, eight block. Histograms are plotted in Matlab.

Position X, Y, Z is given with coordinates easting (X), northing (Y) and height (Z).

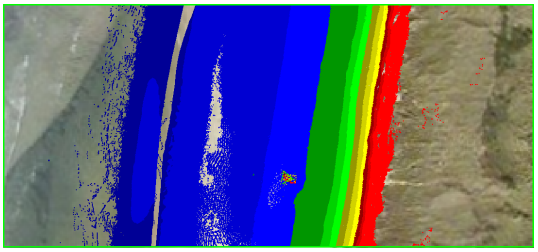

Figure 3.14: Laser points of the cross-strip in block 8 color coded by elevation.

Intensity I**.** The definition of intensity is given in Section 3.3.1. In Fig. 3.15 higher intensities occur on the right side of the test area, i.e. upper beach (light grey), and lower intensities on the left side (dark grey), closer to the waterline. The reason for this trend might be, that the dry sand on the upper beach reflects the laser light better than the wet sand by the waterline. The intensity values measured by StreetMapper laser scanners are shown in Fig 3.15(b). The laser scanner Q140 has on average higher intensities than the other two scanners. This can be explained by the fact, that Q140 is a long range scanner and thus emits and receives laser beams with more energy (higher intensity).

Class C**.** Using the user-defined macros in Terra Solid modules (see also section 3.5.1), the laser points were classified into 6 classes [TerraSolid, 2010]. Each class has a unique value: Ground (Value 2), Low vegetation (Value 3), Medium vegetation (Value 4), High vegetation (Value 5), Control points (Value 8), Building (Value 9). Fig. 3.16(b) shows a profile situation of classified points, where the brown color (ground points) prevails over green (vegetation). In this profile an object on the beach is depicted (red colored points). When looking at the acquisition mission videos, it turns out that red points represent the crane.

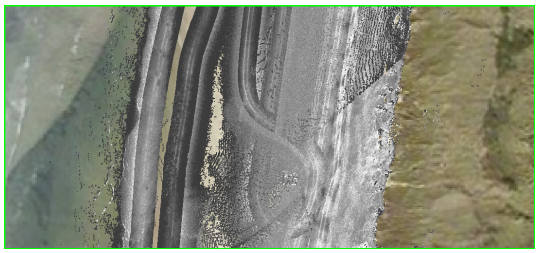

(a) Laser points of the cross-strip in block 8 color coded by intensity.

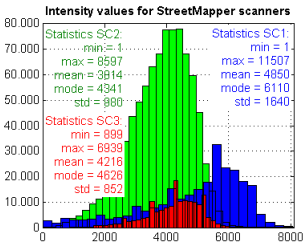

(b) Histograms of intensities, as measured by laser scanners.

Figure 3.15: An example of intensity measurements.

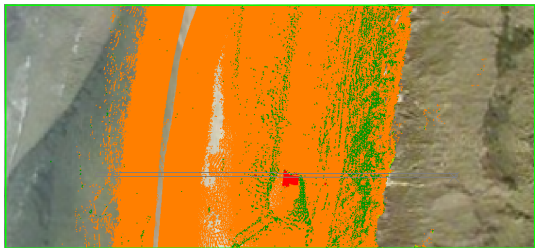

(a) Brown indicates a ground point, green a vegetation point and red a building point.

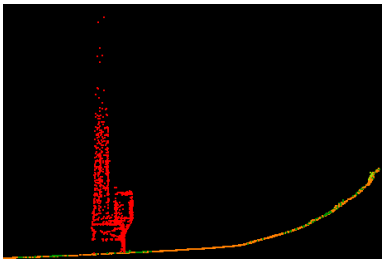

(b) Profile of the laser points. The 2D position of profile is shown in Fig. 3.16(a)

Figure 3.16: Laser points of the cross-strip in block 8 color coded by class number.

Scan angle SA or Θ. As explained in Section 3.4.1, laser scanners have different orientation. Therefore they measure scan angles within different intervals, however they have all 80° FOV. Besides the laser scanner orientation, the relatively flat acquisition area leads to the scan angle measurements as seen in Fig. 3.17. Scanner Q120i (SC2) directed down acquire the full FOV i.e. from 50° to 130°. Due to the relatively flat beach area, the side scanners acquire the laser points mostly below the horizon. This results in the scan angle measurements to be from 50° to 90° in case of the scanner Q140 (SC1), and from 130° to 90° in case of the scanner Q120 (SC3).

Time stamp T. Laser scanners receive the GPS clock pulse that is used in process of measurements integration (step 2 in Section 3.5.1).

Drive-line number DL. The term drive-line is introduced here instead of the common ALS synonym flight-line. Drive-line refer to a continuous section of point cloud data that begin and end where a change in vehicle direction i.e. trajectory approaches 180°. According to this criterion the data were split in Terrasolid's TerraScan suite and the drive-line numbers were derived. The first three blocks (BL1-BL3) include 8 different drive-lines, which are in this report denoted with DL4, DL5, DL7, DL8, DL10, DL11, DL13 and DL14, and the last four blocks (BL4-BL8) include 6 different drive-lines, which are denoted with DL5, DL6, DL9, DL10, DL11 and DL12.

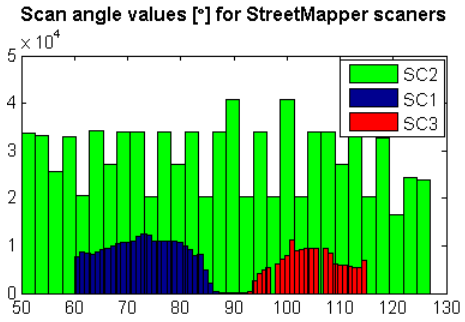

Figure 3.17: Histograms of scan angles, as measured by three StreetMapper laser scanners.

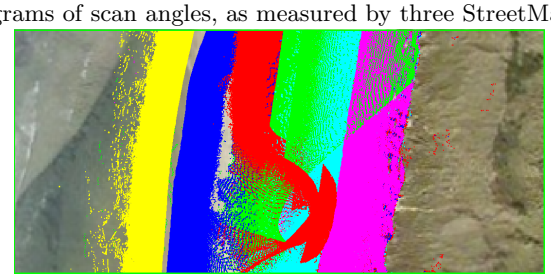

Figure 3.18: Laser points of the cross-strip in block 8 color coded by drive-line number. Six drive-lines (DL) are shown: DL5 pink, DL6 light blue, DL9 green, DL10 red, DL12 blue and DL11 yellow.

Scanner number *SC*. As already described in Section 3.4, three different scanners are mounted on the StreetMapper platform, namely Riegl Q140 on the right side (SC1), Riegl Q120i in the middle and directed down (SC2), and Riegl Q120 on the left side (SC3).

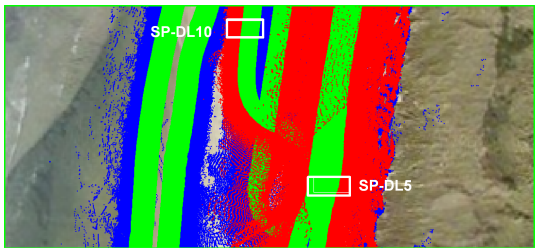

Figure 3.19: Laser points of the cross-strip in block 8 color coded by scanner number. Blue points belong to Q140 (SC1), green to Q120i (SC2) and red to Q120 (SC3). The two white squares indicate the position of the scan patterns shown in Fig. 3.20(a) (SP-DL5) and in Fig. 3.20(b) (SP-DL10).

3.5.2.2 StreetMapper scan pattern

The scan pattern of the StreetMapper drive-lines has some kind of a U-form (see Fig. 3.11(a)). The pattern and the width of the drive-lines is changing over the acquisition area, depending on the orientation and position of the surface with respect to the vehicle. Fig. 3.20 shows an example of the scan pattern in area just behind the vehicle (close to the trajectory). The pattern of driving-line 5 (DL5) in Fig. 3.20(a) is less regular than the one of driving-line 10 (DL10) in Fig. 3.20(b). The reason is that in the first case (DL5) the

underling surface is more rough, than in the second case. The colors in the figures indicate the laser scanner number (see Fig. 3.19). The drive-line 5 was acquired driving from the north to the south and the drive-line 10 in the opposite direction. Distances measured in the figures give an idea firstly about the swath width of SC2, which is in a regular case (DL10) around $9m$. Secondly, an overlap between scanners SC1&SC2 and SC2&SC3 is measured in Fig. 3.20(b) and is $1.14m$ and $1{,}43m$, respectively. Thirdly, the between line point resolution of the side scanner SC1 is indicated, which is around $12cm$ (Fig 3.20(a)) or $14cm$ (Fig. 3.20(b)).

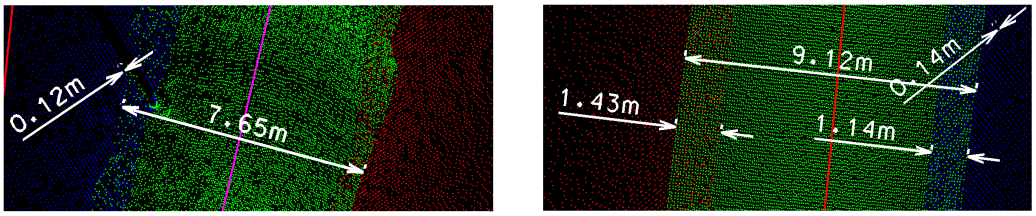

(a) Scan pattern of DL5.

(b) Scan pattern of DL10 (SC-2).

Figure 3.20: Scan pattern of two different drive-lines on two different areas that are shown in Fig. 3.19

3.5.2.3 Trajectories

Besides the 3D laser point cloud, the StreetMapper dataset includes the position of trajectories. The trajectories files (*.trj) describe the system dynamics. They include the position of the sensor system (X,Y,Z), which is moving during the acquisition, and the orientation of the sensor frame with respect to the reference mapping frame i.e. the angles ω, φ, κ; see Fig. 3.6. The trajectory points are registered on average at every 0.15 s, giving the 3D sensor position approximately every 0.5 m. The position resolution depends on the driving speed of the vehicle. The average values of the angles are computed, taking into account all trajectories covering the acquisition area and are -0.4° for roll ω, 1.3° for pitch φ and -172° or 8° for κ. The values of κ depend weather the vehicle is moving along the beach to the south or to the north, respectively.

3.6 Summary

The MMS is an extensive multi-tasking and multi-sensor technique used for diverse applications. In this chapter an attempt is made, to embrace the whole concept of the technology. Thus, a reader gets the impression of its extend and finds further references according to his/her interest. In this research the main topic is, as indicated in the title, the MMS system that includes the laser scanner(s) and is mounded on the vehicle. The laser Land-based Mobile Mapping System (L-MMS) is capable to directly acquire the 3D metric information of the real world in a form of a point cloud. This is enabled by integrating the

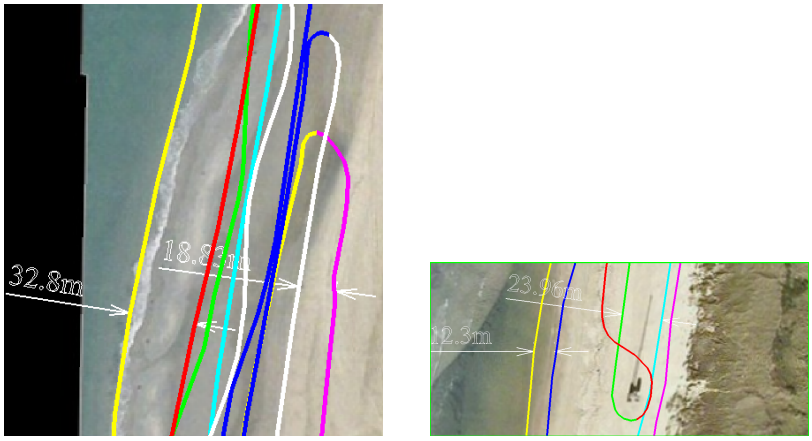

(a) Trajectories in the cross-strip in block 1.

(b) Trajectories in the cross-strip in block 8.

Figure 3.21: Position of trajectories within two different acquisition areas. Within block 1 there are more trajectories than within block 8.

range and scan angle measurements from line laser scanners, and position and orientation measurements from GPS/INS system. The 3D point cloud is available almost real-time. Different of-the-shelf L-MMS sensors are available that have different specifications and can be uniquely mounted on a rigid platform. Therefore, also different operating laser L-MMS systems exist on the market. Here the so-called StreetMapper system is described in detail, because its data are later used to evaluate the laser L-MMS performance for measuring the sandy coast morphology. StreetMapper incorporates four line Riegl laser scanners, which have different orientation, i.e. two lie horizontal directed up and down and two lie vertical directed left and right. Laser scanner measurements are of different quality, which is evident from the manufacturer specifications. On a relatively horizontal surface laser scanners acquire a typical U-shape pattern. The actual point resolution depends on the laser measurement rate, scanning rate, speed of the vehicle and surface orientation with respect to the laser beam. The initial examination of the StreetMapper data shows a dense data coverage of the beach and less in the dune area. Besides, most of the points are classified as a ground points and are acquired by the down-ward directed laser scanner. In this particular pilot-project the acquisition area is covered with many drive-lines. All laser L-MMS measurements presented in this chapter and thus also the derived laser point cloud include errors. Their size and impact on the quality of the 3D point positioning and derived DTM will be in detail investigated in the following four chapters.

Chapter 4

StreetMapper error budget

The analysis, propagation and mathematical formulation of errors is indissoluble from correct interpretation of the data and use of the derived results. To have confidence in using a Land-based Mobile Mapping System (L-MMS) for detailed on demand survey, an extensive validation of the system and derived results is necessary. In this chapter an a-priory validation of the L-MMS system is discussed. The aim is, to define the overall expected quality of the L-MMS laser points derived from the L-MMS measurements. Because in general all measurements have an error, the question to be answered here is, how the measurement errors propagate to the end-product, 3D position of the laser points.

In Section 4.1 first the commonly used and sometimes interchanged words describing the data quality, namely the accuracy and precision, are defined. Secondly, the different types and properties of errors are discussed. This theory is used in Section 4.2 to construct the first order random error propagation model, which is based on the L-MMS geo-referencing model. The model includes many parameters (observations): measurements of L-MMS subsystems and calibration parameters that connect the measuring sensors. In Section 4.3 for each group of observations, i.e. component, typical error sizes are examined and numerical examples are given for StreetMapper. In Section 4.4 a rigorous first order error analysis of the geo-referencing equations is undertaken for the StretMapper system. Finally, in Section 4.5 the main results are summarized.

4.1 Error properties and propagation law

The derivation of theoretical accuracy models, prediction of the expected accuracy and error propagation are not a straightforward task. For this reason first the basics of estimation theory on statistical properties of observations (random variables) is shortly explained here. In Section 4.1.1 the terms accuracy and precision are explained. They are often used in relation with observations to summarize their statistical properties. The concept of precision and accuracy is closely related to the topic of observation errors, which is therefore discussed in Section 4.1.2. According to the error properties of observations included in a mathematical model, a proper error propagation technique must be chosen. Shortly the

theory on error propagation is given in Section 4.1.3.

4.1.1 Concepts of precision and accuracy

Precision, also called reproducibility or repeatability, is the degree to which further measurements show the same result, or in other words, the degree of closeness among a set of observations of the same random variable i.e. the closeness of observations to their mean. The precision can be indicated with the spread (or dispersion) of the measurement's probability distribution function. In a one dimensional case the precision of the data can be represented with the standard deviation σ, on condition that σ can be defined for probability distribution function of the data [Mikhail, 1976; TerraSolid, 2010].

Accuracy, on the other hand, is closeness of the best estimated value obtained by the measurements, to the accepted "true" value of the measured quantity. In other words, accuracy is the degree of closeness of a measured quantity to its actual (true) value. To determine accuracy, the measurements are compared to data of higher quality (representing "true" values) to see how well they agree.

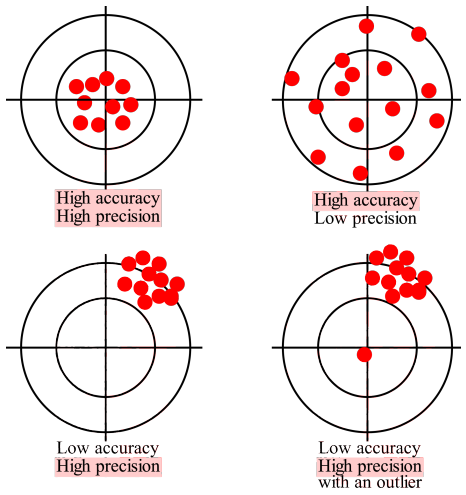

Figure 4.1: The concept of the precision and accuracy, explained with target analogy.

The described concept is illustrated with a target analogy in Fig. 4.1. The center of the target represents the accepted "true" value. The closer the observation is to the center, the more accurate it is. The extent of the scattered data is a measure of the precision.

Another explanation of the relation between the accuracy and precision is illustrated in fig. 4.2, using the probability distribution of a measurement set m_j. m on the x-axis indicates the true value. The least precise is m_2, having the biggest spread (standard deviation) and the most precise is m_3. On the contrary m_3 is lees accurate in comparison to m_1 and m_2 that are equally accurate. To sum up, the difference between the precision and accuracy lies in the possible presence of bias or systematic errors. Precision includes

only random effects and the accuracy encompasses systematic effects.

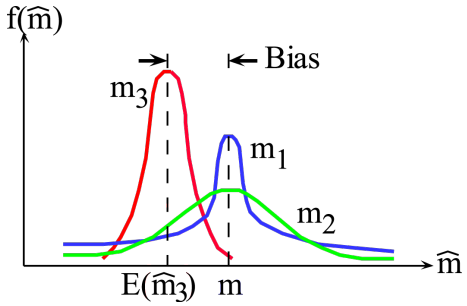

Figure 4.2: The concept of the precision and accuracy, explained on the basis of the probability distribution (after [Mikhail, 1976]).

The use of the terms accuracy and precision is often confused in the literature and they can be quoted differently in different sources. Therefore, the values for precision/accuracy (for example in the laser scanner specifications) should be taken with care and a proper understanding to what they refer is important. For example, the error of a parameter or measurement given in specifications is typically about twice the standard deviation. In this way, 95% of errors should be smaller then the error given in specifications.

4.1.2 Three types of errors

The errors are divided in three types: (i) random errors, (ii) systematic errors and (iii) blunders (also gross errors or outliers). They are explained in the following.

4.1.2.1 Random errors

From the statistical point of view, observations are considered as samples from probability distributions of random variables, thus observations always include some error or uncertainty. The basic and inherent property that the estimates of random variable do not agree with its expectations, results in the observation error or random error ϵ_i of an observation i as defined in Eq. 4.1 [Mikhail, 1976]:

$$\epsilon_i = \overline{x}_j - x_{ij} \tag{4.1}$$

where:

- $\overline{x}_j$ is the expectation mean of random variables in sample j.
- x_{ij} is an observation i in a sample j.

The magnitude of the random errors for L-MMS depends on the quality of the systems measurements. These include position and orientation measurements from the GPS/IMU unit, and scan angles and ranges from the laser scanner unit. Effect of random errors in the system measurements can be dissected into position noise, orientation noise and range noise. Noise in some of the system measurements affects the relative precision of the

derived point cloud, which means for instance, noise in the GPS/IMU derived orientation affects the region closer to the trajectory less significantly than regions further away [Habib et al., 2008].

4.1.2.2 Systematic errors

Systematic error is constant at certain conditions and is introduced into all measurements. Hence the resultant bias is deterministic, but can not be detected neither reduced by repeated measurements (unlike random errors). They cause the measured quantity to be shifted away from the "true" value, thus the systematic effect of observations concern just the location parameter (the mean). This means that nothing is wrong with the observations, but the systematic error indicates the inconsistency between observations and functional model. There are several ways to optimize the functional model to account for systematic effects (for details see [Mikhail, 1976], p. 67-71). Systematic effects can have different forms (constant, counteracting) depending on the value and sign of each of the effect and their magnitude varies from one situation to another (can not be predicted). They occur due to physical causes (atmosphere changes), instrumental errors and/or observer's human limitations etc. Besides, they can arise due to high correlated random errors that are not accommodated in the stochastic model.

Systematic errors of the L-MMS in the mounting parameters relating the system components, as well as in the system measurements, might result in biases in point positioning. Systematic errors in the system measurements include systematic errors in the laser scanner (e.g. biases in the range and scan angle measurements) and systematic errors in the derived GPS/IMU position and orientation (e.g. differential troposphere and ionosphere, multi-path, IMU initialization and misalignment errors, and gyro drifts). Position and orientation drifts might have a more significant impact and moreover cannot be considered in the calibration process since their magnitude and impact change from one mission to another. But the impact of those drifts does not come as a surprise, if the quality of the GPS/IMU integration process is carefully examined e.g. through the forward and backward processing of the individual drive-lines. On the other hand the systematic errors in the mounting parameters as well as in the range and scan angle measurements do not come with prior warning regarding the potential of having discrepancies in areas of overlapping strips, but can be determined in the calibration procedure [Habib et al., 2008].

4.1.2.3 Blunders or outliers

The blunder, called also outlier or gross error, is an observation that does not fit with most of the other observations and the assumed model. Their values are far too high or much too low. Outliers are considered as erroneous observations or mistakes that can occur due to e.g. wrong reading of a scale, wrong recording, failure of equipment etc. Therefore it is important to detect and remove them from the dataset, before the processing and

describing the data, what usually require tedious manual editing.

When scanning the beach topography, outliers might result from the laser beam reflection on birds or people. In [Lichti et al., 2005] few examples of points having a gross error are given including (i) the angular displacement of features due to the finite laser beamwidth, (ii) mixed pixels, occurring when the laser beam illuminates two surfaces separated less than half the pulse length, and (iii) detector saturation[1], blooming[2] and multipath[3], occurring when scanning high reflective surfaces.

4.1.3 Error propagation law

In statistics the propagation is defined as a technique to determine stochastic properties of the dependent variable y from a given characteristics of the independent variable x. It is assumed that the functional relationship relating the two sets of variables is known. The function can be linear or nonlinear. In practice the solution for a nonlinear function present problems, while it involves double integrals. Therefore it must be linearized first. Three propagation rules can be distinguished, depending on the input [Mikhail, 1976]:

- Propagation of means (expectations).
- Propagation of random errors (variances and covariances).
- Propagation of systematic errors.

Since in this research the main concerns are the errors of observations, included in georeferencing formula, and because they are quoted as random errors with one sigma value, the variances and covariances propagation law is used. For nonlinear functions this law is formulated in the following manner. The two random vectors

$$\widetilde{y} = [\widetilde{y}_1 \widetilde{y}_2 \dots \widetilde{y}_n] \text{ and } \widetilde{x} = [\widetilde{x}_1 \widetilde{x}_2 \dots \widetilde{x}_m]$$

with two variance-covariance matrices

$$\Sigma_{xx} = \begin{bmatrix} \sigma_{x1}^2 & \sigma_{x1x2} & \dots & \sigma_{x1xm} \\ \sigma_{x1x2} & \sigma_{x2}^2 & \dots & \sigma_{x2xm} \\ \vdots & \vdots & \ddots & \vdots \\ \sigma_{x1xm} & \sigma_{x2xm} & \dots & \sigma_{xmxm}^2 \end{bmatrix} \text{ and } \Sigma_{yy} = \begin{bmatrix} \sigma_{y1}^2 & \sigma_{y1y2} & \dots & \sigma_{y1yn} \\ \sigma_{y1y2} & \sigma_{y2}^2 & \dots & \sigma_{y2yn} \\ \vdots & \vdots & \ddots & \vdots \\ \sigma_{y1yn} & \sigma_{y2yn} & \dots & \sigma_{ynyn}^2 \end{bmatrix}$$

are related with a nonlinear function $\widetilde{y} = y(\widetilde{x})$. Then the variance and covariance law (in matrix form) defines Σ_{yy} as in Eq. 4.2.

$$\Sigma_{yy} = J_{yx} \cdot \Sigma_{xx} \cdot J_{yx}^T \tag{4.2}$$

[1] Detector saturation occurs when the reflected energy exceeds the dynamic range of the laser scanner detector.

[2] Blooming occurs when the laser light is reflected also from the side of a highly reflective target, which then appear larger in size.

[3] Range measurements are made from backscattered laser energy, that was reflected by more than one surface.

Where J is the Jacobian matrix (size $m \times n$), which include all partial derivatives of function(s) y over the variables x evaluated at initial values of variables $x_1^0, x_2^0 \ldots x_n^0$, as written in Eq. 4.3.

$$J_{yx} = \begin{bmatrix} \frac{\partial y_1}{\partial x_1} & \frac{\partial y_1}{\partial x_2} & \cdots & \frac{\partial y_1}{\partial x_n} \\ \frac{\partial y_2}{\partial x_1} & \frac{\partial y_2}{\partial x_2} & \cdots & \frac{\partial y_2}{\partial x_n} \\ \vdots & \vdots & \ddots & \vdots \\ \frac{\partial y_m}{\partial x_1} & \frac{\partial y_m}{\partial x_2} & \cdots & \frac{\partial y_m}{\partial x_n} \end{bmatrix} \tag{4.3}$$

Propagation of the random errors through the functional model for scanner point positioning produces a 3×3 covariance matrix that contains all point positional precision information.

4.2 First order random error model of L-MMS

In the previous section the basics of the error theory are given. In order to exploit the expected quality of final 3D laser point coordinates the observation equations are required to propagate the L-MMS measurement errors. Therefore, in the following first the laser scanning mathematical model, which relates the system measurements to the ground coordinates of the laser points, is developed. This so-called geo-referencing model is then used to obtain the first order random error model of L-MMS as explained in the following.

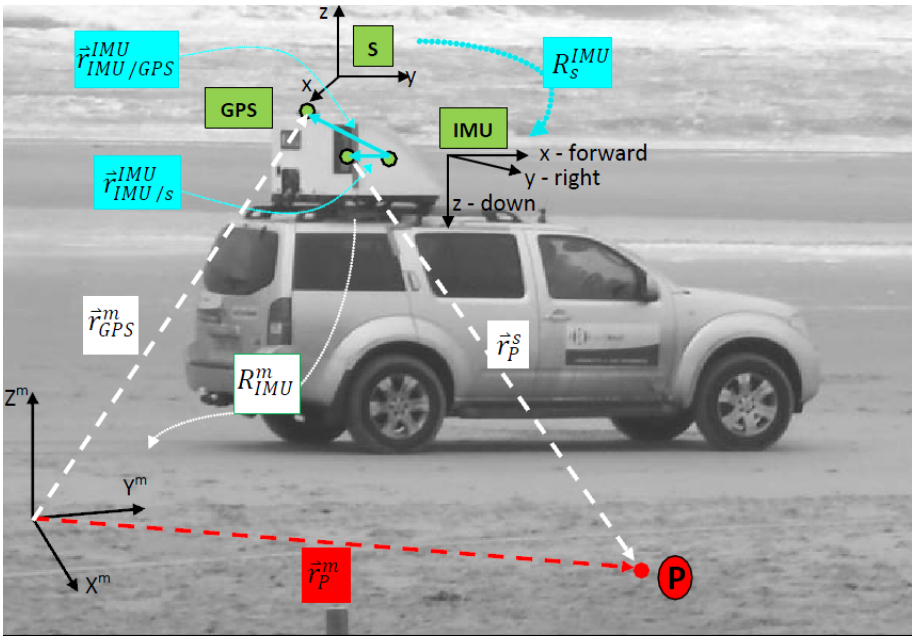

Figure 4.3: Principle of laser L-MMS geo-referencing.

Employing the laser scanning mathematical model the points with coordinates in an

arbitrary sensor frame ($\vec{r}_P^{\,s}$) are converted into a reference geodetic (mapping) coordinate frame ($\vec{r}_P^{\,m}$). This transformation is called also geo-referencing. Geo-referencing enables to merge and compare different datasets (from different epochs and/or techniques) in a common reference space. The basis of the geo-referencing formula is a seven parameter transformation, where parameters of 3D rotation and translation transformation, and scale are computed as given in Eq. 4.4, see also Fig. 4.3.

$$\vec{r}_P^{\,m} = \vec{r}_S^{\,m} + \mu_s^m \cdot R_s^m \cdot \vec{r}_P^{\,s} \tag{4.4}$$

Where:

- $\vec{r}_P^{\,m}$ is the position vector of a target point P in the mapping (m) frame.
- $\vec{r}_S^{\,m}$ is the position vector of the laser scanner S in the mapping (m) frame.
- μ_s^m is the scale between the laser scanner (s) and the mapping (m) frame, which equals to one in case of laser measurements.
- R_s^m is the rotation matrix from laser scanner (s) frame to the mapping (m) frame.
- $\vec{r}_P^{\,s}$ is the position vector of target point P in the laser scanner (s) frame.

The coordinates of the laser points are calculated by combining the measurements from each of the L-MMS system components (laser scanner, GPS and IMU system) and mounting parameters relating those components. Thus Eq. 4.4 can be extended to account for those indirect measurements of the transformation parameters and for the movement of the platform in time (position and orientation are changing). The relationship between the system measurements and parameters is embodied in so-called LIDAR equation. Lidar equation is written in Eq. 4.5, which shows also one intermediate step of geo-referencing formula development from Eq. 4.4 [Ellum and El-Sheimy, 2002]. A graphical representation of the terms in lidar equation is shown in Fig. 4.3 and their definitions are given in Table 4.1 [Glennie, 2007b].

$$\begin{aligned} \vec{r}_P^{\,m} &= \vec{r}(t)_{GPS}^{\,m} + R(t)_{imu}^m \cdot \left(\vec{r}_{IMU/S}^{\,imu} - \vec{r}_{IMU/GPS}^{\,imu} \right) + R(t)_{imu}^m \cdot R_s^{imu} \cdot \vec{r}_P^{\,s} \\ \vec{r}_P^{\,m} &= \vec{r}(t)_{GPS}^{\,m} + R(t)_{imu}^m \cdot \left(\vec{r}_{IMU/S}^{\,imu} - \vec{r}_{IMU/GPS}^{\,imu} + R_s^{imu} \cdot \vec{r}_P^{\,s} \right) \end{aligned} \tag{4.5}$$

The quantities (17 parameters) on the right hand side of the Eq. 4.5 are all measured during the acquisition mission or determined through a calibration process. For this reason they all contain errors. Those errors can be best examined, if Eq. 4.5 is first expressed with all seventeen observations as follows [Glennie, 2007b]. The position vector of the target point P in laser scanner (s) frame is indirectly measured by the laser scanner and therefore depends on its configuration, i.e. the orientation of the laser scanner frame (s). In this research a straightforward model for the operation of the 2D laser scanner is used (see Fig. 3.3), so the Cartesian coordinates of the point P in laser scanner frame (s) can be calculated as in Eq. 4.6:

$$\vec{r}_P^{\,s} = d_P^s \cdot \begin{bmatrix} \sin\Theta \\ 0 \\ \cos\Theta \end{bmatrix}_P^s \tag{4.6}$$

where:

Table 4.1: Elements of the geo-referencing formula (Eq. 4.5), 3 unknowns of laser point and 17 observations, i.e. measurements and calibration parameters. Numbers in the brackets enumerate the observations.

Variable	Description
	Unknowns
$\vec{r}_P^m$	Position vector [X,Y,Z] of the target point P in mapping frame(m). Three unknowns.
	Measurements
$\vec{r}(t)_{GPS}^m$	Position vector [X(1),Y(2),Z(3)] of the GPS antenna in mapping frame (m). Measured by DGPS navigation subsystem.
$R(t)_{imu}^m(\omega,\varphi,\kappa)$	Rotation matrix with rotation angles roll $\omega(4)$, pitch $\varphi(5)$, yaw $\kappa(6)$, relating the IMU (imu) and mapping frame (m). Determined through integrated IMU measurements
$\vec{r}_P^s(d,\Theta)$	Position vector of the target point P in laser scanner frame (s). Measured indirectly by laser scanner through scan angle $\Theta(7)$ and range $d(8)$.
	Calibration parameters
$\vec{r}_{IMU/S}^{imu}$	Lever arm (offset) [X(9),Y(10),Z(11)] between the origin of the IMU sensor and the laser scanner (S), given in IMU coordinate frame (imu). Determined by measurement or system calibration.
$\vec{r}_{IMU/GPS}^{imu}$	Lever arm (offset) [X(12),Y(13),Z(14)] between the origin of the IMU sensor and the GPS antenna given in IMU coordinate frame (imu). Determined by measurement or system calibration.
$R_s^{imu}(d\omega,d\varphi,d\kappa)$	Rotation or boresight matrix with the boresight angles $d\omega(15)$, $d\varphi(16)$, $d\kappa(17)$, relating the laser scanner (s) and the IMU frame (imu). Determined by system boresight calibration.

- d_P^s is the observed laser range (distance) to the object point P in the laser scanner frame (s).
- Θ is the scan angle in xz-plane from the z-axis to the vector of the object point P in the laser scanner frame (s).

Now, the geo-referencing formula can be written as in Eq. 4.7:

$$\begin{bmatrix} X \\ Y \\ Z \end{bmatrix}_P^m = \begin{bmatrix} X \\ Y \\ Z \end{bmatrix}_{GPS}^m + R(t)_{imu}^m(\omega,\varphi,\kappa) \cdot \left(\begin{bmatrix} X \\ Y \\ Z \end{bmatrix}_{IMU/S}^{imu} - \begin{bmatrix} X \\ Y \\ Z \end{bmatrix}_{IMU/GPS}^{imu} + R_s^{imu}(d\omega,d\varphi,d\kappa) \cdot \vec{r}_P^s(d,\Theta) \right) \quad (4.7)$$

The covariances and variances propagation law introduced in Section 4.1.3 is now used for the L-MMS observations to propagate their random error through geo-referencing model given in Eq. 4.7. Because the main aim of this research is to estimate the effect of the

individual observation on the ground coordinates of laser points, it is assumed there is no correlation between observations. Considering all error sources included in goe-referencing formula (Eq. 4.7) and using the variance propagation law (Eq. 4.2) the result is 3×3 covariance matrix of a directly georeferenced laser point. However, the error propagation is simplified to the variance computation (not also covariances) of unknowns. Therefore both variance matrices Σ_{xx} and Σ_{yy} are diagonal with off-diagonal elements equal to zero. Then the variance of dependent variable y writes as in Eq. 4.8.

$$\sigma_{yi}^2 = \left(\frac{\partial y_i}{\partial x_1}\sigma_{x1}\right)^2 + \left(\frac{\partial y_i}{\partial x_2}\sigma_{x2}\right)^2 + \ldots \left(\frac{\partial y_i}{\partial x_n}\sigma_{xn}\right)^2 \tag{4.8}$$

Where y_i in our case represents 3 coordinates of the ground points ($i = 1, 2, 3$). On the left hand side the influences of all 17 observation errors are summarized ($n = 1 \ldots 17$, as described in Table 4.1).

The partial derivatives of the geo-referencing formula, which are obtained by differentiating Eq. 4.7 w.r.t all seventeen parameters, are multiplied by the observations' variances. The result is a first order error model given in Eq. 4.9, which enables the estimation of the total 3D laser point positioning error.

$$\begin{bmatrix}\sigma_X^2\\ \sigma_Y^2\\ \sigma_Z^2\end{bmatrix}_P = \begin{bmatrix}\sigma_X^2\\ \sigma_Y^2\\ \sigma_Z^2\end{bmatrix}_{GPS} + \tag{4.9a}$$

$$\left[\left(\frac{\partial R_{imu}^m}{\partial \omega}\vec{v}\cdot\sigma_\omega\right)^2 + \left(\frac{\partial R_{imu}^m}{\partial \varphi}\vec{v}\cdot\sigma_\varphi\right)^2 + \left(\frac{\partial R_{imu}^m}{\partial \kappa}\vec{v}\cdot\sigma_\kappa\right)^2\right] + \tag{4.9b}$$

$$\left(R_{imu}^m \cdot R_s^{imu} \cdot \begin{bmatrix}\sin\Theta\\ 0\\ \cos\Theta\end{bmatrix}^s_P\right)^2 \cdot \sigma_d^2 + \tag{4.9c}$$

$$\left(R_{imu}^m \cdot R_s^{imu} \cdot d_P^s \cdot \begin{bmatrix}\cos\Theta\\ 0\\ -\sin\Theta\end{bmatrix}^s_P\right)^2 \cdot \sigma_\Theta^2 + \tag{4.9d}$$

$${R_{imu}^m}^2 \cdot \begin{bmatrix}\sigma_X^2\\ \sigma_Y^2\\ \sigma_Z^2\end{bmatrix}^{imu}_{IMU/S} + \tag{4.9e}$$

$${R_{imu}^m}^2 \cdot \begin{bmatrix}\sigma_X^2\\ \sigma_Y^2\\ \sigma_Z^2\end{bmatrix}^{imu}_{IMU/GPS} + \tag{4.9f}$$

$${R_{imu}^m}^2 \cdot \left[\left(\frac{\partial R_s^{imu}}{\partial d\omega}\sigma_{d\omega}\right)^2 + \left(\frac{\partial R_s^{imu}}{\partial d\varphi}\sigma_{d\varphi}\right)^2 + \left(\frac{\partial R_s^{imu}}{\partial d\kappa}\sigma_{d\kappa}\right)^2\right] \cdot (\vec{r}_P^s)^2 \tag{4.9g}$$

Where $\vec{v} = \vec{r}^{imu}_{IMU/S} - \vec{r}^{imu}_{IMU/GPS+R_s^{imu}\cdot\vec{r}_P^s}$ and $\vec{r}_P^s$ is defined by Eq. 4.6. The definition of the elements in equation 4.9 is given already before in Table 4.1.

Each line stands for an error vector, which has X, Y and Z direction. Each vector results from one error source and thus forms a component of the random error budget. The first four error components originate from the measurement errors, i.e. from GPS (Eq. 4.9a), IMU (Eq. 4.9b), range (Eq. 4.9c) and scan angle (Eq. 4.9d) measurements respectively. The last three components present errors of calibration parameters, i.e. the IMU/laser scanner offset (Eq. 4.9e), IMU/GPS offset (Eq. 4.9f) and boresight angles (Eq. 4.9g).

4.3 Components of the L-MMS error budget

When composing the error budget for L-MMS laser points, one must consider the nature of the observation errors, which can be random and/or systematic errors (as described in section 4.1.2). For the purpose of this research, just the random errors are considered. The law of error propagation, as explained in Section 4.1.3, is used to evaluate the effect of the random errors of individual measurements and parameters on the accuracy of the derived ground coordinates of laser points, through the geo-referencing mathematical model. The result is the random error budget, which dependents on the chosen geo-referencing method.

In the following, each component of the L-MMS random error budget, as written in Eq. 4.9, is described in more detail. In Section 4.3.1 and 4.3.2 the GPS/INS and laser scanner measurement random errors are examined, respectively. The actual values of those errors are usually given in manufacturer specifications. In Section 4.3.3 the performance of calibration approach is discussed, because it determines the calibration parameter errors. A numerical example of the StreetMapper random errors is added in each of the mentioned sections. For sake of completeness at the end in Section 4.3.4 the error arising from sensor synchronization is introduced. It is finally not included in this random error budget, because of the lack of information.

4.3.1 Positioning and orientation errors

The GPS conditions in a L-MMS system are deteriorated by multipath effect and by shading of the signals caused by trees and buildings. On the other hand, the distance between the scanner and the measured object is typically some ten meters (compared to several hundred meters for Airborne Laser Scanning (ALS)). Therefore the contribution of the GPS positioning error to the overall error budget is expected to be much larger than contribution of the error from the attitude determination [Kremer and Hunter, 2007]. Besides, the integrated GPS/IMU positioning errors directly effect the 3D point position error, because of the employed geo-referencing model (see Eq. 4.9). If the GPS is the only device that provides absolute positional measurements, it bounds the accuracy of the POS subsystem to the accuracy of the GPS data.

In the following two sections each error source, GPS positioning errors and IMU orientation errors, are discussed and evaluated for the StreetMapper system.

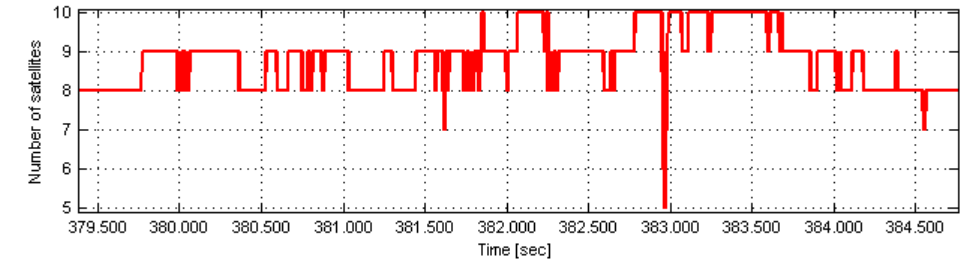

(a) Number of visible GPS satellites.

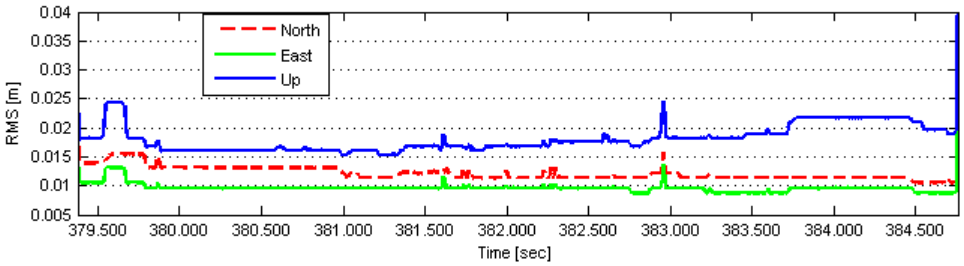

(b) GPS/INS position RMS.

Figure 4.4: Visibility of the GPS satellites and the accuracy of the integrated GPS/IMU system, as observed during the StreetMapper mission on Egmond aan Zee.

4.3.1.1 GPS positioning error (C1)

It is difficult to predict the level of the positioning error, while there are many factors directly influencing on the positioning accuracy of the kinematic DGPS measurements e.g. atmospheric errors, multipath, poor satellite geometry, baseline length and loss of lock [Glennie, 2007b][4]. But it is known that the absolute position accuracy greatly depends on the GPS satellite visibility. In comparison with ALS, which has fairly uniform satellite visibility and therefore also the positional accuracy, the L-MMS systems can experience variable satellite visibility that influences the positional accuracy. The GPS signal quality can vary especially in city canyons and less in open areas like on the beach.
When using GPS positii, the behavior of horizontal and vertical error is quite independent of each other and is therefore usually analyzed separately [Baltsavias, 1999b].

StreetMapper. The typical GPS positioning errors for StreetMapper are estimated approximately to 5 cm in vertical positioning and 2-3 cm in horizontal positioning in case of good GPS conditions, which means visibility of at least 6 satellites. On the opposite, in case of poor GPS conditions, the elevation error increases up to 1 m [StreetMapper, 2010]. Values are valid, if the distance between moving platform (rover) and the GPS base station is smaller than $30km$. In case of the pilot project Egmond aan Zee, the distance is smaller than $3km$ [Cox, 2009].
The Dutch beach consist mostly of completely open area (flat, sandy beaches), thus one can

[4] A detailed examination of DGPS error sources can be found in [Bruton, 2000] or [Raquet, 1998].

expect good GPS satellite visibility. This presumption is indeed confirmed in Fig. 4.4(a) that shows the GPS satellite visibility during the 5380s long ($\approx$ 90 min) acquisition mission on Egmond aan Zee. Those data were recorded during the acquisition [Cox, 2009].

Most of the time 8 or more satellites are visible. Two times during the acquisition in drive-

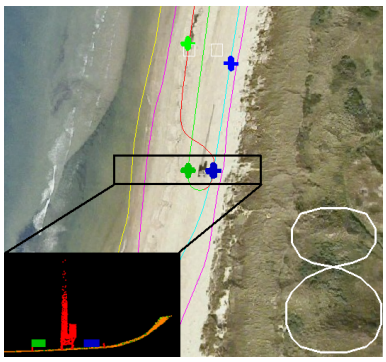

Figure 4.5: The location of the first (blue crosses) and second (green crosses) drop of the visible GPS satellite number and the profile of the laser points in this area, showing the vertical structure of 36m height (in block No.8).

line 6 and 13, for the time interval of 17s and 13s respectively 7 satellites are observed. Additionally in drive-line 9 that continues to drive-line 10 just 5 satellites are observed for 29s. The first and second drop in the number of visible satellites (see Fiq. 4.4(a)) happened in the block number 8, which is shown in Fig. 4.5. The blue crosses show the start and end position of the first drop (on drive-line 6) and the green crosses the second one. As can be seen in the bird-eye photo and the profile of the laser points in this area (Fig. 4.5), there is a 36m high crane tower, that might obstruct the GPS signal. The reason for the second drop is most likely the turning of the vehicle for 180°, when the number of observed satellites usually drops. A smaller number of observed satellites projects into higher 3D positioning error as seen in Fig. 4.4(b). Figure 4.4(b) shows the INS position Root Mean Square Error (RMSE), which is the difference in forward and reverse processing solutions from the Kalman filter. The error is therefore a combination of GPS and IMU measurement errors and is given separately for the north, east and up axis of the mapping coordinate frame WGS84. In case of the StreetMapper mission the maximum vertical error is 2.45 cm (upper blue solid line), while the horizontal error along the Y-axis equals 1.58 cm (north - red dashed line) and along the X-axis equals 1.37 cm (east - green solid line). Those error values are then used in the StreetMapper error pre-analysis (see Table 4.3).

4.3.1.2 IMU attitude error (C2)

The IMU orientation information $(\omega, \varphi, \kappa)$ depends on the performance of the chosen IMU sensor. IMUs are available as commercial off the shelf systems and their accuracy specifications can be easily determined by examining the manufacturer's technical specifications (some examples are in [Glennie, 2007b]).

StreetMapper. The StreetMapper system includes the TERRAcontrol hardware with a

high accuracy class IMU (IGI IMU-IId fibre-optic gyro). The expected angular accuracies in a circle of less than $30km$ radius around GPS base station, as stated in the specifications [StreetMapper, 2010], are 0.004° for the roll (ω) and pitch (φ) and 0.01° for heading/yaw (κ). Those values are used in the StreetMapper error pre-analysis (see Table 4.3).

4.3.2 Laser scanner errors

The errors derived from a laser scanner subsystem, so-called internal sources of the error budget, depend on [Soudarissanane et al., 2008]:

1. The scanner mechanism properties, which are given in manufacturer's specifications, and instrument calibration i.e. error in range and scan angle measurements.
2. Material properties of the scanned surface e.g. wet or dry sand, roughness, reflectivity, color.
3. Environmental (atmospheric) conditions e.g. ambient light, humidity, temperature, atmosphere.
4. Scanning geometry e.g. the range and the incidence angle. Therefore the quality of 3D points vary through the point cloud.

Those factors effect the quality with which the laser scanner subsystem is able to measure the scan angle and the distance from laser scanner to the target (range). Typically the factors of second and third group are included in the error values (i.e. range accuracy) given in manufacturers specifications for particular laser scanner and are not investigated here. The fourth group of factors usually results in systematic errors, which are not know in advance and could be asses with post-processing quality control procedure. The attempt do do so for Streetmapper data are described in Chapter 5. Thus for the purpose of the error pre-analysis (random error budget), just the two major error components, namely random errors in distance and random errors in scan angle, are considered as explained in the following.

4.3.2.1 Range error (C3)

In [Baltsavias, 1999b] the basic equations are given to compute the range accuracy, depending on the laser ranging principle. For Time-Of-Flight (TOF) scanners it is mainly dependent on the internal accuracy of the clock utilized to measure time, and for the Phase Difference (PD) scanners on the accuracy of phase measurements. However, the value of range error (accuracy) is usually given in manufacturer's specifications.

StreetMapper. Although the scanners mounted in the StreetMapper system originate from the same company, their quality measures given in the specifications [Riegl, 2010] are not consistent. The scanners Q120 and Q120i have specified their accuracy and precision, but for the Q140 just the accuracy is given (see Table 3.2). Therefore, to be able to compare scanners performance, only the values stated for each scanner as the "Precision" in

Table 3.2 are included in this error pre-analysis (Table 4.3).

4.3.2.2 Scan angle error (C4)

The scan angle error is not always directly stated in the manufacturer's specifications. In [Glennie, 2007b] the angular error is considered as a results from two error sources: the angular resolution of the laser scanner angle encoder and uncertainty due to beam divergence (beamwidth). The value for the first error source can be straightforward read out from the laser scanner specifications, but the second one requires more discussion.

As it is explained already in Section 3.3.1 the laser beam divergence causes the positional uncertainty. The error can not be predicted a-priori, because it depends on the location and shape of the scanned objects (not know a-priori). A probabilistic model is therefore required to quantify the anticipated level of uncertainty [Lichti et al., 2005]. Assuming a laser beam of circular cross section having diameter β and a uniform level of laser power across the entire beam width diameter, the beam width uncertainty equals to one-quarter of the laser beam width diameter in angular units [Lichti et al., 2005]. However, the uniform distribution of the power is typically not the case. The actual relative power distribution within a footprint has a very definite peak and slope and is influence by incidence angle [Schaer et al., 2007]. This would suggest that the uncertainty is smaller than one fourth of the beam divergence. The greater power near the center of the beam increases the probability that a return signal comes from a surface nearer to the emitted beam centerline [Glennie, 2007b]. But according to Glennie [2007b] the one-quarter seems reasonable assumption, since the effect of incidence angle and the terrain slope are not included into the a-priori error budget computation. The total error of the scan angle is then computed as in Eq. 4.10.

$$\sigma_{\Theta} = \sqrt{\Delta\Theta^2 + (\beta/4)^2} \tag{4.10}$$

Where:

- $\Delta\Theta$ is scan angle resolution.
- β is laser beamwidth.

StreetMapper. An example of a scan angle error computation is given in Table 4.2 for the StreetMapper system.

4.3.3 Calibration parameter errors

Since many sensors are used within the L-MMS system, the geometrical relations between them must be accurately measured i.e. the lever arm offsets and the bore-sight angles (see Fig. 4.3 and definitions in Table 4.1). The mounting parameters as well as their errors are determined with a proper calibration procedure [Skaloud, 2006]. The calibration process can be executed in laboratory, measuring known points, or during the acquisition mission by taking measurements over a calibration field. The third option is to use some other

Table 4.2: The computation of the scan angle errors for the laser scanners mounted on StreetMapper.

Laser scanner	Angular resolution $\Delta\Theta$ [°]	Beamwidth β [mrad]	Total angular error σ_Θ [°]
Q140	0.036	3	0.056
Q120i/Q120	0.01	2.7	0.04

measurement equipment (e.g. tape, theodolite) and measure the mounting parameters on the platform itself. It is assumed that the calibration parameters do not change in time (during acquisition), since all sensors are rigidly mounted on the platform.
The nature of calibration parameter errors is systematic, in case parameters are not known exactly or if they are not included in the functional model (see Section 4.1.2). But in this research it is assumed that their exact values with the belonging standard deviations are known (obtained prior, with a calibration process). Therefore the errors are modeled in the random error budget as a random effect. In the following both two components of the calibration parameters, namely the lever-arm offset errors and boresight misalignment angle errors, are discussed.

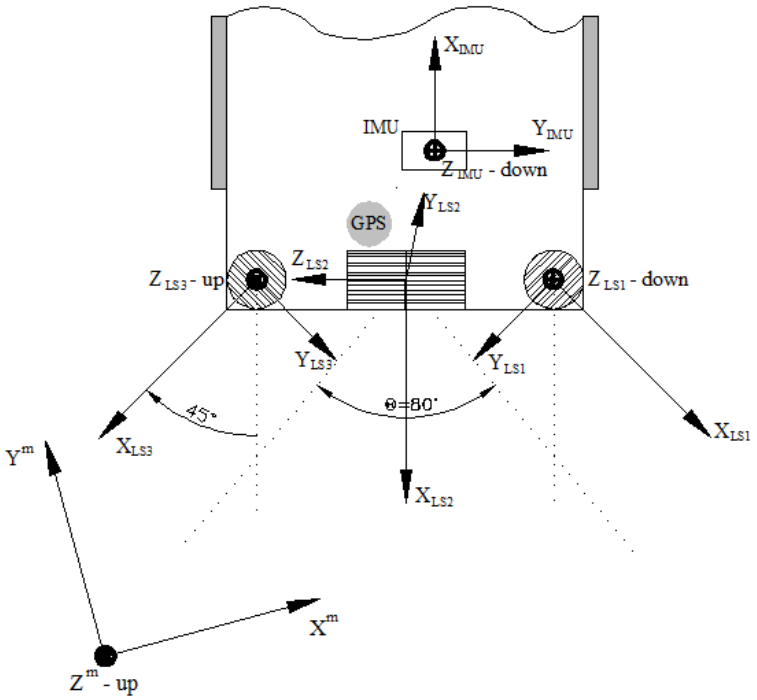

Figure 4.6: The configuration of GPS and IMU sensor, and three laser scanners as mounted on the StreetMapper platform.

4.3.3.1 Lever-arm offset error (C5 and C6)

The lever-arm (offset) between the laser scanner center and the navigation subsystem center (to IMU and/or GPS sensor) can not be measured physically, therefore there are two common methods to obtain offsets indirectly. In the first method the lever-arm offset is determined through calibration measurements of known points. But while the components of the lever-arm correlate strongly with other error sources, the obtained values are questionable. The second method combines the physical measurements, using a tape measure, with the values on engineering drawings supplied for the IMU and laser scanner. While the second method is easier to implement, it is used in majority of cases.

StreetMapper. The lever arm offsets are determined by a combination of physical measurements and the use of engineering drawings [Cox, 2009]. Their errors are therefore estimated with a rule of thumb as given in [Glennie, 2007b] and are for this research set to $5mm$ (see Table 4.4).

4.3.3.2 Boresight misalignment angle error (C7)

The body frame of the IMU does not exactly match with the laser scanner frame. Even more, in case of the L-MMS the orientation of the laser scanner(s) can be very different and unique, since they may be pointing in any number of orientations. To determine the actual laser scanner attitude, the angles between both frames have to be calculated. In general two approaches are used, that both take advantage of overlapping strips, usually acquired in different directions. A first option is a manual adjustment, where features visible in laser point cloud, as building edges, are used to line up the data. The process is time consuming, dependent on the operator skills and has low accuracy in case not many features are visible in the laser data. In case of manual calibration the errors are estimated with a rule of thumb or from other discussions like in [Glennie, 2007b]. The second approach is least squares adjustment, where tie or control points between overlapping strips are aligned and the best fit boresight angles are determined. Statistics from the least squares adjustment give the accuracy for the boresight angles [Glennie, 2007b].

StreetMapper. The error of boresight angles is estimated with a rule of thumb, since it is known that the calibration angles were manually modified in TerraMatch software until everything looked as if it matched well (this step was done by Geomaat). According to Glennie [2007b] the accuracy of the manual adjustment for boresight angles is no better then accuracy of the IMU measurements itself. Therefore the error of boresight angles rotating the laser scanner frame around x and y-axis equals to $0.004°$ (as error of roll and pitch measurements) and the error of the boresight angle rotating the frame around z-axis equals to $0.01°$ (as error of yaw measurements), see Table 4.4.

4.3.4 Synchronization error

In [Ellum and El-Sheimy, 2002] the first order error model derived from the georeferencing formula includes also the synchronization error. All measurements from different sensors

(GPS, IMU and Laser scanner) are required to be taken at the same time. If there is a time offset and this is not known precisely, it will cause a variable error. The error increases with increasing change rate of the related measurements, e.g., while a time offset between range and rotation angles can have a small effect for a calm/smooth drive (rotation angles are relatively stable), it can influence the 3D accuracy a lot for a rough drive [Baltsavias, 1999b]. Therefore all subsystems must be precisely time-tagged to minimize errors from insufficient sensor synchronization. In most cases GPS technology provides a well-defined time signal to which the other sensors can be slaved [El-Sheimy, 2005]. Results in [Barber et al., 2008b] show that synchronization errors using up to the 1 pulse per sec (1 PPS) GPS signal do not significantly impact the laser point positioning. Therefore the time synchronization error is omitted in this error budget.

4.4 Results of the StreetMapper error budget

In this section the theory about random error propagation through the geo-referencing model is used to calculate the StreetMapper random error budget. The values of observations (measurements and calibration parameters) and their errors, which are expected to occur in case of scanning the Dutch coast by StreetMapper, are summarized in Table 4.3 and Table 4.4). These values are inserted in the random error budget model given in Eq. 4.9.

Table 4.3: Expected values of GPS, IMU and laser scanner measurements and their standard errors included in pre-analysis of StreetMapper error budget.

Component	Random error source	Measurements for each LS		Expected values	Standard error (σ)
C1 (Eq. 4.9a)	GPS error	$\vec{r}(t)^m_{GPS}$		-	$[13.7; 15.8; 24.5]mm$
C2 (Eq. 4.9b)	IMU error	$(\omega, \varphi, \kappa)$		(0,0,8)°	(0.004, 0.004, 0.01)°
C3 (Eq. 4.9c)	Range error	d^s_P	Q140	$25m$	$25mm$
			Q120i	$6m$	$15mm$
			Q120	$25m$	$15mm$
C4 (Eq. 4.9d)	Scan angle error	Θ^s_P	Q140	80°	0.056°
			Q120i	90°	0.040°
			Q120	100°	0.040°

The theoretical StreetMapper values of random errors σ for measurements and calibration parameters are discussed already in Section 4.3. Besides, the first order error model given in Eq. 4.9 requires estimation of the initial values of measurements and calibration parameters, i.e. to compute the Jacobian matrix, see Eq. 4.2. Therefore, before presenting the results of random error budget, the determination of observation initial values is discussed in the following.

Table 4.4: System calibration parameters and their standard errors included in pre-analysis of StreetMapper error budget.

Component	Random error source	Parameters for each LS		Calibrated values	Standard error (σ)
C5 (Eq. 4.9e)	Lever-arm LS	$\vec{r}^{imu}_{IMU/S}$	Q140 Q120i Q120	[-171; 499.5; -189.6]mm [-243.3; -106.5; -27.9]mm [-78.4; -461.9; -42.9]mm	[5; 5; 5]mm
C6 (Eq. 4.9f)	Lever-arm GPS	$\vec{r}^{imu}_{IMU/GPS}$		[-281; -3; -466]mm	[5; 5; 5]mm
C7 (Eq. 4.9g)	Boresight angle	($d\omega$, $d\varphi$, $d\kappa$)	Q140 Q120i Q120	(0, 0,-135)° (90, 20, 180)° (180, 0, 135)°	(0.004, 0.004, 0.01)°

The magnitudes of StreetMapper calibration parameters are for this project given in the internal files of TERRAcontrol system, which were delivered with the laser scanner data. The **.gla* file includes lever arm between GPS antenna and IMU sensor (lever arm GPS) and three **.sdp* (Session description Protocol) files the calibration parameters for each laser scanner. The boresight angles for each laser scanner are written indirectly in the rotation matrices. Therefore the knowledge of the position and orientation of the IMU sensor and all three laser scanners, as presented in Fig. 4.6, is used to define the boresight angles as follows. The IMU frame and all three laser scanners frames are right-handed. The IMU frame has X-axis pointing forward, Y-axis pointing on the right, and Z-axis pointing down. The X-axis of rear scanner Q120i (LS2) is looking backwards, and down at 20°, the X-axis of right scanner Q140 (LS1) is looking back and right at 45° and the X-axis of left scanner Q120 (LS3) is looking back and left at 45° (see also section 3.4.1 and Fig. 3.11). The Z-axis of LS1 and LS3 are pointing in opposite direction, i.e. down and up, respectively. The Z-axis of LS2 points on the left. Y-axes are perpendicular to X- and Z-axis, complementing the coordinate system into the right-handed system. Considering this information, the boresight angles are determined as angles rotating a laser scanner frame first around x, then around y and finally around the z-axis to align it with the IMU frame. A positive rotation around axes is in counter-clockwise direction. The calibration parameter values of each scanner are given in Table 4.4.

In Table 4.3 the expected values of measurements are given, considering the acquisition system, i.e. StreetMapper, and area, i.e. relatively flat coast. The initial values of the IMU angles and scan angles are determined by examining the original StreetMapper dataset. Those measurement values are described already before in Section 3.5. For the simplicity of analysis the roll and pitch angles are set to 0° and the yaw/heading angle equals 8°[5]. Scan

[5]As it is found out during the error budget computation, the value of the initial yaw angle does not

angle values differ between the laser scanners according to their orientation (see Fig. 3.17). The expected scan angle of each laser scanner is taken as the most frequent value of the scan angle measurements.
The typical values of the range measurements are estimated according to the specifications and orientation of each StretMapper laser scanner, described in Section 3.4. In case that the scan angle for the scanner Q120i equals 90° (as decided in the previous paragraph), then its typical range is set to $6m$. The typical range value of scanner Q140 and Q120 is set to $25m$, however the scanner Q140 is capable to measure slightly larger ranges as Q120. In this way the comparison of results is simplified. The range $25m$ for side scanners correspond to the expected swath width (see Section 3.4).

Those values (see Table 4.3 and Table 4.4) are now used to compute the random error budget for each StreetMapper laser scanner. Results of the scanner random error budget are presented as a total 3D positioning error, horizontal and vertical error. Because it is assumed that all individual error sources are uncorrelated and that the random errors in observations lead to the random errors in the derived point cloud, the following equations are used to compute the total 3D $\sigma_{T,P}$, horizontal $\sigma_{H,P}$ and vertical $\sigma_{V,P}$ error for a parameter set P:

$$\sigma_{T,P} = \sqrt{\sigma^2_{xC1,P} + \sigma^2_{yC1,P} + \sigma^2_{zC1,P} + \ldots + \sigma^2_{xC7,P} + \sigma^2_{yC7,P} + \sigma^2_{zC7,P}} \tag{4.11a}$$

$$\sigma_{H,P} = \sqrt{\sigma^2_{xC1,P} + \sigma^2_{yC1,P} + \ldots + \sigma^2_{xC7,P} + \sigma^2_{yC7,P}} \tag{4.11b}$$

$$\sigma_{V,P} = \sqrt{\sigma^2_{zC1,P} + \ldots + \sigma^2_{zC7,P}} \tag{4.11c}$$

Here $\sigma^2_{xCi,P}, \sigma^2_{yCi,P}, \sigma^2_{zCi,P}$ are variances of the i-th error budget component computed for a parameter set P.

The analysis of error budget is based on the variation of the two main L-MMS operational variables, i.e. the range and the scan angle. The IMU orientation angles are assumed to be constant. Two parameter sets are used in this analysis (see Table 4.5). Some combinations of operational variables are not possible for a certain laser scanner, due to its orientation and flat acquisition area (unreal case). For example, the scanner Q120i can not measure ranges bigger than approximately $10m$, due to the horizontal mounting position,

Table 4.5: The two parameter sets of range and scan angle values, which are used in the error budget computation.

		Parameter set 1	Parameter set 2
Variable parameter		R = [$5m$, …, $45m$]	SA = [50°, …, 130°]
Fixed parameter	Q140	SA = 80°	R = $25m$
	Q120i	SA = 90°	R = $6m$
	Q120	SA = 100°	R = $25m$

influence the results.

and the scanners Q140 and Q120 mostly do not measure scan angles above horizontal plane laid through their centers, because the acquisition area is mostly flat. However, the same parameter sets are used for all scanners for sake of completeness. In analysis the distinction is made between described unreal and real cases.

Results of the horizontal and vertical error budget are presented per laser scanner in Fig. 4.8 using parameter set 1 (variable range and fixed scan angle) and in Fig. 4.9 using parameter set 2 (variable scan angle and fixed range). These figures show in percentage the relative contribution of the seven components to the horizontal and vertical error of laser points. Besides, in Table 4.6 the actual values of horizontal (H) and vertical (V) errors, resulting from seven components, are written. The values are given for all three laser scanners, assuming the parameter set 1, i.e. at range $5m$ - $45m$. Analyzing the results, one must have in mind the first order propagation model through geo-referencing formula (see Eq. 4.9) and the size of the errors itself (see Table 4.3 and 4.4).

Table 4.6: Results of the horizontal (H) and vertical (V) accuracy of StreetMapper laser point positioning written for each component of random error budget.

		Q140	Q120	Q120i
C1	H	0.0209		
	V	0.0245		
C2	H	0.0009 - 0.0078		0.0008 - 0.0075
	V	0.0004 - 0.0031		0.0003 - 0.0029
C3	H	0.0247 - 0.0255	0.0149 - 0.0157	0.0142 - 0.0149
	V	0.0044 - 0.0045	0.0026 - 0.0028	0.0052 - 0.0054
C4	H	0.0008 - 0.0076	0.0006 - 0.0054	0.0035 - 0.0314
	V	0.0048 - 0.0434	0.0034 - 0.0309	0
C5	H	0.0071		
	V	0.0050		
C6	H	0.0071		
	V	0.0050		
C7	H	0.0009 - 0.0078		0.0008 - 0.0075
	V	0.0003 - 0.0031		0.0003 - 0.0030
total	H	0.0339 - 0.0370	0.0276 - 0.0306	0.0274 - 0.0431
	V	0.0263 - 0.0507	0.0259 - 0.0404	0.0260 - 0.0264

The impact of the GPS error (C1) is constant, as expected looking at the Eq. 4.9a, and directly influences the laser point positioning. It behaves like a constant decrease of both the vertical and horizontal accuracy, where the vertical error is bigger than horizontal (see Table 4.6). C1 dominates the relative error budget in almost all cases shown in Fig. 4.8 and 4.9. The real exceptions are horizontal error of SC Q140, and vertical error of SC Q140 and Q120, for ranges bigger than approximately $20m$ and $30m$, respectively. In these cases the error budgets are dominated by laser scanner errors (C3 and C4, green colors). The

impact of the scanner errors on vertical and horizontal positioning error depends on the scanner orientation. The range error (C3) influences more the horizontal positioning error, which in general slightly increases with the range. The scan angle error (C4) in general causes positioning error in direction of the laser beam movement (laser scanning plane). Its impact significantly increases with the range. This phenomena is illustrated in Fig. 4.7, where the laser beam with a beamwidth β moves over a flat horizontal terrain in a plane perpendicular to the surface. The range is fixed within the beam width and the random scan angle error is $\delta\Theta$. The consequence is that C4 mainly influences on the horizontal

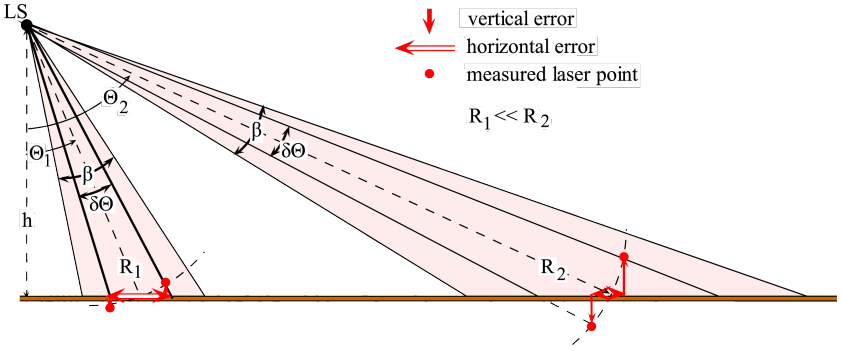

Figure 4.7: The impact of the scan angle error on the horizontal and vertical error.

error of SC Q120i and on the vertical error of SC Q140 and Q120 (see Fig. 4.8 and 4.9). The notice should be paid on a fast and big increase of the C4 impact on vertical error of SC Q140 and Q120, as can be seen in Fig. 4.8(a) and 4.8(c), respectively. For the SC Q140 the scan angle error causes almost 75% of the vertical error at the range $45m$, which is $4.34cm$.
The impact of the IMU attitude errors is very small, due to the small ranges normally taken by L-MMS system. Looking at the Fig. 4.8 there is almost no IMU effect for ranges up to $10m$ and when the range is $45m$ C2 effect is smaller than 5% for all scanners. The values of horizontal error given in Table 4.4 are slightly bigger than for the vertical error. The impact of C2 is almost independent on the laser scanner orientation.
The impact of the lever-arm (C5 and C6) is modulated just by IMU attitude angles (see Eq. 4.9e amd 4.9f) and is therefore independent of range, scan angle and laser scanner orientation. Considering the estimated values given in Table 4.4, C5 and C6 have small impact on laser point positioning error, i.e. few mm. However, the impact as well as the actual values are bigger in case of horizontal error.
The impact of the boresight-angles errors (C7) behaves similar than in case of IMU errors. Also the positioning error values are similar to C2 case, which are again almost independent of the laser scanner orientation. (see Table 4.6). It grows with increasing range (see Fig. 4.8) and is in general bigger for the horizontal error, i.e around $7.5mm$.

Last two rows in Table 4.6 give the numerical values for total horizontal and vertical error of all three laser scanners using parameter set 1. In Fig. 4.10(a) and Fig. 4.10(b) the plots of positioning error are shown, considering parameter set 1 and parameter set 2, respectively. The graphs show the joined impact of all random errors in the system

measurements and calibration parameters on the laser point positioning error. For all laser scanners the total 3D error (solid line, T) increases with the increasing range (see Fig 4.10(a)), but does not change with the scan angle (see Fig 4.10(b)). In the later case the horizontal (H) and vertical (V) error themselves slightly change, but in the opposite direction.

In Fig 4.10(a) one can see that the total error of the scanners Q120i and Q120 is the same and is much smaller than the total error of Q140. This is expected, knowing laser scanners specifications. The differences of horizontal and vertical errors between Q120 and 120i, are due to the different orientation of those two scanners.

In general the horizontal error of laser point exceeds the vertical (see research in [Glennie, 2007b]). But in Fig. 4.10(a) one can observe that the vertical errors for Q140 and Q120 at certain range, at approximately $24m$ and $16m$ respectively, raises above their horizontal error. The effect is mostly due to the scan angle error, as discussed in paragraph above (see Fig. 4.7). The vertical error increases rapidly with the range.

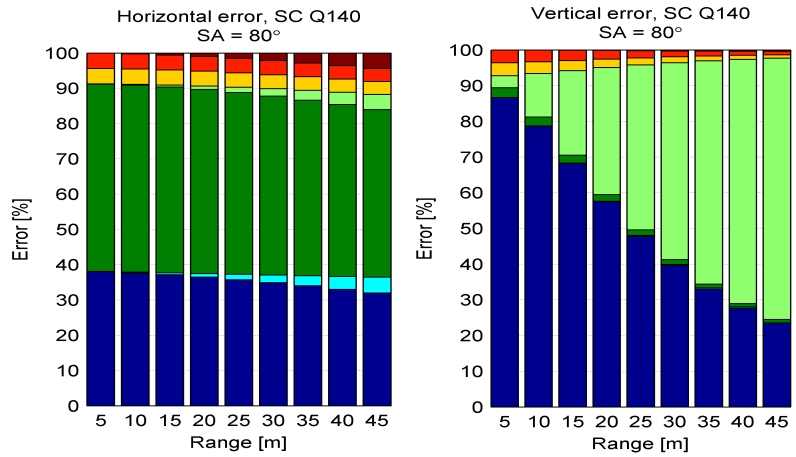

(a)

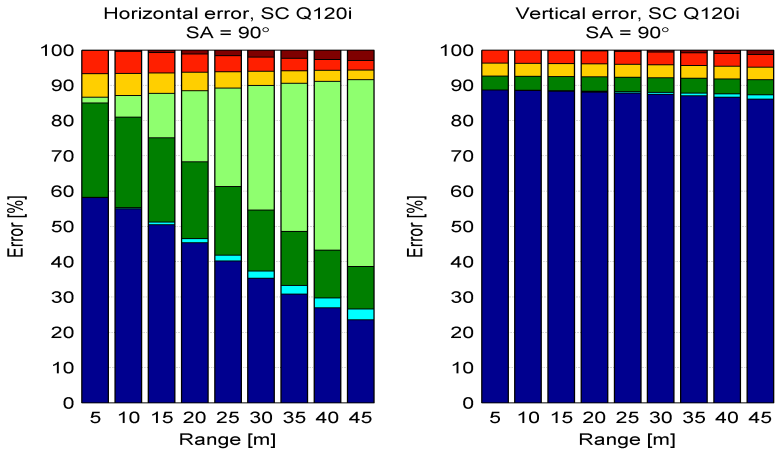

(b)

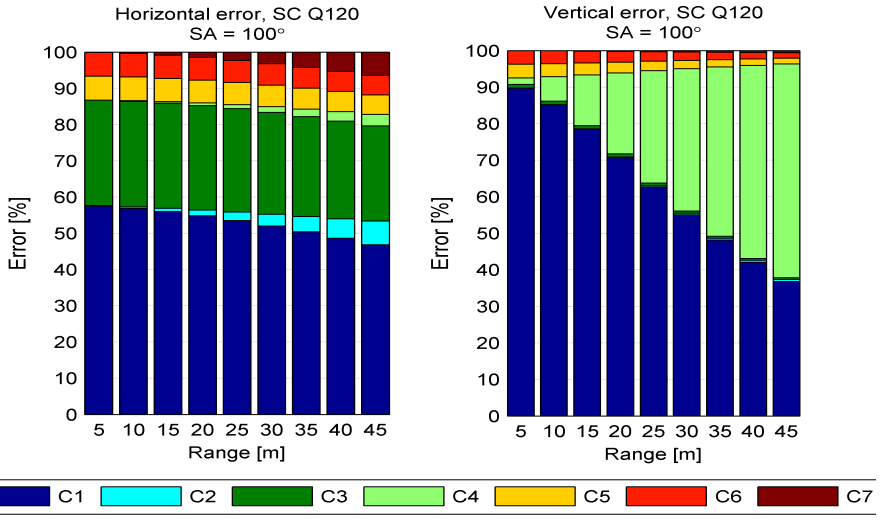

(c)

Figure 4.8: Relative error budgets for the three laser scanners, analyzed according to horizontal and vertical positioning error using parameter set 1.

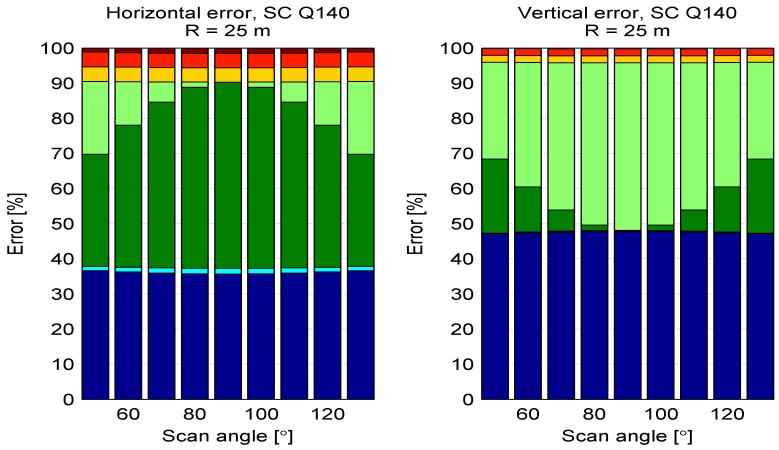

(a)

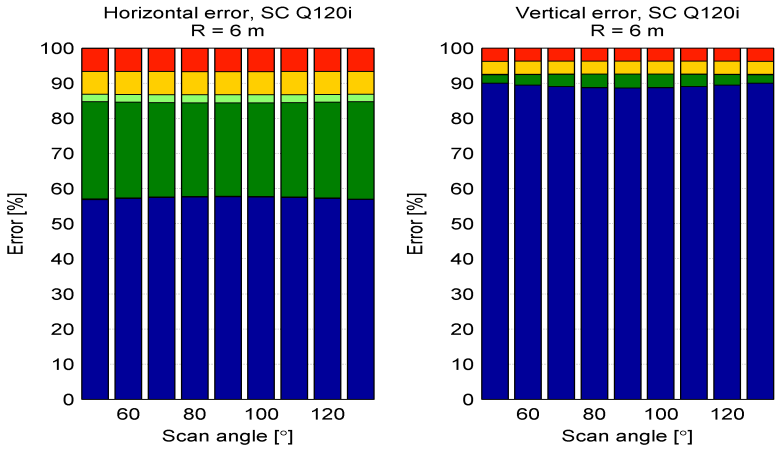

(b)

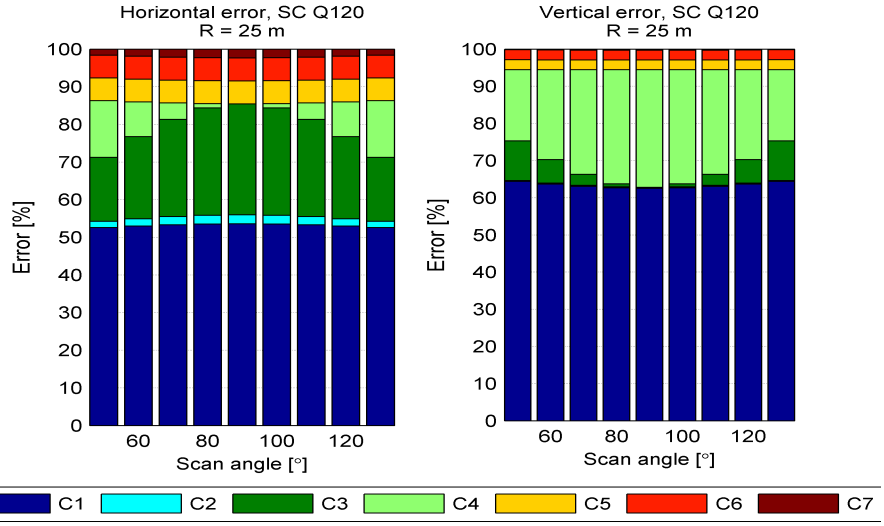

(c)

Figure 4.9: Relative error budgets for the three laser scanners, analyzed according to horizontal and vertical positioning error using parameter set 2.

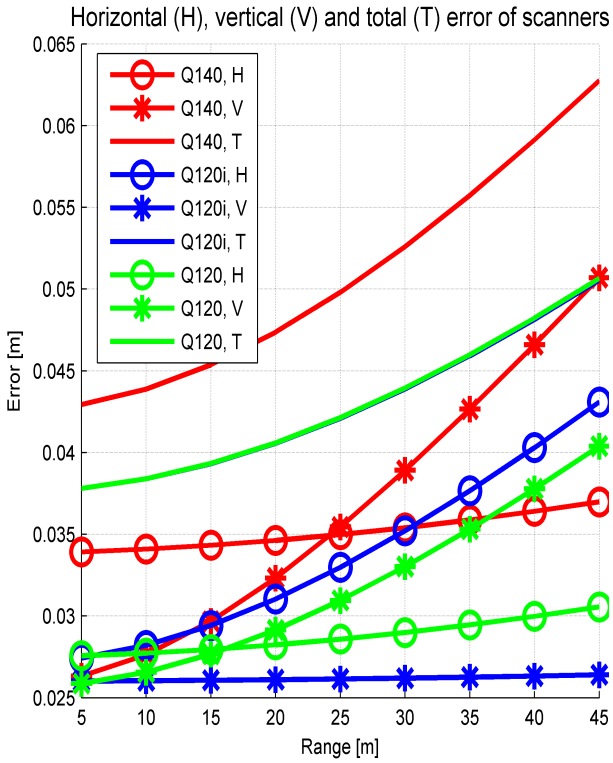

(a) Variable range measurements (parameter set 1).

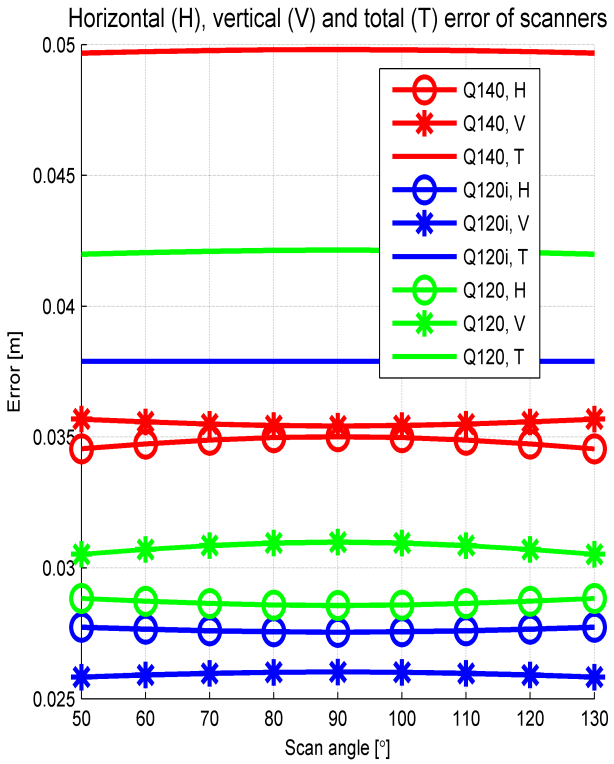

(b) Variable scan angle measurements (parameter set 2).

Figure 4.10: The total 3D (T), horizontal (H) and vertical (V) error for three laser scanners; red lines for Q140, blue for Q120i and green for Q120.

4.5 Summary

In summary, the StreetMapper random error budget mainly results from the GPS and laser scanner errors. Because the advanced positioning method is used in pilot-project Egmond aan Zee, which integrates DGPS solution with baseline less than $3km$ and high accurate INS measurements, and because of the open acquisition area on Dutch coast, the final GPS errors are considered small. This small GPS noise leads to a similar noise level in the derived point cloud. The effect is independent of the system measurements. Therefore, it is obvious that further improvement to the StreetMapper system depend upon quality improvements in the laser scanners performance. The range error impact is mostly dependent on the size of the random range error itself, which is rather small for Q120 and Q120i. The effect is almost independent of the measured range, but depends on the scan angle. It mainly affects the horizontal component of the derived coordinates. On the other hand, the scan angle impact rapidly grows with the distance and is dependent also on scan angle. The vertical coordinates are affected more than horizontal. In the worst case, i.e. using the scanner Q140, which has the beamwidth of 3 mrad and the angular resolution equals $0.036°$, the positioning error is $4.4cm$ at the range of $45m$. Therefore it is important to use laser scanners with smaller beamwidth and angular resolution. For comparison see the typical values of laser scanner range and angle accuracy in [Glennie, 2007b]. The effect of IMU error sources on the quality of the 3D laser point coordinates is small, due to the short ranges normally measured with the L-MMS system. It slightly increases with the range and effects more the horizontal coordinates. The total 3D error due to IMU attitude noise is around $8mm$ at the range of $45m$.

The quality of a laser point cloud is changing within a drive-line across its trajectory. Assuming flat acquisition area, this effect is mostly due to the scan angle error, which deteriorates especially the vertical positioning error. Further away from the trajectory the total 3D error grows and is approximately 5 to $6cm$ at the range of $45m$.

In this analysis just the random errors in the L-MMS system measurements and calibration parameters are taken into account. The systematic biases, which lead to systematic errors in the derived point cloud, are assumed to be zero. They are not included into the error budget, because they are not know a-priori for this research and for the L-MMS system in hand (i.e. StreetMapper). But it should be noted that their influence on the laser point quality might be bigger and more significant than one of the random errors. Therefore and attempt is made to detected possible systematic errors using a proper Quality Control (QC) of laser points, as described in the following chapter, Chapter 5.

Chapter 5

L-MMS laser point quality assessment

In the previous chapter a pre-analysis of laser L-MMS quality is performed. The result is an a-priori random error budget, which is based on the direct geo-referencing model. This random error model is used to compute the expected quality of laser points, once the calibration parameters and their errors are known and the expected measurement values and their errors are estimated. Besides, the quality of a single laser point is governed by a variation of the range error due to the changing scanning geometry [Schaer et al., 2007]. This impact of the scanning geometry on each laser point is usually not considered in a standard a-priori error analysis (as stated already in Section 4.3.2). The reason is that the terrain slope and aspect, with respect to the laser scanner position, are not known in advance. However, one can expect that in case of scanning a relatively flat and horizontal area, such as Dutch beach, the scanning geometry is changing a lot with the distance to the sensor. The consequence is that also the quality of points differ within the dataset. Therefore, to get an insight into the quality of L-MMS laser points as a whole, a proper QC must be used. Here, the word proper refers to the type of available data.

In Section 5.1, background information is given about the mathematical and statistical procedures, which are used later in this chapter. In order to asses L-MMS laser point quality, first the scanning geometry is reconstructed for each laser point, as presented in Section 5.2. The obtained geometric attributes form the input to the mathematical models and so the theoretical laser point height precision is estimated in Section 5.3. In Section 5.4 an overview of empirical Quality Control (QC) procedures is given. According to the data available for this research, a relative QC employing so-called identical points is developed in Section 5.5. This way an empirical quality measure for the laser L-MMS point heights is obtained. In Section 5.6 the main ideas, how to asses the quality of individual laser point, are summarized.

5.1 Mathematical and statistical preliminaries

In this section theory on mathematical and statistical topics, which are employed later in the research, is given. In Section 5.1.1 an efficient algorithm is described to find the nearest neighboring laser points in a L-MMS dataset. In Section 5.1.2 the calculation of robust statistics is explained. Such statistics are used to describe the distribution of a variable in case outliers are present in the dataset.

5.1.1 Tree data structure for finding k Nearest Neighbors

Having two subsets of laser points, for example subsets that belong to two different drivelines, we would like to find those points that lie close together. For this reason for each query point in the first subset the closest point in the second, i.e. reference, subset is searched for. In this research the k Nearest Neighbor (kNN) search in 3-dimensional Euclidean space is used.

The kNN algorithm computes the Euclidean distance from the query point to every reference point and identifies the k neighbors nearest to the query point. This algorithm, sometimes referred to as the naive approach or brute-force search, works for small databases but quickly becomes intractable as the number of query or reference points becomes large. Therefore, in case of L-MMS data consisting of millions of points, a more effective algorithm for nearest neighbor search should be used. The solution is to first structure the reference points in 3D, thus to narrow the search for the closest reference point to a given query point. One of these so-called space-partitioning methods is the kd-tree, which iteratively bisects the search space into two regions containing half of the points of the parent region. Queries are performed via a traversal of the tree from the root to a leaf by evaluating the query point at each split. Alternatively, the R-tree data structure has been designed to support the nearest neighbor search in a dynamic context, as it has efficient algorithms for insertions and deletions [Arya et al., 1998].

In this research an effective algorithm designed by Luigi Giaccari is used. Giaccari [2010] named the data structure the GLTree and stated that the tree construction has linear time complexity instead of $n \cdot \log(n)$ like the kd-tree. There n is the number of reference points. Therefore, the tree construction is considered fast and becomes advantageous against brute-force search even for a small number of points. The implementation of the algorithm is available on the Advanced Matlab code website [Giaccari, 2010].

5.1.2 Robust statistics

The word robustness signifies insensitivity to small deviations from the assumptions. It is typically assumed that measurement errors are distributed normally. But if they include a small proportion of outliers some more robust and resistant estimators of the mean and standard deviation must be used. Different approaches are described in the literature, but for the purposes of this research the method of the median and Median Absolute Deviation (MAD) is used, following the explanation in [Huber, 1981; Hampel et al., 1985].

The median $\hat{\mu}$ is computed as the central value of the ordered data x_i. It is a robust estimator of the mean, since it does not change however the value of the outlier increases.

$$\hat{\mu} = median(x_i) \tag{5.1}$$

To find the standard deviation of the median, the Median Absolute Deviation (MAD) is defined as in Eq. 5.2. Again, increasing the outlying values has no effect on the value of MAD.

$$\text{MAD} = median(|x_i - \hat{\mu}|) \tag{5.2}$$

In most cases it is convenient to standardize the estimates such that they are consistent at the ideal model distribution. In order to use the MAD as a consistent estimator for the estimation of the standard deviation σ, it is multiplied with a constant scale factor K, which is dependent on the distribution. For normally distributed data the robust standard deviation estimate is obtained by Eq. 5.3, which can be used to measure confidence in statistical conclusions.

$$\hat{\sigma} \approx 1.4826 \cdot \text{MAD} \tag{5.3}$$

The robust statistical model of height differences (ΔZ) provides a good method for identifying suspect extreme values, which lie outside the symmetric interval $(\hat{\mu}-k\hat{\sigma}, \hat{\mu}+k\hat{\sigma})$. The constant k is determined according to the recommendations in literature [AMC, 2001]. Its value is set to 3 and is thus expected that more than 89% of the data lie within the mentioned symmetric interval for all distributions of ΔZ for which the standard deviation is defined (Chebyshev's inequality, see [Teunissen et al., 2008], p. 34).

5.2 Geometric attributes describing the scanning geometry

~~The instantaneous scanning geometry of a laser point can be described by the range and the incidence angle. Those two values influence the laser beam width (footprint size) and thus the laser point quality. For this reason the method to compute the range, incidence angle and footprint diameter is described in this section. Those geometric attributes are computed for each 3D laser point using the 3D laser point cloud and the 3D trajectory position. Both datasets include the X, Y and Z coordinates.~~ The definitions of the geometric attributes are given in Section 3.3.1.

The range of each laser point can be computed once the sensor position at the time of the laser point acquisition is known, see Section 5.2.1. In Section 5.2.2 the computation of incidence angle is described, where the original laser points are employed to define the normal of a local surface. Once knowing the incidence angle for each laser point, its footprint diameter can be obtained as described in Section 5.2.3.

5.2.1 Range

For each laser point and the position of the car during the acquisition the time of acquisition is available. Therefore, the laser scanning geometry (see Fig. 5.1) at the time of pulse

firing can be reconstructed. The sensor position at the time stamp of each laser point is linearly interpolated using the consecutive trajectory positions. Here it is assumed that the trajectory position directly represents the laser scanner position (offsets between different scanners and GPS/INS system are not taken into account).

The vector $\vec{p}$ from the laser point P to the sensor position T at time t is computed with a simple vector summation as in Eq. 5.4.

$$\vec{p} = \vec{r}_T(t) - \vec{r}_P(t) \tag{5.4}$$

Where:

- $\vec{r}_T(t)$ is the position vector of the sensor (T) in reference mapping frame (m).
- $\vec{r}_P(t)$ is the position vector of the laser point (P) in reference mapping frame (m).

The range R, the distance between the laser scanner and the laser point, is the length of the vector $\vec{p}$ as given in Eq. 5.5.

$$R = \sqrt{X_{\vec{p}}^2 + Y_{\vec{p}}^2 + Z_{\vec{p}}^2} \tag{5.5}$$

Where:

- $X_{\vec{p}}, Y_{\vec{p}}, Z_{\vec{p}}$ are the components of the vector $\vec{p}$ from the sensor position T to the point P.

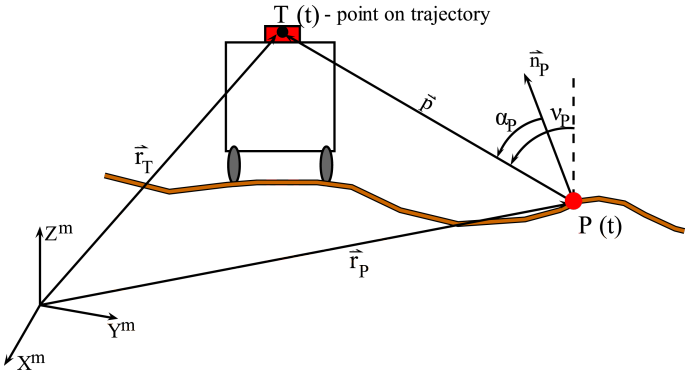

Figure 5.1: Graphical representation of the geometric attributes attached to each laser point: range $R = |\vec{p}|$ and incidence angle α_P.

5.2.2 Incidence angle

To compute the incidence angle α_P (see Fig. 5.1), the vector of the laser beam ($\vec{p}$) and the upward normal ($\vec{n}$) to the surface at the laser point P must be known. The vector $\vec{p}$ is computed already above (Eq. 5.4) and the normal vector $\vec{n}$ is computed as follows. For each laser point the closest 4 points are determined using the k Nearest Neighbor algorithm, as described in Section 5.1.1. ~~The number $k = 4$ of neighboring laser points participating in plane fitting is chosen such that the computed normals reflect just a local surface.~~ The laser point cloud includes also a few points reflected on higher objects and vertical planes.

Because those points appear in smaller groups (around 10 points or more), k should be small, in order not to smooth out vertical surfaces. The kNN algorithm returns also the distance d_i between the query point and the k-nearest reference points. ~~A plane is fitted to all 5 points using Least Squares. The result is the normal $\vec{n}$ of a plane at a laser point~~ P.

Once the normal vector at the laser point is computed, the incidence angle is computed as in Eq. 5.6 [Lutz et al., 2003a].

$$\begin{aligned} \alpha_P &= \arccos\left(\frac{\vec{p}\cdot\vec{n}}{|\vec{p}|\cdot|\vec{n}|}\right) \\ &= \arccos\left(\frac{X_{\vec{p}}X_{\vec{n}} + Y_{\vec{p}}Y_{\vec{n}} + Z_{\vec{p}}Z_{\vec{n}}}{\sqrt{X_{\vec{p}}^2 + Y_{\vec{p}}^2 + Z_{\vec{p}}^2}\cdot\sqrt{X_{\vec{n}}^2 + Y_{\vec{n}}^2 + Z_{\vec{n}}^2}}\right) \end{aligned} \tag{5.6}$$

Where:

- α_P is the incidence angle of laser point P.
- $X_{\vec{n}}, Y_{\vec{n}}, Z_{\vec{n}}$ are components of the normal vector $\vec{n}$ at point P.

5.2.3 Footprint diameter

The last attribute added to each laser point is the footprint diameter D_{fp}. A general formula to calculate the laser footprint diameter D_{fp}, in case the incidence angle equals zero (see Figure 5.2(a)) is given in Eq. 5.7:

$$D_{fp} \approx D + 2R\cdot\tan(\beta/2) \tag{5.7}$$

Where D is the diameter of the laser beam at the exit of the emitter, R is the measured range and β is the laser beam width.

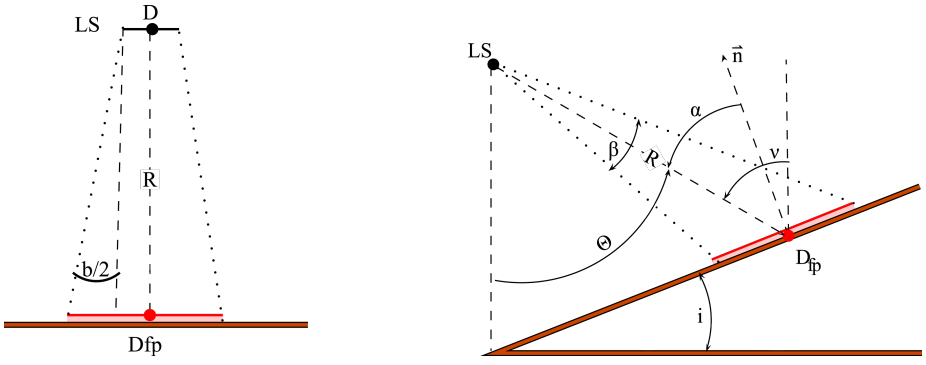

(a) General situation. (b) L-MMS situation.

Figure 5.2: Representation of attributes used to calculate the laser footprint diameter.

Since firstly D is in general small (few mm to few cm, known from laser scanner specifications) compared to the measured range and secondly β is considered small [Baltsavias, 1999b] Eq. 5.7 simplifies to Eq. 5.8:

$$D_{fp} \approx R \cdot \beta \tag{5.8}$$

If the laser beam is hitting the surface at non-perpendicular angle the footprint size in general increases and gets an elliptic form. The ellipse is formed in 3D by the intersection between a cone and the local tangent plane with normal $\vec{n}$. The cone has the origin in the laser scanner emitter, direction of the laser beam $\vec{p}$ and size of beam divergence β. The main axes of the ellipse are then computed in 3D using cone canonicals as explained for the ALS case in [Schaer et al., 2007]. However, the L-MMS ranges are much smaller than ALS, thus the footprint size is expected to be smaller. That is, the major and minor axes do not differ much. Therefore the footprint shape is approximated by a circle and the footprint diameter D_{fp} is assumed to be equal to the major axis. The ~~footprint diameter~~ ~~D_{fp}~~ ~~is computed in terms of the changing incidence angle~~ ~~α~~ as written in Eq. 5.9 and depicted in Fig. 5.2(b):

$$D_{fp} = \frac{R \cdot \beta}{\cos \alpha} \tag{5.9}$$

The plots in Fig. 5.3 show the size of D_{fp} on the left y-axis, which increases with increasing range R and α. In this graphs it is assumed that the scanned surface is horizontal and flat. It is expected that scanning geometry gets better, if the laser scanner system is higher above the ground. Therefore the computation of the footprint diameter is performed for different heights, i.e. for 2, 3 and $4m$. The range R is changing between $0m$ and $40m$ and the incidence angle is changing with the range R and depends on the height h (see Fig. 3.4). The beam width β is taken constant to 2.7 mrad. In Fig. 5.3(a) the dependency between the footprint diameter D_{fp} and the range R is plotted and in Fig. 5.3(b) the dependency between the footprint diameter D_{fp} and incidence angle α. At a range of $25m$ and at a laser scanner height of $2m$, the incidence angle is 85.4° and the footprint diameter D_{fp} measures $84.4cm$. When the incidence angle is smaller that 78°, which happens at the range smaller than $9.81m$, the footprint diameter measures less than $25cm$.

5.3 Estimating the laser point height precision using theoretical models

In this section the theoretical models of error propagation are used to estimate an expected vertical (height) precision of each laser point. This height precision σ_{Zi} is computed using Eq. 5.10:

$$\sigma_{Zi} = \sqrt{\sigma^2_{Zi,m} + \sigma^2_{Zi,\delta R}} \tag{5.10}$$

Here, the computation of height precision σ_{Zi} employs two components $\sigma_{Zi,m}$ and $\sigma_{Zi,\delta R}$, which are explained in the following.

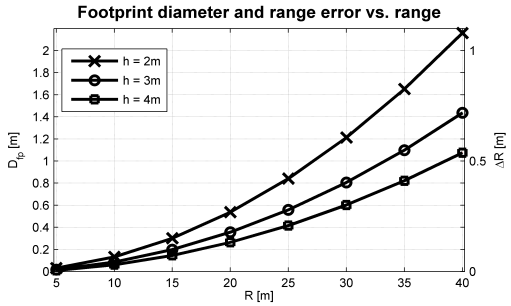

(a) Footprint diameter D_{fp} and range error δR vs. range R.

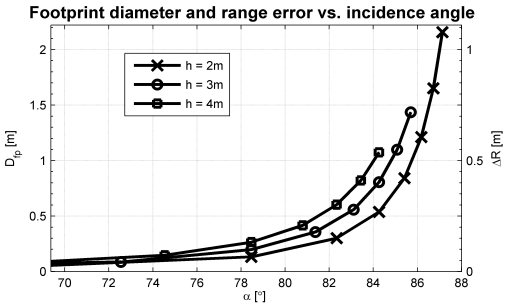

(b) Footprint diameter D_{fp} and range error δR vs. incidence angle α.

Figure 5.3: Size of the footprint diameter D_{fp} and the range error δR, where the incidence angle α depends on the range R and height from the ground h (see Fig. 3.4). It is assumed that the ground surface is horizontal.

In Chapter 4 the theoretical random error budget is presented and the results give an a-priory estimation of the StreetMapper precision. Here, in Section 5.3.1 the real L-MMS measurements are used, to compute the vertical error $\sigma_{Zi,m}$ due to the L-MMS measurement random errors for each laser point This standard deviation is here named measuring precision $\sigma_{Zi,m}$.

In this a-priori analysis, the random range error is taken from the laser scanner specifications and is considered more or less constant. This value is valid when the laser beam falls perpendicular to the target [Schwarz, 2009]. In practice the incidence angle is changing over the acquisition area and is usually non-perpendicular. Therefore additionally, the second component of the laser point vertical error $\sigma_{Zi,\delta R}$, which occurs due to the (non-perpendicular) scanning geometry, is computed. This standard deviation is here named geometrical precision $\sigma_{Zi,\delta R}$. The computational method is explained in Section 5.3.2.

5.3.1 Influence of the L-MMS measurement random errors

The random errors of L-MMS measurements and calibration parameters are propagated through the functional model of geo-referencing and the laser point precision is estimated for each point by Eq. 4.9. The real L-MMS measurements of range R, scan angle Θ and IMU rotation angles ω, φ, κ that were acquired during pilot-project Egmond aan Zee are inserted into Eq. 4.9 for each laser point. The measurement random errors (see Table 4.3), and the values of the calibration parameters (see Table 4.4) stay the same for all laser points. The result is the standard deviation $\sigma_{Zi,m}$ of the laser point height due to the measurements random errors (measuring precision) for each laser point.

5.3.2 Influence of the scanning geometry

The effect of scanning geometry on the quality of the 3D point positioning depends mainly on the incidence angle, which was proved in many researches such as [Soudarissanane et al., 2009; Lichti and Gordon, 2004; Schaer et al., 2007; Alharthy et al., 2004]. High incidence angles result in poor intersection geometry and affect the range measurements. The range error further on influences the laser point positioning error. This error is estimated in here by a theoretical model. For sake of completeness and comparison, analytical values are shown for vertical (height) and horizontal positioning error.

Range error due to scanning geometry. To estimate the influence of incidence angle on the L-MMS range measurements, the approach in [Lichti et al., 2005] is used. This approach is valid for the Time-Of-Flight i.e. pulse laser scanners, which are used in this research. When a narrow beam hits the surface at non-perpendicular direction, the relative power distribution spreads within a bigger footprint and the return pulse has an increased rise-time. The uncertainty in the time recording causes a range error δR. In other words, it is not known exactly to which point within the footprint the actual range is measured, as illustrated in Fig. 5.4.

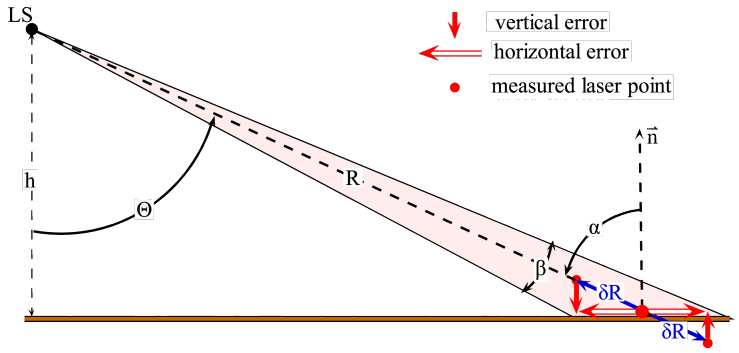

Figure 5.4: The range error δR due to the non-perpendicular scanning geometry and the influence of δR on vertical and horizontal laser point positioning error.

At a given range R and knowing the beam width β from the laser scanner specifications, the range error δR is parameterized in terms of incidence angle α as given in Eq. 5.11 [Lichti et al., 2005]:

$$\delta R = \frac{R \cdot \beta \cdot \tan \alpha}{2} \tag{5.11}$$

Here β is the laser beam width, R is the range and α is the incidence angle. In general it is assumed that the smaller the incidence angle, the higher the accuracy of the range distance measurement [Lichti and Gordon, 2004]. The range error δR increases very fast when the incidence angle is bigger than 80°; see the right y-axis in Fig. 5.3(b). For example, at the range of $25m$, the incidence angle on a horizontal surface reaches 85° and the range error δR is $0.42m$, where h = $2m$ and $\beta = 2.7$ mrad. The value computed by Eq. 5.11 is

the maximum absolute random error that can occur per range measurement, however the range error can be smaller.

Laser point precision due to the scanning geometry. To estimate the influence of the range error δR due to the scanning geometry on the 3D laser point positioning, Eq. 4.9c is used, where σ_d is replaced with δR. This equation propagates the error of the range measurements in the 3D laser point position. In Fig. 5.5 the horizontal and vertical error are plotted for three different heights h of the sensor above the ground. A horizontal surface is assumed. The bottom red x-axis denotes dependency of the positional error on the incidence angle and the top blue x-axis denotes dependency on the range.

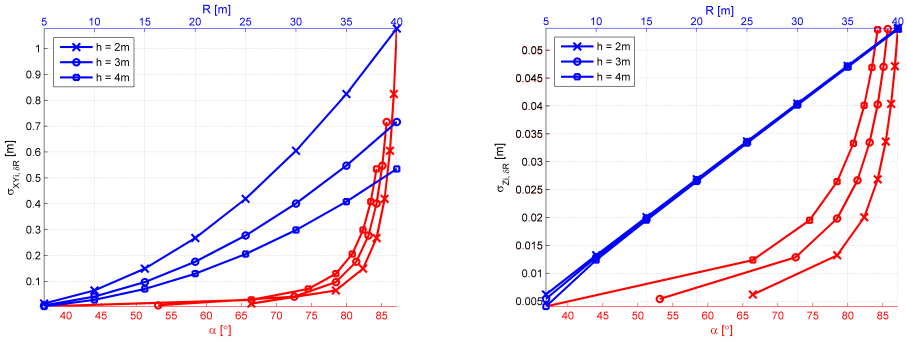

(a) Horizontal precision $\sigma_{XYi,\delta R}$. (b) Vertical precision $\sigma_{Zi,\delta R}$.

Figure 5.5: The horizontal and vertical error of laser points due to the scanning geometry. A horizontal surface is assumed, the range increases and the height of laser scanners above ground is changing.

As can be seen in Fig. 5.5(b), the vertical precision $\sigma_{Zi,\delta R}$ does not change much with the height h of the sensor above the ground. At certain range the vertical precision has almost the same value for all heights h. On the other hand, the horizontal precision $\sigma_{Zi,\delta R}$ that is shown in Fig. 5.5(a) decreases significantly, if the laser scanner is put higher. Besides, the values of the horizontal precision increases fast with the range, i.e. at $5m$ range the error is $1.4cm$ and at $40m$ range it theoretically grows up to $1.077m$ for height $h = 2m$. The vertical precision increases from $0.62cm$ at $5m$ range up to 5.38 cm at $40m$ range. In this research, as stated already before, just the standard deviation of heights $\sigma_{Z,\delta R}$ due to the scanning geometry (geometrical precision) is computed.

5.4 Overview of empirical Quality Control procedures

In general it is important to know the laser point quality, prior to using points in further processing, i.e. computing the DTM. But the computation of the laser point coordinates is not based on redundant measurements, which could be manipulated in an adjustment procedure. Consequently, one does not have the associated quality measures, i.e. the a-posteriori variance factor and variance-covariance matrices of the derived coordinates or parameters, which can be used to evaluate the quality of the derived data e.g. point cloud and final products e.g. Digital Terrain Model (DTM) [Habib et al., 2008]. Besides, the derivation of the point cloud from the laser measurements is not a transparent process, since the raw system measurements are not always provided to the end user. In Section 5.3 the theoretical laser point height precision is estimated, considering the available L-MMS data (see Section 5.2). To verify those theoretical models and estimate an empirical quality of a laser point position, a proper Quality Control (QC) of a L-MMS laser point cloud is looked for in this section.

While the number of different applications of L-MMS has increased in the past few years, standard and efficient procedures for validating the quality of derived laser points are still missing. One can find an error analysis in the domain of ALS [Baltsavias, 1999a; Habib et al., 2008] and Terrestrial Laser Scanning (TLS) [Soudarissanane et al., 2008; Lichti et al., 2005], but not many exhaustive error model studies can be found in the related literature particularly for L-MMS. The hardware systems of ALS and L-MMS are similar, but are mounted on different platforms. Therefore, it is possible to use ALS equations and principles, modified for different scanning geometry (airborne vs. land-based). On the other hand L-MMS has a scanning geometry similar to TLS, thus the factors influencing L-MMS laser scanner measurements can be studied from TLS literature.

According to Habib et al. [2008] the QC procedures can be divided in to two main categories, absolute and relative Quality Control. In the following Sections 5.4.1 and 5.4.2 these two types of QC are explained in more detail. Besides, the relevance of the described QC methods is given with respect to the available data of the pilot-project Egmond aan Zee.

5.4.1 External or absolute Quality Control measures

The absolute quality describes the quality of laser point positioning in a local mapping coordinate system. It is dominated by the quality of the GPS/INS solution [Kremer and Hunter, 2007]. A commonly used QC procedure to evaluate the absolute accuracy of data, compares the laser surface with independently collected control points having higher accuracy [Wotruba et al., 2005; Hodgson and Bresnahan, 2004]. Besides being expensive, this procedure does not provide accurate verification of the horizontal quality of the laser footprints. The approach of vertical-only QC is satisfactory for collecting topographic information from airborne systems. But for new applications such as producing planimetric maps (using intensity) and emerging laser L-MMS, the vertical only error analysis of a

laser system is inadequate to determine the overall expected accuracy of the end-products. It should be noted that the horizontal accuracy is in most cases lower than the vertical [Glennie, 2007b]. A solution to estimate also the horizontal absolute quality is to use specifically-designed targets as it is described in [Csanyi and Toth, 2007].

Pilot-project Egmond aan Zee. In the specifications of the StreetMapper system the absolute accuracy of a 3D laser point position is claimed to be from $3cm$ up to $0.5m$, depending on the accuracy of the GPS/INS trajectory [StreetMapper, 2010]. In order to estimate the actual absolute quality of the L-MMS data acquired on the Egmond aan Zee beach, reference data were acquired by RTK GPS simultaneously[1] with the L-MMS mission. The standard deviation of RTK GPS heights reported in [Rijkswaterstaat, 2009] is approximately 4-5 centimeters (see also Section 2.3.3). But according to later information, the topographic GPS survey has an error bigger than $5cm$ [Van Waarden, 2009]. Because this error is bigger than the one expected for the L-MMS data, the RTK GPS data could not be used for the absolute quality validation of StreetMapper data.
Airborne Laser Scanning (ALS) data are available for this research, but those data were acquired seven months before the L-MMS mission. Therefore, they can not be used to perform the absolute QC.

5.4.2 Internal or relative Quality Control measures

~~The relative quality describes the relation between two points acquired in the same region in a short time period (point-to-point quality). In general the idea of validating the relative quality of laser data is based on checking the compatibility of laser points in areas, where data overlap. The error between the two points is dominated by the noise of the single laser scanner measurements and is nearly independent of the short term GNSS conditions [Kremer and Hunter, 2007].~~ Therefore, the difference between the relative and absolute accuracy is the remaining systematic error of the geo-referencing procedure, which stays unknown here.
For the ALS technique the relative QC procedure is described in many papers (see the references in [Habib et al., 2008]). An extensive explanation of the QC procedures that assess the coincidence of conjugate features in overlapping strips and use this degree of coincidence as a data quality measure, is given in [Li et al., 2005], Chapter 9. Laser point clouds from different flight-lines (strips) are compared to ensure data coherence, integrity and correctness. The degree of coincidence of the conjugate surface elements (linear or planar features) in overlapping strips is then a measure of the data quality. The presence of systematic errors in the measurements as well as the random errors in the derived point cloud can be determined. Both, the vertical and horizontal quality can be tested [Habib et al., 2008].

[1] Therefore they share a similar GPS constellation.

Pilot-project Egmond aan Zee. The relative quality of 3D point positioning, i.e. point-to-point quality within the data, is for the StreetMapper system written to be better than 30mm [StreetMapper, 2010]. This value actually equals the range accuracy taken from the laser scanner specifications. The relative quality of the whole L-MMS depends on the quality of the system calibration. Because the calibration quality varies depending on the experience of the data processor, it is impossible to quote relative accuracy a-priory [Cox, 2009]. Therefore, the real dataset, i.e. the 3D point cloud and the trajectory position acquired during pilot-project Egmond aan Zee, is used here to estimate the actual StreetMepper relative accuracy.
The acquisition area discussed in this research, i.e. the sandy beach, does not include (many) steady points or lines, that are sufficiently well defined in the laser point cloud. In other words, the beach area lacks artificial sharp edges or planes, for example edges of buildings, facade surfaces, road lines etc., which could be extracted from the laser points and used in a relative QC procedure. Besides, the terrain on the beach is changing smoothly. Thus finding and aligning breaklines of beach morphology is not a promising method either. One of the approaches suggested in [Li et al., 2005] is to use intensity measurements. The intensity images are compared and in their overlap conjugate features are extracted. The differences of 3D coordinates of conjugate features indicate the presence of biases in the (ALS) data acquisition system. However, in case of L-MMS, the intensities of laser points vary a lot (see Fig. 3.15(a)): firstly, due to the changing scanning geometry (the range and the incidence angle); secondly, due to the use of different laser scanners, i.e. long range and short range, mounted on StreetMapper platform. This results in different intensity values for the same area and thus the extraction of features might not be exact. The intensities should be first normalized in order to be used in the QC procedure.

Instead, a point-to-point comparison is used in this research, were the height differences of laser points that have partly overlapping footprints are considered. It is assumed that those so-called identical points represent the same point on the surface. Therefore, if the points are error free, one would expect that the height difference between the identical points are almost zero. Because this is not the real case, the non-zero height differences are used to evaluate the relative quality of the laser points in (just) vertical direction. This relative QC method is explained in detail in Section 5.5.

5.5 Height differences of identical points

To investigate the relative height errors of L-MMS laser points, the advantage of high laser point density is used. The laser scanning technique enables acquisition of a big amount of data in a short time. In case of land-based system, where ranges are relatively small, the point density is even bigger, compared to ALS. Besides, the point density increases a lot, when the vehicle is moving very slowly or is scanning in standing position. Those redundant measurements, when the laser footprints overlap, are taken into account to perform the relative QC of L-MMS laser points.

The algorithm to find points that lie within each other footprints, so-called identical points, is described in Section 5.5.1. The height differences between identical points are considered as a measure of the relative QC. The methodology of examining the height differences is presented in Section 5.5.2.

5.5.1 Finding the identical points

The identical points are defined as those point pairs, where the two points lie so close together that their footprints partly overlap. Due to the beam width uncertainty it is assumed that in a first approximation those points are identical in 3D. Because the footprint diameter might be unreasonably big in case the incidence angle is close to 90° (see Fig. 5.3 and discussion about Fig. 6.3), just the laser points that have an incidence angle less than 89.9° are considered in the algorithm of finding identical points.

First, pairs of closest points in 3D are found using the kNN algorithm, which is explained in Section 5.1.1. The kNN search implemented in the Luigi Giaccari code [Giaccari, 2010] can be performed within 4 seconds, when $k = 1$ and the size of reference and query points is approximately one million. The output is a set of reference points that are closest to the query points. Optionally the algorithm returns the distance 3D d_i between the query point P_{qi} and the closest reference point P_{ri}.

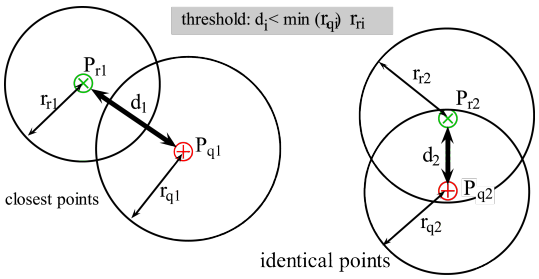

Figure 5.6: Simplified 2D graphical representation of the closest points in 3D. Two datasets are taken: query points P_q and reference points P_r. Points P_{q2} and P_{r2} are defined as identical point pair considering the footprint threshold.

Setting the threshold on the 3D distance d_i between the query point P_{qi} and its closest reference point P_{ri} (closest points), so-called identical points (IPs) are defined as follows (see Fig. 5.6). First the distance threshold is determined individually for each pair of the closest points (P_{qi} and P_{ri}) according to their footprint size, i.e. the radius of the footprint r_{qi} and r_{ri}. If the distance d_i is smaller than the radius of the smallest footprint $min(r_{qi}, r_{ri})$, the point pair enters the selection of possible identical points. Additionally a second threshold is needed, because the footprint size is here approximated with a circle. In general it is expected that for bigger incidence angles in combination with the increasing range the footprint gets an elliptical shape. For more rough surfaces, the footprint can have any shape in 3D. Therefore, the circle approximation results in an overestimated footprint size when the incidence angle increases. To reduce the influence of this effect a second threshold is set and equals here to $5cm$.

To conclude, a laser point enters the set of identical point pair, if the next two conditions are fulfilled:

- the incidence angle of both laser points is smaller than 89.9°: $\alpha_{Pqi} < 89.9°$ and $\alpha_{Pri} < 89.9°$.
- the 3D distance d_i between laser point from query set P_{qi} and its nearest neighbor from reference set P_{ri} is smaller then the minimal size of their footprint radii. At the same time the 3D distance d_i should be smaller than $5cm$: $d_i \leq Min(min(r_{qi}, r_{ri}), 5cm)$.

The derived set of identical points is actually a set of point pairs, where each point has its attributes as given in Section 6.1. One point belongs to the query point set (P_q) and the another to the reference point set (P_r).

5.5.2 Methodology to analyze the height differences of identical points

From the definition of the identical points given in the previous section it can be assumed to some extend that the identical points represent the same part of the surface. Therefore, it is expected that the mean of signed height differences ΔZ between identical points equals approximately zero. Because just the vertical component of the two points in the identical point pair is taken into account, those two points should lie on an almost horizontal plane in order to avoid the influence of surface slope. Deviations from the zero mean could indicate the presence of systematic biases in the L-MMS system. On the other hand, the spread or variability of height differences ΔZ indicates random noise of laser point heights. The relative QC of laser L-MMS points has two objectives.

1. To analyze the signed height differences (in the following height differences) of identical points and use those differences as a measure for the relative quality of laser point heights. Different analyses of height differences between identical points are performed as follows. During the pilot project Egmond aan Zee many L-MMS strips were acquired in short time, which consequently have wide overlapping areas (See Fig. 3.18). Besides, the StreetMapper system incorporates three laser scanners, which scan the same area of at least $1m$ width within one drive-line (see Fig. 3.20(a) and Fig. 3.20(b)). Taking the advantage of the high laser point density and considering the mentioned overlapping areas, i.e. scanner and drive-line overlap, the height differences ΔZ of identical points are investigated for three different cases:
   (a) **Identical points (IP) from complete dataset (ALL).** All L-MMS laser points are taken as query points and at the same time as reference points. That is, the laser point attributes are not considered here. Analyzing the height differences ΔZ, the relative height precision of laser points can be estimated.
   (b) **Identical points (IP) belonging to different scanners (scanner overlap).** After finding the identical points in the complete dataset, here just the ones having different scanner number and the same drive-line number are taken

into account. Deviations from zero mean might indicate the laser scanners calibration inaccuracies (systematic errors), the differences in errors, which are typical for each laser scanner (errors given in specifications), and the influence of different scanning geometry.

(c) **Identical points (IP) belonging to adjacent drive-lines (drive-line overlap).** After finding the identical points in the complete dataset, here just the ones having different drive-line number and the same scanner number are taken into account. Deviations from zero mean might indicate the sensor (GPS/INS, laser scanners) calibration inaccuracies (systematic errors).

For each case the correlation between geometric attributes of laser points, which are presented in Section 5.2, and the height differences of identical points is investigated.

2. To compare the theoretical precision of L-MMS laser point heights, which are obtained through the geo-referencing mathematical model (see Eq. 4.9), with the empirically estimated relative quality of laser point heights.

5.6 Summary

In addition to the a-priori error budget constructed in Chapter 4 in this chapter the individual L-MMS laser point quality is assessed using a real L-MMS data. The 3D position of the laser points and trajectories are used to reconstruct the scanning geometry. That is, geometric attributes like the range, the incidence angle and the footprint diameter are computed for each laser point. They are needed to asses the quality of the individual laser point. In this research the quality is estimated as a height precision using two approaches. In the first approach a theoretical height precision of the laser points is estimated. This precision is defined by the random error propagation through the first order error model based on geo-referencing formula. The random errors considered in this computation result first from the L-MMS measurements (measuring precision) and secondly, form the non-perpendicular scanning geometry (geometrical). The analytical plots of theoretical height precision show that both the measuring and geometrical precision decrease with the range. Besides, the geometrical precision decreases very fast, when the incidence angle approaches 90°. In the second approach a relative QC procedure is used to asses an empirical laser point height precision. According to the available L-MMS data, employed already for the geometrical attributes computation, the QC is developed based on the height differences between so-called identical points. This method aims to check for the presence of systematic errors in the data acquisition system and to evaluate the noise level in the delivered point cloud. Therefore, three different cases to investigate the height differences between identical points are distinguished. Finally, the objective is to compare the results of theoretical and empirical quality measures. That is, to evaluate the theoretical models and at the same time the reliability of the developed relative QC procedure. Numerical values and figures of herewith presented attributes and measures are given in the following Chapter 6.

Chapter 6

Results of L-MMS laser point quality estimation

The equations and methodology to asses the L-MMS laser point quality are given in previous Chapter 5. In this chapter they are implemented on the real laser L-MMS StreetMapper data. The 3D position of laser points and their measurements, i.e. the scan angle and the IMU attitude angles, and the 3D position of trajectory are examined and used to: (i) reconstruct the scanning geometry and, using the theoretical models, estimate its impact on the individual laser point quality; (ii) use the relative QC of height differences between identical points, and so empirically estimate the quality of laser points; (iii) compare those theoretically and empirically obtained laser point quality measures.

Results of laser point attributes, i.e. scanning geometry and theoretical precision attributes, are presented and discussed in Section 6.1. The results of relative QC of height differences between identical points are presented in Section 6.2. In Section 6.3 the empirical laser point quality measures are compared with the theoretical values. The comparison aims to decide weather the QC results are acceptable. Finally, in Section 6.4 all results and findings for individual precision of laser points are shortly summarized.

6.1 Results of laser point attributes

In the previous sections the method to compute additional attributes for each laser point is described. In this section attribute values of the real dataset obtained on the Dutch beach by the StreetMapper L-MMS system are presented. Each laser point has all together 15 attributes (Att.), which are written one per column (Col.) in a text file (see Table 6.1): 9 original attributes and 6 additional attributes.

The original attributes, which are described already before in Section 3.5.2, are: 3D laser point position X, Y, Z, intensity I, class number C, scanning angle Θ, time of point acquisition T, drive-line number DL and scanner number SC. The additional attributes

Table 6.1: Original attributes as recorded in *.las files and additional attributes, calculated in this section. Attributes are saved per laser point in *.txt files.

	Original attributes									Additional attributes					
Col.	1	2	3	4	5	6	7	8	9	10	11	12	13	14	15
Att.	X	Y	Z	I	C	Θ	T	DL	SC	R	α	D_{fp}	δR	$\sigma_{Z,m}$	$\sigma_{Z,\delta R}$

are: range R, incidence angle α, footprint diameter D_{fp}, range error due to scanning geometry δR, laser point precision $\sigma_{Z,m}$ due to L-MMS measurement errors (measuring precision) and laser point precision $\sigma_{Z,\delta R}$ due to the scanning geometry (geometrical precision). The computation of additional attributes is explained in Section 5.2 for the geometric attributes (R, α and D_{fp}) and Section 5.3 for the precision attributes (δR, $\sigma_{Z,m}$ and $\sigma_{Z,\delta R}$).

In this section an example is given, showing how the values of laser point attributes vary over a part of the acquisition area. The laser points are taken from the cross-strip in block 1 (test area), which presents the Dutch beach. In order to make scatter plots in Matlab, a smaller number of laser points is arbitrarily selected within the test area according to the acquisition time T. Those points belong to one drive-line, i.e drive-line 11 (DL11). Therefore a typical StreetMapper U shape pattern (see also Fig. 3.11(a)) is observed in Fig. 6.1, 6.2 and 6.5. The vehicle is moving from the top of the figures to the bottom.

6.1.1 Original attributes

First in Fig. 6.1 the spatial distribution of original attributes is shown, however they are visualized and described already in Section 3.5.2. The aim is to show their values within one drive-line and thus enable a direct comparison with the additionally computed attributes, which are presented later in this section. The triangles in Fig. 6.1(a), 6.1(c) and 6.1(d) are just a consequence of laser point visualization in Matlab.

In Fig. 6.1(a) the typical drive-line pattern acquired by the three StreetMapper laser scanners is shown. Drive-line 11 lies the closest to the waterline, therefore in Fig. 6.1(b) one can observe low elevations from -0.548m up to 0.662m that vary smoothly within this small interval of 1.2m. The intensities shown in Fig. 6.1(c), due to its definition do not have a unit. They are changing within a wide interval, from 1 up to around 8500. In general the intensity decreases toward the edges of the drive-line. The intensity pattern confirms the statement in Section 3.5.2, this is, the intensities are not normalized. Therefore different types of laser scanners employed within the StreetMapper system result in different intensity values of the same area under similar scanning geometry conditions; the intensities recorded by scanner Q140 are much higher (red color) than those recorded by scanner Q120i (underlying green color). Less difference is observed between laser points

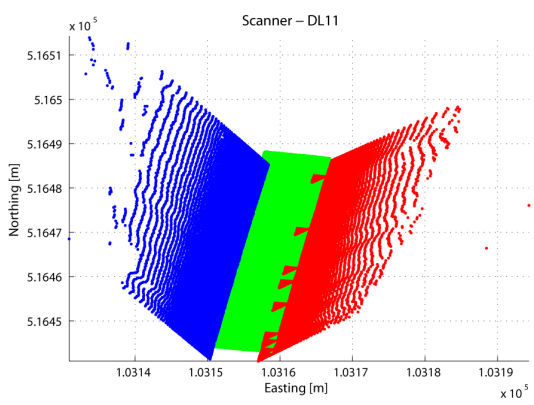

(a) Scanner Q140 (blue), Scanner Q120i (green), Scanner Q120 (red).

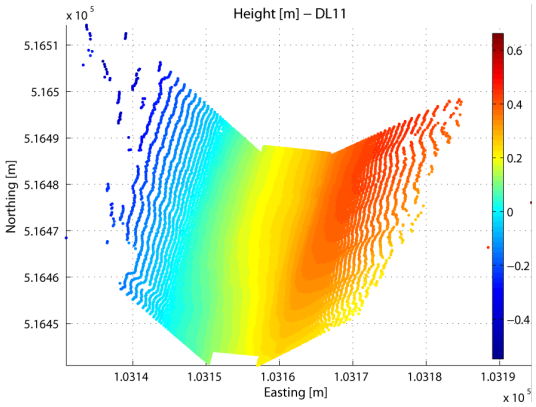

(b) Elevation Z.

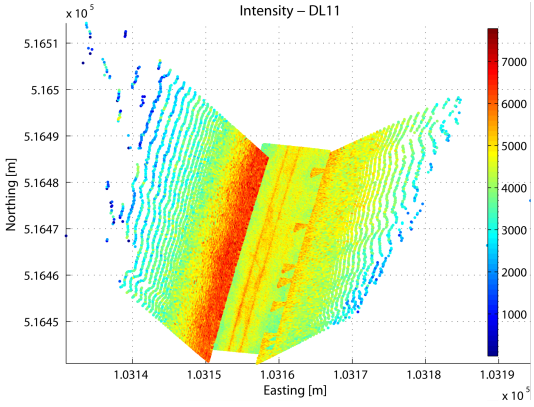

(c) Intensity I.

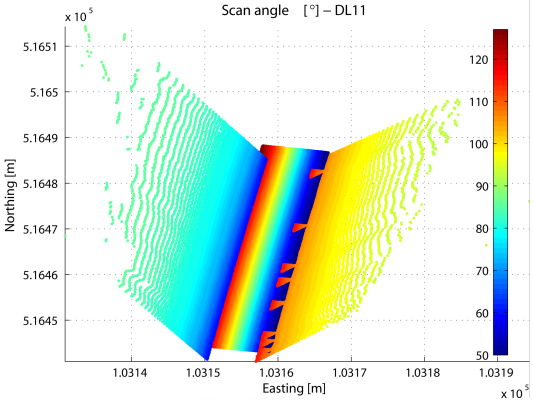

(d) Scan angle Θ.

Figure 6.1: Values of original attributes presented for a small subset of laser points acquired during drive-line DL11 in block 1.

acquired by laser scanner Q120i and Q120. StreetMapper laser scanner have different orientation, therefore they measure scan angles within different intervals (see also explanation in Section 3.5.2). In Fig. 6.1(d) those intervals are clearly visible, where the middle scanner Q120i measure scan angles from 50° to 130° and the side scanners Q140 and Q120 measure scan angles from 50° and 130°, respectively, up to 90°.

6.1.2 Additional attributes

In Fig. 6.2 the geometric attributes are visualized on a smaller set of laser points belonging to drive-line 11 (DL11). The distribution of the geometric attribute's values is shown in Fig. 6.3, where all points within the test area are taken into account.

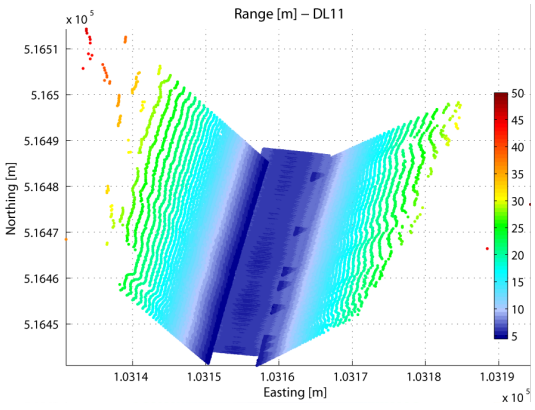

(a) Range R.

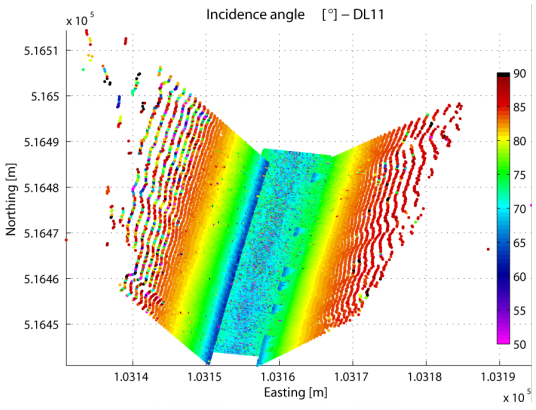

(b) Incidence angle α.

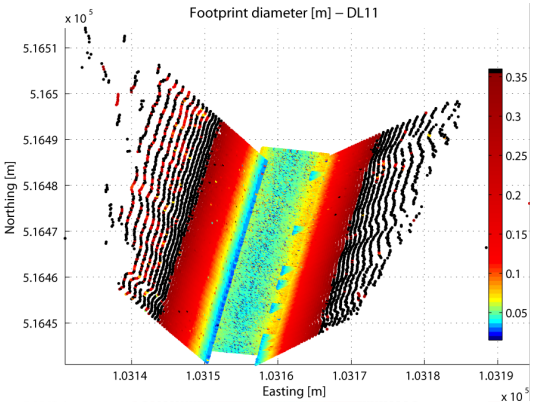

(c) Footprint diameter D_{fp}.

Figure 6.2: Geometrical attributes presented for a small subset of laser points acquired during drive-line DL11 in block 1.

In Fig. 6.2(a) the computed range values are shown. It gives an idea about the swath width (SW) of a drive-line, which is estimated to be on average $25m$ on both sides of the trajectory. The main limiting factor for the range measurements is the relatively flat acquisition area, which in combination with the height of the laser scanners (2 m above the ground) results in decreasing resolution of the laser points with increasing distance to laser scanners. Practically this means that further away than approximately $30m$ almost no laser reflection is recorded. Just a few points have a range of more than $45m$ (colored red in Fig. 6.2(a)). Considering all points in the test area the distribution of ranges is shown in Fig. 6.3(a). Now the maximum range is around $180m$, that can theoretically be measured by laser scanner Q140, when the illuminated targets has the reflectivity ρ bigger than 80% (see specifications in Table 3.2). The minimum range is around $4.3m$ and the median range is around $6.5m$.

An example of the incidence angle values is given in Fig. 6.2(b). The incidence angle increases fast toward the edges of a strip. Black points have an incidence angle bigger

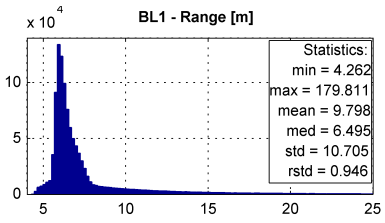

(a) Range R.

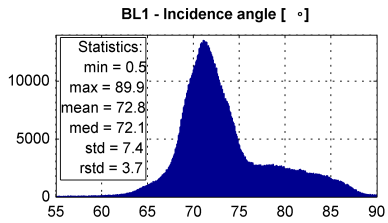

(b) Incidence angle α.

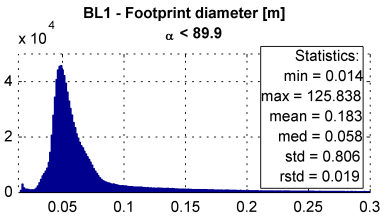

(c) Footprint diameter D_{fp}.

Figure 6.3: Histograms of geometric attribute values and statistical measures computed for the whole test area (cross-strip in block 1).

than 89.9°. In the whole test area those points present 0.02% of all points. In practice the incidence angles close to 90° are unlikely to be recorded. Because inserting incidence angles equal to 90° in Eq. 5.9 and Eq. 5.11 returns infinity, the points with incidence angle α bigger than 89.9° are not considered in the computation of histograms for the following attributes: (D_{fp}, δR and $\sigma_{Z,\delta R}$). However, those points are not removed from the dataset and are still shown in scatter plots.
The median of the incidence angles in Fig. 6.3(b) is 72.1° and corresponds to the mentioned median range (see Fig. 6.3(a)). Those values that are measured on the relatively flat Dutch beach, agree with the theoretical ones computed for a horizontal surface and shown in Fig. 3.4.

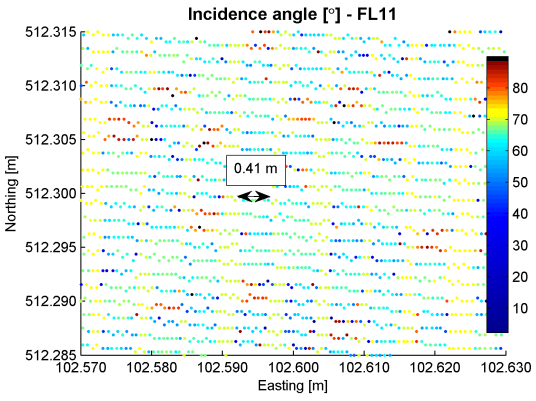

Figure 6.4: Detail of the area acquired with the scanner 2 (SC2), color-coded by incidence angle. Features i.e. ripples smaller than $0.5m$ can be observed.

The incidence angle is of laser points is changing very locally, because the normal vector

computation considers just 4 neighboring points. Therefore on interesting pattern occurs when visualizing the incidence angles of a small area. Fig. 6.4 shows such a detailed surface of $6\times3m$, which is scanned by the down-directed scanner (SC2). A vertical bars of a smaller incidence angles around 40° are interchanging with thin strips of incidence angle higher than 70°. Looking at the laser point heights in a profile, a horizontal steps, i.e. constant height of laser points, of length around $0.4m$ occur at every centimeter of height.

Fig. 6.2(c) presents values of the footprint diameter. As follows from the range and incidence angle values, the footprint diameter has the biggest values at both edges of the strip. Approximately 5% of points in Fig. 6.2(c) has a footprint diameter bigger than $35cm$ (colored black). However, due to the large amount of small ranges and incidence angles as discussed in previous paragraphs (see the median value in Fig. 6.3), the footprint diameter measures on average $5.8cm$.

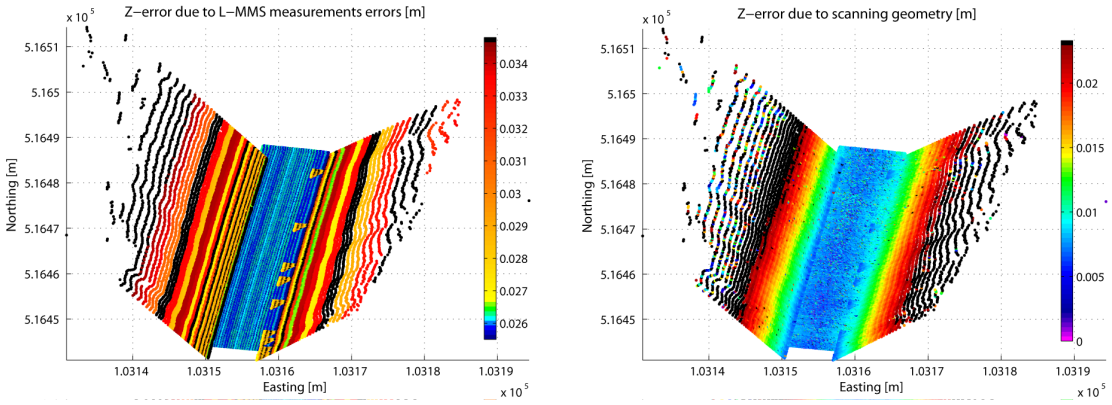

(a) Measuring precision $\sigma_{Zi,m}$. (b) Geometrical precision $\sigma_{Zi,\delta R}$.

Figure 6.5: Theoretical precision of the laser point heights presented for a small subset of laser points acquired during drive-line DL11 in block 1.

Every laser point exhibits certain quality. In this research the laser point height precision is considered. It consists of two components: (i) measuring precision $\sigma_{Zi,m}$ and (ii) geometrical precision $\sigma_{Zi,\delta R}$. Both values are obtained employing the theoretical model of geo-referencing, as explained in Section 5.3.

In Fig. 6.5 the spatial distribution of the laser point height precisions $\sigma_{Zi,m}$ and $\sigma_{Zi,\delta R}$ is shown, for a small subset of test area laser points.
In Fig. 6.5(a) an interesting pattern is observed for the side scanners (i.e. Q140 and Q120), where the values of the measuring precision $\sigma_{Zi,m}$ change very rapidly in the direction perpendicular to the driving path. However, they change within a small interval of $9.3mm$. The possible reason is discussed in the following. The results of error pre-analysis for those two laser scanners in Section 4.4 show, that the vertical precision increases very fast with the range, but does not change much with the scan angle (see Fig. 4.10). The IMU attitude measurements are taken as constant. Here the measured IMU attitude angles

of each laser point are considered to estimate the measuring precision $\sigma_{Zi,m}$. The IMU angles are slightly and gradually changing along a drive-line, i.e. with the time. Because the attitude angles $(\varphi, \omega, \kappa)$ enter the error computation through the rotation matrix, they might impact the vertical error in the direction perpendicular to the driving path, as seen in Fig. 6.5(a). That is to say, other parameters included in the first order error model, as the measurement errors and calibration parameters and their errors, are constant for all laser points of a laser scanner.
In Fig. 6.5(a) the black points have a measuring precision $\sigma_{Zi,m}$ bigger than $3.47cm$. This occurs for about 10% of the visualized laser points. In Fig. 6.5(b) the black points have a geometrical precision $\sigma_{Zi,\delta R}$ bigger than $4cm$. This occurs for about 2% of the visualized laser points. Unlike the measuring precision, the geometrical precision increases rapidly toward the edges of a drive-line. This follows from the computational model of the range error (Eq. 5.11), which is propagated through the first order error model (Eq 4.9c). The range error depends on a laser beam-width, range and incidence angle. In Fig. 6.2 the increase of both the range and incidence angle with the distance from the trajectory is observed. When the range is bigger than approximately $15m$, an incidence angle on the horizontal beach acquired in drive-line 11 is around 85° and a geometrical precision $\sigma_{Zi,\delta R}$ is bigger than $4cm$. Those results confirm the analitical plot in Fig. 5.3, where a horizontal area is assumed.

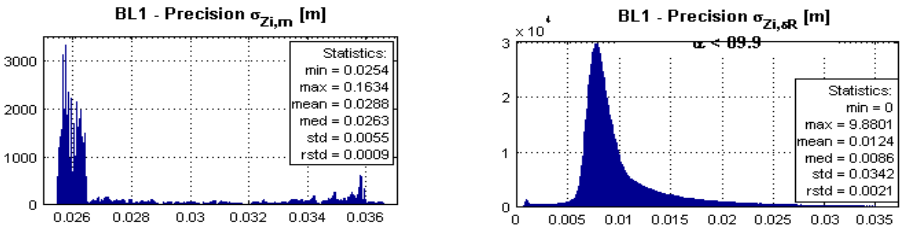

(a) Measuring precision $\sigma_{Zi,m}$. (b) Geometrical precision $\sigma_{Zi,\delta R}$.

Figure 6.6: Theoretical precision of the laser point heights, computed by the random error budget formula (Eq. 4.9).

In Fig. 6.6 the distribution of the measuring precisions $\sigma_{Zi,m}$ and geometrical precision $\sigma_{Zi,\delta R}$ is shown. Laser points within the whole test area are considered. Because the geometrical precision $\sigma_{Zi,\delta R}$ increases to infinity, when the incidence angle approaches 90°, the computation of statistical measures in Fig. 6.5(b) considers just points that have incidence angle α smaller than 89.9°. The median measuring precision $\sigma_{Zi,m}$ is $2.63cm$ and the median geometrical precision $\sigma_{Zi,\delta R}$ is much smaller and is $0.86cm$. On the other hand the dispersion of $\sigma_{Zi,\delta R}$ is as expected from Fig. 5.5(b) much bigger than for the $\sigma_{Zi,m}$. The minimum measuring precision $\sigma_{Zi,m}$ is $2.54cm$, which is due to the main error contributor, i.e. the GPS error (see results in Section 4.4).

In Fig. 6.7 the dependency between the theoretical height precisions and the geometric attributes is presented. Because it is difficult to plot in Matlab the height precision indi-

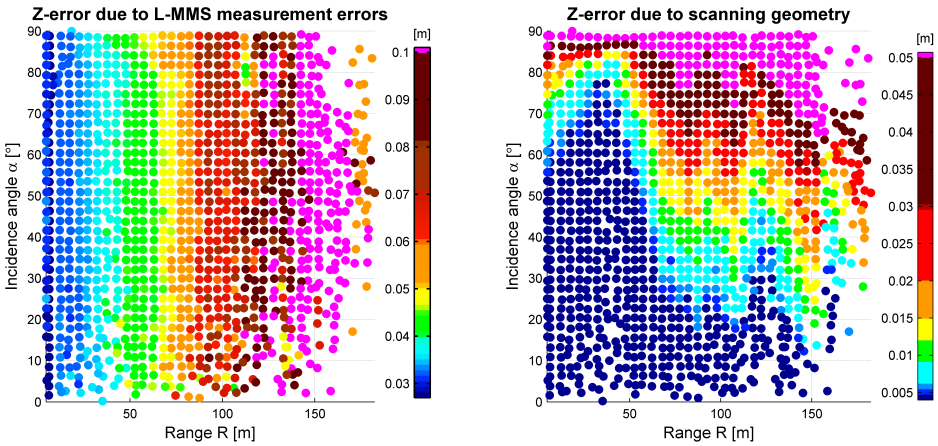

(a) Measuring precision $\sigma_{Zi,m}$. (b) Geometrical precision $\sigma_{Zi,\delta R}$.

Figure 6.7: Correlation between scanning geometry attributes and the theoretical precision of the laser point heights.

vidually for more than one million laser points, the dots in the plots are computed as an average value of laser points, having a range and incidence angle within certain intervals (bins). The pattern of measuring precision shown in Fig. 6.7(a) is clearly changing with the range. When the range is bigger than $140m$, the error exceeds $10cm$. However, at the ranges from $165m$ up to $180m$ the vertical measuring error inexplicably drops again. In Fig. 6.7(b) the geometrical precision is changing in both direction, i.e. for increasing range and incidence angle. In case the incidence angle increases also the geometrical error grows, which does not hold always for increasing range. For example, when the range increases from $75m$ to $120m$ and the scan angle is $50°$, orange and yellow dots interchange. Besides, an interesting pattern is observed for the ranges around $40m$. On the left side of $40m$ the geometrical error mostly deceases and on the right side, i.e. for ranges bigger than $40m$, the geometrical error mostly increases. The reason could be in the employed mathematical model of random range error propagation. Thus, in the described case the scan angle is around $90°$, which causes that the vertical error approaches zero.

6.2 Results of height differences of identical points

In this section the analysis of the signed height differences ΔZ of identical points (in the following height differences) is presented, using the StreetMapper original dataset. The original dataset, which is described in Section 3.5.2, is extended with geometric attributes, as described in Section 5.2. The goal of this section is to reach the first objective, while investigating the three cases ALL, scanner overlap and drive-line overlap, as described in Section 5.5.2.

First, an overview of results valid for all three cases is presented in Section 6.2.1. Further on in Section 6.2.2, Section 6.2.3 and Section 6.2.4 the results are discussed individually for each case.

6.2.1 Overview of analysis and results

~~The cross-strip in block 1 is taken as test area. This area of 213×101m is covered by 8 strips, see Fig. 6.8. The trajectories driven from the north to the south are marked by a dashed black line and the trajectories driven in the opposite direction by a solid black line.~~

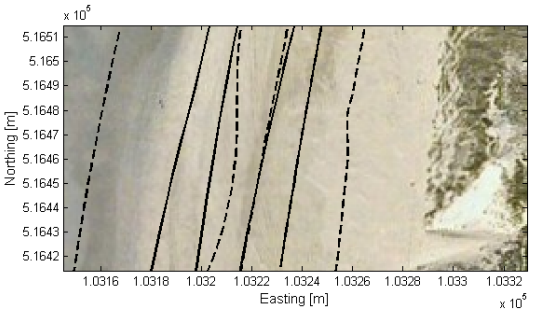

Figure 6.8: The digital photo of the test area [GoogleMaps]. The black dashed lines mark the trajectories driven downward i.e. from the north to the south and the solid lines mark the trajectories driven in the opposite direction.

~~The dataset covering the test area consists of 1 220 825 points. Those points form the input for the identical points finding algorithm. The output is a set of laser point pairs, that are considered to be identical in 3D position.~~ The 2D horizontal distance between identical points is calculated and is denoted by d_H. The height differences ΔZ of those identical points are studied considering the geometric attributes of laser points, i.e. footprint diameter D_{fp}, range R and incidence angle α. Besides, the unit vector of the upward normal $\vec{n}$ to the surface at the laser point is used. It is computed as explained in Section 5.2.2. If the z-component of the vector $\vec{n}$, denoted by N_z, is close to one, it is assumed that the laser point lie on an almost horizontal plane.
To simplify the analysis of identical point pairs (denoted with IP), one value of footprint diameter, incidence angle and range is taken per IP pair (IP attribute). For footprint diameter D_{fp} the minimum value of the two points in the IP pair is taken, in order to represent the distance threshold, as explained in Section 5.5.1. For range R and incidence angle α the maximum value of the two points in the IP pair is taken, because it is expected that the bigger those values are, the bigger the ΔZ. Therefore we stay at the worse case side. The minimum value of N_z is taken per identical point pair, in order to find the identical points IP that lie on horizontal plane. ~~In Table 6.2 the median values of IP attributes and the results of height differences of identical points are presented.~~

From 36 656 identical point pairs, the majority, i.e. 58%, belongs to the same scanner and the same drive-line. This high percentage indicates that the laser point cloud includes quite a lot of redundant data, i.e. points with overlapping footprint. Around 24% of identical points belongs to different scanner and drive-line. The rest, i.e. 1,7% and 15%,

Table 6.2: Mean values of IP attributes and statistics of height differences of identical points.

Attribute name	IP attribute	ALL	Scanner overlap	Drive-line overlap
	No.Points	35 656	608 (1.7%)	5 473 (15%)
Horizontal distance	Avg d_H [m]	0.0349	0.0313	0.0349
Footprint diameter	Avg min(D_{fp}) [m]	0.1191	0.0672	0.1302
Range	Avg max(R) [m]	12.1720	7.5457	17.4979
Incidence angle	Avg max(α) [°]	79.5971	75.4899	83.1788
Z-component of normal	Avg min(N_z)	0.9976	0.9986	0.9989
Height difference	ΔZ min [m]	-0.0490	-0.0200	-0.0470
	ΔZ max [m]	0.0500	0.0360	0.0460
	ΔZ avg [m]	0.0005	0.0002	0.0000
	ΔZ std [m]	0.0050	0.0025	0.0035

belongs to the scaner overlap and drive-line overlap respectively, which are considered in the following analysis.
The average values of IP attributes show the differences of scanning and positioning geometry of identical points found for three cases. In case of scanner overlap the identical points have the best scanning geometry, i.e. the average of maximum ranges max(R) is the smallest and is around $7m$, and the average of maximum incidence angles max(α) is the smallest and is 75°. Besides, also the average of the minimum footprint diameters min(D_{fp}) and the average of horizontal distances d_H are the smallest. The mean (avg) of height differences ΔZ is very close to zero for case ALL and scanner overlap. In case of drive-line overlap the average of height differences ΔZ as expected equals to zero. The zero mean indicates that there are no systematic errors between identical points. The standard deviations (std) are equal or smaller than $5mm$ for all three cases. Therefore, the relative precision of L-MMS laser points is at worst case $5mm$. More detailed discussion of numbers in Table 6.2 is given in the following three sections, separately for each case.

6.2.2 Relative height precision of laser points (ALL case)

In Fig. 6.9(a) the spatial distribution of height differences ΔZ for the case ALL is shown. The extreme values above $4mm$ and below -$4mm$ are colored black and represent 9% of identical points. They mostly occur in the dune area, which is most probably the consequence of sloped terrain. In Fig. 6.9(b) the horizontal distances d_H between identical points are visualized. Most of the identical points, i.e. 92%, lie from $3cm$ up to $4.5cm$ appart. In the beach area the corespondence between height differences ΔZ and horizontal distances d_H can be observed, namely for small horizontal distances close to trajectories (blue color) also height differences are small (grey color). This relation does not hold in the dune area. This is expected, because the steep slope of the dunes can still influence the height difference, even though the identical points are close in X and Y. Besides, points on

the dunes might be reflected from the dune vegetation, causing the height difference when they are compared with the nearby points reflected from the gorund. Indeed, most of the identical point pairs colored black in Fig. 6.9(a) belong to different classes vegetation and ground, considering the original attribute, the class number.

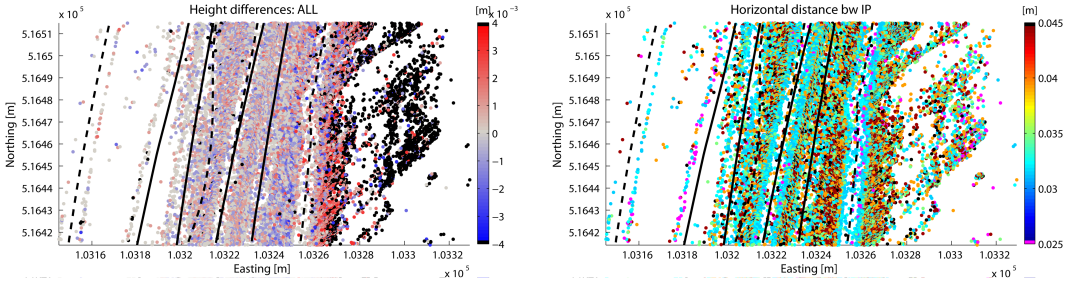

(a) Height differences ΔZ of identical points (IP). (b) Horizontal distances d_H between identical points (IP).

Figure 6.9: The vertical and horizontal differences between identical points.

Before analyzing the influence of the range and incidence angle on the height differences, their maximum values per identical point pair are presented. Fig. 6.10(a) shows that bigger IP ranges, i.e. above $60m$ (black color), occur mostly in the dune area and ranges below $10m$ (pink color) on the beach close to the trajectories marked by black lines. On the other hand Fig. 6.10(b) shows that most of the IPs lying in the dune area have smaller incidence angles. The incidence angles bigger than 85° occur mostly on the beach.

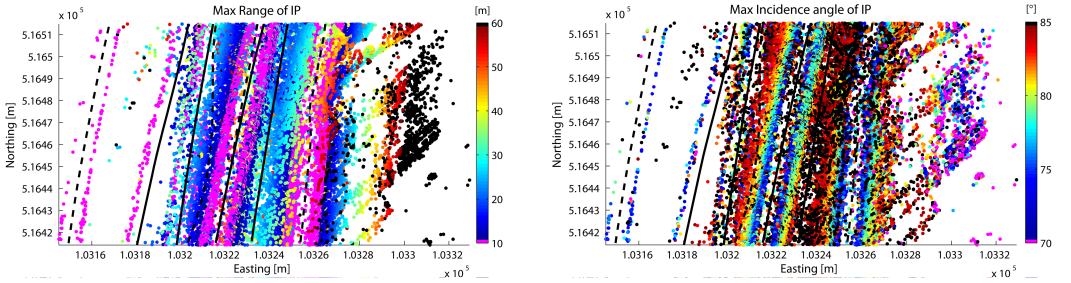

(a) Maximum range R per identical point pair. (b) Maximum incidence angle α per identical point pair.

Figure 6.10: Geometric attributes of identical points.

In Fig. 6.11 the absolute height differences $abs(\Delta Z)$ are shown in relation with the IP attributes range $\max(R)$ and incidence angle $\max(\alpha)$; gray dots are identical point pairs belonging to the same class and the blue dots represent identical point pairs belonging to different classes. To show the changes of $abs(\Delta Z)$ more clearly, the mean (black squares) is computed for a certain interval, i.e. bin of IP attribute values, and the standard deviation shows the spread of the absolute height differences $abs(\Delta Z)$ within corresponding bin (red error bars).

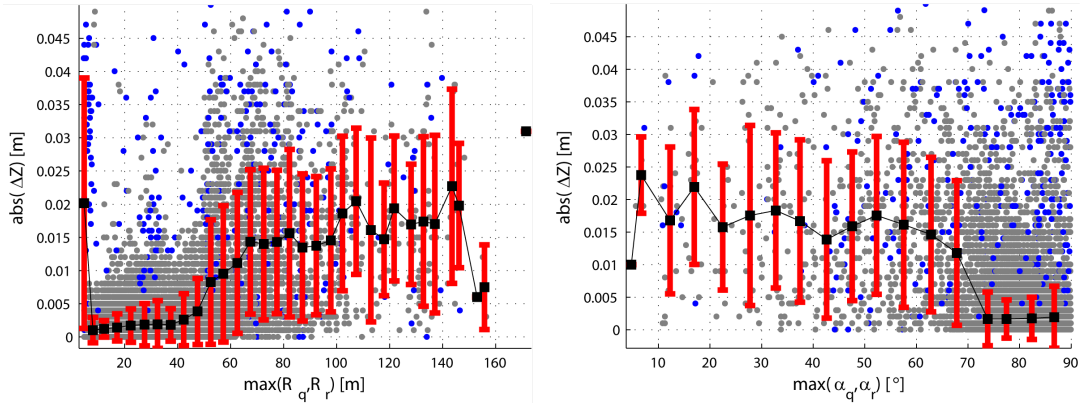

(a) Range R. (b) Incidence angle α.

Figure 6.11: The relation of the height differences ΔZ and scanning geometry attributes.

An interesting phenomena in Fig. 6.11(a) is observed for IP ranges smaller than $10m$. There the mean absolute height difference is $2cm$ and the standard deviation is $1.9cm$, which is considerably larger than for the consecutive ranges. The reason for high standard deviation might be small number of identical points in this bin, which is 22, in comparison with the next bin, which has more than 10 000 identical points. However, the grey and blue dots form a distinct vertical line for IP ranges smaller than $10m$. Therefore, an investigation is done in the identical point pairs having IP range smaller than $10m$ and besides, absolute height difference higher than $0.1cm$. They lie randomly on the flat beach and belong to the same scanner and drive-line. The average horizontal distance between them is small and is $1.96cm$, but the average incidence angle is high and is 84°. For comparison, the average incidence angle of all identical points having the IP range smaller than $10m$ is 75°. An explanation of this phenomena is, that high absolute height differences result from close by points being reflected from different part of a vertical surface, i.e piece of wood or litter lying on the beach. Thus those points are not identical, however they lie less than $2cm$ apart in horizontal plane and have overlapping footprints in 3D. As seen also in Fig. 6.11, most of the dots having IP range smaller than $10m$ and absolute height difference bigger than $0.1cm$ indeed belong to different classes (are colored blue).
The mean absolute height difference of identical points that have IP range below $55m$ is smaller than $2.5mm$. At the IP range of approximately $55m$ the mean absolute height difference and its standard deviation rapidly increases. The reason is most probably the sloped terrain, because most of those identical points with IP range bigger than $55m$, lie in the dune area (see Fig. 6.10(a)).

In Fig. 6.11(b) the trend of the absolute height differences is shown with respect to the IP incidence angle. The trend runs in the opposite direction as in Fig. 6.11, thus for the increasing IP incidence angle the mean absolute height difference decreases. This is most probably the result of the sloped dune surface, as discussed in previous paragraph for Fig. 6.11(a). For IP incidence angle higher than approximately 70° the mean absolute

height differences are small i.e. below 2.5mm. For IP incidence angle smaller than 70°, which mostly occur in the dune area (see also Fig. 6.10(b)), the mean $abs(\Delta Z)$ increases to approximately 2cm.

To eliminate the influence of terrain slope on the height differences, only the identical points lying on an almost horizontal surface are selected from the set of ALL identical points. This selection is performed ~~using the z-component of the normal vector N_z, which is computed for each laser point as explained in Section 5.2.2. For each identical point pair the smallest N_z should be bigger than 0.9976 to enter the selection.~~ This threshold is taken as the average value of variable N_z, see Table 6.2. 17 754 identical point pairs are found. Most of those identical points lie on the relatively flat and horizontal beach. Therefore, in Fig. 6.12 the results are presented for a zoom-in area of Fig. 6.11. In Fig. 6.12(a) 17430 identical points (98%) are considered that have the IP range smaller than 55m. In Fig. 6.12(b) 17 592 identical points (99%) are considered that have the IP incidence angle bigger than 70°.

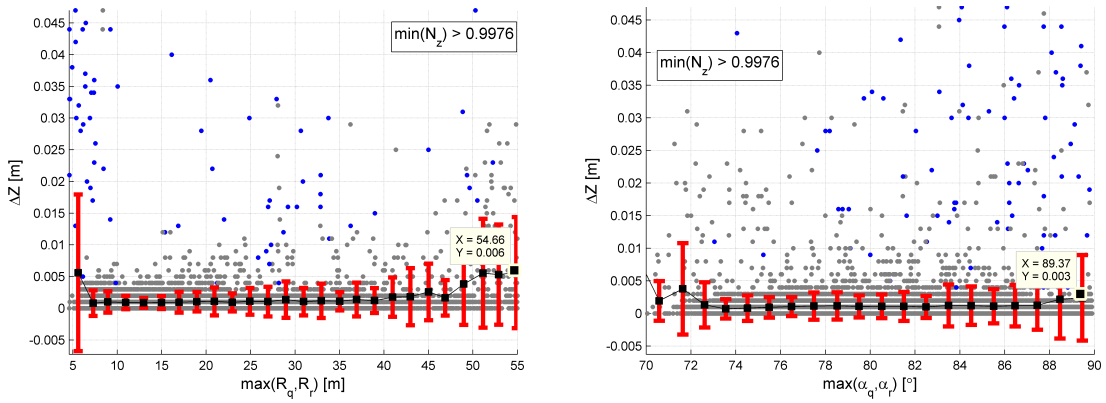

(a) Range R.

(b) Incidence angle α.

Figure 6.12: Zoom in the graphs for the identical points lying on an almost horizontal surface, i.e. $min(N_z) > 0.9976$.

The average absolute height differences, shown as black squares in Fig. 6.12, draw a similar trend than the one in Fig. 6.11. The average values are now in general smaller. For example at the range of 55mm the average absolute height differences are now 5.6mm (before 9.1mm), and for the scan angle 89.5° the average absolute height differences are now 2.4mm (before 3.9mm). Fig. 6.12(a) shows that the extreme absolute value, regarding the following mean values, at the range around 5m is still present (compare to the firs black square in Fig. 6.11). Because here more, i.e. 71 identical points fall within the first bin, the mean absolute height difference equals 5.6mm (before 2cm). Most of the identical points with the IP range smaller than 10m and absolute height difference bigger then 1cm belong to different classes (see blue dots). However, those points present just 0.2% of identical points having IP range smaller than 10m. When the IP range increases

from $7m$ to $45m$, the mean values slowly increase from $0.8mm$ to $2.5mm$. In Fig. 6.12(b) the average absolute height differences are almost constant for incidence angles changing from 72° to 87°. The average values are around $1.1mm$.

~~In both cases presented in Fig. 6.12 the changes and values of absolute height differences are very small. Therefore it is concluded that the range and incidence angle almost do not influence the height differences ΔZ between identical points lying on horizontal surface.~~

6.2.3 Overlapping area of scanners

The identical points in the scanner overlap area lie, due to the definition of the overlap, close to trajectories as show in Fig. 6.13. Therefore, IP ranges $\max(R)$ and IP incidence angles $\max(\alpha)$ are small, see the average values in Table 6.2. The average IP footprint size $\min(D_{fp})$ is $6.72cm$ and the average horizontal distance d_H between identical points is $3.31cm$, which is small in comparison with the case ALL and drive-line overlap. The IP z-normal $\min(N_z)$ of identical points is mostly, i.e. for 50% of identical points, bigger than 0.9986. This means that most of the identical points in scanner overlap lie on horizontal plane. The mean height difference is $0.2mm$ and their standard deviation is $2.5mm$ (see Table 6.2). ~~The offset from the expected zero mean could indicate the scanners calibration error, which is in any case very small.~~ The highest height differences, i.e. above $\pm 2mm$ (black dots), occur in the most right drive-line (DL5). This might be the result of the rough surface or the presence of vegetation in this pre-dune area. Identical points that have ΔZ bigger than $1cm$ belong to different classes, namely to low vegetation class and ground class.

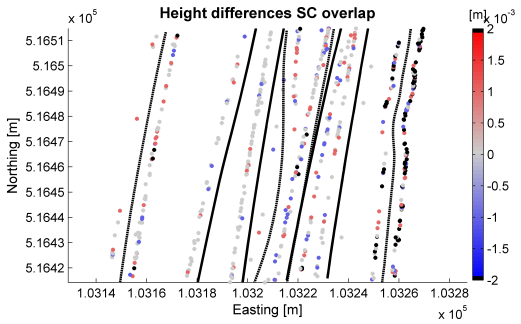

Figure 6.13: Height differences ΔZ of identical points (IP) in the scanner overlap.

Most identical points (513 IP, 84%) are found in the overlap of the scanners Q120i (SC2) and Q120 (SC3), which have the same characteristics for the range and scan angle error. The rest of the identical points lie in the overlap of the scanners Q120i (SC2) and Q140 (SC1), which acquire measurements of different quality (see specifications in Section 3.4). Table 6.3 shows the statistics of the height differences for these two overlaps.

In both scanner overlaps the mean of ΔZ is very close, but not zero. The height differences ΔZ are slightly bigger in SC2&SC3 overlap, which might be a consequence of different

Table 6.3: Statistics of the height differences in scanner overlap SC2 & SC1 and SC2 & SC3.

		SC2 & SC1	SC2 & SC3
ΔZ	min [m]	-0.0400	-0.0360
	max [m]	0.0200	0.0060
	mean [m]	0.0005	-0.0003
	std [m]	0.0025	0.0024

measurements quality. Elevations derived from the measurements of scanner Q120i are on average $0.5mm$ bigger than those derived from the measurements of scanner Q140. On the other hand, the scanner Q120 measures points on average $0.3mm$ higher than the scanner Q120i. However, those numbers are very small and bigger dataset should be investigated to confirm those findings.

In Fig. 6.14 the relation between the height differences (colorbar) and the attributes of laser points that belong to two different scanners (on x- and y-axis) is plotted. The graphs present the height differences of identical points found in the SC2&SC3 overlap. To visualize this relation independently of the number of points with a certain attribute value, the mean height difference is computed for equal intervals of attribute values presented on x- and y-axis. As can be seen in the figures, the laser points of SC2 and SC3 share almost the same scanning geometry. Values of range are similar for both scanners and are limited to short intervals from $5m$ to $9m$. Incidence angles have values mostly from 65° to 90°. Black dots indicate the attribute values where the mean height difference exceeds $2mm$. No obvious pattern of height differences ΔZ can be seen.

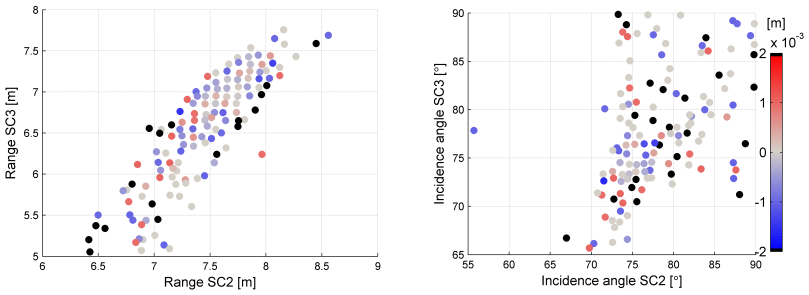

(a) Height differences vs. measured ranges of SC2 and SC3.

(b) Height differences vs. incidence angles of SC2 and SC3.

Figure 6.14: The relation between the scanning geometry attributes and the height differences ΔZ in the SC overlap of scanner Q120i (SC2) and scanner Q120 (SC3).

6.2.4 Overlapping area of drive-lines

Identical points found in the drive-line overlap lie on the beach and in the dunes, as shown in Fig. 6.15. Black color indicate identical points having a height difference bigger than $\pm 2mm$. They represent approximately 9% of identical points in the drive-line overlap. IP footprint diameter is on average $13.02cm$, IP range and IP incidence angle are on average approximately $17m$ and 83°, respectively. Most of the points lie on a horizontal plane, because the IP z-normal is on average 0.9989 (see Table 6.2). The mean height difference is here as expected zero, ~~thus it can be assumed there is no offset between drive-lines. In other words there is no systematic error in GPS/INS positioning.~~

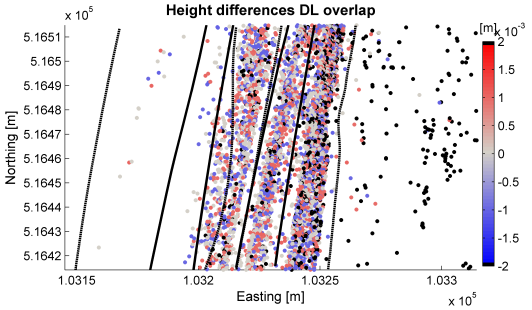

Figure 6.15: Height differences ΔZ of identical points (IP) in the drive-line overlap.

To study the standard deviation of the height differences, which is here $3.5mm$ (see Table 6.2), the laser point attributes of scanning geometry, R and α, are investigated. Fig. 6.16 shows the relation between those attributes and the height differences ΔZ of identical points that are found in the overlap of drive-lines 5 and 7. Points in those figures present the mean height differences per 2D bin of attribute values, as explained already in Section 6.2.3. Again no obvious pattern of height differences ΔZ can be observed.

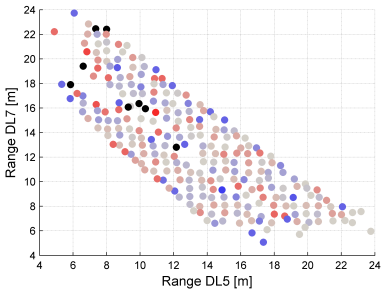

(a) Height differences vs. measured ranges of DL5 and DL7.

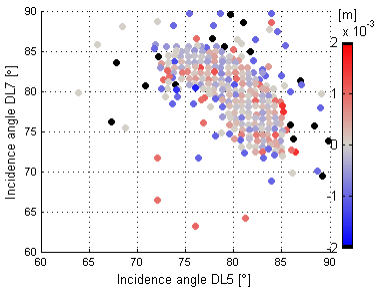

(b) Height differences vs. incidence angles of DL5 and DL7.

Figure 6.16: The relation between the scanning geometry attributes and the height differences ΔZ in the DL overlap of drive-line 5 (DL5) and 7 (DL7).

6.3 Comparison of empirical and theoretical height precision

The empirically assessed relative precision of L-MMS laser points computed in Section 6.2, is in this section compared to the theoretical precision. The theoretical precision σ_{Zi} of laser point heights is computed first due to the L-MMS measurement errors (measuring precision) and secondly due to the scanning geometry (geometrical precision). Those two components, i.e. measuring precision $\sigma_{Zi,m}$ and geometrical precision $\sigma_{Zi,\delta R}$, are computed for each laser point as explained in Section 5.5. Using the law of error propagation, the theoretical precision of height difference between two laser points is computed as written in Eq. 6.1:

$$\sigma_{\Delta Z} = \sqrt{\sigma_{Zq}^2 + \sigma_{Zr}^2} \tag{6.1}$$

Here q and r denote an identical point pair, where one point belongs to the query q and the other point to the reference r dataset. The theoretical precision of height differences $\sigma_{\Delta Z}$ is computed for each height difference between identical points. In Table 6.4 the statistics of empirical and theoretical precision measures are given.

Table 6.4: Comparison of the empirical and theoretical precision measures.

		min	max	mean	std	RMSE
Empirical	$\Delta Z_{ALL,Nz}$ [m]	-0.0470	0.0460	0.0001	0.0031	0.0031
Theoretical	$\sigma_{\Delta Z}$ [m]	0.0376	4.8515	0.0573	0.0658	0.0872
Theoretical	$\sigma_{\Delta Z,m-gps}$ [m]	0.0099	0.1478	0.0272	0.0102	0.0290

The computation of the empirical height differences $\Delta Z_{ALL,Nz}$ between identical points considers ALL identical points that lie on an almost horizontal plane. Those identical point pairs, of which the minimal z-component of the two normals is bigger than 0.9976, are taken into account. The aim is to reduce the influence of surface slope and roughness on the computed height differences (see also Section 6.2). All together 17 754 identical points are taken into account, which is approximately 50% of identical points considered in the case ALL. The mean of empirical height differences $\Delta Z_{ALL,Nz}$ is almost zero and the standard deviation is $3.1mm$. The comparison between empirical RMSE of $\Delta Z_{ALL,Nz}$ and theoretical RMSE of $\sigma_{\Delta Z}$ in Table 6.4 shows big differences; the empirical RMSE equals to $0.3cm$ and the theoretical RMSE equals to $8.72cm$. Possible reasons are:

- Overestimated errors included in error budget, i.e. L-MMS measurements and calibration parameters random errors;
- Overestimated error due to the scanning geometry;
- When computing height differences, some errors might cancel out against each other;
- Wrong assumption on identical points;

Overestimated error budget. High theoretical RMSE of $\sigma_{\Delta Z}$ might result from the overestimated random errors of L-MMS measurements. Especially due to the theoretically

computed scan angle random error, where uniform laser power distribution over the entire footprint is assumed. As a result an overestimated one quarter of the beam width is added to the scan angel resolution (see Eq. 4.10). In reality the relative power distribution has a Gaussian form as shown in [Glennie, 2007b], which suggests that the level of uncertainty is less than one quarter of the beam divergence. The scan angle error strongly influences the theoretical height error of laser points and increases fast with the range (see Fig. 4.8). Besides, the highest GPS/INS positioning error is considered into the random error budget computation; compare the plot of GPS/INS RMSE in Fig. 4.4 with the GPS error values in Table 4.3. Thirdly, the values of calibration parameters error are taken as a rule of thumb and should be verified by the calibration procedure (see Section 4.3.3). However, the calibration parameters errors do not influence much on measuring precision $\sigma_{Zi,m}$ and therefore on theoretical precision of height differences $\sigma_{\Delta Z}$.

From the results of the random error budget presented in Section 4.4 it is concluded that the GPS random errors significantly influence 3D laser point position, but are not dependent on L-MMS measurements, i.e. range, scan angle or IMU measurements. The GPS noise is in general changing during the acquisition since it depends on the number and position of visible satellites with respect to the vehicle position (see Fig. 4.4). Since the beach is open area, which means less or no objects appear in the receiver vicinity that would block GPS signal, the GPS noise lead to a similar noise level in the derived point cloud of the whole acquisition area. Thus the GPS error results in almost constant positioning error for each laser point. Because the median value of time interval between the acquisition of identical points is $38s$, it is possible that the majority of GPS random errors drop out, when computing the height differences.

Overestimated influence of scanning geometry. The scanning geometry, i.e. the geometrical precision $\sigma_{Zi,\delta R}$, adds the biggest part to theoretical precision of height differences $\sigma_{\Delta Z}$. Nevertheless geometrical precision $\sigma_{Zi,\delta R}$ is on average small, its high standard deviation (see Fig. 6.6) results in big RMSE. The theoretical values of $\sigma_{Zi,\delta R}$ might be overestimated, because it is calculated by using the maximum absolute range error δR. This range error is obtained by the theoretical model given in Eq. 5.11, which is valid for pulsed laser scanners. Here it is assumed that it is not known exactly when the returned laser pulse triggers the time of laser range recording. If a laser scanner uses an advanced method to record the time of returned pulse, range error δR might reduce. Besides, if the time is recorded always at the same point on the slope of the returned laser signal, all range measurements have the same offset from the true value. This systematic range error of a laser scanner can be estimated with a proper calibration method and should be eliminated before computing the laser point position. However, when computing the relative precision of height differences between laser points belonging to the same scanner (65% of all identical points considered in height differences $\sigma_{\Delta Z}$ computation) and if they both share the same scanning geometry, the range bias will drop out. This effect might be a reason that no influence of scanning geometry could be observed in the plots of Section 6.2 (see Fig. 6.12, Fig. 6.14 and Fig. 6.16).

Elimination of errors. From the previous two paragraphs it follows that the actual precision of height differences seems smaller then the theoretically computed precision of height differences $\sigma_{\Delta Z}$. Assuming that the GPS random errors and the errors due to the scanning geometry cancel out when computing the height differences between two identical points, the precision of height differences $\sigma_{\Delta Z,m-gps}$ is presented in Table 6.4. However, the RMSE of theoretical error $\sigma_{\Delta Z,m-gps}$ is still approximately 10× bigger than the RMSE of empirical error $\Delta Z_{ALL,Nz}$.

In Fig. 6.17 a spatial distribution of theoretical precision $\Delta Z_{ALL,Nz}$ and empirical precision $\sigma_{\Delta Z,m-gps}$ is compared. A spatial correlation between these two precision measures can be observed.

In Fig. 6.17(a) the empirical absolute height differences $\Delta Z_{ALL,Nz}$ are plotted and in Fig. 6.17(b) the theoretical precision of height differences $\sigma_{\Delta Z,m-gps}$. The colorbar is the same in both figures. The black color indicates 10% of plotted identical points, which have absolute height differences $\Delta Z_{ALL,Nz}$ above $2mm$ (Fig. 6.17(a)) and the theoretical precision $\sigma_{\Delta Z,m-gps}$ bigger than $3.62cm$ (Fig. 6.17(b)). The black points in both cases mostly occure in the dune area.

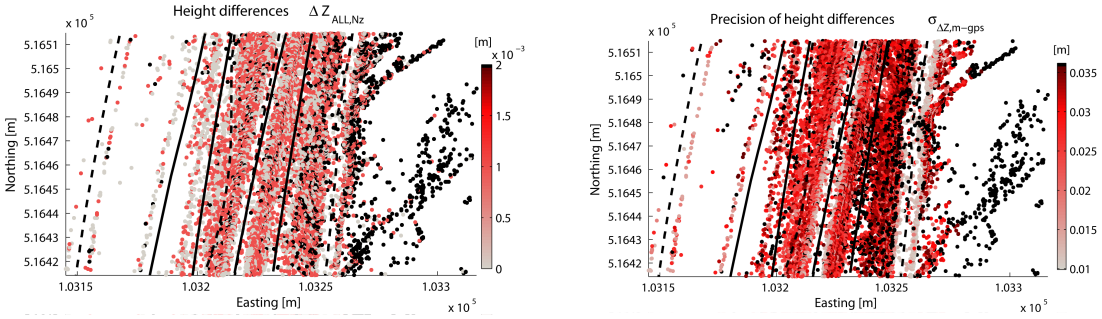

(a) Height differences $\Delta Z_{ALL,Nz}$. (b) Standard deviation $\Delta Z_{ALL,Nz}$.

Figure 6.17: The spatial coherence between empirical and theoretical precision measure.

Wrong assumption of identical points. As stated in the previous paragraph, the theoretical RMSE of height differences $\sigma_{\Delta Z,m-gps}$ is still much higher than the empirical RMSE of height differences $\Delta Z_{ALL,Nz}$. A reason might be a wrong assumption on identical points. The algorithm to find the identical points, explained in Section 5.5.1, considers the laser beam footprint size and 3D distance between laser points. If the laser points lie so close together that their footprints partly overlap and, if in any case their 3D distance is not bigger than $5cm$, they are considered as identical points. This means, they represent almost the same point on the surface, due to the beam width uncertainty. Other random errors, which influence the laser point positioning precision and are included in the the-

oretical random error budget computation, are not taken into account. This might be a necessary step, because, if the 3D point spacing (PS) between the L-MMS laser points is smaller than the size of the error ellipsoid denoting 3D laser point positioning error, the assumption of identical points might be wrong. This situation is illustrated in Fig. 6.18, where identical points between query q set and reference r set are looked for. For a better visualization the 3D situation is shown from a side in 2D (e.g. in XZ plane).

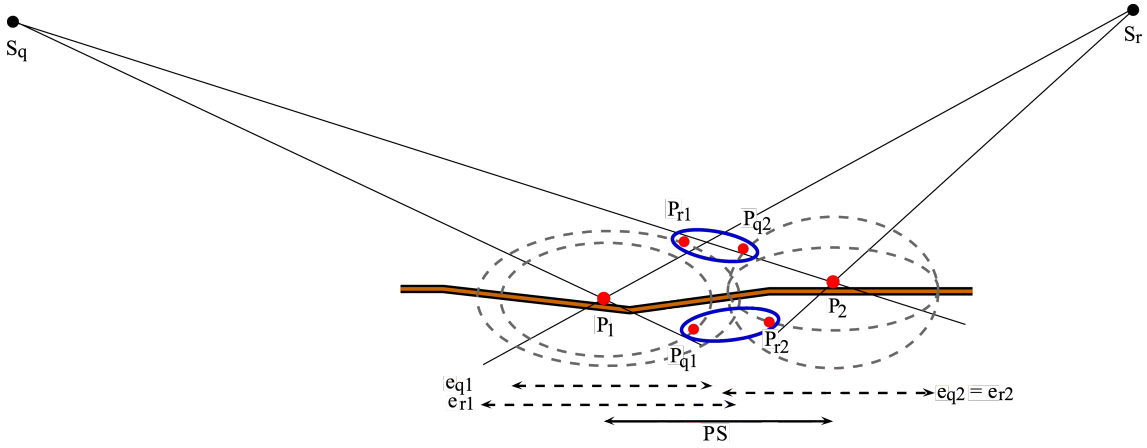

Figure 6.18: Finding the pseudo-identical points. The situation when the point spacing PS between neighboring laser points P_1 and P_2 is smaller than the positional error ellipsoid e_i of measured laser points P_{q1} and P_{r1} of true surface point P_1, and P_{q2} and P_{r2} of true surface point P_2.

Laser points P_{qi} and P_{ri} ideally represent the same point P_i on the surface. Here $i = 1, 2$. But in reality P_{qi} and P_{ri} both include a (different) 3D positioning error. Considering the random errors the measured laser points can lie anywhere within their error ellipsoid denoted in Fig. 6.18 with dashed ellipses. In case that the point spacing PS between neighboring but not identical laser points P_2 and P_1 is smaller than the size of their error ellipsoids e_i, the pseudo-identical point pairs are now P_{r1} and P_{q2}, and P_{q1} and P_{r2} (in Fig. 6.18 encircled by blue line). Obviously, the height difference between pseudo-identical points, which are defined just according to the 3D distance, is smaller that the height difference between real identical points P_{q1} and P_{q2}, and P_{r1} and P_{r2}.

In case that the error ellipsoid e of laser points is smaller or in case that the point spacing PS between laser points on surface is bigger, so it holds $PS > 2 \cdot e$, then the identical points considered in this research are correct. This is difficult to prove here, because it is not known exactly what the actual precision of the L-MMS points acquired during pilot-project Egmond aan Zee is. A reference data would be needed to independently obtain the precision of laser points. This precision could be compared to the empirical precision of height differences between identical points ΔZ.

6.4 Summary

Analyzing the laser point attributes of the test area, i.e. the cross-strip in block 1 that measures 213×101m, one can get an idea about the real StreetMapper dataset. The original attributes, as presented already in Section 3.5.2, are in this Chapter visualized for a single drive-line. One can observe varying patterns of those attributes. Namely, the data of three laser scanners, which are of different type and have different orientation, are incorporated. Intensity values are not normalized (i.e. calibrated) and therefore can not be merged into one dataset.
Additionally computed geometric attributes, i.e. the range, incidence angle and footprint diameter, describe the relation between the laser scanner position and each illuminated target. As expected, their values increase fast toward edges of a drive-line. The maximum range acquired on the flat sandy beach indicates the maximum swath width and is approximately 25m on both sides of trajectory. Thus, StreetMapper can measure at least 50m wide strip on a horizontal surface.
The maximum range in the test are is 180m, which is measured by the laser scanner Q140 on the vegetated dune slopes. The maximum incidence angle is close to 90°, which causes the footprint diameter to approach infinity. For this reason the maximum footprint diameter at 89.9° is computed as 126m. However, the median values of the geometrical attributes show that the actual scanning geometry on the Dutch beach is on average good; a median range is around 6.5m, a median incidence angle is 72.1° and they together result in a median footprint diameter of 5.8cm.

The results of scanning geometry are incorporated in the computation of the theoretical laser point height precision. First the vertical error resulting from L-MMS measurement errors (measuring precision) is computed. It has a minimum value of 2.54cm due to the GPS vertical error. The maximum measuring precision equals 16.34cm, but only 10% of the analised laser points within the test area have a measuring precision worse than 3.47cm. Analysing the scanning geometrty attributes, the range has bigger influence on the measuring precision than incidence angle. When the range is bigger than 140m, most of the points exhibits a measuring precision worse than 10cm. The median measuring precision is 2.88cm. The spatial variation of the measuring precision shows an interesting "zebra" pattern, fast but small changes of the measuring precision accross the drive-line. To explaine it more detailed, analyse of components included in the first order error propagation model for measuring precision computation would be needed.
Secondly, the non-perpendicular scanning geometry is taken into account to compute the resulting range error. This range error is considered as a maximum random error. Therefore, it is inserted in the first order error propagation model and the height variance of the range error component is computed. This so-called geometrical precision has values from zero to around 10m. The high maximum value is a consequence of the incidence angle close to 89.9°. Nevertheless, the geometrical precision is on average good. Its median equals 8.6mm. The reason is that most of the acquired laser points have a good scanning geometry, as stated above. In other words, the intersection geometry of the laser beam with the scanner surface is on average good.

The results of presented relative Quality Control (QC) employing height differences between so-called identical points show very small numbers. Analyzing those height differences with respect to the geometrical attributes, i.e. range and incidence angle, show the influence of the terrain slope on the size of the height differences. Therefore, just the identical points lying on the horizontal plane are considered. In this case, the average height differences slightly decreases. The identical points that have height difference bigger than 3× standard deviation mostly belong to different classes. This means they do not represent the same surface, thus are actually not identical.
The mean of signed height differences is almost zero for all three cases, i.e. case ALL, scanner overlap and drive-line overlap. Therefore, it can be concluded that no systematic errors are presented in the derived laser point cloud. Results of the case scanner overlap indicate there is no bias in the laser scanner calibration parameters and results of the case drive-line overlap show there is no bias in GPS/INS position measurements. However, the set of identical points found in the overlaps, especially scanner overlap, is small. Therefore, more laser points should be analyzed to confirm the statements above.
~~Analyses of the correlation between height differences of identical points and the geometric attributes do not show clear trend. Therefore, it is concluded that height differences do not depend neither on the range neither on the incidence angle.~~

The comparison of theoretical and empirical precision of height differences between laser points shows big differences. The theoretical RMSE is approximately 28 times bigger. This could partly be expected, because the estimation of the theoretical height precision rely on many assumptions (e.g. about calibration parameters, scan angle error, error due to non-perpendicular scanning geometry), which err on the side of caution. To approve the theoretical precision measures, reference data should be employed.
On the other side, the empirical estimation of the relative height precision might not include all errors that are considered for the theoretical height precision computation. Therefore, the empirical values are too small. The reason is, that the empirical precision is obtained from the laser points (i) that lie close together, (ii) that were on average acquired in short time interval and (iii) that share almost the same scanning geometry, i.e. identical points. Starting with the last reason, the following conclusions are made.
In Section 6.1 it is shown, that the theoretical laser point precision decreases with increasing range (measuring precision) and the incidence angle (geometrical precision). However, the analysis of the empirical precision does not show dependency on the geometric attributes (see Section 6.2). This might indicate that the range error due to the non-perpendicular scanning geometry causes a systematic error in the derived laser point position. Therefore, the geometrical error drops out when calculating the empirical height differences.
Besides, also the impact of the GPS error might partially drop out, when subtracting the heights of laser points that were acquired in a short time interval. The INS/GPS positioning error almost do not change over an open acquisition area, like the Dutch beach.
When the impact of geometrical error and GPS error are not taken into account, the theoretical RMSE reduces. However, it is still 9 times bigger than empirical RMSE.
The last reason for the small empirical RMSE is, that the distance between L-MMS laser

points might be smaller than is the size of their error ellipsoid. Therefore, it might happen that the points reflected from different part of the surface appear closer together than they really are. Considering just the footprint size and 3D distance between laser points to choose the identical points, might cause that the height differences reduce. To prove the (un)reliability of the identical points method, more research should be done using reference data and test the method on bigger set of laser points.

Chapter 7

Digital Terrain Model quality assessment

The definition of DTM is not straightforward, since there are many different techniques of DTM recording, modeling and visualization, and many fields of interest for DTM applications. One of the definitions found in [Shan and Toth, 2008] says, that a DTM is a continuous function that maps from 2D planimetric position to terrain elevation. This function $z = f(x, y)$ is stored digitally, together with a method on how to evaluate it from geometrically and possibly explicitly stored topological entities. In other words, a DTM can be understood as a "digital description of the Earths surface", which does not include only representation of the relief itself, but also its description, as slope, aspect, contour lines, break lines (sudden change of a terrain surface), peaks, and other characteristic points. The idea of DTMs has been proposed nearly 50 years ago. Still the best technologies for both data acquisition technique and the data processing are under active research. Currently, DTMs constitute a fundamental data base for Geographical Information System (GIS)s. ~~The importance of DTM applications makes it inevitable to provide DTMs with adequate quality measures at a high level of detail. The idea is to inform the user about the DTM quality and warn them of weakly determined areas. The main question for this research is, how good a laser L-MMS performs on the Dutch beach and what the final quality of the main beach attribute i.e. the height is. Therefore in this chapter an approach to evaluate the laser L-MMS DTM is discussed.~~

First background information about the construction of the DTM and methods to estimate its quality is given in Section 7.1. In Section 7.2 the theory of the least squares adjustment is described. The so-called Moving Least squares is used in this research to interpolate the grid point heights and estimate its precision. In Section 7.3 the background information and theory are joined to determine the methodology for the laser L-MMS DTM quality assessment. Finally, the discussion on DTM quality assessment is summarized in Section 7.4.

7.1 Background information

In this section background information on DTM interpolation and quality estimation is given. In Section 7.1.1 different data structures and interpolation methods employed for DTM construction are described. ~~Many researches and books exist for those topics, however they are not discusses further in this master thesis. The main emphasis is on the DTM quality estimation.~~ In Section 7.1.2 first a general list and description of factors that influence the DTM quality is given. This theory is then incorporated in our research according to the available L-MMS data and our objectives. In Section 7.1.3 the measures and models that describe the DTM quality are discussed. Again, the theory is shortly linked to our research.

7.1.1 DTM data structure and interpolation

A laser point cloud is by nature an irregularly spaced dataset which usually consists of millions or billions of points. To easier control this very large amount of data, the transformation into other data formats is indispensable. Most commonly the raster format is applied, where available observations are interpolated to a regular grid and an interpolation method is used to interpolate heights within a grid mesh [Shan and Toth, 2008].
The process of converting the point cloud into a regularly spaced dataset by means of interpolation is called gridding. There are many different algorithms to compute grid heights. The more common are Nearest Neighbor, Inverse Distance Weighting, Moving Least Squares and Kriging [Shan and Toth, 2008], p.310. Because the number as well as density of laser points is typically very high, it is not always necessary to apply best predictors (e.g. Kriging). It might be better to choose a method that has better computational performance.
Surfaces can be represented by discontinuous, continuous or even smooth functions. It has been found that the continuous surface consisting of a series of contiguous linear facets is the least misleading; see [Li et al., 2005], Chapter 4. If the grid is enhanced with linear structures and special points, so-called hybrid grid structure is obtained [Shan and Toth, 2008], p.310. The regular nature of the grid allows the analyst to perform many mathematical operations such as area and volume computations, grid algebra, grid calculus, differentiation, gradients, grid comparison, as well as image processing operations.

An method alternative to gridding is the Triangulation with Linear Interpolation, which results in so-called Triangular Irregular Network (TIN) data structure. The difference is that the surface is reconstructed from the original data points, which might be time consuming for big datasets. The discussion on advantages and disadvantages of different data structures can be followed in the research literature, e.g. in [Ackermann and Kraus, 2004].

7.1.2 Factors influencing the DTM quality

As stated in the introduction of this chapter, the QC of DTM is an inevitable process accompanying the DTM construction and its use. ~~In general the quality of a DTM depends~~

~~on a number of individual influencing factors~~ such as:

- **Quality of the original laser point cloud (FD).** The influence of the original laser points on the DTM quality can be dissected according to the attributes of the original laser dataset, namely the point density (FD1), the accuracy and/or precision of individual points (FD2) and the distribution (FD3) of terrain laser points. All three attributes have a large influence on the quality of the final DTM. The first attribute, the individual terrain point quality (FD2), is related to the measurements. It determines the grid point precision through error propagation. The density (FD1) can be specified by measures like the distance between two points, the number of points per unit area or the cutoff frequency (for details see [Li et al., 2005], Chapter 2). The number of original laser points included into the grid point computation influence the grid point reliability. More points within the grid cell result in a higher redundancy. A lager redundancy enhances the possibility to check for errors and so increases the precision of the derived results [Teunissen et al., 2008]. Therefore the interpolated DTM can achieve better quality than a single point measurement. The density (FD1) and distribution (FD3) are related to the sampling of terrain surface characteristics. An example of the combined effect of FD1 and FD3 is as follows. If there are a lot of points in smooth or flat areas and only a few points in the rough areas, then the DTM quality can be low.

- **Roughness of the terrain surface (FR).** Terrain roughness is an important terrain descriptor in the context of terrain surface modeling. It describes the complexity of a terrain surface and determines the difficulty to model the terrain surface. In [Li et al., 2005] and [Huaxing, 2008] different parameters describing the terrain complexity are listed and explained. Examples of such parameters are variance or standard deviation of elevations, frequency spectrum, fractal dimension, curvature, covariance and auto-correlation and semivariogram. Their computation requires availability of a sampled terrain points from the project area. On the other hand, to obtain descriptors for project planning and design, prior to acquisition, Li et al. [2005] recommends to use relief, slope and wavelength as main descriptors of the terrain to be modeled. The slope is the most important one, because it is widely used in the practice of surveying and mapping [Li et al., 2005]. However, it was found out that roughness can not be completely defined by any single parameter, but rather by a set of parameters composing so-called roughness vector [Li et al., 2005].

- **Quality of the filtering (FF).** From the definition of DTM it follows that DTM presents ground. Therefore the laser point cloud must be first classified into terrain and off-terrain points, and just the terrain points are then considered for the DTM construction. The elimination of off-terrain points, which lie on e.g. buildings, tents, trees, bushes and high grass is of crucial importance to obtain reliable terrain surface. This process is also called filtering. Different methods exist to remove the off-terrain points e.g., Simple Filters, Morphological Filter, Surface-based Filter, Segmentation-based filter. A comparison of filtering methods is given in [Shan and Toth, 2008], Chapter 11. The quality of filtering depends on the type of surface that the DTM

actually represent. In built-up regions the quality can be very high, because the distinction between ground points and object points is typically clear. In areas covered by low vegetation as for example grass, the quality of filtering cannot be separated from the quality of the original measurements. In this case the quality of the derived DTM depends on vegetation heights and vegetation density within the laser footprint [Pfeifer et al., 2004].

- **Quality of DTM interpolation (FI).** As introduced in Section 7.1.1 the DTM can be constructed from grid data or from TIN data. In the latter, the original irregularly distributed laser points are used directly in the DTM. On the contrary, grid data are preliminarily interpolated via a random-to-grid interpolation. Li et al. [2005] stated that the quality of a DTM surface constructed indirectly will be lower than one constructed directly, due to accuracy loss in the random-to-grid interpolation method. But in case of high redundant laser data, least squares can be used as a random-to-grid interpolation method, which can minimize measurement noise. As consequence higher quality DTMs can be derived. When estimating the quality of the hybrid grid structure, the quality of break line modeling has to be considered. Finally the surface interpolation method influences on the quality of the terrain representation i.e. the quality of the model between original or grid points [Li et al., 2005]. In general different interpolation methods result in DTMs of different quality (closeness to the reality).

Considering the described influencing factors the final quality of DTM grid point can be mathematically expressed as (Eq. 7.1):

$$\sigma_{DTM} = f(FD1, FD2, FD3, FR, FF, FI) \tag{7.1}$$

Relevance to this research. When the DTM is constructed from the existing laser data, the first three influencing factors, point density (FD1), individual terrain point quality (FD2) and distribution (FD3) of laser points, are usually known or can be estimated. The fourth influencing factor, the terrain roughness (FR), is related to the interpolation method (FI). If the terrain is simple, then only a few points need to be sampled and also a simple surface model can be used to represent its topography. For example, if the terrain is flat, a plane can be used to model this piece of terrain surface. On the other hand, if the surface is complex, then more points are needed, and some more complicated mathematical functions may be used for modeling this terrain. Kraus et al. [2006] stated that, if considering only the DTM grid point quality, as in this research, a simple functional/stochastic models can be applied to estimate the quality of every grid point, even if more complex functional/stochastic models are employed for DTM generation. In this research a grid point elevation and its precision are estimated by linear interpolation (FI). The filtering methods (FF) are not considered and further discussed here. The assumption is made that the classification done by the commercial contractor Geomaat (see the data set description in Section 3.5) using the TerraSolid modules is correct. In this case Eq. 7.1 reduces to 5 influencing factors FD1, FD2, FD3, FR and FI, which are included in the final computation

of the DTM grid point quality.

7.1.3 DTM quality description

DTM quality description can be obtained in different ways. An empirical description can be obtained from real experimental data, on the other hand a theoretical description is established by mathematical functions. Usually these two concepts overlap. For examples and equations of different empirical and theoretical approaches see [Li et al., 2005]. Some models enable a prediction of the DTM accuracy beforehand, which is useful for acquisition mission planing and choosing an appropriate data sampling interval. For example the so-called Koppe formula can be applied [Karel and Kraus, 2006; Li et al., 2005]. Other models require availability of the measurements, so the quality descriptors are obtained in the data post-processing steps. In the following, models and measures taken into account in this research are presented. They incorporate the influencing factors, described in Section 7.1.2, as indicated by the corresponding influencing factor notation.

Theoretical models for DTM quality. Since the early 1970s attempts have been made to establish a mathematical model for the prediction of DTM quality through experimental analyses. In [Li et al., 2005] a mathematical expression for DTM quality is given in terms of standard deviation as (Eq. 7.2):

$$\sigma_{DTM}^2 = \sigma_{Data}^2 + \sigma_R^2 \tag{7.2}$$

Where:

- σ_{DTM} is the quality of the resulting DTM.
- σ_{Data} is the quality of original data.
- σ_R is the quality loss due to representation of terrain surface.

Here σ_{Data} represents the first influencing factor FD and so accounts for the errors in the original laser points (FD2), their density (FD1) and distribution (FD3). The second term σ_R^2 depends on the chosen method of surface modeling (FI) and varies with the roughness of the terrain surface (FR). Therefore it is different from place to place and is in general not described by an analytical method, especially for small local deviations. Its characteristics are typically handled by using statistical methods. The value σ_R does not depend on the errors of original laser data.

Local quality measures. If a grid is used to represent a DTM, the DTM quality can be assessed during its interpolation (generation process) by error propagation. The result of least squares adjustment gives a good estimate of the DTM precision, but might reach end users as a "black box", that they will not trust. It is important to describe the influencing factors and the final DTM quality as local as possible.
An empirical-stochastic approach for deriving local quality measures in a general framework

of error propagation is presented in [Karel and Kraus, 2006]. The quality of every DTM grid point is estimated from the original laser data acquired with ALS[1] and already existing DTMs. This quality is estimated taking into account the influencing factors, so-called local quality measures:

- the representative accuracy of the original height observations (FD2), computed as the height difference between the elevation of the original laser point and the elevation extracted from a DTM, for the same XY position of the laser point.
- the number (FD1) and distribution (FD3) of the original points in the grid point neighborhood.
- the terrain curvature (FR).

Relevance to this research. The described empirical-stochastic approach is taken as a base of our research. Therefore Section 7.2 explains in more detail the framework of error propagation through linear regression. The results of least squares are inserted in the theoretical model given in Eq. 7.2 to compute the final quality of each grid point.

7.2 Interpolation and quality estimation by Least Squares

In this thesis least squares is used as interpolation method to estimate the height and height variance at grid point locations. Rules of error propagation based on variances and co-variances of the original terrain laser points are applied, to estimate the quality of the grid points. The output is then strictly speaking the precision of a grid point, which is denoted by a standard deviation σ_{DTM}. It is assumed that systematic errors of original laser points are already eliminated, particularly those of the geo-referencing procedure [Kraus et al., 2006]. This random-to-grid interpolation method accounts for the laser point redundancy and the estimated height is expected to be of higher quality then the source data.

In Section 7.2.1 a short explanation of different matrices, comprising the quality of input data, is given. More details on this topic can be found in [Mikhail, 1976]. In Section 7.2.2 the theory of Moving Least Squares (MLS) adjustment is explained. Besides, a numerical example of grid point interpolation using MLS is given.

7.2.1 Variances, cofactors and weights

The quality of observations as well as results of adjustment are described by terms as accuracy and precision (See Section 4.1.1). The description of the precision of a random variable is often given as a standard deviation σ. When more than one variable is used in least squares, their precisions are given by a variance-covariance matrix Σ. In practical applications of adjustment Σ is often replaced with the so-called relative variance-covariance matrix Q. Another commonly used term for matrix Q is the cofactor matrix and its elements q_i are named weight coefficients or cofactors. Besides, in classical error and adjustment theory, the concept of weights is used. High weight means high precision and on

[1] The method can be also applied for photogrametric data [Kraus et al., 2004].

the other hand small standard deviation. Although it is always possible to switch from cofactors to covariances and vice versa, care must be taken when using the weight matrix. If the matrices Σ, Q and W are assumed to be diagonal with off-diagonal elements equal to zero, as written in Eq. 7.3, the relation between precision (variances), cofactors and weights is given by Eq. 7.4 [Mikhail, 1976]:

$$\begin{bmatrix} w_1 & & & 0 \\ & w_2 & & \\ & & \ddots & \\ 0 & & & w_n \end{bmatrix} = \sigma_0^2 \begin{bmatrix} \sigma_1 & & & 0 \\ & \sigma_2 & & \\ & & \ddots & \\ 0 & & & \sigma_n \end{bmatrix}^{-1} \tag{7.3}$$

$$W = Q_{yy}^{-1} = \sigma_0^2 \Sigma_{yy}^{-1} \tag{7.4}$$

Where:

- W is a weight matrix.
- Q_{yy} is a cofactor matrix of observations.
- Σ_{yy} is a variance matrix of observations.
- σ_0^2 is an a-priori reference variance, chosen arbitrary or based on e.g. description of the measurements precision to scale the variances of observations.

The variances σ_i can be derived directly from observations, whereas the weights w_i can not. For this reason the concept of weights is considered as a secondary concept. In this research the variances of observations (laser point heights) are used in the least squares adjustment as explained in the following section.

7.2.2 Moving Least Squares

The grid point height is interpolated from the terrain laser points within the corresponding grid cell. To model terrain surface of a grid cell a mathematical function is used. In general the mathematical expression is written as $Z = f(X, Y)$. An often used function f is the polynomial function of a certain order [Li et al., 2005]. An example of a second order polynomial is written in Eq. 7.5:

$$Z = a_0 + a_1 X + a_2 Y + a_3 X^2 + a_4 Y^2 + a_5 XY \tag{7.5}$$

Fig. 7.1 shows the first three terms of the polynomial function given in Eq. 7.5. When using just the zero order polynomial, the elevation is constant $Z = a_0$ and can be computed as the mean of the terrain laser points within a grid cell. The graphical representation of such a function is a horizontal plane fitted to terrain laser points. In this research for each grid cell a tilted linear surface is fitted to the original terrain laser points. The first three terms of the polynomial are used, thus the elevation is expressed as a linear function of X and Y as given in Eq. 7.6

$$Z = a_0 + a_1 X + a_2 Y \tag{7.6}$$

Where:

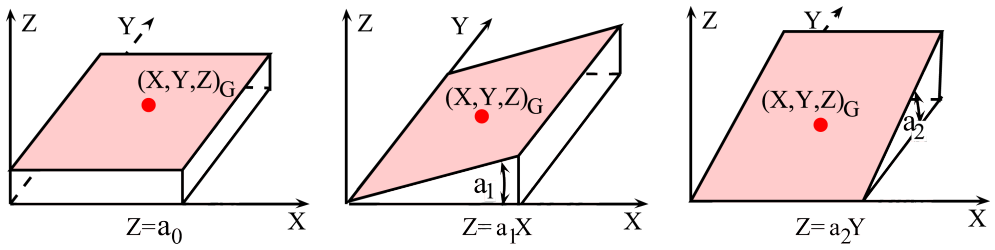

Figure 7.1: A graphic representation of first three terms of general polynomial function given in Eq. 7.5; after [Li et al., 2005].

- X, Y, Z are the coordinates of the terrain laser points (observations) that lie withing the grid cell and are included into the plane computation.
- a_0, a_1 and a_2 are the unknown plane coefficients.

When the number of terrain points exceeds 3 (more equations than unknowns), the overdetermined system of plane fitting is solved by least squares adjustment. The least squares solution minimizes the sum of (weighted) squares of residuals (best fit). In matrix vector notation the least squares model is written as in Eq. 7.7:

$$y \approx A \cdot x \tag{7.7}$$

Where:

- y is a vector of n observations.
- x is a vector of u unknown parameters, which is here 3.
- A is a design rectangular matrix of order $n \times u$.

To make the least squares computation more efficient, a new coordinate system is used with the interpolation grid point (X_G,Y_G) as the origin; therefore the method is called Moving Least Squares (MLS) adjustment [Karel and Kraus, 2006]. The equation of a plane (Eq. 7.6) simplifies, so the plane coefficient a_0 becomes the elevation of the grid point itself.

$$Z_G = a_0 \tag{7.8}$$

The mathematical model of Moving Least Squares for linear surface fitting is then given in matrix vector as in Eq. 7.9b:

$$y \approx A \cdot x \tag{7.9a}$$

$$\begin{bmatrix} Z_1 \\ Z_2 \\ \vdots \\ Z_n \end{bmatrix} = \begin{bmatrix} 1 & X_1 - X_G & Y_1 - Y_G \\ 1 & X_2 - X_G & Y_2 - Y_G \\ \vdots & \vdots & \vdots \\ 1 & X_n - X_G & Y_n - Y_G \end{bmatrix} \begin{bmatrix} a_0 \\ a_1 \\ a_2 \end{bmatrix} \tag{7.9b}$$

Where:

- X_i, Y_i, Z_i for $i = 1 \ldots n$ are the coordinates of the n original laser terrain points that are included into the plane computation.

- X_G, Y_G are the coordinates of the grid point.
- a_0, a_1 and a_2 are the unknown plane coefficients.

Then the unknowns a_0, a_1 and a_2 and their cofactor matrix $Q_{\hat{x}\hat{x}}$ are computed in a least squares adjustment, solving the normal equations N. First the matrix of normal equations is written in Eq. 7.10b:

$$N = A^T Q_{yy}^{-1} A = A^T W_{yy} A \tag{7.10a}$$

$$= \begin{bmatrix} \sum_{i=1}^{n} w_i & \sum_{i=1}^{n} w_i X_{ri} & \sum_{i=1}^{n} w_i Y_{ri} \\ \sum_{i=1}^{n} w_i X_{ri} & \sum_{i=1}^{n} w_i X_{ri}^2 & \sum_{i=1}^{n} w_i X_{ri} Y_{ri} \\ \sum_{i=1}^{n} w_i Y_{ri} & \sum_{i=1}^{n} w_i X_{ri} Y_{ri} & \sum_{i=1}^{n} w_i Y_{ri} 2 \end{bmatrix} \tag{7.10b}$$

Where:

- Q_{yy} is the cofactor matrix of observations derived from the observation variance-covariance matrix Σ_{yy} (see Eq. 7.4).
- W_{yy} is the weight matrix of observations derived from the observation variance-covariance matrix Σ_{yy} (see Eq. 7.4).
- w_i are weights of individual elevation observations i.e. elements of the matrix W_{yy}.
- X_{ri}, Y_{ri} are coordinates of original terrain points reduced for the grid point coordinates i.e. $X_{ri} = X_i - X_G$ and $Y_{ri} = Y_i - Y_G$).

The unknowns are computed as described in Eq. 7.11b:

$$\hat{x} = N^{-1} A^T Q_{yy}^{-1} y \tag{7.11a}$$

$$= \left(A^T Q_{yy}^{-1} A\right)^{-1} A^T Q_{yy}^{-1} y \tag{7.11b}$$

As written in Eq. 7.8 the interpolated height of the grid point equals the unknown a_0. To obtain its precision, first the corresponding cofactor matrix $Q_{\hat{x}\hat{x}}$, carrying the weight coefficients of the unknowns is computed as the inverse of the normal matrix N, see Eq. 7.12b:

$$Q_{\hat{x}\hat{x}} = N^{-1} \tag{7.12a}$$

$$= \left(A^T Q_{yy}^{-1} A\right)^{-1} \tag{7.12b}$$

The weight coefficient q_{a0} is the first element of matrix $Q_{\hat{x}\hat{x}}$ i.e. $N_r^{-1}[1,1]$, which is computed as in Eq. 7.13 (derived from Eq. 7.10b):

$$q_{a0} = \frac{\left| \begin{bmatrix} \sum_{i=1}^{n} w X_{ri}^2 & \sum_{i=1}^{n} w X_{ri} Y_{ri} \\ \sum_{i=1}^{n} w X_{ri} Y_{ri} & \sum_{i=1}^{n} w Y_{ri}^2 \end{bmatrix} \right|}{|N|} \tag{7.13}$$

The standard deviation σ_{a0} is strictly speaking obtained from the weight coefficient q_{a0} and the a-priori reference standard deviation σ_0 (see Section 7.2.1) as given in Eq. 7.14

$$\sigma_{a0}^2 = \sigma_0^2 \cdot q_{a0} \tag{7.14}$$

When σ_0^2 equals to one, the spatial variation of the standard deviation σ_{a0} depends on the standard deviations of observations σ_i (FD2) entering the MLS through weights w_i. Besides, it depends on the number (FD1) and spatial distribution (FD3) of original terrain points incorporated into the grid point interpolation, through the coordinates summations in Eq. 7.10b and 7.13 [Kraus et al., 2006].

The objective of this surface fitting method is to minimize the residuals in the least squares sense. The residuals e present the vertical distance between the original terrain points and the modeled plain, and are computed as in Eq. 7.15:

$$e = A\hat{x} - y \tag{7.15a}$$

$$\begin{bmatrix} e_1 \\ e_2 \\ \vdots \\ e_m \end{bmatrix} = \begin{bmatrix} 1 & X_1 - X_G & Y_1 - Y_G \\ 1 & X_2 - X_G & Y_2 - Y_G \\ \vdots & \vdots & \vdots \\ 1 & X_n - X_G & Y_n - Y_G \end{bmatrix} \begin{bmatrix} \hat{a_0} \\ \hat{a_1} \\ \hat{a_2} \end{bmatrix} - \begin{bmatrix} Z_1 \\ Z_2 \\ \vdots \\ Z_m \end{bmatrix} \tag{7.15b}$$

For each plane the Root Mean Square Error (RMSE) is computed as given in Eq. 7.16:

$$RMSE = \sqrt{\frac{e^T e}{n}} \tag{7.16}$$

Example of the MLS adjustment. In the following a numerical example of the Moving Least Squares (MLS) adjustment is given. For simplicity a grid cell with just four terrain points P is considered. Their coordinates (X,Y,Z) in ND coordinate systems and the elevation standard deviations σ are know and are:
$P_1 = (103131.700, 516416.800, -0.139), \sigma_1 = 0.0712$
$P_2 = (103131.900, 516416.000, -0.130), \sigma_2 = 0.0397$
$P_3 = (103131.000, 516416.700, -0.143), \sigma_3 = 0.0479$
$P_4 = (103131.200, 516416.100, -0.132), \sigma_4 = 0.0492$

Assuming that the observations are uncorrelated and setting the reference standard deviation σ_0 to one, the cofactor matrix of observations equals to the variance matrix. Its inverse is:

$$Q_{yy}^{-1} = \begin{bmatrix} 197.4156 & 0 & 0 & 0 \\ 0 & 635.4497 & 0 & 0 \\ 0 & 0 & 434.9143 & 0 \\ 0 & 0 & 0 & 413.8155 \end{bmatrix}$$

The objective is to interpolate the elevation of the grid point that lies in the middle of the corresponding grid cell. The position (X,Y) of the grid point is $P_G = (103131.500, 516416.400)$. Now the MLS mathematical model is written as $y \approx A \cdot x$, where:

$$y = \begin{bmatrix} -0.139 \\ -0.130 \\ -0.143 \\ -0.132 \end{bmatrix}; A = \begin{bmatrix} 1.0000 & 0.2031 & 0.3750 \\ 1.0000 & 0.4141 & -0.4063 \\ 1.0000 & -0.5000 & 0.3125 \\ 1.0000 & -0.2656 & -0.2500 \end{bmatrix}$$

The results of the MLS, i.e. the unknown plane coefficients (a_0, a_1, a_2) in the vector $\hat{x}$ and their precisions in the cofactor matrix $Q_{\hat{x}\hat{x}}$, are:

$$\hat{x} = \begin{bmatrix} -0.1361 \\ 0.0027 \\ -0.0139 \end{bmatrix}; Q_{\hat{x}\hat{x}} = \begin{bmatrix} 0.00068 & 0.00050 & 0.00084 \\ 0.00050 & 0.00633 & 0.00454 \\ 0.00084 & 0.00454 & 0.00860 \end{bmatrix}$$

The interpolated height of the grid point is now $Z_G = a_0 = -0.1361m$ (first element of $\hat{x}$). The square root of the first element in the cofactor matrix $Q_{\hat{x}\hat{x}}$ is multiplied by $\sigma_0 = 1$. Finally, the standard deviation σ_{a0} of the plane coefficient is: $\sigma_{a0} = 1 \cdot \sqrt{0.00068} = 0.0260m$

The resulting vector of residuals is:

$$\begin{bmatrix} e_1 \\ e_2 \\ \vdots \\ e_m \end{bmatrix} = \begin{bmatrix} -0.0018 \\ 0.0007 \\ 0.0012 \\ -0.0014 \end{bmatrix}$$

RMSE equals $0.0013m$.

7.3 Methodology to estimate the grid point height precision

The background information on DTM quality given in Section 7.1 and the interpolation method Moving Least Squares (MLS) described in Section 7.2 are here combined to define the methodology to calculate the grid point heights and estimate their precision using the laser L-MMS StreetMapper data. Case studies are presented at the end to enable better understanding of the described method.

In the following paragraphs the processing steps to calculate the five influencing factors (see Section 7.1.2) and some other side results of MLS (as e.g. slope) are described in detail. In the last paragraph three case studies are analysed to illustrate how the described method actually works.

Attributes of laser L-MMS dataset. A grid of $1 \times 1m$ is laid over the terrain laser points. The geometric attributes of terrain laser points, discussed already in Chapter 5, are analyzed per grid cell. The range R and incidence angle α influence first on the number of points n per grid cell and secondly on the geometrical precision $\sigma_{Zi,\delta R}$ through the range error δR (see the paragraphs below).

Number of points (FD1). The points falling within each grid cell are counted and this integer number n is then used as a measure for point density (FD1). It indicates how well an area is sampled. The number of points n (FD1) used in Moving Least Squares (MLS) to define a plane, influences the reliability of the MLS results. When more terrain laser points are employed in the plane computation, random errors can be eliminated and the precision of plane coefficients is improved.

Standard deviation of terrain laser point heights (FD2). The standard deviation σ_{Zi} of terrain laser point heights depends on the L-MMS measurement errors, i.e. on the measuring precision $\sigma_{Zi,m}$ as computed in Section 5.3.2, and the instantaneous scanning geometry, i.e. the geometrical precision $\sigma_{Zi,\delta R}$ as computed in Section 5.3.2. The values $\sigma^2_{Zi,m}$ and $\sigma^2_{Zi,\delta R}$ are summed up to calculate the precision of laser point height σ_{Zi} (see Eq. 5.10). The variances σ^2_{Zi} are used to determine the diagonal elements of the observation variance matrix Σ_{yy}. Its inverse Σ^{-1}_{yy} directly enters the MLS adjustment as the weight matrix W_{yy}, because the reference variance σ^2_0 is taken equal to one (see Eq. 7.4). This way the bigger weights are assigned to observations that have smaller standard deviations (are more precise). Thus, they influence stronger on the least squares solution and a smaller standard deviation of plane coefficient σ_{a0} is expected.

Slope. The terrain slope is one of the morphologic terrain parameters, which is here calculated to indicate the morphologic variation of the terrain. In this research the term slope refers to a gradient and is defined as in Eq. 7.18, if the surface function is as written in Eq. 7.17.

$$z = f(x, y) \tag{7.17}$$

$$\begin{aligned} Slope_x &= \frac{df}{dx} = f_x \\ Slope_y &= \frac{df}{dy} = f_y \end{aligned} \tag{7.18}$$

The plane coefficients a_0, a_1 and a_2 computed for every grid cell, define the surface function in Eq. 7.17. The coefficient a_1 and a_2 presents the gradient in x-direction and y-direction respectively (see Fig. 7.1). The average slope is then computed as given in Eq. 7.19.

$$Slope = \tan \nu = \sqrt{a_1^2 + a_2^2} \tag{7.19}$$

In angular units, the slope defines the angle ν between the modeled terrain surface and the horizontal plain in the grid point.

Terrain roughness (FR) and random-to-grid interpolation (FI). The value of the Root Mean Square Error (RMSE) computed by Eq. 7.16 tells how well the tilted plane model fits to the terrain laser points. Smaller RMSE means higher confidence in the grid point height estimation. Therefore the RMSE is considered as a measure of the terrain surface roughness (FR) with respect to the plane modeled by the chosen random-to-grid MLS interpolation (FI). The error in grid point estimation due to the terrain roughness is denoted by σ_e and defined as in Eq. 7.20:

$$\sigma_e = RMSE \tag{7.20}$$

Quality of original laser data (FD) and random-to-grid interpolation (FI). In contrast to the RMSE or standard deviation σ_e, the standard deviation of the plane coefficient σ_{a0} (Eq. 7.14) does not change with the deviations of the laser points from the plane. In other words σ_{a0} does not incorporate the roughness. The size of σ_{a0} depends just on the a-priori quality of the terrain laser point cloud (FD), which propagate through the chosen

random-to-grid MLS interpolation (FI). The influencing factors FD1 and FD2 are already described above. In the case studies below an example of joined FD influence is presented.

Final precision of grid point heights. According to the described characteristics of influencing factors and considering the theoretical model discussed in Section 7.1.3 the final standard deviation of the grid point heights σ_{DTM} is defined as given in Eq. 7.21:

$$\sigma_{DTM} = \sqrt{\sigma_{a0}^2 + \sigma_e^2} \tag{7.21}$$

The grid point height precision σ_{DTM} results from two independent and uncorrelated components, which are in this report called data quality component σ_{a0} and terrain roughness component σ_e.

In the following two case studies are presented, where the precision of the grid points is estimated following the method explained above. The aim is to show all influencing factors and components participating in the DTM quality computation on a real case or terrain laser points.

Case study 1: Influence of a-priory precision (FD2) and roughness (FR, IF). Two grid cells of a size $1\times1m$ are taken, which include almost the same number of terrain laser points n (FD1), i.e. 22 and 23 points. On the other hand, the standard deviation of those terrain laser points σ_{Zi} (FD2) and the standard deviation of terrain roughness σ_e (FR, FI) for these two grid cells are different. In Fig. 7.2 and Fig. 7.3 the input data and results of MLS are presented. Note, the scale of elevation axis is not the same in those two figures. The grid cell presented in Fig. 7.2 lies on the beach and has small slope, i.e. ν is around 1° (beach case). The grid cell presented in Fig. 7.2 lies in the dunes and has therefore bigger slope; ν equals 34° (dune case).

The input data are the terrain laser points (black dots), given by X,Y and Z coordinates and their height precision σ_{Zi} (sum of the blue and the pink error bar in Fig. 7.2(b) and Fig. 7.3(b)). The blue error bar presents the measuring precision (see Section 5.3.1) and the pink error bar the geometrical precision (see Section 5.3.2). The standard deviation σ_{Zi} propagates through the MLS and results in the data quality component σ_{a0}. It is indicated by the red error bar and also numerically written in Fig. 7.2(b) and Fig. 7.3(b). In the first case height precision σ_{Zi} is good for most of the terrain point, therefore σ_{a0}) is small.

The vertical distances from the terrain laser points to the modeled plane are indicated in Fig. 7.2(a) and Fig. 7.3(a) by red lines. In the case shown in Fig. 7.2 those residuals are small, therefore also the resulting terrain roughness component σ_e is very small. It is indicated by the green error bar drawn on the place of the grid point. Besides, its numerical value is written in Fig. 7.2(b) and Fig. 7.3(b). In the second case the terrain roughness σ_e

is much higher, which is a consequence of the more rough and overgrown dune surface.

The sum of data quality component σ_{a0}) and terrain roughness component σ_e (see Eq. 7.21) result in standard deviation σ_{DTM} of the grid point. Its value is written in Fig. 7.2(b) and Fig. 7.3(b). It is smaller in the first beach case, i.e. $0.75cm$, than in the second dune case, where it reaches $3.3cm$. From those results one can predict the spatial variability of the grid point precision.

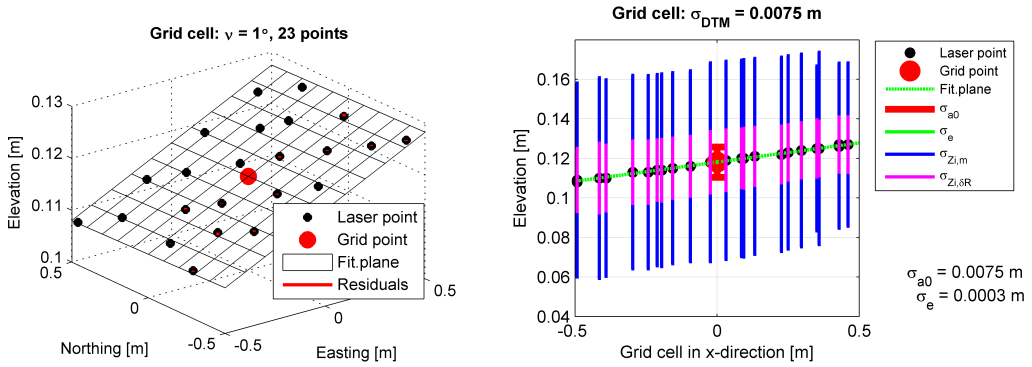

(a) 3D plot of points, plane and residuals.

(b) Profile in x-direction of points, plane and standard deviations.

Figure 7.2: Terrain laser points, the grid cell and the fitted plane visualized with influencing factors. A good case of small σ_{Zi} (DF1) and σ_e (FR).

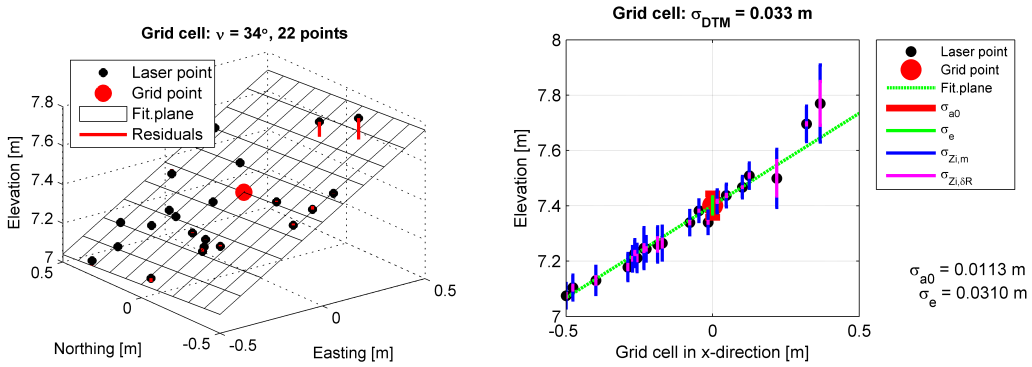

(a) 3D plot of points, plane and residuals.

(b) Profile in x-direction of points, plane and standard deviations.

Figure 7.3: Terrain laser points, the grid cell and the fitted plane visualized with influencing factors. A bad case of big σ_{Zi} (DF1) and σ_e (FR).

Case study 2: Influence of point distribution (FD3). In Fig. 7.4 another beach case is shown. The slope ν, height precision σ_{Zi} of the terrain laser points (FD2) and the

number of points (FD1) is similar those in Fig. 7.2. Due to the position of the terrain laser points (black dots) on one side of the grid point (red dot), the least squares solution is not good. Therefore, the value of data quality component σ_{a0} is much bigger in comparison with the value written in Fig. 7.2(b). The resulting grid point height precision σ_{DTM} is then also larger and is $2.02cm$.

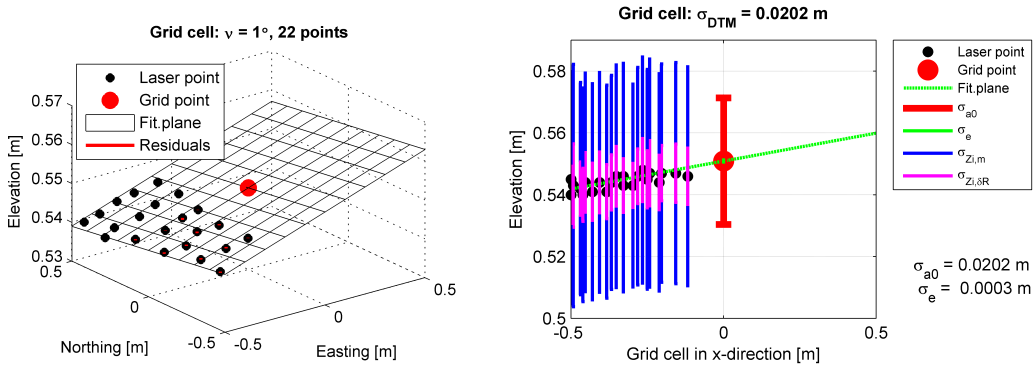

(a) 3D plot of points, plane and residuals.

(b) Profile in x-direction of points, plane and standard deviations.

Figure 7.4: Terrain laser points, the grid cell and the fitted plane visualized with influencing factors. A case of bad laser point distribution (FD3).

Besides the influence of factors FD2, FD3, FR and FI, the number of points (FD1) strongly influences the final grid point precision. More points in general results in better grid point height precision σ_{DTM}. For more detailed interpretation see the results and discussion in Chapter 8.

7.4 Summary

Due to the importance of the DTM information, many researches and books were already written on this topic, i.e. filtering the data, constructing the surface and estimating its quality. In this research the main focus is to assess the quality of the DTM generated from laser L-MMS data. Information obtained in the literature study is adapted to the data available in this research. The factors influencing the laser L-MMS DTM quality investigated here are: ~~the number of terrain points n, height precision of individual terrain point, terrain point distribution, the terrain roughness and interpolation method. These are influencing the final result, i.e. the grid point height precision, through the linear mathematical model. That is, the methodology of the DTM quality evaluation is based on the weighted Moving Least Squares (MLS) adjustment of a tilted plane using the terrain laser points. It must be mentioned, that MLS output is strictly speaking the precision of the grid point. In other words, the systematic errors are assumed to be zero.~~ Besides, this interpolation is performed for the grid cells including more then three terrain laser points. The DTM quality can be then shown very detailed for each of those grid cells.

The remaining grid cells, which have non or less than three terrain laser points, should be appropriately marked. The visualization and discussion on actual L-MMS DTM interpolation and quality estimation results are presented in Chapter 8.

Chapter 8

Results of laser L-MMS DTM evaluation

In this chapter the laser L-MMS DTM is computed from the StreetMapper dataset, acquired during the pilot project Egmond aan Zee. In sections 8.1 and 8.2 terrain laser points of the cross-strip in block 1 (test area) are used. The main objective in these two sections is, to estimate the StreetMapper DTM quality, following the methodology explained in Section 7.3. First in Section 8.1 the attributes of the L-MMS dataset are presented per grid cell. Those attributes indirectly or directly influence the DTM computation and its quality (see Section 7.1.2). The results of Moving Least Squares (MLS), which is the method used in this research to interpolate the grid point heights and estimate their precision, are presented and discussed in Section 8.2. The findings on the DTM quality are implemented in constructing an optimal measurement set-up. That is, in Section 8.3 few suggestions are given for the acquisition mission and the DTM processing that might improve the laser L-MMS DTM quality. In Section 8.4 all L-MMS points acquired during pilot project Egmond aan Zee are taken into account and are compared to another dataset i.e. to the Airborne Laser Scanning (ALS) point cloud. Because the ALS data are not acquired at the same time as the L-MMS data, it can not be used for the validation of the L-MMS point cloud. However, an initial comparison of these two datasets is made. Finally, in Section 8.5 the main results on the DTM evaluation are outlined.

The Easting-Northing figures in this chapter are visualized as a raster image, where each pixel is a grid cell of size $1 \times 1m$. Their values per grid cell are compared and analyzed using robust statistics (see Section 5.1.2). In the first two sections the Easting-Northing figures include also the positions of L-MMS trajectories. The solid lines show the trajectories driven from the south to the north and the dashed lines the trajectories driven in opposite direction.

8.1 Attributes of laser L-MMS dataset

In this section the attributes of laser L-MMS dataset that indirectly (geometric attributes) and directly (FD, see Section 7.1.2) influence on the DTM computation and its quality are presented. In Section 8.1.1 first a general discussion about results and an overview of attribute values is given. The geometric attributes as range R and incidence angle α indirectly influence the DTM through the number of points n acquired per square meter, i.e. point density (FD1). Results of range, incidence angle and point density are shown in Section 8.1.2. In Section 8.1.3 the second influencing factor from the group "quality of the original laser point cloud (FD)", i.e the height precision $\overline{\sigma}_{Zi}$ of individual terrain L-MMS points (FD2), is discussed.

8.1.1 Overview of attributes and their results per grid cell

The methods to compute the L-MMS laser point attributes such as range, incidence angle and height precision of individual laser point heights are presented already in Chapter 5. There, the attribute values are shown per laser point belonging to a small part of one driveline. In this section, the attributes are presented for the whole test area, i.e. a cross-strip in block 1, in order to discuss their influence the derived DTM. The test area of $213 \times 101m$ size is sampled by more than a million points. To be able to visualize attribute values in Matlab and to compare them with other influencing factors (e.g. number of points, slope), the average of attribute values assigned to terrain points is computed for each grid cell. Those variables are denoted with a bar above the attribute sign. Their statistics are presented in Table 8.1.

Table 8.1: Statistics of average attribute values computed per grid cell of the test area.

	$\overline{Z}$ [m]	$\overline{R}$ [m]	$\overline{\alpha}$ [°]	n	$\overline{\sigma}_{Zi,m}$ [m]	$\overline{\sigma}_{Zi,\delta R}$ [m]	$\overline{\sigma}_{Zi}$ [m]
min	-0.63	5.02	5.4	1	0.026	0.0000	0.026
max	22.01	177	89.8	333	0.16	4.49	32.6
med	1.28	11.23	74.6	53	0.031	0.011	0.034
rstd	1.39	6.51	6.4	67	0.0072	0.0045	0.0098

The median of the average attribute values, which is computed for each grid cell, is taken as a representative attribute value of the test area. Half of the grid cells have an average height $\overline{Z}$ below $1.28m$. The median range $\overline{R}$ from the laser scanner to grid cells is around $11m$. The median incidence angle per grid cell $\overline{\alpha}$ is around 75°. About 50% of the grid cells contain more than 53 terrain points. The median measuring precision $\overline{\sigma}_{Zi,m}$ per grid cell is $3.1cm$ and the median geometrical precision $\overline{\sigma}_{Zi,\delta R}$ is $1.1cm$. Finally, the median height precision $\overline{\sigma}_{Zi}$ per grid cell is $3.4cm$.

In Fig. 8.1 the mean heights of terrain laser points per grid cell are shown. In this DTM representation the grid point height equals to a constant coefficient ($Z = a_0$, where a_0 is the mean height) and the local surface is represented by a horizontal plane of $1 \times 1m$ size. Besides, in Fig. 8.1 bottom, a typical profile of the Dutch beach, as can be acquired by a the L-MMS system, is shown corresponding to the grey line in Fig. 8.1 top. The data cover most of the flat beach and part of the dunes.

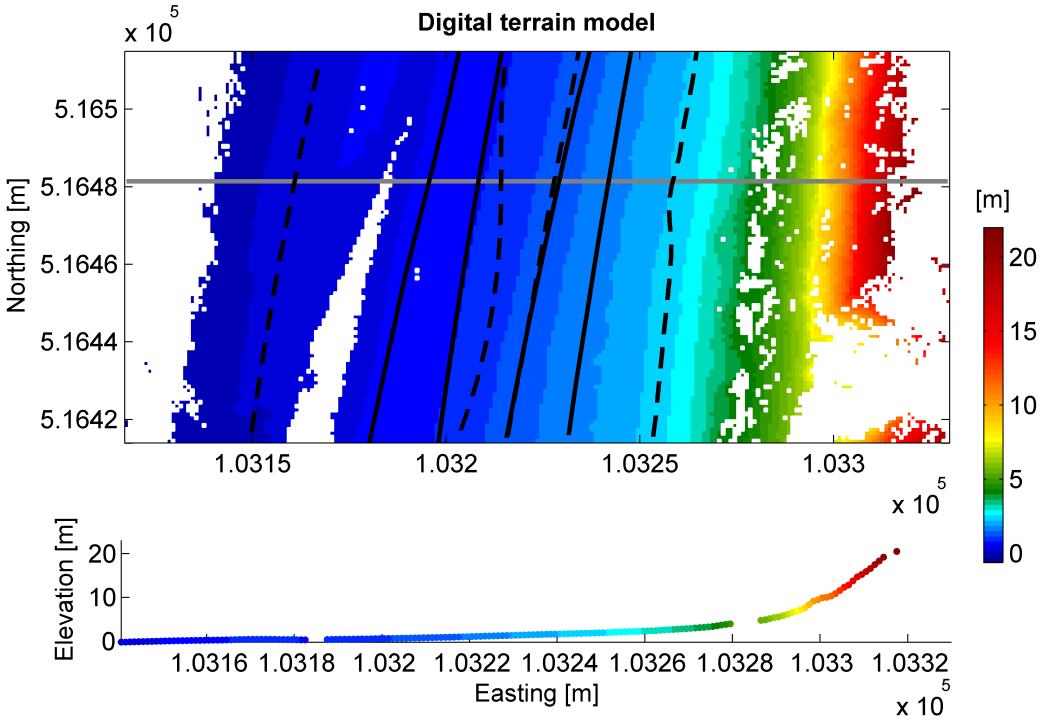

Figure 8.1: The DTM of mean terrain point heights and the typical profile of this DTM.

8.1.2 Attributes of scanning geometry and number of terrain points (FD1)

The grid cells in Fig. 8.2(a) and Fig. 8.2(b) are color-coded by the mean range $\overline{R}$ and mean incidence angle $\overline{\alpha}$, respectively. Intuitively, grid cells close to the trajectory (on driving path) have the smallest mean ranges i.e. from $5m$ to $9m$ and mean incidence angles around $72°$. When the range increases on the flat horizontal beach, also the incidence angle increases (see Fig. 3.4). However, grid cells further away in the dune area have a mean range bigger than $50m$ (colored reddish and black in Fig. 8.2(a)), but small mean incidence angle, i.e below $70°$. The reason is the sloped terrain, which improves the scanning geometry (smaller α).

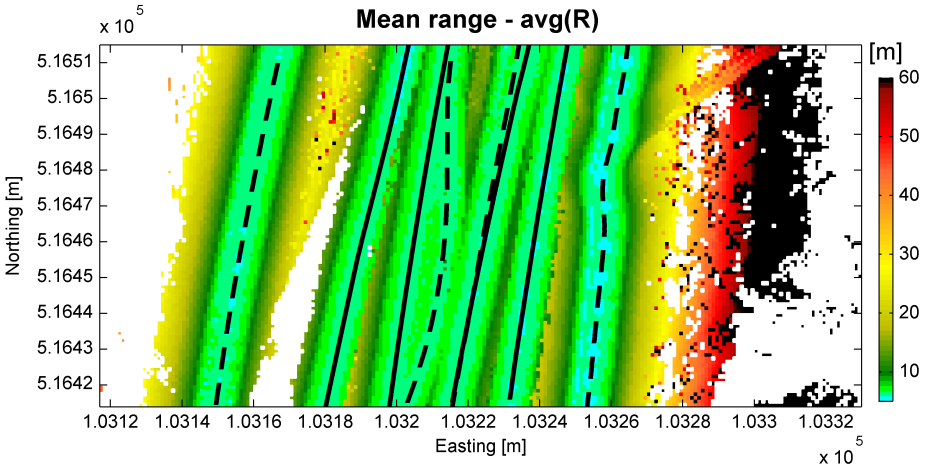

(a) Mean range $\overline{R}$ of terrain points laying within the grid cell.

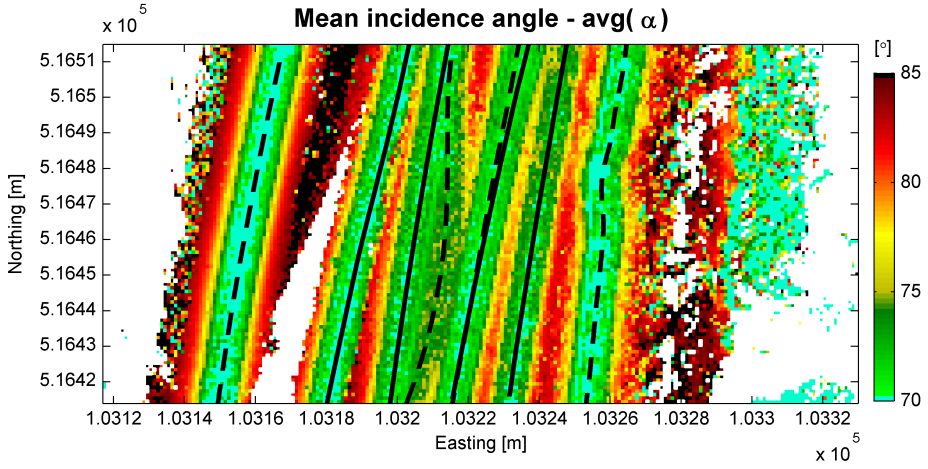

(b) Mean incidence angle $\overline{\alpha}$ of terrain points laying within the grid cell.

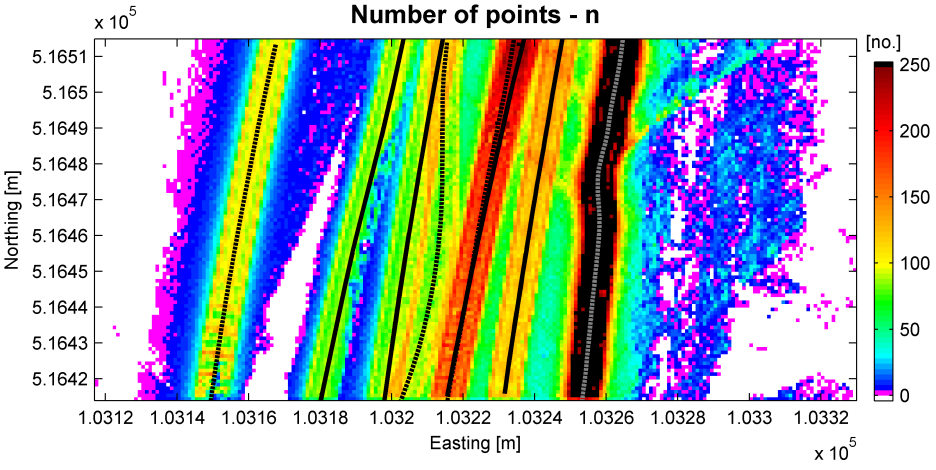

(c) Number of points n per $1{\times}1m$ grid cell. Grid cells that contain less than 3 terrain points are colored pink.

Figure 8.2: The influence of the scanning geometry, given by the range and incidence angle, on the point density.

The influence of the range and incidence angle on the number of points per square meter i.e. on the point density (FD1) is shown in Fig. 8.3. Smaller ranges and incidence angles (i.e. relatively good scanning geometry) in general results in a higher point density. As seen in Fig. 8.3(a), a point density higher than 100 points/m^2 occurs when the range is smaller than $20m$. The upper part of the plot in Fig. 8.3(b), i.e. at mean incidence angles close to its median 74.6°, shows slight negative correlation between the incidence angle and number of points. Thus, the smaller the incidence angle, the bigger the number of terrain laser points. Higher point densities around 330 points/m^2 are achieved, when the incidence angle is around 70°. The spatial correlation between scanning geometry attributes and point density can be observed in Fig. 8.2.

Fig. 8.2(c) shows the number of terrain laser points per grid cell. The grid cells on the driving path, which have good scanning geometry, have the highest point density. The number of points on the ground drops rapidly when the distance to the sensor increases. However, on the sloped dune area, which has bigger mean ranges, the number of points per grid cell increases as well. The reason is smaller incidence angle.

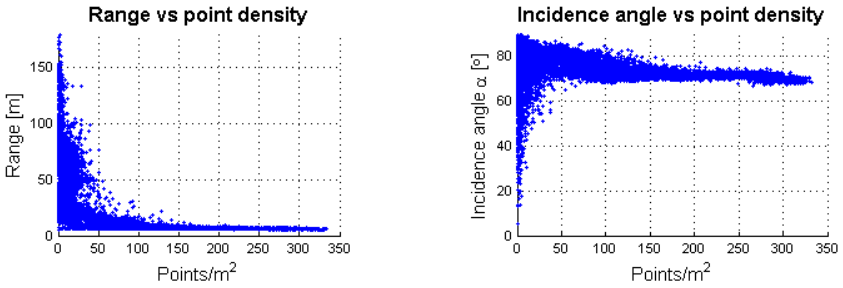

(a) Range vs. point density

(b) Incidence angle vs. point density

Figure 8.3: Correlation between the scanning geometry attributes and the point density.

Besides the influence of scanning geometry, the number of points n differs a lot over the acquisition area, because the driving speeds of the vehicle are changing among different drive-lines. The effect is best observed in areas close to trajectories. For example the grid cells on the driving path of drive-line 5 (DL5) have more than 250 points (black color); see the most right drive-line in Fig. 8.2(c). On the contrary the grid cells on the driving path of drive-line 11 (DL11) have approximately 100 terrain points; see the most left drive-line in Fig. 8.2(c). In case of drive-line DL5 the speed is approximately 7 km/h and in case of drive-line DL11 around 32 km/h. The second reason for varying point densities among drive-lines is that in some cases (drive-lines) not all scanners mounted on StreetMapper were switched on.

In Fig. 8.2(c) one can see that the areas behind the pre-dunes and dunes cannot be observed from the scanners mounted on the car. These data gaps are a consequence of

the so-called shadow effect. Grid cells without points occur also on the beach close to the waterline (in the lower left part of Fig. 8.2(c), around X=103160m). The reason might be that the area was covered with water during acquisition and therefore could not be observed by the laser system. Laser light often reflects specular or mirror-like on the water surface.

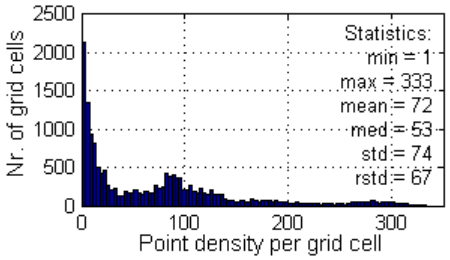

Figure 8.4: Influencing factor (FD1) number of terrain laser points n.

In Fig. 8.4 the histogram shows the distribution of the point density per square meter, i.e. per grid cell. Two distinct peaks can be observed; one around zero and another at around 85 points per square meter. Half of the grid cells contain less than 53 terrain points, however the average number of points within a grid cell is high and equals 72.

8.1.3 Precision of laser point heights (FD2)

In this section the results of the influencing factor FD2, which stands for the height precision of individual terrain laser points, is presented. The height precision of each terrain laser point is calculated using the theoretical model of error propagation, as described in Section 5.3. It has two components: (i) measuring precision $\overline{\sigma}_{Zi,m}$, which is derived from the a-priori known L-MMS measurement errors and (ii) geometrical precision $\overline{\sigma}_{Zi,\delta R}$, which incorporates the height error due to the non-perpendicular scanning geometry. In Table 8.1 the statistics of average standard deviation $\overline{\sigma}_{Zi,m}$ and $\overline{\sigma}_{Zi,\delta R}$ are written. Although the maximum value of average geometrical precision $\overline{\sigma}_{Zi,\delta R}$ is very high, i.e. 4.49m, due to an incidence angle close to 90°, its median is small, i.e. 1.1cm. It is much lower than the median of average measuring precision $\overline{\sigma}_{Zi,m}$, which is 3.1cm. On the other hand the values of measuring precision $\sigma_{Zi,m}$ differ less within the test area than the geometrical precision $\sigma_{Zi,\delta R}$. This is indicated by the robust standard deviation, which is 0.45cm for the average measuring precision $\overline{\sigma}_{Zi,m}$ and 0.72cm for the average geometrical precision $\overline{\sigma}_{Zi,\delta R}$.

In Fig. 8.5 the average standard deviations of heights per grid cell are shown. Grid cells that have this value close the median of the average standard deviation of heights, which is given in Table 8.1, are colored green. The black colored grid cells in Fig. 8.5(a) have an average measuring precision $\overline{\sigma}_{Zi,m}$ bigger than 4cm. The black colored grid cells in Fig. 8.5(b) have an average geometrical precision $\overline{\sigma}_{Zi,\delta R}$ bigger than 2.6cm. In both cases those grid cells represent about 10% of the grid cells within the test area. The values of $\overline{\sigma}_{Zi,m}$ and $\overline{\sigma}_{Zi,\delta R}$ are smallest on the driving path, because the scanning geometry is best,

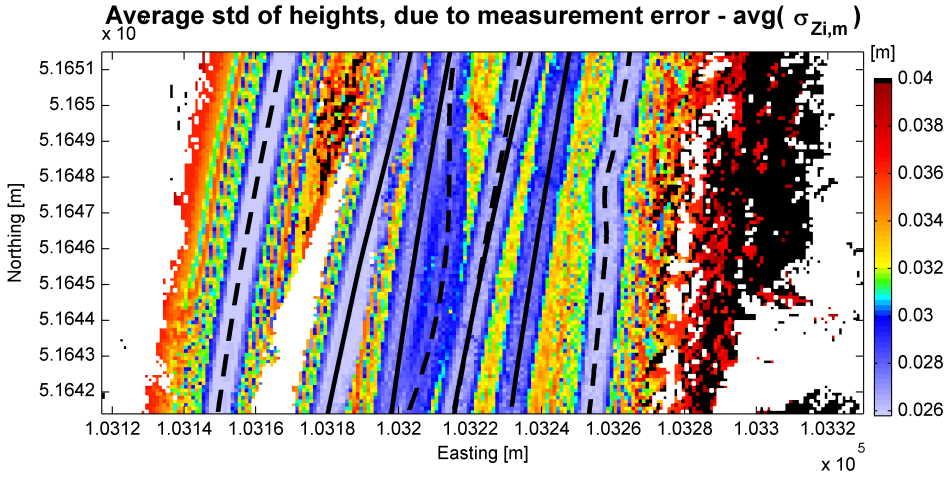

(a) Average measuring precision $\overline{\sigma}_{Zi,m}$.

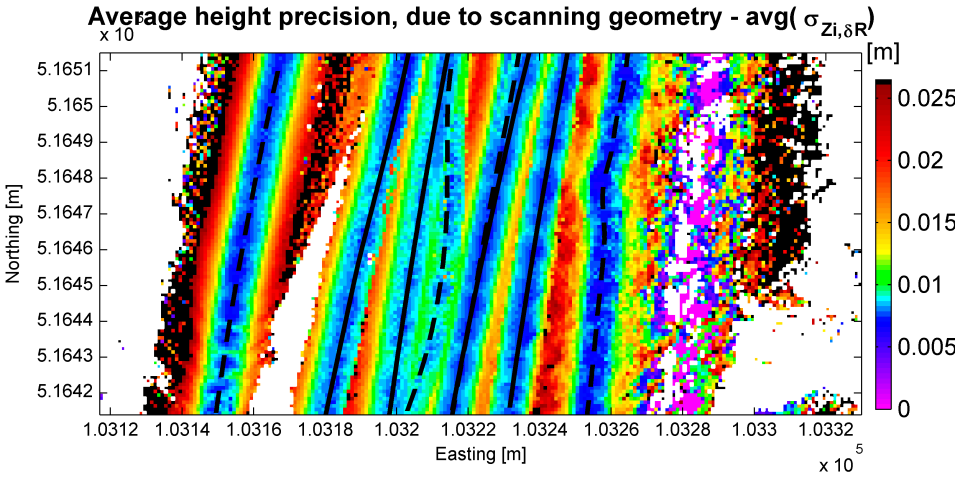

(b) Average geometrical precision $\overline{\sigma}_{Zi,\delta R}$.

Figure 8.5: Average standard deviations of terrain point heights computed per $1\times1m$ grid cell.

i.e. small ranges and vertical angles.

Fig. 8.5(a) shows that the average measuring precision $\overline{\sigma}_{Zi,m}$ for grid cells on the driving path is below $3cm$. the largest contributor to the measuring precision is the GPS error (see Fig. 4.8). Further away from the trajectory, the average measuring precision $\overline{\sigma}_{Zi,m}$ mostly increases and is the highest, i.e. more then $3.65cm$, in the dune area.

In Fig. 8.5(b) one can observe that the pattern of the average geometrical precision $\overline{\sigma}_{Zi,\delta R}$ partly follows the one in Fig. 8.2(a) and Fig. 8.2(b). The grid cells on the driving path have an average geometrical precision $\overline{\sigma}_{Zi,\delta R}$ below $0.008cm$, see the dark blue ar-

eas. The grid cells with an average geometrical precision $\overline{\sigma}_{Zi,\delta R}$ bigger than $2.65cm$ (black color) lie in the dune area or at the edges of the drive-lines. In the first case, i.e. black cells in the dune area, the most probable reason is high mean range, which is bigger than $50m$ (see black and red areas in Fig. 8.2(a)). In the case of black cells at the edges of the most left drive-line in Fig. 8.5(b) the reason is a high incidence angle (see black areas in Fig. 8.2(b)). The areas colored pink in Fig. 8.5(b) indicate an average geometrical precision $\overline{\sigma}_{Zi,\delta R}$ close to zero, however the mean incidence angle here is big, i.e. more than 84°. This pattern occurs due to the error propagation model based on the geo-referencing formula (see Eq. 4.9). That is, the vertical error computed by Eq. 4.9c is almost zero, because the scanning angle is exactly 90°.
High spatial variability of the average geometrical precision $\sigma_{Zi,\delta R}$ on the edges of the most left drive-line and in the dune area is a consequence of locally changing incidence angle.

8.2 Moving Least Squares DTM analysis

In this section the results of the StreetMapper DTM interpolation and quality estimation are presented. The StreetMapper sub-dataset employed in the DTM computations is the same as the one used in Section 8.1, i.e. the terrain laser points of the cross-strip in block 1. The method used in this research is based on the Moving Least Squares (MLS) adjustment as described in Section 7.3. The MLS adjustment of a plane is only possible, if a grid cell contains more than 3 terrain points. As a consequence 11% of the grid cells, colored pink in Fig. 8.2(c), do not enter the MLS computation. The statistics of the factors FD1 and FD2, which directly influence the DTM quality, are computed again for the remaining 89% (see Table 8.2). Besides, an overview of the results from the MLS is given in Table 8.2. Robust statistics (see Section 5.1.2) are used to compare the values of different variables.

Table 8.2: Statistics of the values obtained in Moving Least Squares.

	n (FD1)	$\overline{\sigma}_{Zi}$ (FD2) [m]	Z_{MLS} [m]	ν [°]	σ_{a0} [m]	σ_e [m]	σ_{DTM} [m]
min	4	0.026	-0.19	0.034	0.0015	0.0000	0.0018
max	333	0.85	21.88	62.2	2.9	0.1001	2.9
med	69	0.033	1.25	1.6	0.0042	0.0008	0.0047
rstd	76	0.0080	1.28	0.92	0.0030	0.0006	0.0030

The interpolated height Z_{MLS} of the grid points and the terrain slope ν are presented in Section 8.2.1. The two components employed in the final DTM quality computation, namely the data quality component σ_{a0} and the terrain roughness component σ_e, are discussed in Section 8.2.2. Both components depend on the chosen interpolation method, i.e. fitting a tilted plane by least squares. Finally, in Section 8.2.3 the grid point height

quality σ_{DTM} is shown.

8.2.1 Interpolated heights and terrain slope

In this section the side results of the DTM quality estimation are presented. The interpolated height of a grid point and the slope of a plane, which is fitted to the terrain points of a grid cell, are derived directly from the plane coefficients; see Eq. 7.8 and 7.19, respectively.

In Fig. 8.6 a 3D surface of the interpolated DTM is shown. In this raster image each pixel represents an $1 \times 1m$ grid cell and the pixel color shows the corresponding grid point height. The grid point elevation is changing from -0.19m up to 22m. The white holes in the DTM are results of the shadow-effect (white holes in green area) and most probably of the presence of water-bodies on the beach (white holes in blue area).

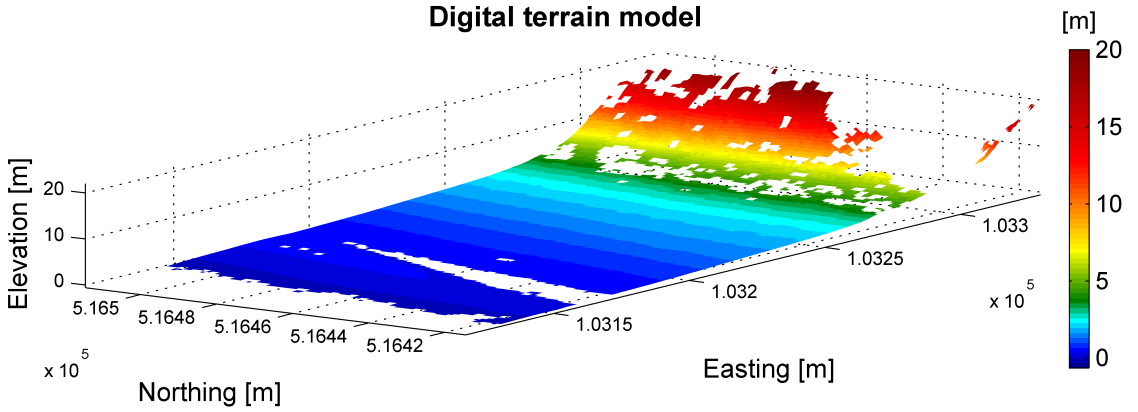

Figure 8.6: Raster image of interpolated DTM grid points visualized in 3D.

The interpolated grid point heights (Fig. 8.6) are compared to the mean heights computed per grid cell (se Fig. 8.1). In Fig. 8.7 the histogram of the differences is shown. The mean of the differences is almost zero and their robust standard deviation is 2.74cm. Those small values prove, that the mean height values are a good first order approximation of the grid point heights in case of a mostly flat acquisition area, like the sandy Dutch beach.

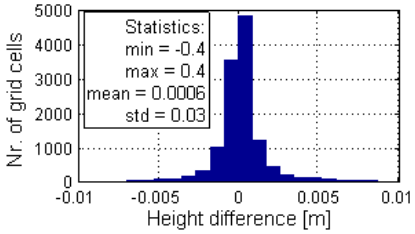

Figure 8.7: Height differences between mean height of terrain points (see Fig. 8.1) and grid point height interpolated from a plane.

The slope is not directly used in the DTM quality computation, but indicates how the terrain is changing. One can expect that the larger the change the more difficult it is to represent the terrain with a linear model. Therefore, Fig. 8.8 shows the slope of the terrain in the test area. The terrain on the lower beach closer to the waterline is mostly flat and is changing smoothly (green color). The upper beach has more rough terrain; light and dark green are interchanging fast. The slope on the beach reaches 5°. In the pre-dune area the slope increases up to 13° (light brown area on the right side of the figure). The steeper dune area has slopes of 20° or more (red colored areas). The maximum slope in the test area is around 62°.

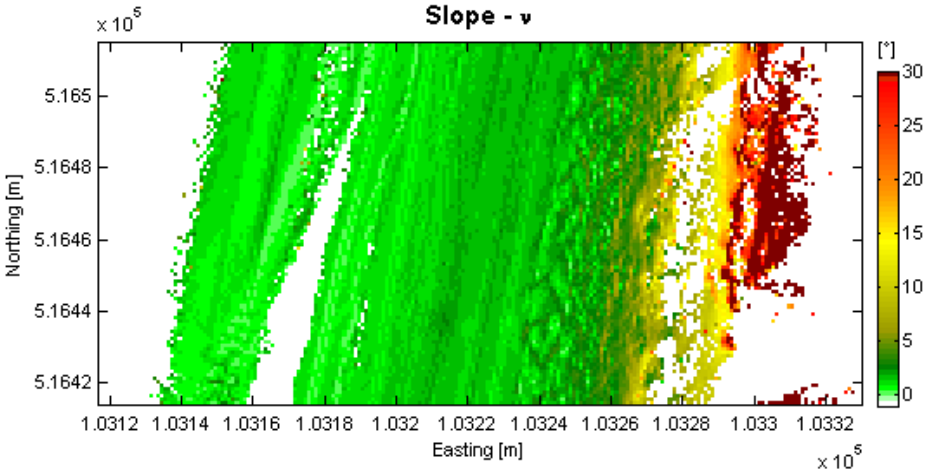

Figure 8.8: The slope ν of a plane, which is fitted to terrain points per grid cell.

8.2.2 Data quality and terrain roughness component

The data quality component is represented by the standard deviation σ_{a0} of a plane coefficient computed as explained in Section 7.2.2. The size of σ_{a0} depends on the quality of the original laser point cloud (FD), i.e. on the number of points n (FD1) and the quality of the individual terrain laser point σ_{Zi} (FD2), which are presented in Section 8.1. Besides, also the distribution of terrain laser points (FD3) influences on the data quality component σ_{a0}, through the mathematical model given in Eq. 7.13. However, this influencing factor is not quantified in this research.

In Fig. 8.9 the relation between the data quality component σ_{a0} (y-axis), the number of points n (x-axis) and the average height precision $\overline{\sigma}_{Zi}$ of terrain laser points (colorbar), is presented. Most of the grid cells with a data quality component σ_{a0} bigger than $4cm$, also have a big average height standard deviation $\overline{\sigma}_{Zi}$, i.e. bigger than $4cm$. Those grid cells include less than 10 terrain laser points (see Fig. 8.9(a)). Besides, the standard deviation σ_{a0} of the plane coefficient a_0 dramatically increases, i.e. up to $3m$ (see Fig. 8.9(a)), due to the terrain laser point distribution (FD3). If for example the terrain points lie almost on a line and the grid point is located aside, the plane is not defined well and the standard deviation of plane coefficient σ_{a0} is large.

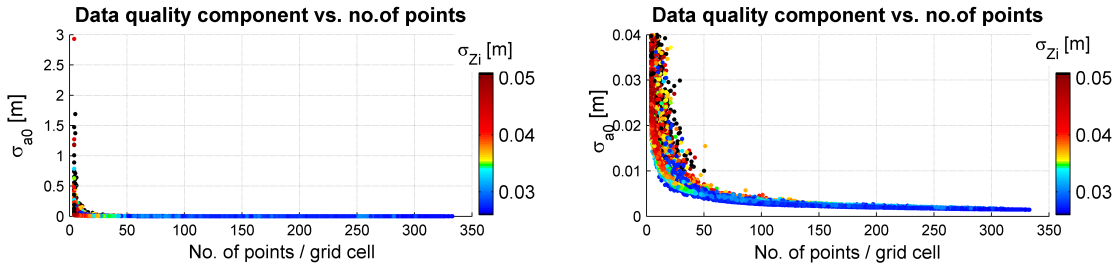

(a) Data quality component σ_{a0} vs. no.points n.

(b) Zoom-in of scatter plot in Fig. 8.9(a).

Figure 8.9: Correlation between the data quality component σ_{a0} and the number n of terrain laser points; color-coded by the standard deviation of the individual terrain laser point.

In Fig. 8.9(b) a zoom-in plot better shows the relation between the data quality component σ_{a0} and the number of points n. When a grid cell includes more than 50 points, the standard deviation σ_{a0} is smaller than $6mm$. Besides, most of those grid cells include terrain points of a good precision, i.e. the average height precision $\overline{\sigma}_{Zi}$ is below $3cm$ (blue color).

The spatial variation of the data quality component σ_{a0} is presented in Fig. 8.10(a). The position of the driving-lines is drawn as in Fig. 8.2 and Fig 8.5. The standard deviation σ_{a0} is smallest, i.e. below $2mm$, within the driving path of drive-line DL5 (light blue strip on the right side of the figure). The main reason is the high number of terrain laser points, which is here more than 250 points (see Fig. 8.2(c)). The green color indicates grid cells, having a standard deviation σ_{a0} around the median, which is $4.2mm$. The black colored points correspond to 10% of the analysed grid cells with a standard deviation σ_{a0} bigger than $2.32cm$. They lie mostly in the dune area and on the edges of the drive-lines.

The second component in Eq. 7.21 for DTM quality computation, is the terrain roughness σ_e. It is represented by the root mean square error (RMSE) of the vertical residuals between terrain laser points and fitted plane. Once the grid size is determined, which is here $1\times1m$, and the functional model to represent the surface is chosen, which is here the tilted plane, σ_e depends mainly on the terrain surface complexity. The quality of the measurements is assumed to be high enough. The spatial variability of the terrain roughness component σ_e is shown in Fig. 8.10(b). This pattern is almost independent of the laser point height precision. However one can observe lines in the direction of trajectories, the pattern better corresponds to the terrain morphology shown in Fig. 8.8. In the pre-dune area, where the slope is changing fast, higher values of the terrain roughness component σ_e occur. 10% of the grid cells, which have a terrain roughness component σ_e bigger than $4.5mm$ (black color), occure mostly in the pre-dune and dune area. Therefore, these parts of the test area are considered more difficult to be modeled with a linear surface of $1\times1m$ size. However, the values are very small; the median of all grid cells within the test area is $0.8mm$.

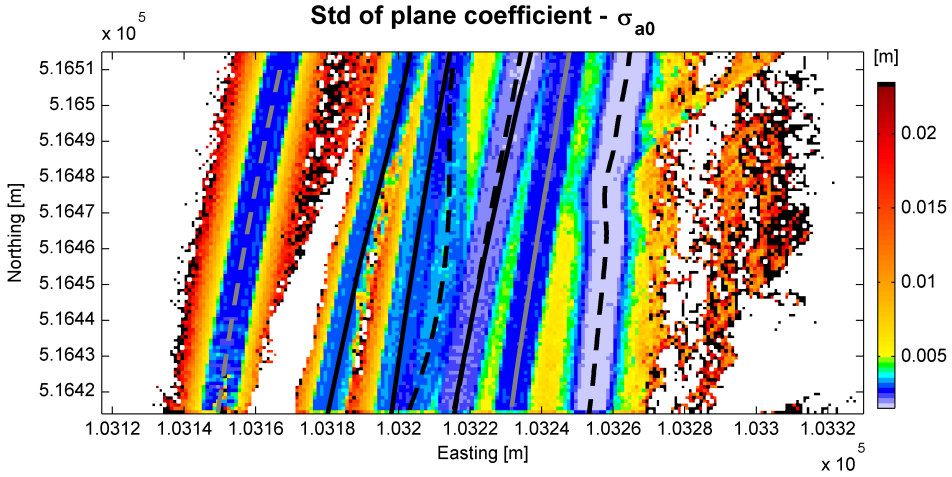

(a) Data quality component σ_{a0}.

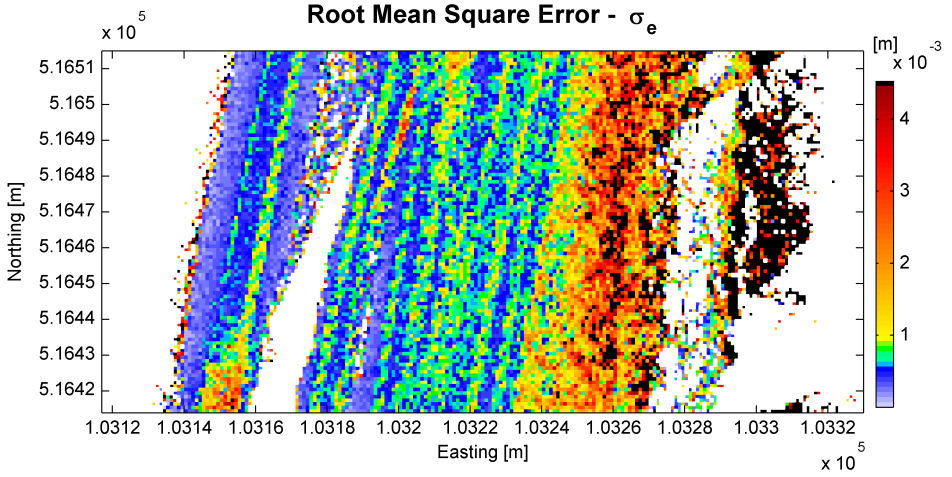

(b) Terrain roughness component σ_e.

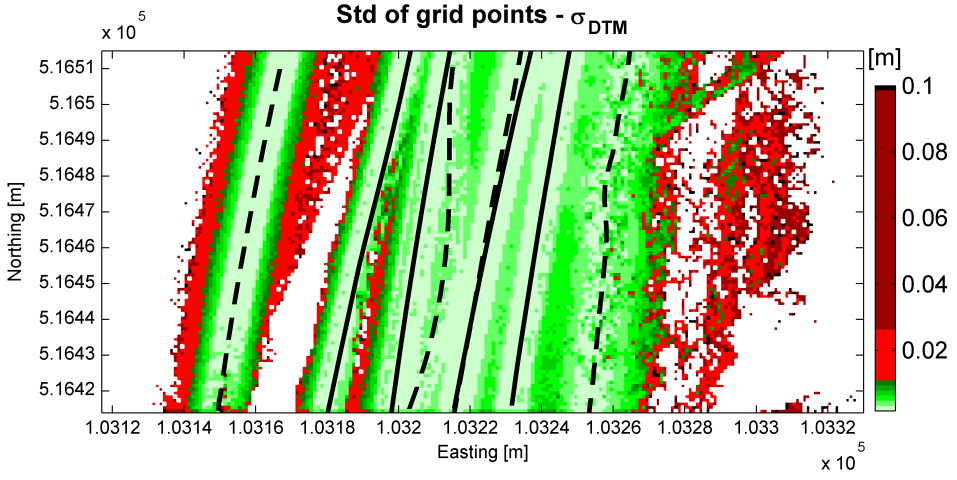

(c) Grid point height precision $\hat{\sigma}_{DTM}$.

Figure 8.10: The two components directly employed in the computation of the grid point height precision and the final grid point height precision. Values are shown per $1\times1m$ grid cell.

8.2.3 Grid point height precision

The standard deviation of grid points σ_{DTM} is finally estimated by Eq. 7.21, employing the data quality component σ_{a0} and the terrain roughness component σ_e. The size of the grid point height precision σ_{DTM} depends mainly on the data quality component σ_{a0}. The terrain roughness σ_e adds just a small part to the total value (see numbers in Table 8.2). The height precision of grid points σ_{DTM} varies between 0.0018 and 2.9m. The average precision of grid points σ_{DTM} equals to 4.7mm, which is more than 7 times better than the precision of the observations σ_{Zi}, which is on average 3.4cm (see Table 8.1).

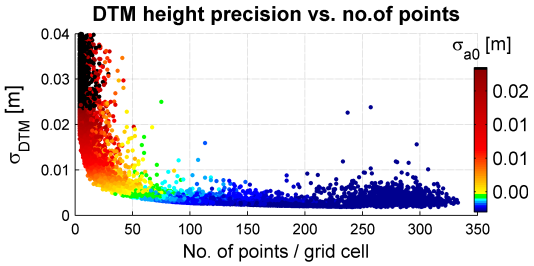

Figure 8.11: Correlation between the grid point height precision σ_{DTM} and the number n of terrain laser points; color-coded by the data quality component σ_{a0}.

As shown in Fig. 8.9 the data quality component σ_{a0} strongly correlates with the number of points n. Almost the same phenomena can be observed in Fig. 8.11. The difference between Fig. 8.9(b) and 8.11 is intuitively the terrain roughness component σ_e. In case of drive-line DL5, which has more than 250 points per square meter on its drive path, the terrain is more rough. Therefore, one can observe the dispersed values of σ_{DTM} for the number of points n more than 250 points. In Fig. 8.11 one can observe, if approximately 50 of more points are included in the grid point computation, that the standard deviation of grid point heights σ_{DTM} drops below 1cm.

In Fig. 8.10(c) the spatial variation of the grid point height precision σ_{DTM} over the test area is shown. The grid cells having a standard deviation σ_{DTM} higher than 2.56cm are colored dark red and black. They represent approximately 10% of all grid cells. Green color shows grid points having a height precision σ_{DTM} smaller than 1cm. Most of the beach area has good DTM quality, which decreases with the distance from the trajectory. For example, the precision at the edges of the drive line DL11 (most left one) decreases and is at some point worse than 2.56cm, mostly due to the number of points n (compare to the dark blue areas in Fig. 8.2(c)). The DTM quality gets worse also in the dune area, due to the low quality of terrain laser points (compare to Fig. 8.10(a)) and high terrain roughness (see Fig. 8.10(b)).

8.3 Measurement set-up for optimal quality of laser L-MMS DTM

In this section the suggestions for the laser L-MMS measurement set-up and the further processing steps to obtain a final result, i.e. laser L-MMS DTM, of a certain quality are given. Those suggestions are based on the analytical and empirical results of the previous sections. The empirical results are obtained from the L-MMS terrain laser points acquired by the StreetMapper system. Therefore, also the suggestions given here presume this or a similar system (see the StreetMepper description in Section 3.4).

DTM precision. The results of the grid point height precision estimation in Section 8.2 show, that the final standard deviation of the DTM depends mostly on the number of terrain points included in the grid point height computation. In other words, the terrain point density is the factor that influences the DTM quality most. In the following few parameters of the measurement set-up that influence the point density are discussed.
If the acquisition area is relatively flat, than the point density drops very fast further away from the trajectory. If the surface is inclined downward, less laser points are acquired, If on the other hand the slope is inclined upward, like in case dunes are scanned from the beach, more laser points are measured. Therefore, to ensure a uniform point density of 50 points or more per square meter, the trajectories should not be more than $40m$ apart. This estimation is deduced from Fig. 8.2.
Intuitively, the point density increases, if the vehicle is moving slower. However, to ensure the efficiency of the acquisition a compromise between a driving speed and the sufficient point density must be found. An analytical computation of the laser point density on the horizontal surface is performed. The specifications and orientation of the Rigel Q120 line laser scanner is considered. Results of the point density for changing driving speed and different distances from the trajectory are shown in Fig. 8.12. To attain a point density of at least 50 points/m^2 at a distance of $10m$ from the trajectory, the driving speed can be maximum 35 km/h.

The second influencing factor that directly propagates to the DTM precision, is the precision of the individual terrain laser points. In this research the height precision of the laser points is estimated by the theoretical models and has two components: the measuring precision and geometrical precision (see Section 5.3). Because the comparison of this theoretical measures with the empirical ones in Section 6.3 reveals big discrepancies, the theoretical models should be first validated. However, the computation of the measuring precision is validated already in some other researches [Glennie, 2007b; Schaer et al., 2007; Barber et al., 2008b] and could be therefore used as an a-priory estimation of laser L-MMS performance. The results on the error budget in Section 4.4 suggest to use a laser scanner with narrow beam-width, i.e. smaller than $2.7mrad$, to efficiently minimize the vertical error of laser points. On the other hand, the theoretical model of the geometrical precision is not verified with ground truth so far. The analytical plots in Fig. 5.5 show, that the

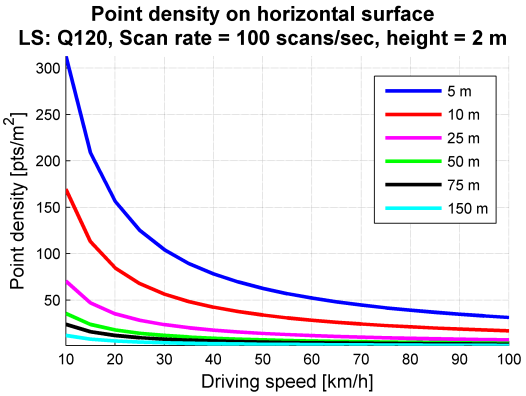

Figure 8.12: Laser point density on a horizontal surface at different ranges from the trajectory and changing the speed of the vehicle. Specifications of the Rigel Q120 line laser scanner is considered.

horizontal and vertical geometrical error increase very fast when the incidence angle is bigger than approximately 78°. This angle is reached already at ranges around $10m$, if a laser scanner is just $2m$ above the ground and if a horizontal surface is scanned. One solution to improve the geometrical precision or at least extend the range of certain vertical error is, to lift the laser scanners higher above the ground. In this case, the influence of the wind and terrain roughness on the position and orientation measurements should be investigated. However, for a land-based system and using a precise INS system, the impact of the INS orientation error on the 3D laser point position is small (see results of the error budget in Section 4.4).

DTM resolution. In this research the DTM resolution is set to $1\times1m$ grid cell size. However, a better grid size should be chosem with respect to the terrain surface characteristics and point density. The morphologic detail in grid cells that have high point density is in case of too big grid cell size lost. Because it is difficult to obtain a uniform point density from the land-based laser system, the suggestion is to adapt the grid cell size to the number of points that are measured in a certain area. For example on the beach, where the point density is typically higher (see Fig. 8.13), the grid cell size could be smaller than $1m$. That is, if assuming 100 terrain points per square meter (compare to Fig. 8.2(c)) and the random errors of those points are small (compare to results in Section 6.3), the grid cell size of $1\times1dm$ is suggested. In this way, smaller features can be mapped for the well sampled beach. In the pre-dune area typically less points can be measured due to the shadow-effect (see Fig. 8.14). Therefore, the grid cell should be bigger than $1m$ in order to include more than 3 terrain points. On the other hand the grid cell size could be $1dm$, but another method should be considered for those grid cell that include less than 3 terrain points. In this way the DTM in the pre-dune area would be more reliable and complete.

DTM completeness. Besides the precision of the grid point heights, one of the DTM quality parameters is also its completeness. A DTM surface can be interpolated also over

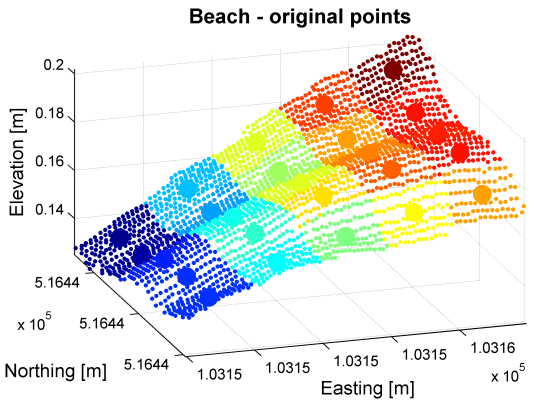

(a) Measured terrain laser points.

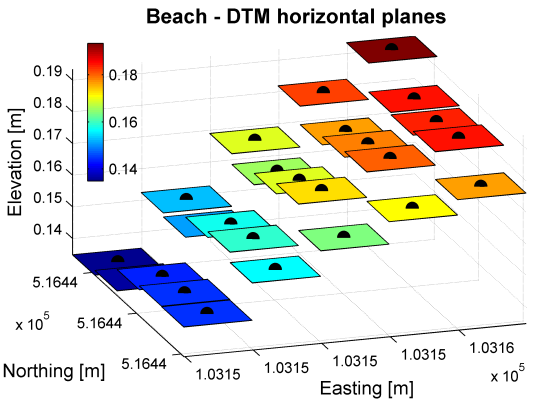

(b) Interpolated grid points and horizontal planes of $1\times1m$ size representing DTM.

Figure 8.13: DTM resolution on the beach.

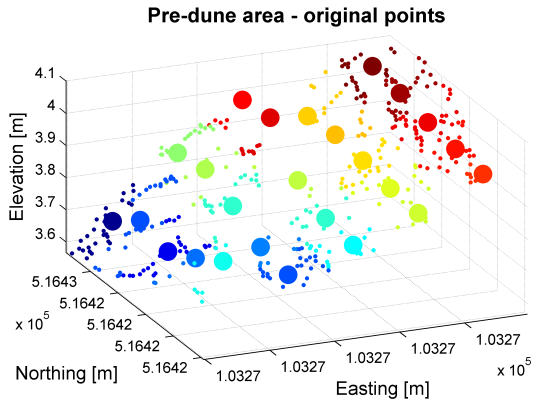

(a) Measured terrain laser points.

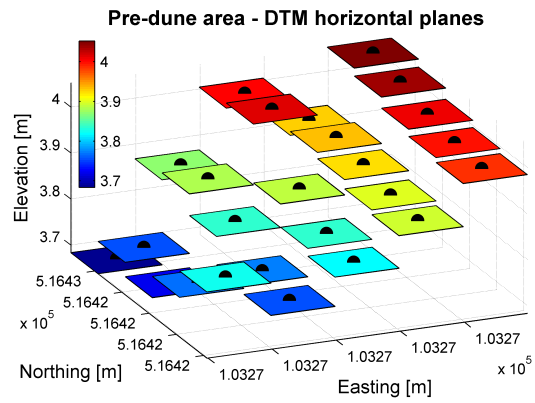

(b) Interpolated grid points and horizontal planes of $1\times1m$ size representing DTM .

Figure 8.14: DTM resolution in the pre-dune area.

areas where no original terrain laser points are measured, but those DTM heights are less reliable. Measuring the Dutch coast, those data voids occur mostly due to the remnant water bodies on the lower beach and due to the shadow effect behind the elevated terrain structures in the pre-dune area. To avoid the impact of water on the beach, the acquisition time must be planned in advance, i.e. the mission should be carried out at low tide, and the usage of a green-light laser scanner should be considered. The impact of shadows reason could be partly alleviated by lifting the laser scanner higher above the ground. As discussed already above, this set-up could also improve the intersecting geometry and in case of a rigid, well designed platform the impact of GPS/INS measurement errors on the 3D positioning should not increase. It is expected that more data could be acquired on the surface behind the pre-dunes structures. The shadow-effect is also reduced if the vehicle drives closer to the dunes.

8.4 Comparison of L-MMS and ALS data

Airborne Laser Scanning (ALS) is an already approved technique for DTM construction. It is gradually replacing the photogrammetrically acquired DTMs, because the laser scanning DTMs feature higher point density. Besides, the procedure to obtain the laser scanning DTM is automated to a higher degree. First commercial projects to acquire terrain data by laser scanning from airborne platforms were performed in Europe by TopScan in 1994/1995 employing an Optech laser scanner [Shan and Toth, 2008]. The Netherlands is one of the few European countries that offers a national-wide airborne laser scan product. The first version of DTM, the so-called Actueel Hoogtebestand Nederland (AHN, The current elevation map of the Netherlands), was completed in 2003 [AHN, 2010]. Already since 1996, the Dutch department of Rijkswaterstaat (RWS) uses airborne laser scanning to acquire JARKUS profiles. The acquisition takes place yearly in the period between March 15 and April 15, after the storm season and before the dune vegetation grows. An ALS dataset from the 2008 mission (acquired on April 25) is available for this research and is used as a first validation of the L-MMS data. However, the validation of the L-MMS DTM is not reliable, since the time interval between acquisitions is seven months.

For the coastal survey on Egmond aan Zee (Midnorth area) in April 2008 an ALS dataset was collected by the German company Toposys GmbH, using the Harrier56 system. Table 8.3 shows some specifications of the system. The ALS data of around 10.5 million points are stored in one ASCII file that has three columns for the 3D coordinates of the laser points (X, Y, Z) and no intensity values. The laser point cloud was filtered already before and includes just terrain points. In [Richardson, 2008] a detailed description is given of the ALS 2008 dataset and results. They state that for the North Holland acquisition area the point density is 9.85 points per square meter and the root mean square error for heights is 7.8 cm.

Table 8.3: The ALS acquisition mission over North Holland with the Harrier56 in April 2008.

Pulse rate	160 KHz effective Measurement rate
Flight height	350 m above Ground
Speed of flight	30m/s
Field of view	60° but only 45° was used for the data processing

RWS made a comparison between the airborne laser data acquired with the Harrier56 system and terrestrial laser data acquired with StreetMapper. The point cloud was examined, namely the absolute altitude position, and transverse profiles have been made to be able to see mutual differences (see Fig. 8.15).
In [Rijkswaterstaat, 2009] it is concluded that small height differences of the terrain surface cause a L-MMS data gap (no altitude information) in shadow areas. Furthermore, measuring not from above but from the side, has an impact on coverage. For example, the obtained L-MMS terrestrial laser data frequently do not indicate the dune top. Sometimes up to 5 meters of the dune is missing [Rijkswaterstaat, 2009].

Figure 8.15: The profile of the beach measured by ALS Harrier56 system in April 2008 (green line) and by L-MMS StreetMapper system in November 2008 (red line) [Rijkswaterstaat, 2009].

In this research the comparison of the L-MMS and ALS dataset is done using a grid of $1 \times 1m$, which is common for both datasets. All available points are used in both cases, thus the L-MMS dataset includes also some points classified as vegetation points. On the contrary, like stated before, the ALS data include just terrain points. For each grid cell and for both datasets the following parameters are calculated:

- point density (n) - the number of laser points per square meter.
- average height ($\overline{Z}_{als}$ and $\overline{Z}_{lmms}$) - the mean Z coordinate of all laser points falling within a grid cell.
- standard deviation of the height values (σ_{Zals} and σ_{Zlmms}) - the standard deviation of the Z coordinate of all laser points falling within the grid cell.

In the following figures (Fig. 8.16 - 8.18) the grid cells are color-coded by those parameters. They show a zoom-in of the acquisition area on the Egmond aan Zee beach with a size of $500 \times 540m$ in X and Y direction, respectively. The area of figures is the same, however the shape and the number of visualized grid cells differ a lot. As stated already before, the coverage of an airborne system is different than of a land-based. The L-MMS data have a data voids behind the elevation differences e.g. pre-dunes due to the shadow effect. Both datasets have data voids (white area) also on the beach due to water pools. The histograms of parameter values are computed for the whole overlapping acquisition area (BL3 - BL8, see Fig. 3.13).

A first review of the data shows an interesting difference between ALS and L-MMS datasets concerning the point density. The spatial distribution of point density values is presented in Fig. 8.16, where different colorbars must be used for ALS and L-MMS data. The point density of L-MMS point cloud differs within a drive-line from 4 up to 1887 points/m^2 (see Fig. 8.16(b)). The maximum L-MMS point density is a result of measuring a vertical object - the crane (see Fig. 2.7(d) and Fig. 3.16(b)). However, considering just the terrain laser points the density is below 300 points/m^2. It is the highest on the driving

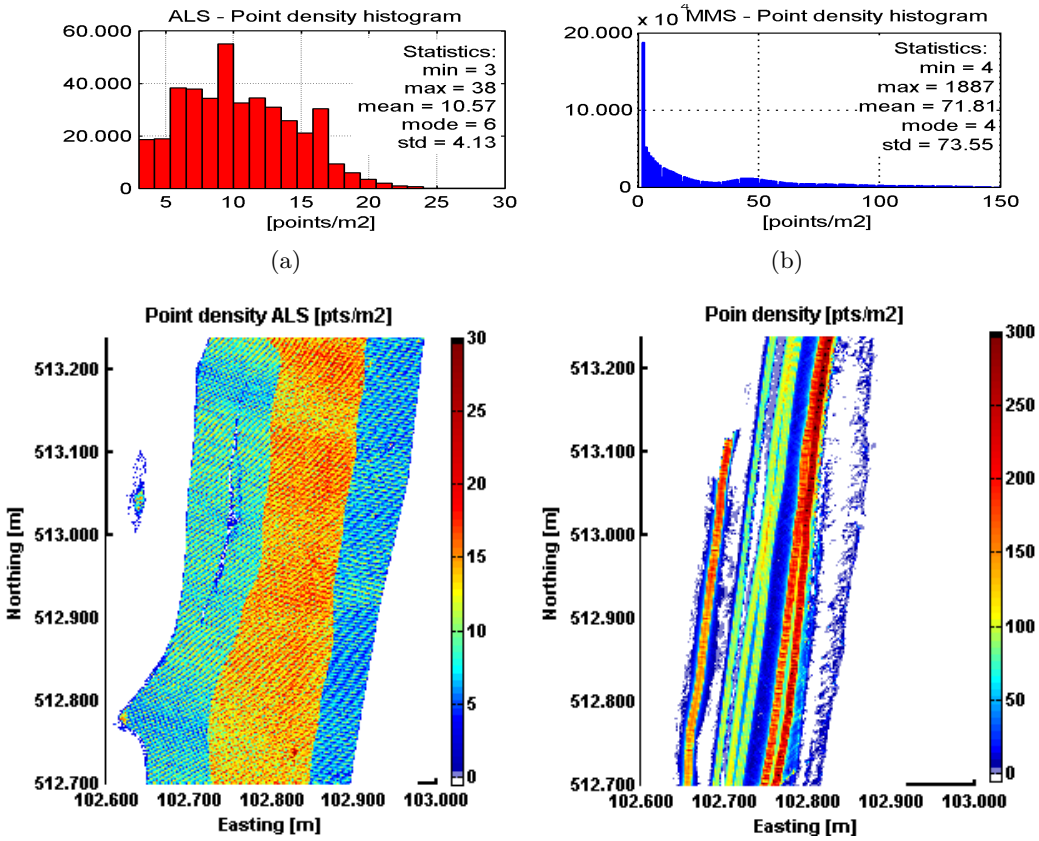

(a) (b)

(c) Point density for ALS dataset. (d) Point density for L-MMS dataset.

Figure 8.16: The histograms of point density and $1\times1m$ grid color-coded by point density for ALS and L-MMS data set.

path (as seen already in Fig. 8.2(c)). The ALS data show relatively homogeneous point density reaching around 15 points/m^2 in the middle area i.e. in the flightline overlap and can be as low as 8 points/m^2 on the edge of the flightlines (see Fig. 8.17(c)). The statistics in Fig. 8.17(a) show that the point density of the ALS dataset varies less over the acquisition area. This is because the measurement range and incidence angle are more uniform (see discussion in Section 8.1.2).

The histogram of mean ALS heights per grid cell in Fig. 8.17(a) shows a strong peak at approximately $1.5m$, and a less obvious peak at approximately $19m$. The first one indicates that the main part of the acquisition area is relatively flat and low. The second more extended peak indicates the average height of the dunes. The histogram of the mean L-MMS heights per grid cell in Fig. 8.17(b) does not have a second peak. Here the mean height as well as standard deviation of mean heights are lower that for the ALS data. However, the maximum mean L-MMS height is very high afound $42m$. It results from the unfiltered L-MMS points lying on the crane. Mean height values in Fig. 8.18(c) and 8.18(d) could be used as a first approximation of the DTM. Their difference is shown later in Fig. 8.19.

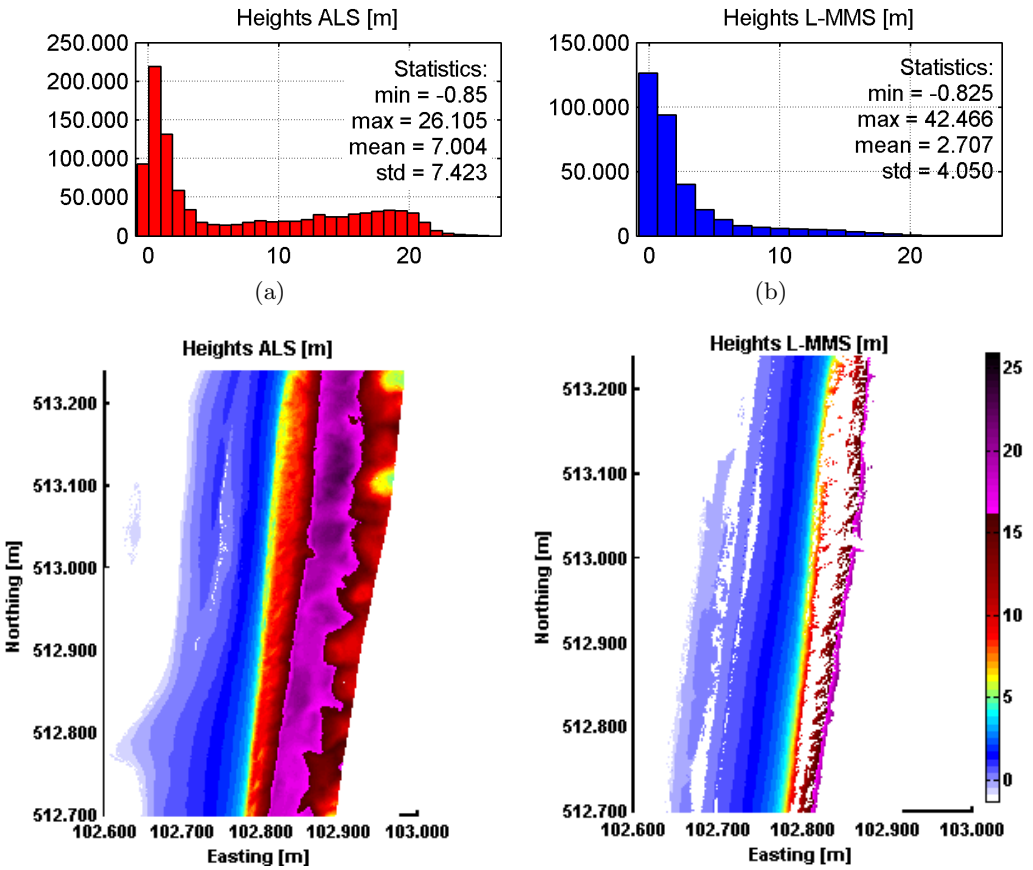

(a) (b)

(c) Mean heights for ALS dataset $\overline{Z}_{als}$. (d) Mean heights for L-MMS dataset $\overline{Z}_{lmms}$.

Figure 8.17: The histograms of mean heights per grid cell and $1\times1m$ grid color-coded by mean heights for ALS and MMS data set.

Histograms in Fig. 8.18(a) and 8.18(b) show the variation of heights within the grid cells. Most of the grid cells for ALS and L-MMS data have a standard deviation of heights below $5cm$. In case of ALS data (but not also the L-MMS) the distribution of standard deviation of heights has a longer tail, which indicates there are grid cells with a bigger σ_{Zals} value. As seen in Fig. 8.18(c) those grid cells lie in the dune area (red color). The intuitive reason is a sloped terrain of the dunes and or the non-filtered vegetation points. However, the mean of standard deviation of heights is smaller for L-MMS and is $3.6cm$ (see Fig. 8.18(b)). The standard deviation of σ_{Zmms} is $11.3cm$ and exceeds the one for ALS data that is $8.6cm$. The reason is again the non-filtered data, where points on higher objects increase the height variation within the grid cells.

The standard deviation σ_Z gives an information on how the terrain morphology is changing. In Fig. 8.18(c) lines of higher σ_{Zals} are observed on the beach. The lines could indicate break-lines in the DTM (sudden change of the terrain surface). Besides, areas

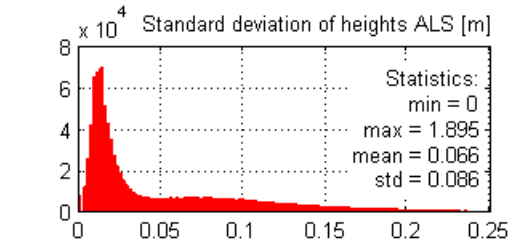

(a)

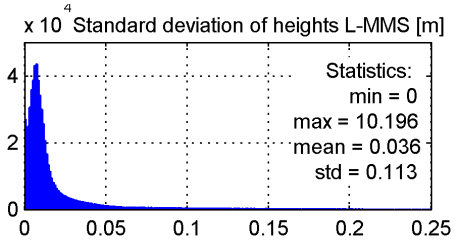

(b)

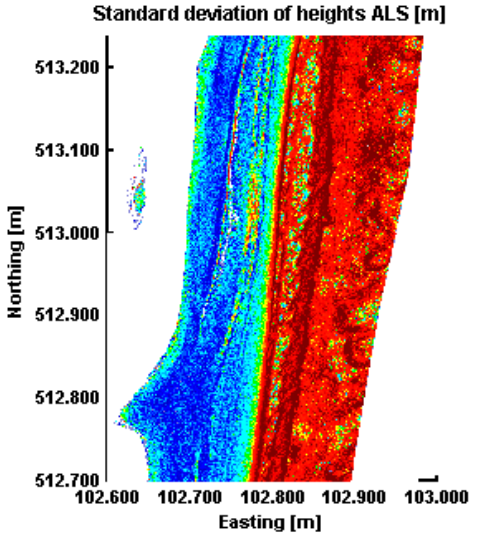

(c) Standard deviation of heights σ_{Zals} for ALS dataset.

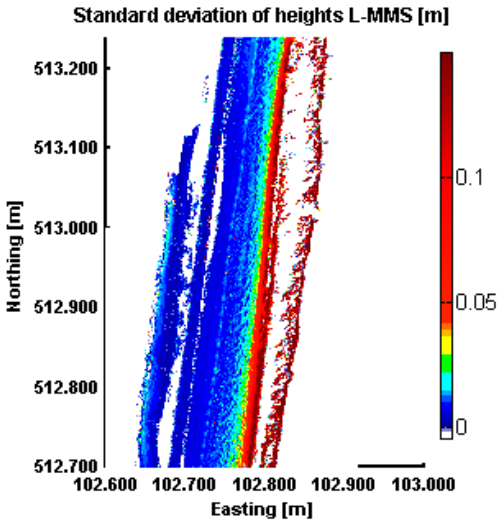

(d) Standard deviation of heights σ_{Zlmms} for L-MMS dataset.

Figure 8.18: The histograms of standard deviation of heights and $1\times1m$ grid color-coded by standard deviation of heights for ALS and MMS dataset.

of lower σ_{Zals} are observed in the dune area. Since they occur as spots on the equally sloped terrain in north-south direction (compare to the Fig. 8.17(c)), the lower σ_{Zals} could indicate the non-vegetated parts of the dunes.

The height differences between the L-MMS and ALS datasets are computed for the overlapping grid cells. The mean ALS heights as shown in Fig. 8.17(c) are subtracted from the corresponding mean L-MMS heights shown in Fig. 8.17(d). The result is shown in Fig. 8.19, where the visualized area has a different shape than the one in figures Fig. 8.17(c) and 8.17(d). Note that just the overlapping grid cells are taken into account.

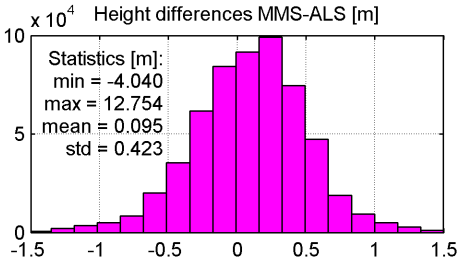

(a)

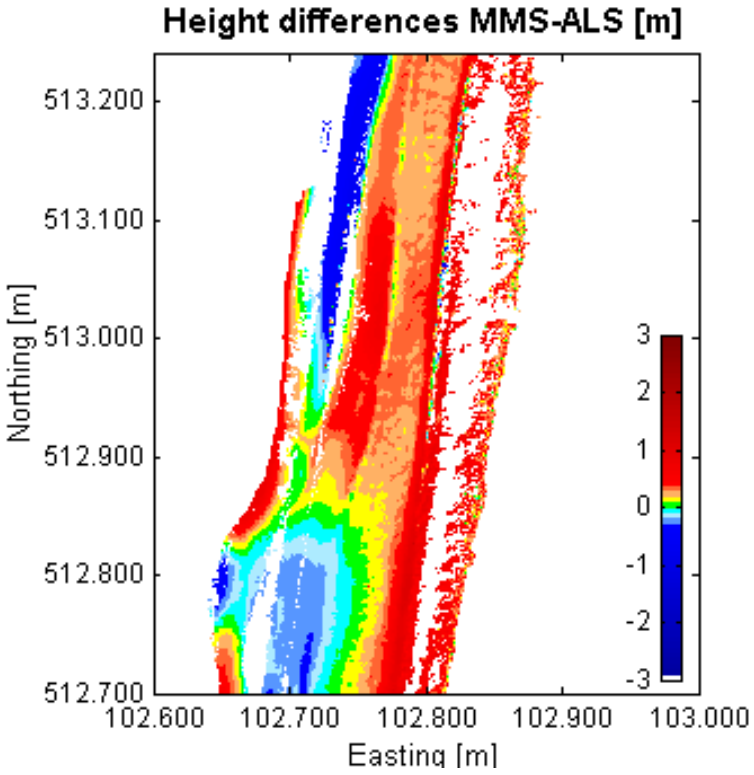

(b) Height differences L-MMS - ALS data sets.

Figure 8.19: The histograms of height differences and $1 \times 1m$ grid color-coded by height differences between overlapping grid cells of ALS and L-MMS data set.

The main objective of computing the height differences is to detect the changes or terrain. However, in this computation the non-filtered L-MMS data are used and the filtered

ALS data still include a few vegetation points in the dune area. Besides, the height differences might include the inaccuracies of the acquisition techniques.

The mean of the height differences is a positive value and equals $9.5cm$ (see histogram in Fig. 8.19(a)). Thus, the measured laser points of the non-filtered L-MMS dataset are in general higher than the laser points of filtered ALS data. A high standard deviation of height differences, which is $0.423m$, is a result of big height differences in the dune area.

The biggest height differences, i.e. more than $0.5m$, occur in the pre-dune and dune area. The differences are mostly positive (reddish color), which means that the L-MMS data are higher. This might result from using non-filtered L-MMS data or from the real rise of terrain heights in this area. The height differences on the sandy beach are more reliable (no vegetation points) and are most probably the result of the morphologic changes in the time interval between acquisitions in April (ALS data) and November (L-MMS data). The biggest height differences (bigger than $\pm 0.5m$) occur close to the waterline and in the foreshore. Blue color indicates the areas where the L-MMS data are lower, thus the sand might be washed away by waves. On the opposite, the red color indicates the areas where the L-MMS data are higher than ALS, thus areas where probably sand was deposited.

8.5 Summary

In Section 8.2 the quality of a laser L-MMS DTM is estimated using the original L-MMS data and a linear interpolation model. Results are presented for the chosen test area, which represents the Dutch beach as acquired by the L-MMS StreetMapper system. A tilted plane is fitted to each grid cell containing more than 3 terrain laser points. First, a proper estimation of the observation variances is needed. In this research the theoretical standard deviation of terrain laser point heights σ_{Zi}, as computed in Section 5.3, is considered in the weight matrix of Moving Least Squares (MLS). In this way a bigger weight is given to more precise observations. The final result in Section 8.2 is the spatial variation of the StreetMapper DTM quality. It is described very detailed for $1 \times 1m$ grid. For 90% of the grid cells, including more than 3 terrain laser points, the estimated DTM precision is better than $2.56cm$.

The main influencing factor on the grid point height precision σ_{DTM} is the number of terrain points n (FD1) included in the DTM grid point computation. This is because a higher number of observations (i.e. terrain laser points) enables elimination of the observation noise. The consequence is, that the precision of the adjusted grid point height σ_{DTM} improves with the increasing number of terrain laser points and exceeds the height precision σ_{Zi} of the individual terrain laser points. The average grid point height precision σ_{DTM} equals to $0.47cm$ and the average individual terrain laser point heigh precision σ_{Zi} equals $3.29cm$. The average number of points n for the grid cells entering the MLS is high and equals 69 points.

It is presumed that the L-MMS laser points are free from systematic errors. In Chapter 5 the analysis of height differences between identical points partly confirmed this assumption. However, an independent validation of the L-MMS data would be needed using external data set of higher quality.

The primary objective of the L-MMS and ALS data comparison is to validate the L-MMS heights. But the results in Section 8.2 showed higher L-MMS DTM precision than the one that can be expected for ALS DTM. Therefore the ALS data could not be used for L-MMS data validation. However, the densities and heights of laser points are compared through a grid of the same size and position. It is found that the laser point density is much higher in case of the L-MMS data. The point density per square meter is on average 72 points for L-MMS non-filtered data and 11 points for ALS filtered data. On the other hand, the ALS data more uniformly cover the whole beach area from the coastline to the back of the dunes. Moreover, the differential DTM is computed for the overlapping grid cells. The mean of height differences is $9cm$ and the standard deviation is $0.4m$. Therefore, it is concluded that the resulting height differences are most probably a consequence of the actual morphologic changes that occurred during six months. Besides, the height inaccuracies of both data sets might partly influence those height differences.

Chapter 9

Conclusions and recommendations

This master thesis focused on the evaluation of the performance of a laser Land-based Mobile Mapping System (L-MMS) to measure the morphology of sandy coasts. More precisely, the quality of the measured 3D laser points and the derived Digital Terrain Model (DTM) were investigated. This means that the height precision was calculated for each laser point and also for each grid point within a grid of $1 \times 1m$ size.

The conclusions of this work are presented in Section 9.1 and recommendations are discussed in Section 9.2.

9.1 Conclusions

In this section the conclusions that followed from the practical results of the thesis are given. They are structured according to the research questions defined in the introduction.

1. What error components contribute to the performance of the laser L-MMS system? The components of the laser L-MMS error budget were defined according to the mathematical model of direct geo-referencing. Thus, seven error components were distinguished according to their source: Global Positioning System (GPS), Inertial Measurement Unit (IMU), range, scan angle, lever arm from laser scanner to IMU and from IMU to GPS antenna, and boresight angle components. In the pre-analysis of all contributing random error sources, it was concluded that the random error budget mainly depends on GPS and laser scanner errors. In case of the pilot-project Egmond aan Zee high quality GPS/INS sensors were used. Besides, the positioning precision is high, because of good GPS visibility on the open acquisition area, i.e. the Dutch beach. Therefore, it was concluded that further improvements to the StreetMapper system should focus upon quality improvements in the laser scanners performance. It was shown that especially the scan angle error causes a fast increase of the vertical positioning error. Because of the scan angle error definition, it was evident that the beam divergence is a significant factor to the overall system performance. Choosing a laser scanner with narrower beam width, will result in more precise 3D laser point position. The effect of IMU error sources on the quality of the 3D laser point coor-

dinates was small, due to the short ranges normally measured with the L-MMS system. Finally, it was shown that the expected quality of laser points changes strongly with the range but less with the scan angle. Further away from the trajectory the total a-priori 3D laser point positioning error grew to approximately 5 to 6cm at a range of 45m.

2. What is the quality of the individual L-MMS laser points? In this research the quality of the individual L-MMS laser point was estimated as a height precision. Two approaches were used. In the first approach a theoretical height precision of the laser points was defined by the random error propagation through the geo-referencing formula. The random errors considered in this first order error model result arise from:

1. The L-MMS measurements resulting in the measurement precision of laser points.
2. The non-perpendicular scanning geometry resulting in the geometrical precision of laser points.

Both the measuring and geometrical precision decreased with the range. Besides, the geometrical precision decreased very fast, when the incidence angle approached 90°. The median measuring precision was 2.88cm. The spatial variation of the measuring precision showed an interesting "zebra" pattern, i.e. fast but small changes of the measuring precision across the drive-line. To explain this pattern in more detail, the analysis of individual error components included in the first order error model and computed for individual laser points would be needed. The geometrical precision was on average very small. Its median equals 8.6mm. The reason was that most of the L-MMS laser points have small ranges and therefore the beam divergence was small too. In other words, the intersection geometry of the laser beam with the scanner surface is on average good.

In the second approach a relative Quality Control (QC) procedure was developed to asses empirical laser point height precision. The QC results, employing height differences between so-called identical points, showed very small numbers. The average precision of the height differences between identical points lying on the horizontal plane was 3mm. Because the mean of the signed height differences was almost zero for three different analyzed cases, it was concluded that almost no systematic errors were presented in the derived laser point cloud. In case of the scanner overlap the mean deviated from the zero for few sub millimeters. However, just 608 identical points were considered in computation. To state with certainty that there is a bias in the laser scanner calibration parameters more laser points should be analyzed. In case of the drive-line overlap 5 473 identical points were found and the mean of their height differences equaled zero to a sub-milimeter scale. Thus, it is concluded there was no bias in GPS/INS position measurements. The analysis of the correlation between height differences of identical points and the geometric attributes did not show a clear trend.

In the last step of the individual laser point quality evaluation, the results of the theoretical and empirical quality measures were compared. The theoretical RMSE of height differences between identical points was approximately 28 times bigger than the empirical RMSE. Most likely the theoretical precision was estimated too pessimistic, because the

random errors of the measurements and calibration parameters were mostly overestimated. On the other side the empirical precision might result in a smaller value for the following reason. When computing the height differences between close-by laser points and estimating the precision of those hight differences, some errors like GPS error and geometrical error might cancel out. Considering those reasons and recomputing the theoretical precision of height differences, the theoretical RMSE was still 9 times bigger than the empirical. Another explanation of the small empirical precision measures was, that the distance between L-MMS laser points might be smaller than is the size of their error ellipsoid. Therefore, it might happen that the points reflected from different parts of the surface appear closer together than they really are. Thus, choosing the nearest neighbors might already minimize the empirical error. To prove the (un)reliability of the identical points method, it was concluded that more research should be done on the identical points assumption. The theoretical precision of the individual laser points should be verified by using reference data.

3. What is the quality of the derived laser L-MMS DTM? The laser L-MMS DTM quality was estimated using the original L-MMS data and a linear interpolation model. A tilted plane was modeled by a weighted Moving Least Squares (MLS) for each grid cell containing more than 3 terrain laser points. The theoretical standard deviation of terrain laser point heights σ_{Zi} was considered in the weight matrix of MLS. In this way, a bigger weight was given to more precise observations. With this method a spatial variable DTM quality was obtained.
It was found that the main influencing factor on the grid point height precision σ_{DTM} was the number of terrain points n (FD1), which was included in the DTM grid point computation. That was, because a higher number of observations (i.e. terrain laser points) enabled partly elimination of the observation noise. The consequence was, that the precision of the adjusted grid point height σ_{DTM} improved with an increasing number of terrain laser points and exceeded the height precision σ_{Zi} of the individual terrain laser points. Using the StreetMapper terrain laser points, the average precision of grid point height σ_{DTM} equaled to $0.47cm$ and the average theoretical precision of individual terrain laser points σ_{Zi} equaled $3.29cm$. On average the grid cells entering the MLS included 69 terrain points. Therefore, the estimated DTM precision was better than $2.56cm$ for 90% of those grid cells. The Dutch Ministry of Transport, Public Works and Water Management (RWS, Rijkswaterstaat) required a $1\times1m$ DTM having precision better then $10cm$. Thus, it was concluded those requirements can be easily met employing laser L-MMS.

4. What are the advantages of the laser L-MMS technique compared to Airborne Laser Scanning (ALS)? The laser L-MMS was evaluated as a promising new technique for measuring coastal morphology. From the comparison with the ALS technique, which is most widely used till now, it was concluded that the L-MMS system is very flexible. This means it can be deployed immediately after the storm and can measure also at night. Besides, the vehicle can drive at any speed, can turn and measure in any direction. Thus, a high L-MMS laser point resolution can be obtained on particular areas

to model small details on the coast. The comparison of the two real data sets, acquired by ALS in April 2008 and L-MMS in November 2008, showed that the L-MMS potentially offers higher quality of the laser point cloud and derived DTM. That is:

- The L-MMS laser point cloud has a higher density of on average 72 points per square meter. ALS has 11 points per square meter.
- The individual expected precision of L-MMS laser points is on average $3.3cm$. The root mean square for ALS heights is estimated to be $7.8cm$ [Richardson, 2008].
- The L-MMS DTM precision is on average $4.7mm$ and is higher than the expected ALS DTM precision.

Because the L-MMS data quality was higher, the ALS data could not be used as a reference data to validate the L-MMS data. Instead, the differential DTM was computed for the overlapping grid cells. The mean of height differences was $9cm$ and the standard deviation was $0.4m$. Therefore, it was concluded that the resulting height differences are most probably a consequence of the actual morphologic changes that occurred during six months. Besides, the height inaccuracies of both data sets might partly influence those height differences.
The comparison showed that the disadvantage of the L-MMS against the ALS is the data coverage. The land based system as used in this research had difficulties to acquire the beach surface behind the elevated pre-dunes. A better L-MMS measurement set-up could partly eliminate those data voids, as explained in the following paragraph.

5. What L-MMS measurement set-up leads to optimal results for coastal monitoring? As concluded in answering research question two, the theoretical quality of the measured L-MMS laser points strongly varied over the acquisition area. It depended on the range and incidence angle. Besides, it was shown that those two geometric attributes influenced the laser point density and thus the DTM precision. Therefore, it was suggested to choose a measurement set-up that allows a good scanning geometry. This means that:

1. The measured ranges are shorter than $20m$, when scanning a horizontal surface.
2. The laser scanners are placed higher above the ground.
3. The vehicle is driving as close as possible to the elevated features.

Considering last two suggestions it was expected that the shadow effect behind elevated beach features would be reduced. This way the laser L-MMS DTM completeness and reliability would be improved.
Besides, to achieve a satisfying point density and thus DTM precision, the speed of the vehicle could be optimized. It was shown, that StreetMapper is capable to acquire 50 points per square meter or more at a speed of maximum 35 km/h and for ranges smaller than $10m$. The DTM evaluation showed that this spatial resolution was sufficient to achieve sub-centimeter DTM precision.
Analyzing the measured ranges on a relatively horizontal Dutch beach, it was concluded that StreetMapper can measure at least $50m$ wide strips. At larger distances almost no

energy was reflected back to the system, because the laser beam intersects the surface in a wide footprint. Lifting up the laser scanners would also increase the swath width.

9.2 Recommendations

During the research, various issues have been encountered that need attention in future research on this topic. Thus, in this section a list of recommendations is given.

Verifying the theoretical models of quality estimation. The evaluation of the laser point quality was based on the mathematical model, which includes estimated or expected random errors of L-MMS measurements and calibration parameters. The outcome of the systematic error propagation through a geo-referencing model was confirmed by the reference data in [Glennie, 2007b]. But in order to prove the random error propagation and moreover, to validate the influence of the scanning geometry on the laser point quality, an empirical test on the L-MMS data should be performed. It is recommended to scan a strip of a horizontal surface including sufficient number of ground control points. These points are usually measured by Real-Time Kinematic (RTK) GPS technique. Then the influence of the L-MMS measurements as well as of increasing range and incidence angle on the derived point cloud quality could be verified by the ground truth.

Improving the method of DTM quality estimation. The grid cells with less than 3 terrain laser points were not considered in the DTM computation and quality estimation. Therefore, another method to estimate the DTM quality for those grid cells should be considered, in order not to lose the L-MMS data and leave the area undefined. It was suggested to enlarge the grid cell size such that more than three laser points are considered in the grid point computation. Besides, areas without any terrain laser points, resulting from the shadow-effect or surface covered with a water, must be separately analyzed. If those gaps are not too big, the DTM could be interpolated providing a quality estimation employing one of the alternative methods; for example with the geometrical based approach described in [Kraus et al., 2004].

Assessment of the absolute 3D quality. In this analysis just the random errors in the L-MMS system measurements and calibration parameters were taken into account. The systematic biases, which lead to systematic errors in the derived point cloud, were assumed to be zero. They were not included into the error budget, because they were not known a-priori for this research and for the L-MMS system in hand (i.e. StreetMapper). But it should be noted that their influence on the laser point quality might be bigger and more significant than one of the random errors. An attempt was made to detect possible systematic errors using a relative QC of height differences between identical points. However, it is not known if the identical point method can reveal systematic errors. Thus, in this research just the relative accuracy (precision) was estimated. To asses the absolute quality of the L-MMS data and derived DTM, reference (external) data of higher accuracy should be used.

Furthermore, the presented quality measures focused just on the height (vertical) precision. The planimetric quality is of great importance for object extraction, e.g. positioning the poles on the beach. Besides, the horizontal precision is expected to be worse than the vertical, due to the bad scanning geometry further away from the trajectory on a relatively horizontal surface. Therefore in future research, also planimetry should be considered.

Evaluating the performance of the L-MMS for object extraction. In this research the main interest is the beach morphology and thus the quality of the vertical positioning. Once knowing the expected precision the L-MMS system data, the possibility to extract different objects on the beach could be investigated. For example, to answer the RWS question, if and what size of the litter can be detected in the point cloud. One recommendation as an extension of the work presented here is, to investigate more the outcome of the relative QC. The outstanding large height differences between identical points lying on the beach (had ranges smaller than $10m$) could indicate the position of very small litter.

Using L-MMS system of different characteristics. In this research the data of the StreetMapper system were evaluated. StreetMapper employs laser scanners having certain specifications and orientations. The random error budget results have showed that better scan angle and range accuracy could significantly improve the laser point quality. Besides, it is recommended to lift the laser scanners platform higher than $2m$. In mid-2003 a single laser scanner mounted on the $4.1m$ high pole was used by the Canadian Terrapoint company for the road surveys and mapping in Afghanistan [Newby and Mrstik, 2005]. This system as shown in Fig. 9.1(a) is a modified version of an airborne laser scanners [Shan and Toth, 2008]. Due to its success, Terrapoint developed a new and improved L-MMS system called Tactical Infrastructureand Terrain Acquisition Navigator (TITAN). It features an equipment pod containing the systems laser scanners, IMU, GPS receivers and digital cameras that is mounted on a hydraulic lift attached to the floor of an open-back pick-up truck (see Fig 9.1(b)). A hydraulic lift can raise and lower the instrument pod between two and four meters above the ground. Another system was developed at University of Florida Geosensing Engineering & Mapping research center [Fernandez, 2007]. This system called Mobile Terrestrial Laser Scanning (M-TLS) employs the Optech ILRIS laser scannr mounted on a lift. This lift has a stowed height of $1.97m$ and once deployed it extends to $9.45m$ (see Fig. 9.1(c)). As known to the author, the M-TLS is not yet capable of performing mapping operations in the dynamic mode.

To estimate the L-MMS data coverage in the pre-dues area using elevated laser scanner platform, a theoretical investigation of the visibility is needed. A introduction to this topic, i.e. DTM-based visibility analysis, is given in [Li and Chapman, 2005]. In Fig. 9.2 a viewshed concept is presented, that could be used to obtain the area visible from a L-MMS viewpoint. Based on this pre-analysis for a particular area of interest the optimal height of the laser scanner(s) above the ground could be calculated.

(a) So-called SideSwipe system devised by Terrapoint surveying the road in Afghanistan [Newby and Mrstik, 2005].

(b) Terrapoint's Tactical Infrastructure and Terrain Acquisition Navigator (TITAN) system [Glennie, 2007a].

(c) Mobile Terrestrial Laser Scanning System (MTLSS) [Fernandez, 2007].

Figure 9.1: Examples of a laser L-MMS systems with higher laser scanner platform.

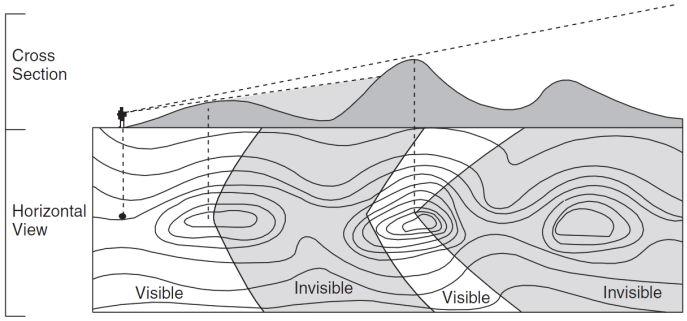

Figure 9.2: The viewshed concept to calculate areas visible from a certain viewpoint [Li and Chapman, 2005].

To eliminate the data voids resulting form the remaining water bodies on the beach, the solution might be to use a laser scanner that sends out the pulses with visible green wavelength. According to the physical properties of the electromagnetic waves, it is expected that visible green light penetrates shallow water and measures also the topography of surface few decimeters under the water. The infra red light in case of the StreetMapper laser scanners specularly reflects on the water surface.

Potential L-MMS topics to be investigated. Due to the limited time of this research, many interesting L-MMS topics were left undiscovered and are therefore shortly listed in the following.

- A potential useful extension of the laser L-MMS data is their combination with the additional L-MMS video or photo information. Coloring the laser point cloud with real world colors obtained from images could improve object extraction and vegetation monitoring. To extract the vegetation and monitor its growth is of special interest, because it is important for the dune subsistence.

- It should be investigated, whether laser point intensities hold information on the surface material properties. To distinguish wet and dry sand on the beach, or vegetation and sand on the dunes. Intensities are expected to be strongly related to the (ever changing) scanning geometry. Therefore, a method should be implemented that eliminate the effect of scanning geometry on laser point intensities.

- In order to be able to measure the beach immediately after a storm, it should be investigated what is the effect of the wind and blowing sand on the measurements. Also a strong sun light might cause problems. Therefore, it is recommended to study under what extreme weather condition laser L-MMS still works.

- Despite the introduction of advanced techniques for coastal monitoring, no single method is free from some major disadvantage. A further approach to integrate of techniques and their data is recommended. The ALS and L-MMS could be used as supplementary techniques to derive DTMs with a more complete coverage, and a high precision and spatial resolution. In [Bitenc et al., 2008] a Kite Aerial Photogrammetry (KAP) was tested for the beach monitoring. KAP could be used to acquire the dunes and the laser L-MMS data to precisely map the beach.

- One of the RWS requirements for the acquisition method was to obtain the final results close to the real-time. Therefore, one of the future L-MMS topic could be to investigate possibilities and limitations of L-MMS data real-time processing.

References

3D laser Mapping (2010). Company 3D laser Mapping. URL. Accessed February 2010 http://www.3dlasermapping.com.

Aarninkhof, S. G. J. (2003). Nearshore bathymetry derived from video imagery. PhD Thesis, Delft University of Technology.

Ackermann, F. and K. Kraus (2004). Grid based digital terrain models. In: *Geo Informatics*, vol. 7(6): pag. 28 - 31.

AHN (2010). The current elevation map of the Netherlands. URL http://www.geo-loket.nl/index.html, accessed February 2010.

Alharthy, A., J. Bethel and E. Mikhail (2004). Analysis and Accuracy Assessment of Airborne Laserscanning System. In: *XXth ISPRS Congress, Istanbul, Turkey*. pag. 144–149.

AMC (2001). Robust statistics: a method of coping with outliers. Analytical Methods Committee (AMC).

Arya, S., D. M. Mount, N. S. Netanyahu and R. Silverman (1998). An Optimal Algorithm for Approximate Nearest Neighbor Searching in Fixed Dimensions. In: *Journal of the ACM (JACM)*.

Baltsavias, E. (1999a). Airborne laser scanning: existing systems and firms and other resources. In: *ISPRS Journal of Photogrammetry and Remote Sensing*, vol. 54, nr. 2-3: pag. 164 - 198.

Baltsavias, E. P. (1999b). Airborne laser scanning: basic relations and formulas. In: *ISPRS Journal of Photogrammetry & Remote Sensing*, vol. 54: pag. 199 to 214.

Barber, D. and J. Mills (2007a). Rapid Mapping Techniques in coastal environments: monitoring the coastline. URL http://www.rics.org/, accessed February 2010.

Barber, D. M., D. Holland and J. P. Mills (2008a). Change detection for topographic mapping using three-dimensional data structures. In: *International Archives of Photogrammetry, Remote Sensing and Spatial Information Sciences*, vol. 37 (B4): pag. 1177 - 1182. URL http://www.isprs.org/congresses/beijing2008/proceedings/4_pdf/206.pdf.

Barber, D. M. and J. P. Mills (2007b). Vehicle based waveform laser scanning in a coastal environ-ment. In: *The 5th International Symposium on Mobile Mapping Technology (MMT07)*. Padua, Italia, 29.-31.5.2007, CIRGEO (Interdepartmental Research Center for Cartography, Photo-grammetry, Remote Sensing and GIS) University of Padua.

Barber, D. M., J. P. Mills and S. Smith-Voysey (2008b). Geometric validation of a ground-based mobile laser scanning system. In: *ISPRS Journal of Photogrammetry and Remote Sensing*, vol. 63, nr. 1: pag. 128–141.

Bitenc, M., M. R. Bloemsma, K. Duijnmayer, K. Lin, S. Pizziol, M. A. G. Saleh, J. Stam, E. Widiastuti and Y. Yin (2008). Novel techniques for coastal monitoring: A case study near monster Ter Heijde. Tech. rapp., Delft University of Technology. The final report of the Geomatics Synthesis Project 2008.

Blug, A., C. Baulig, M. Dambacher, H. Wolfelschneider and H. Hofler (2007). Novel platform for terrestrial 3D mapping from fast vehicles. In: *International Archives of Photogrammetry, Remote Sensing and Spatial Information Sciences*, vol. 36: pag. 7–12.

Bruton, A. M. (2000). Improving the Accuracy and Resolution of SINS/DGPS Airborne Gravimetry. PhD Thesis, The University of Calgary.

CERC (1984). *Shore protection manual*. Coastal engineering Research Center, Department of the Army, Waterways Experiment Station.

Coastalwiki (2010). URL http://www.coastalwiki.org, accessed February 2010.

Collins, D. B. and R. Kayen (2006). Land-Based Lidar Mappinga New Surveying Technique to Shed Light on Rapid Topographic Change. URL http://pubs.usgs.gov/fs/2006/3111/, accessed February 2010.

Colorado (2010). University of Colorado, Geographer's Craft materials. URL http://www.colorado.edu, accessed February 2010.

Cox, C. (2009). Subject: Questions regarding the StreetMapper system. Personal communication. 3D Laser Mapping Ltd.

Cramer, M. (1997). GPS/INS Integration. In: D. Fritsch and D. Hobbie (red.), *Photogrammetric Week '97*. pag. 1–10. Stuttgart, Germany.

Csanyi, N. and C. Toth (2007). Improvement of LiDAR Data Accuracy Using LiDAR-Specific Ground Targets. In: *Photogrammetric Engineering & Remote Sensing*, vol. 73, nr. 4: pag. 385–396.

Deltares (2010). The Dutch institute for Delta Technology. URL http://www.deltares.nl, accessed February 2010.

El-Sheimy, N. (2005). An Overview of Mobile Mapping Systems. In: *Proceedings of the FIG Working Week 2005 and GSDI-8*. pag. 16–21.

Ellum, C. and N. El-Sheimy (2002). Land-based mobile mapping systems. In: *Photogrammetric Engineering and Remote Sensing*, vol. 68(1): pag. 13–17; 28.

Faro (2010). URL http://www.faro.com, accessed February 2010.

Fernandez, J. C. (2007). *Scientific applications of the mobile terrestrial laser scanner (MTLS) system.* Master's thesis, University of Florida.

Gandolfi, S., M. Barbarella, E. Ronci and A. Burchi (2008). Close photogrammetry and laser scanning using a mobile mapping system for the high detailed survey of a high density urban area. In: *Proceedings of ISPRS congress in Beijing.*

Geomaat (2010). URL http://cms.geomaat.pageflow.nl, accessed February 2010.

Giaccari, L. (2010). Fast K-Nearest Neighbors Search. URL http://www.advancedmcode.org/gltree.html, accessed February 2010.

Glennie, C. (2007a). A kinematic terrestrial LiDAR Scanning system. In: *InsideGNSS*, pag. 22–31.

Glennie, C. L. (2007b). Rigorous 3D Error Analysis of Kinematic Scanning Lidar Systems. In: *Journal of Applied Geodesy*, vol. 1: pag. 147–15.

Grejner-Brzezinska, D. (2000a). Mobile Mapping Technology: Ten Years Later, part I. In: *2000Surveying and Land Information Systems*, vol. 61, nr. 2: pag. 79–94.

Grejner-Brzezinska, D. (2000b). Mobile Mapping Technology: Ten Years Later, part II. In: *Surveying and Land Information Systems*, vol. 61, nr. 3: pag. 83–100.

Grinstead, B., A. Koschan, D. P. A. Gribok and M. A. Abidi (2005). Vehicle-borne Scanning for Detailed 3D Terrain Model Generation. In: *SAE (Society of Automotive Engineers) Commercial Vehicle Engineering Congress.* URL http://imaging.utk.edu/publications/papers/2005/215_BGrinstead_SAE.pdf, chicago, IL, November, 2005.

Habib, A. F., M. Al-Durgham, A. P. Kersting and P. Quackenbush (2008). Error budget of lidar systems and quality control of the derived point cloud. In: *The International Archives of the Photogrammetry, Remote Sensing and Spatial Information Sciences.* Beijing, vol. 37, part B1, pag. 203 – 209.

Hampel, F. R., E. M. Ronchetti, P. J. Rousseeuw and W. A. Stahel (1985). *Robust statistics.* John Wiley, New York.

Hasegawa, H. (2006). Evaluations of LIDAR reflectance amplitude sensitivity towards land cover conditions. URL http://www.gsi.go.jp/ENGLISH/RESEARCH/BULLETIN/vol-53/53-6.pdf.

Hodgson, M. E. and P. Bresnahan (2004). Accuracy of Airborne LiDAR Derived Elevation: Empirical Assessment and Error Budget. In: *Photogrammetric Engineering and Remote Sensing*, vol. 70, nr. 3: pag. 331 - 337.

Hohner, N. L. (2008). Oregon tests mobile scanning: Business and technology trends in 3D imaging for engineering/construction/manufacturing. In: *On line article in e-newsletter SparView*, vol. 6, nr. 13.

Huaxing, L. (2008). *Advances in Digital Terrain Analysis*, Springer Berlin Heidelberg, hfdst. Modelling Terrain Complexity (Section 2), pag. 159–176. Lecture Notes in Geoinformation and Cartography.

Huber, P. J. (1981). *Robust Statistics*. John Wiley, New York.

Hunter, G. (2006). Accurate Terrestrial Laser Scanning from a Moving Platform. In: *Geomatics World, PV Publications*, vol. July/August 2006: pag. 29–30. URL http://www.streetmapper.net/articles/Paper%20-%20Geomatics%20World%20-%20Accurate%20Terrestrial%20Laser%20Scanning%20-%20July%202006.pdf.

IGI (2010). Engineering German company Ingenieur-Gesellschaft fuer Interfaces. URL. Accessed February 2010 http://www.igi-systems.com.

Karel, W. and K. Kraus (2006). Quality parameters of digital terrain models. In: J. Hhle (red.), *EuroSDR seminar on Automated Quality Control of Digital Terrain Models. Aalborg, Denmark.* URL http://people.land.aau.dk/~jh/dtm_checking/SpecialContribution.pdf.

Kraus, K., C. Briese, M. Attwenger and N. Pfeifer (2004). Quality Measures for Digital Terrain Models. In: *International Archives of Photogrammetry and Remote Sensing, XXth ISPRS Congress, Istanbul, Turkey, 1223 July 2004, CD-ROM.*

Kraus, K., W. Karel, C. Briese and G. Mandlburger (2006). Local accuracy measures for digital terrain models. In: *The Photogrammetric Record*, vol. 21, nr. 116: pag. 342 – 354. URL http://www3.interscience.wiley.com/cgi-bin/fulltext/118627452/PDFSTART.

Kremer, J. and G. Hunter (2007). Performance of the StreetMapper Mobile LIDAR Mapping System in Real World Projects. In: Fritsch (red.), *Photogrammetric Week'07*, Wichmann Verlag, Heodelberd, pag. 215–225. URL http://www.ifp.uni-stuttgart.de/publications/phowo07/240Kremer.pdf.

Leica (2009). URL http://www.leica-geosystems.com.

Lemmens, M. (2007). Terrestrial Laser Scanners. In: *GIM International*, vol. 21, nr. 8: pag. 41–45.

Li, J. and M. A. Chapman (2005). Introduction to MMS Special Issue. In: *Photogrammetric Engineering & Remote Sensing Journal of the American Society for Photogrammetry and Remote Sensing (PE&RS)*, vol. 71, nr. 4: pag. 6. URL http://www.asprs.org/publications/pers/2005journal/april/intro.html.

Li, Z., Q. Zhu and C. Gold (2005). *Digital terrain modeling: principles and methodology.* New York: CRC Press.

Lichti, D. D. and S. J. Gordon (2004). Error Propagation in Directly Georeferenced Terrestrial Laser Scanner Point Clouds for Cultural Heritage Recording. In: *Proceedings of FIG Working Week 2004*. Athens, Greece, May 22 27, 2004.

Lichti, D. D., S. J. Gordon and T. Tipdecho (2005). Error models and propagation in directly georeferenced terrestrial laser scanner networks. In: *Journal of Surveying Engineering*, vol. 131 (4): pag. 135 - 142.

Lutz, E., T. Geist and J. Stotter (2003a). Investigations of airborne laser scanning signal intensity on glacial surfaces Utilizing comprehensive laser geometry modelling and orthophoto surface modelling (A case study: Svartisheibreen, Norway). In: *ISPRS Workshop on 3-D reconstruction from airborne laserscanner and INSAR data*. Dresden, Germany.

Lutz, E., T. Geist and T. Sttter (2003b). Investigations of airborne laser scanning signal intensity on glacial surfaces-utilizing comprehensive laser geometry modelling and orthophoto surface modelling (a case study: Svartisheibreen, Norway). In: *IAPRS, 34(3/W 13). Dresden*. pag. 143 –148.

Madeira, S. R., L. C. Bastos, A. M. Sousa, J. F. Sobral and L. P. Santos (2005). Automatic traffic signs inventory using a mobile mapping system. URL http://gec.di.uminho.pt/psantos/docs/Papers/GP2005.pdf.

Mikhail, E. M. (1976). *Observations and least squares*. IEP-A Dun-Donnelley Publisher, New York.

Mills, J. P., S. J. Buckley, H. L. Mitchell, P. J. Clarke and S. J. Edwards (2005). A geomatics data integration technique for coastal change monitoring. URL www.interscience.wiley.com, published online in Wiley InterScience.

NCK (2010). Netherlands Centre for Coastal Research. URL. Accessed February 2010 http://www.nck-web.org.

Newby, S. and P. Mrstik (2005). LiDAR on the level in Afghanistan. URL www.gpsworld.com.

Peel, R. (2008). 3D mapping: A new perspective on managing grid assets. URL http://pepei.pennnet.com/, article on-line in Power Engineering International Magazine.

Pfeifer, N., G. Gorte and S. O. Elberink (2004). Influences of vegetation on laser altimetry - analysis and correction approaches. In: *IAPRS XXXVI 8/W2, Freiburg, Germany*.

Raquet, J. F. (1998). Development of a Method for Kinematic GPS-Carrier Phase Ambiguity Resolution Using Multiple Reference Receivers. PhD Thesis, The University of Calgary.

RealityMapping (2010). A service company Reality Mapping. URL. Accessed February 2010 http://www.realitymapping.co.uk.

Redstall, M. (2006). Accurate Terrestrial Laser Scanning from a Moving Platform. In: *Geomatics World, PV Publications*, vol. July/August 2006: pag. 28–30. URL http://www.streetmapper.net/articles/Paper%20-%20Geomatics%20World%20-%20Accurate%20Terrestrial%20Laser%20Scanning%20-%20July%202006.pdf.

Redstall, M. (2007). Rapid 3D Terrestrial Mapping from a Moving Vehicle. Civil Engineering Surveyor. URL www.streetmapper.net/.../Paper%20-%20Civil%20Engineer%20Surveyor%20-%20Rapid%203D%20terrestrial%20mapping%20-%20awaiting.pdf, awaiting publication.

Richardson, L. R. A. (2008). Kwaliteitsdocument laseraltimetrie Projectgebied Kust 2008. Tech. rapp., Rijkswaterstaat.

Riegl (2010). Riegl homepage. URL http://www.riegl.com, accessed February 2010.

Rijkswaterstaat (2009). Pilot laserscanmeting op strand bij Egmond. Tech. rapp., Rijkswaterstaat, Ministry of Transport, Public Works and Water Management. 29. April 2009.

Rijn, L. C. V. and D. J. Walstra (2002). Basic features of morphodynamics at the Egmond site on the short term time scale of storms. In: L. C. van Rijn, B. G. Ruessink and J. P. M. Mulder (red.), *Coast3D-Egmond. The Behaviour of a Straight Sandy Coast on the Time Scale of Storms and Seasons*, Aqua Publications, Amsterdam, pag. I1 – I16.

RWS (2010). Ministry of Transport, Public Works and Water Management. URL http://www.rijkswaterstaat.nl/, accessed February 2010.

Schaer, P., J. Skaloud, S. Landtwing and K. Legat (2007). Accuracy Estimation for Laser Point-cloud including Scanning Geometry 2007. In: *5th International Symposium on Mobile Mapping Technology (MMT2007), Padua, Italy.*

Schwarz, K. P. and N. El-Sheimy (2004). Mobile mapping systems - state of the art and future trends. In: *International Archives of Photogrammetry, Remote Sensing and Spatial Information Sciences*, vol. vol. 35, Part B: pag. 10.

Schwarz, R. (2009). Subject: Questions about the accuracy and precision. Personal communication. RIEGL Laser Measurement Systems GmbH.

Shan, J. and C. K. Toth (red.) (2008). *Topographic laser ranging and scanning : principles and processing.* Taylor & Francis Group.

Skaloud, J. (2006). Reliability of direct georeferencing phase an overview of current approaches and possiblities. In: *EuroSDR Official Publication 51.* pag. 143 - 168.

Song, J. H., S. H. Han, K. Yu and Y. Kim (2002). Assessing the Possibility of Land-cover Classification Using Lidar Intensity Data. In: *IAPRS 34, 4. Graz, 9-13 September.*

Soudarissanane, S., R. Lindenbergh and B. Gorte (2008). Reducing the error in the terrestrial laser scanning by optimizing the measurement setup. In: *International Archives of Photogrammetry, Remote Sensing and Spatial Information Science*, vol. 37, Part B5: pag. 615–620.

Soudarissanane, S., R. Lindenbergh, M. Menenti and P. Teunissen (2009). Incidence Angle Influence on the Quality of Terrestrial Laser Scanning Points. In: *ISPRS Workshop Laserscanning'09*. Paris, France; September 1 2, 2009.

StreetMapper (2010). Mobile Mapping System StreetMapper. URL http://www.streetmapper.net, accessed February 2010.

Tao, C. V. (1998). Mobile Mapping Technology for Road Network Data Acquisition. In: *Journal of Geospatial Engineering*, vol. 2, nr. 2: pag. 1–13.

TerraSolid (2010). Terrasolid software solutions. URL http://www.terrasolid.fi, accessed February 2010.

Teunissen, P. J. G., D. G. Simons and C. C. J. M. Tiberius (2008). *Probability and observation theory*. Department of Earth Observation and Space systems, Faculty of Aerospace engineering, Delft University of Technology, The Netherlands.

Toth, C. and D. Grejner-Brzezinska (2001). Modern mobile mapping: On-the-fly image processing. In: *Proc. of the 3rd International symposium on mobile mapping*. pag. 12. January 3-5, Cairo, Egypt.

Waarden, P. van (2009). Subject: Figures of the acquisition area. Personal communication. Rijkswaterstaat Data-ICT-Dienst.

Wagner, W. (2005a). Physical Principles of Airborne Laser Scanning. In: *Paper from University Course: Laser scanning - Data Acquisiton and Modeling, TU Vienna, 6. 10.-7. 10.*, Institute of photogrammetry and remote sensing.

Wagner, W. (2005b). Physical Principles of Airborne Laser Scanning. In: *University Course: Laser scanning - Data Acquisiton and Modeling. Institute of photogrammetry and remote sensing, TU Vienna, 6. 10.-7. 10. 2005.*

Warner, W. S., R. W. Graham and R. E. Read (1996). *Small format aerial photography*. Whittel.

Wotruba, L. F., E. Morsdorf and D. Nuesch (2005). Assessment of Sensor Characteristics of an Airborne Laser Scanner using Geometric Reference Targets. In: *ISPRS Working Group III/3 Workshop Laser Scanning 2005*, pag. 1–6.